Development of Protic Acidic Ionic Liquids for Intermediate Temperature Proton-exchange Membrane Fuel Cell Applications (IT-PEMFC)

Zur Erlangung des akademischen Grades eines

Doktors der Naturwissenschaften

(Dr. rer. nat.)

von der KIT-Fakultät für Chemie und Biowissenschaften
des Karlsruher Instituts für Technologie (KIT)

genehmigte

Dissertation

von

M. Sc. Hanno Maria Schütz

1. Referent: Prof. Dr. Stefano Passerini
2. Referent: Prof. Dr. Rolf Schuster
Tag der mündlichen Prüfung: 13.12.2023

“It is a capital mistake to theorise before one has data. Insensibly one begins to twist facts to suit theories instead of theories to suit facts.”

Sherlock Holmes in A Scandal in Bohemia, Sir Arthur Conan Doyle[1]

Kurzfassung

Brennstoffzellen allgemein und vor allem mit Polymerelektrolyt nach dem Bauprinzip der Protonenaustauschmembran-Brennstoffzelle (engl. PEMFC), sind ein wichtiger Baustein, um Treibhausgasneutralität in der Energiewirtschaft und dem Transportsektor zu erreichen. Während PEMFC mit perfluorsulfonsäure-basierten Membranen bei Betriebstemperaturen bis ca. 80 °C und mit phosphorsäure-getränktem Polybenzimidazol über etwa 140 °C eingesetzt werden können, sind derzeit noch keine geeigneten Membransystemen für den Mitteltemperaturbereich um 120 °C (engl. intermediate temperature, IT) verfügbar.

Deshalb wird in dieser Doktorarbeit vorgeschlagen H_3PO_4 als wasserfreien Protonenleiter durch Protische Saure Ionische Flüssigkeiten (engl. PAcILs) für den Einsatz in IT-PEMFC bei 120 °C zu ersetzen.

Während das generelle Konzept Protischer Ionischer Flüssigkeiten (engl. PILs) als protonenleitendes Additiv in PEMFC Membranen literaturbekannt ist, wurden im ersten Teil dieser Arbeit neuartige PAcILs mit funktionalisierten alkylammonium-basierten Kationen mit stark sauren Sulfonsäure, Schwefelsäure und Phosphorsäure Gruppen in der Alkylkette hergestellt und charakterisiert. Durch eine getrennte Variation sowohl der Substituenten an der Ammoniumgruppe als auch der Säuregruppen an der Alkylkette wurden die fünf verschiedenen PAcILs *N*,*N*-diethyl-3-sulfopropan-1-ammonium Triflat [$DESPA^+$][TfO^-], *N*,*N*-diethyl-*N*-methyl-3-sulfopropan-1-ammonium Triflat [$DEMSPA^+$][TfO^-], 2-Sulfoethylammonium Triflat [SEA^+][TfO^-], 2-(Sulfooxy)ethan-1-ammonium Triflat [$SOEA^+$][TfO^-] und 2-(Phosphonooxy)ethan-1-ammonium Triflat [PEA^+][TfO^-] erhalten. Von diesen Kandidaten sind [$DESPA^+$][TfO^-] und [$DEMSPA^+$][TfO^-] die vielversprechendsten PAcILs für eine IT-PEMFC Anwendung, da sie eine hohe thermische Stabilität aufweisen, nicht zu einer Kristallisation neigen und stabil in Gegenwart von Wasser, sowohl bei Raumtemperatur also auch bei 120 °C sind.

Um die PAcILs umweltfreundlicher und tendenziell günstiger in der Produktion zu machen, wird im zweiten Teil der Untersuchung das Triflat Anion durch das fluorfreie Hydrogenmethandisulfonat [$HMDS^-$] Anion ersetzt. Eine übereinstimmende thermische Stabilität von [$DESPA^+$][$HMDS^-$] und [$DESPA^+$][TfO^-] sowie eine vergleichbare ionische Leitfähigkeit bei 120 °C wurde beobachtet. Die vergleichbare ionische Leitfähigkeit der beiden PAcILs trotz der deutlich höheren Viskosität von [$DESPA^+$][$HMDS^-$] wird durch eine Entkopplung der ionischen Leitfähigkeit und der viskosen Bewegung erklärt.

Diese Entkopplung zeigt sich in der geringeren Pseudo-Aktivierungsenergie für die ionische Leitfähigkeit im Vergleich zur viskosen Bewegung und im sehr stark ausgeprägten superionischen Verhalten von [$DESPA^+$][$HMDS^-$] im Walden Plot ($\Delta W > 0.8$). Diffusionskoeffizienten der verschiedenen Protonen in [$DESPA^+$][$HMDS^-$] aus Feldgradienten Spin-Echo NMR Messungen (engl. PGSE NMR) zeigen, dass für Temperaturen über 100 °C das Proton der aziden Sulfonsäure Gruppe im Kation durch einen kooperativen Grotthuss-artigen Transportmechanismus wandert. Dabei kommt es vermutlich zu Protonentransferreaktionen zwischen Kationen und Anionen. Unterhalb von 100 °C wurde ein bisher noch nie beschriebener Übergang von dem kooperativen zu einem vehikularen Transportmechanismus beobachtet. Diese Beobachtung zeigt die Rolle des aziden Protons in der Seitenkette für eine erhöhte Protonenleitfähigkeit aufgrund des kooperativen Protonentransfermechanismus.

Schließlich wurde noch ein für die IT-PEMFC Anwendung breit genügendes elektrochemisches Stabilitätsfenster und der Beginn der Sauerstoffreduktionsreaktion (engl. ORR) in [$DESPA^+$][$HMDS^-$] bei mit [$DESPA^+$][TfO^-] vergleichbaren Potentialen beobachtet. Während die Sauerstoffsättigungskonzentration in beiden PAcILs ähnlich ist, ist der Diffusionskoeffizient von Sauerstoff in [$DESPA^+$][$HMDS^-$] deutlich niedriger als in [$DESPA^+$][TfO^-]. Die Tatsache, dass die diffusionslimitierte Stromdichte in [$DESPA^+$][$HMDS^-$] trotzdem in der gleichen Größenordnung wie in [$DESPA^+$][TfO^-] ist, kann wahrscheinlich dadurch erklärt werden, dass die langsame Diffusion des Sauerstoffes durch den sehr schnellen Protonentransfer mittels des kooperativen Mechanismus in der PAcIL kompensiert wird.

Aufgrund dieser Eigenschaften ist [$DESPA^+$][$HMDS^-$] eine hochgradig interessante PAcIL, sowohl aus wissenschaftlicher Sicht, also auch für eine mögliche IT-PEMFC Anwendung.

Abstract

Fuel cells, especially the proton-exchange membrane fuel cell (PEMFC) with a polymeric electrolyte, are important building blocks in the decarbonization strategy of the energy and transport sector. While PEMFC with perfluorosulfonic acid-based membranes can be operated at temperatures up to 80 °C and with phosphoric acid-doped polybenzimidazoles above 140 °C, there is a lack of suitable membrane systems for the attractive intermediate temperature (IT) range at about 120 °C.

Therefore, in this thesis protic acidic ionic liquids (PAcILs) are proposed as replacement for phosphoric acid as anhydrous proton conductor for IT-PEMFC applications at about 120 °C.

While the concept of protic ionic liquids (PILs) as dopant in PEMFC membranes was already discussed in literature, novel acidic PAcILs with functionalized alkylammonium type cation structures with strong acidic sulfonic, sulfuric and phosphoric acid groups in the alkyl chain are synthesized and characterized in the first part of this study. By independent variation of the substitution pattern at the ammonium moiety and of the acid group in the alkyl chain the five PAcILs *N*,*N*-diethyl-3-sulfopropan-1-ammonium triflate [$DESPA^+$][TfO^-], *N*,*N*-diethyl-*N*-methyl-3-sulfopropan-1-ammonium triflate [$DEMSPA^+$][TfO^-], 2-Sulfoethylammonium triflate [SEA^+][TfO^-], 2-(Sulfooxy)ethan-1-ammonium triflate [$SOEA^+$][TfO^-] and 2-(Phosphonooxy)ethan-1-ammonium triflate [PEA^+][TfO^-] were obtained. From these candidates [$DESPA^+$][TfO^-] and [$DEMSPA^+$][TfO^-] are the most promising PAcILs for IT-PEMFC application due to their thermal stability, reluctance to crystallization and stability in the presence of water, both at room temperature and 120 °C.

To make the PAcILs more environmentally and economically attractive, in the second part of the study, the triflate was replaced with the fluorine-free hydrogen methanedisulfonate [$HMDS^-$] anion. An identical thermal stability for [$DESPA^+$][$HMDS^-$] and [$DESPA^+$][TfO^-] and similar ionic conductivity at 120 °C was observed. The similar ionic conductivity of the two PAcILs despite the much higher viscosity of [$DESPA^+$][$HMDS^-$] was explained by a decoupling of the viscous flow and the ionic conductivity. This decoupling manifests in the lower pseudo-activation energy for the ionic conductivity compared to the viscous flow and in a strongly pronounced superionic behavior of [$DESPA^+$][$HMDS^-$] in the Walden plot ($\Delta W > 0.8$). Diffusion coefficients of the different protons from Pulsed-Field Gradient Spin-Echo (PGSE) NMR measurements reveal, that above 100 °C the proton of the sulfonic acid group in the cation structure moves via a cooperative Grotthuss-like proton transfer mechanism.

Thereby probably a proton transfer between the cations and anions takes place. Towards lower temperatures, an unprecedented switch from the cooperative to a vehicular proton transport mechanism was observed. This finding demonstrates the role of the acidic proton in the side chain for an enhance proton conductivity due to a cooperative proton conduction mechanism.

Finally, a sufficiently wide electrochemical stability window for IT-PEMFC application and an oxygen reduction reaction onset potential for [$DESPA^+$][$HMDS^-$] comparable to [$DESPA^+$][TfO^-] were observed. While the oxygen saturation concentration in both PAcILs is similar, the oxygen diffusion coefficient in [$DESPA^+$][$HMDS^-$] is significantly lower than in [$DESPA^+$][TfO^-]. The fact that the diffusion-limited current density in [$DESPA^+$][$HMDS^-$] is in the same order of magnitude compared to [$DESPA^+$][TfO^-] could probably be explained by a compensation of the slower oxygen diffusion by the fast proton transport through the cooperative proton transport mechanism in the PAcILs.

Due to these properties, [$DESPA^+$][$HMDS^-$] is a highly attractive PAcIL both from a scientific and an IT-PEMFC application perspective.

Contents

Abbreviations of cation and anion structures

Cation structures	
chemical name, (trivial name)	[Abbreviation]
N-**m**ethyl-3-**s**ulfo**p**ropan-1-**a**mmonium, (**m**ethyl**s**ulfo**p**ropyl**a**mmonium)	[MSPA$^+$]
N,*N*-**di**ethyl-3-**s**ulfo**p**ropan-1-**a**mmonium, (**di**ethyl**s**ulfo**p**ropyl**a**mmonium)	[DESPA$^+$]
N,*N*-**di**ethyl-N-**m**ethyl-3-**s**ulfo**p**ropan-1-**a**mmonium, (**di**ethyl**m**ethyl**s**ulfo**p**ropyl**a**mmonium)	[DEMSPA$^+$]
2-aminoethanesulfonic acid, (**s**ulfo**e**thyl**a**mmonium)	[SEA$^+$]
2-(**s**ulfo**o**xy)**e**than-1-**a**mmonium	[SOEA$^+$]
2-(**p**hosphonooxy)**e**than-1-**a**mmonium	[PEA$^+$]
alkylmethylimidazolium	[XMIM$^+$] e.g. [4MIM$^+$] for butylmethylimidazolium*
methylimidazolium	[HMIM$^+$]
1-(4-**b**utyl**s**ulfonic acid)-3-**hex**yl**im**idazolium	[BSHexIM$^+$]
ethylimidazolium	[HEIM$^+$]
dialkylammonium	[NXYHH$^+$] e.g. [N33HH$^+$] for dipropylammonium*
trialkylammonium,	[NXYZH$^+$] e.g. [N222H$^+$] for triethylammonium*
tetraalkylammonium	[NXYZV$^+$] e.g. [N2222$^+$] for tetraethylammonium*
bis(2-**m**ethoxy**e**thyl) **a**mmonium	[BMEA$^+$]
2-(methylazaniumyl)ethanesulfonic acid, (2-**s**ulfo**e**thyl**m**ethyl**a**mmonium)	[2-SEMA$^+$]
penta**f**luoro**p**yridinium	[HPFP$^+$]
pyrrolidinium	[PryHH$^+$]
dialkylpyrolidinium	[PryXY$^+$] e.g. [Pry14$^+$] for N-butyl-N-methyl-pyrrolidinium*
protonated 1,8-**di**aza**bi**cyclo[5.4.0]-**u**ndec-7-ene	[DBU$^+$]

*X,Y,Z,V in the abbreviations correspond to the number of C-atoms in nitrogen bond alkyl chains. H stands for a nitrogen bond hydrogen.

Anion structures	
chemical name, (trivial name)	[Abbreviation]
hydrogen**m**ethane**d**i**s**ulfonate	[$HMDS^-$]
methane**d**i**s**ulfonate	[MDS^{2-}]
tri**f**luoromethanesulfonate, (triflate)	[TfO^-]
hydrogensulfate	[HSO_4^-]
methane**s**ulfonate, (mesylate)	[MS^-]
ethanoate, (**ac**etate)	[Ac^-]
tri**f**luoro**ac**etate	[$TFAc^-$]
tetrachloroaluminate	[$AlCl_4^-$]
bis(pentafluoro**et**hylsulfonyl)**i**mide	[$BETI^-$]
bis(**t**ri**f**luoromethane**s**ulfonyl)**i**mide	[$TFSI^-$]
pentafluorobenzenesulfonate	[PF^-]
bis(**f**luoro**s**ulfonyl)**i**mide	[FSI^-]
(trifluoromethanesulfonyl)-(nonafluorobutanesulfonyl)imide	[$IM14^-$]

1. Theoretical Part: Instrumentation & Techniques

1.1 Nuclear Magnetic Resonance Spectroscopy (NMR)

The progress in the construction of the nuclear magnetic resonance (NMR) spectrometers, especially the introduction of pulse techniques and Fourier-transform spectrometers (Nobel prize in Chemistry for R. R. Ernst 1991)[2,3] with the now achievable high-resolution and relatively short measurement time, makes NMR spectroscopy the gold-standard for molecular structure characterization, especially in organic and polymer chemistry. Additionally, this progress inspired scientists to unravel the full capability of NMR spectroscopy by the development of advanced methods like the Pulsed-Field Gradient Spin-Echo (PGSE) technique, which allows the investigation of physical and chemical parameters beyond molecular structure like the molecular diffusion coefficient of individual species in mixtures.

NMR spectroscopy was widely used in this thesis and therefore will be introduced in details. Measurements of liquid samples with state-of-the-art Fourier-transform spectrometers were performed, therefore only the theory behind this type of device is being discussed. First the basic concepts of NMR spectroscopy will be explained. At the end of this section the more advanced Pulsed-Field Gradient Spin-Echo (PGSE) technique is introduced briefly.

The spinning motion of the positive charged atomic nucleus with its nuclear spin angular momentum **p** generates a magnetic momentum **μ** (eq.(1)). Both the magnetic momentum **μ** and the nuclear spin angular momentum **p** are directly proportional to each other with the proportionality factor γ, the magnetogyric ratio[4] (sometimes called gyromagnetic ratio instead), a constant for each isotope. γ lies between $6.73 \cdot 10^7$ $T^{-1}s^{-1}$ and $26.75 \cdot 10^7$ $T^{-1}s^{-1}$ for typical isotopes like ^{1}H, ^{13}C, ^{19}F and ^{31}P [5].

$$\boldsymbol{\mu} = \gamma \circ \mathbf{p} \tag{1}$$

Like all physical momenta **p** and **μ** can be described as vectors. Due to the quantum mechanical uncertainty principle only the z-component of **p** and **μ** are known and the xy-components are undefined. Therefore, in this vector model (Figure 1) **p** and **μ** lie on a cone around the z-axis.

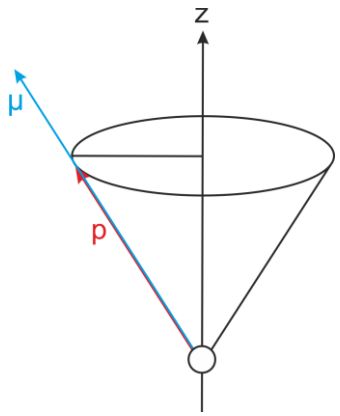

Figure 1 Schematic representation of the nuclear spin angular momentum ***p*** *and the magnetic momentum* ***μ*** *in the vector model.*

The "intensity" of **p** i.e. the modulus of the vector, can be calculated from the nuclear spin quantum number I of a nucleus by equation (2).

$$|\boldsymbol{p}| = \sqrt{I(I+1)}\,\frac{h}{2\pi} \tag{2}$$

Equation (2) shows that only nuclei with a nuclear spin I≠0 (more precis spin quantum number I) have a spin angular momentum **p** and thereby a magnetic momentum **μ**. The nuclear spin I itself originates from the proton and neutron spin. According to a rule of thumb a nucleus with an odd number of protons and neutrons (odd-odd nuclei, like D or ^{14}N) or an odd number of at least one species (odd-even, even-odd nuclei like ^{13}C or ^{19}F) has a non-zero nuclear spin. While in theory all nuclei with a non-zero nuclear spin, and therefore a magnetic momentum (see eq.(1) and (2)) could be studied by NMR measurements , experimental investigations are often limited to spin-1/2 nuclei, because the huge signal broadening by the quadrupole momentum for atoms with a nuclear spin larger than 1/2 prevents measurements with required spectral resolution. Therefore, all the further description focuses on NMR experiments with nuclei with a spin of 1/2.

Without an external magnetic field, the different orientations of the magnetic momentum **μ** are energetically degenerated (Figure 3a). When the sample is placed in a magnetic field B (in positive z-direction of a cartesian coordinate system[a]) of an NMR spectrometer (Figure 2) this has two effects on the magnetic momenta **μ** in the sample.

In analogy to the precession of a spinning top around its own axis of inertia in the earth gravitation field, the magnetic momentum vector starts precessing with the so-called Larmor frequency ν_L around the magnetic field axis.

[a] More accurate B in the equations corresponds to the magnetic flux density of the magnetic field in Tesla T. 1T=1V·s·m^{-2} or in SI units 1T=1kg·A^{-1}·s^{-2}.

The relationship between Larmor frequency ν_L and the external magnetic field B is given by equation (3).

$$\nu_L = \frac{\gamma}{2\pi} \cdot B \tag{3}$$

From equation (3) it can be seen, that the Larmor frequency depends on the strength of the external magnetic field. In addition, due to the relationship to the magnetogyric momentum it is a material constant for a given value of the magnetic field. For ^{1}H nucleus and a magnetic field of 9.5 T ν_L has a value of 400 MHz. For ^{13}C and ^{19}F the Larmor frequency is for the same field instead about 100 MHz and 376 MHz, respectively[6].

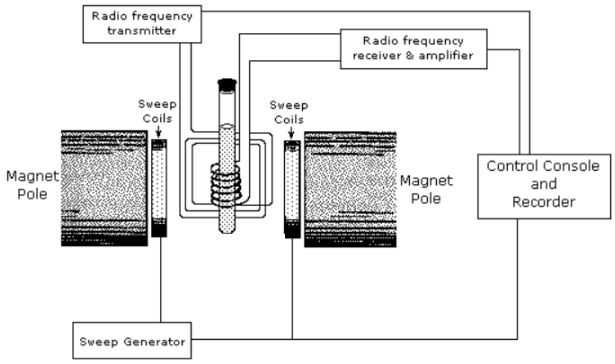

Figure 2 Schematic of an NMR spectrometer. The N_2 and He cooling circuits for the magnet coils are omitted in the drawing for the sake of clarity. "Diagram of NMR spectrometer " by Pavan M. V. Raja & Andrew R. Barron, reprinted from[7], licensed under CC BY 4.0, the sample spinning arrow was removed from the original image.

In addition to the precession of the magnetic momentum vector in the external magnetic field, the energetic degeneration of the different orientations of the magnetic momentum vector is lifted and the nuclear Zeeman-splitting occurs, when an external field is applied. The orientation of the nuclear magnetic momentum **μ** is quantized and a nucleus with a spin I, has 2I+1 possible orientation in the external field. For a 1/2 spin nuclei the two possible different orientations are called spin-up (magnetic spin quantum number m_I=1/2) and spin-down state (m_I= -1/2) and are symbolized by the ↑ and ↓ arrows or by α and β, respectively. The orientation of **μ** in the direction of the magnetic field (with B in positive z-direction the α-state) becomes energetically favored compared to the antiparallel orientation of **μ** (β-state) (Figure 3a). The energy splitting between the two spin states can be calculated by equation (4).

$$\Delta E = \gamma \cdot \frac{h}{2\pi} \cdot B = \nu_L \cdot h \tag{4}$$

This energy splitting is direct proportional to the strength of the magnetic field B, which the nuclei is exposed to and the proportionality factor contains again γ. From equation (4) it is obvious, that the splitting is larger for a stronger magnetic field. For the same magnetic field strength, the splitting for a nucleus with larger γ value is bigger.

This energy difference ΔE directly influences the population of both states in thermal equilibrium. The ratio of the population difference could be described by a Boltzmann distribution. Due to the slightly lower energy of the α-state with the nuclear spin parallel to the magnetic field, this state has a minimal larger population compared to the β-state. However, even with the strongest available magnetic fields the excess is as small as 1 atom in 10^4 atoms [6]. All the different magnetic momentum vectors in a sample can be summed up to a bulk magnetization vector M_0. Due to the population excess of the α-state for the individual magnetic moments M_0 points towards the positive z-direction, too. While the magnetic momentum vectors have a preferential orientation along the external magnetic field in z-direction, in the xy-plane they are randomly distributed on the precession cone. Due to this random distribution the xy-components cancel out each other when the individual magnetic moments are summed and the bulk magnetization vector M_0 lies on the z-axis in the vector model of NMR (Figure 3b).

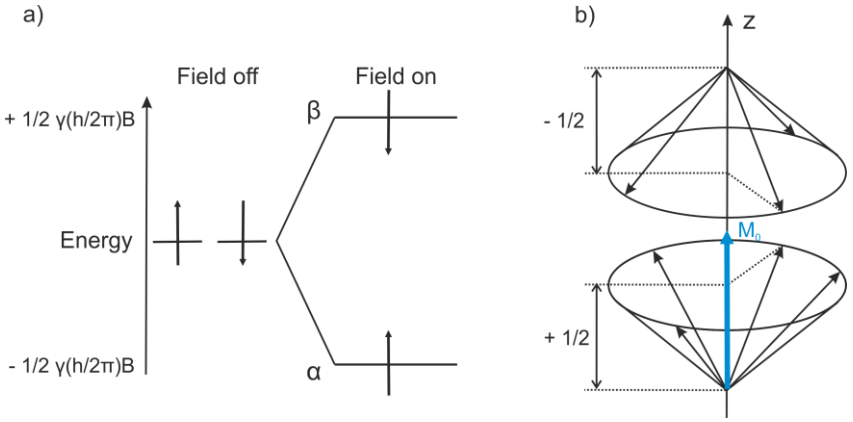

Figure 3 a) Schematic energy diagram of the nuclear spin levels of ^1H. b) individual spins and bulk magnetization M_0 in the vector model.

The above-described situation with the static magnetic field corresponds to the thermal equilibrium state. The system will stay in this state with the slightly higher population of the α-state and the bulk magnetization vector M_0 will therefore be a static vector on the positive z-axis as long as the external static magnetic field is switch on. For any kind of spectroscopy however the investigated system has to be perturbated from its equilibrium for example by an incident electromagnetic wave to provoke a system response. From this response the spectroscopist could gain inside in the structure of the investigated system. If the energy of the incident electromagnetic wave corresponds to the energy difference by the nuclear-Zeeman splitting, absorption, is the dominant process.

Equation (4), shows, that an incident electromagnetic wave with the Larmor frequency fulfills this resonance condition. For a magnetic field in the range of 9.5 T the Larmor frequencies of common nuclei lie in the MHz region- the typical radio frequency (RF) range.

The absorbed energy of the RF wave, will cause a spin flip from the α-state to the energetic higher β-state. As a consequence, the depletion of the population excess of the α-state the magnetization vector M_0 bends from the z-axis toward the xy-plane. Depending on the angle the magnetization bends the RF pulse is classified e.g. as 90° pulse when M_0 vector lies completely in the xy-plane after the spin flip. The nucleus relaxes back to the ground state (α-state) by heat emission to its surrounding. Therefore, this process is called spin-lattice relaxation. The corresponding time for this relaxation is called longitudinal relaxation time or T_1[8]. As relaxation progresses, the magnetization realigns itself back towards the z-axis. When multiple measurements are accumulated to improve the signal-to-noise ratio, it's important that the delay between individual measurements is longer than T_1. Choosing a delay shorter than T_1 results in the system not fully recovering, and therefore, with each accumulated measurement, the signal increases less than for a fully recovered system. If two signals are compared this leads to a wrong signal ratio and therefore to an erroneous interpretation of the data.

In addition to the slow longitudinal relaxation, transverse relaxation, or spin-spin relaxation, also plays a crucial role in NMR signal generation. After the spin flip, the nuclear spins are coherent. Consequently, the magnetization M_0 observed immediately after the RF pulse is at its maximum in the xy-plane. However, since individual nuclear spins have slightly different Larmor frequencies, a dephasing effect occurs and the magnetization decays. This so-called free induction decay i.e. the drop of the magnetization with time after the RF pulse is displayed in Figure 4a) for ethanol in fully deuterated dimethyl sulfoxide (DMSO-d_6). By Fourie transformation the Larmor frequencies of the individual nuclei in the sample are obtained (Figure 4b).

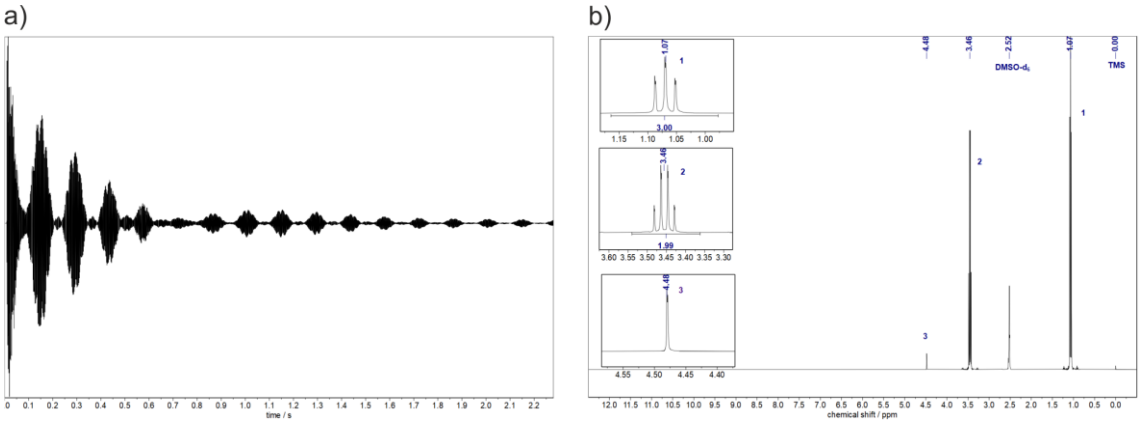

Figure 4 exemplary ^{1}H-NMR of ethanol in DMSO-d_6. a) Free induction decay (FID) b) the NMR spectrum after Fourier transformation.

But why do the different nuclei of one kind of isotope in a molecule have different Larmor frequencies? As obvious from equation (3) the Larmor frequency depends on the magnetic field the nucleus is exposed to. The effective magnetic field B_{eff} experienced by a nucleus slightly deviates from the external magnetic field B of the NMR spectrometer due to shielding and deshielding effects. The electron movement in the electronic cloud around the atomic core induce a magnetic field, that reduce or enhances B to the value of B_{eff}. The shielding/deshielding can be expressed by the unit less shielding constant σ_s.

$$B_{eff} = B(1 - \sigma_S) \tag{5}$$

Interactions and quantum mechanical effects which alter the electron density and distribution influence the shielding. Some examples to illustrate the shielding and deshielding effect are given in Figure 5.

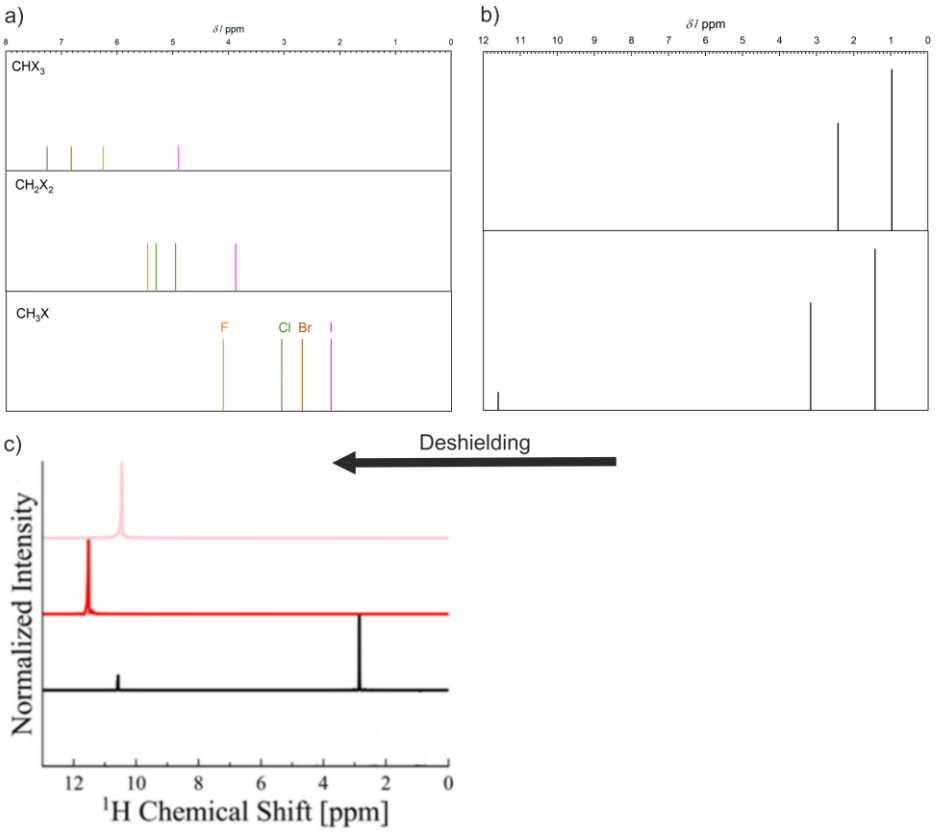

Figure 5 Examples for shielding/deshielding effect in ^{1}H-NMR spectroscopy. Proton peak shift of a) different halomethanes. b) Triethylamine (top) and Triethylammonium chloride (bottom). Data are taken from the Spectral Data Base SDBSWeb : https://sdbs.db.aist.go.jp (National Institute of Advanced Industrial Science and Technology[9], Date of access 16.06.2023). Values of diluted samples in $CDCl_3$, CCl_4 or cyclohexane are referenced to TMS c) ^{1}H-NMR of neat trifluoromethanesulfonic acid (pink), trifluoroacetic acid (red) and methanesulfonic acid (black). Figure 5c)is reproduced with permission from [10] ©2020 Elsevier

Electron withdrawing substituents like halogen atoms reduce the electron density of an atomic nucleus in vicinity and thereby led to a less strong reduction of the external magnetic field i.e. a deshielding. For example, the hydrogen atoms in halomethanes are deshielded. In the homologous row the deshielding increases with the increasing electronegativity of the attached halogen from iodine to fluorine (Figure 5a). Also, with increasing number of electron withdrawing groups the deshielding increases (Figure 5a bottom to top). However, the examples of the haloforms already demonstrate that further effects beside the electronegativity influence the deshielding, because for $CHCl_3$ and $CHBr_3$ the deshielding is stronger than for CHF_3. For these examples, the disruption of the trend might originate from orbital interactions of the halogen atoms.

The electron withdrawing effect i.e. deshielding effect is especially pronounced for positive charged neighboring atoms. In a solution of triethylammonium chloride the protons in the methylene group adjacent to the positive charge nitrogen is more deshielded than in absence of a positive charge in triethylamine. The deshielding effect increases the closer the investigated nucleus is to the charged atom. Therefore, the R_3NH^+ proton, directly bond to the positive charged nitrogen atom is strongly deshielded (Peak at 11.6 ppm in Figure 5b).

In acids electron withdrawing substituents increase both the acidic strength and the deshielding of the proton. Therefore, deshielding can be used to estimate the acidic strength. In Figure 5c the peaks of the acids with the electron withdrawing fluorine atoms i.e. trifluoromethanesulfonic and trifluoroacetic acid are slightly more deshielded than methanesulfonic acid.

In the ^{1}H-NMR spectrum of ethanol in Figure 4b) these deshielding effects are visible, too. Therefore, the signals of the protons adjacent to the oxygen atom (signal 2&3) are shifted compared to the signal of the methylene group (signal 1). The ^{1}H atom of the hydroxyl group (signal 3) is strongly deshielded and therefore shows a significant downfield shift. Due to the specific chemical environment each type of functional group appears in a characteristic frequency range in the spectrum.

While in the early years of NMR spectroscopy the frequency or magnetic field strength was plotted on the x-axes of a spectrum nowadays the chemical shift δ is used to eliminate the dependency of the peak position on the applied magnetic field strength or the measurement frequency of the device. δ is defined according to equation (6) as the difference of the measured Larmor frequency of a nucleus in the sample to the frequency in a reference compound and is normalized to the spectrometer frequency i.e. the frequency of the exciting RF pulse.

$$\delta\ [ppm] = \frac{\nu_L(sample) - \nu_L(refrence)}{\nu(RF - pulse)} \cdot 10^6 \qquad (6)$$

Due to the small differences of the Larmor frequencies of individual nuclei (maximum a few kHz) in comparison to the excitation frequency (hundreds of MHz) the chemical shift is given in parts per millions (ppm). The IUPAC proposes tetramethylsilane $Si(CH_3)_4$ (TMS) as reference for ^{1}H-NMR spectroscopy. In practice often instead of the primary reference TMS the solvent residual peak from only partial deuterated solvent molecules is used as secondary reference for the chemical shift.

Measurements can be performed of neat or diluted sample. For the dilution in ^{1}H-NMR spectroscopy usually deuterated solvents are used to suppress the otherwise to intense solvent signal. If protic solvents like deuterated water (D_2O) are used there is a D-H exchange of acidic protons in the sample and the corresponding signals vanish. In dry DMSO-d_6 no such exchange appears and the signals of the acidic protons are visible, too. However, the interaction with the solvent will influence the spectrum both due to analyte solvent interactions and in case of an equilibrium between different compounds in the sample by shifting the equilibrium. Such an equilibrium might be the protonation equilibrium between an acid and base precursor of a protic ionic liquid (PIL). To observe the neat sample a coaxial configuration is used, were the sample is flame-sealed in a capillary and the deuterated solvent is filled in the gap between the capillary and the tube or vice versa.

Especially for measurements of diluted samples exchange effects might be important[11]. These exchanges might be for example between a sulfonic acid (SO_3H) group and water. Depending on the exchange rates the peak shape changes. For a on NMR timescale slow exchange the peaks from both SO_3H and H_3O^+ might be visible as sharp well separated peaks (Figure 6a). With increasing exchange rate the peaks get broader. At some exchange rate only, a single peak is visible (Figure 6b). With increasing exchange rate this peak becomes narrow and might be erroneous assigned to an individual functional group (Figure 6c). The chemical shift is the population weighted average of the chemical shift of both neat compounds. In the experiments in this dissertation, with highly acidic groups such exchange effects are often observed especially in the presents of traces of water for example from not completely dry NMR solvents.

While in neat samples usually broad peaks are obtained in diluted samples also the fine structure by spin-spin coupling might be visible. The fine structure is a useful information for the interpretation of a NMR spectrum. In the exemplary spectrum of ethanol in Figure 4b) a singlet, quartet and triplet are visible. The spins of magnetically inequivalent atoms might couple to each other. Thereby a ^{1}H nuclei, which couples with n other H-atoms gives a multiplet with n+1 signals. The intensity ratios between the different peaks in a multiplet follows for protons the Pascal's triangle.

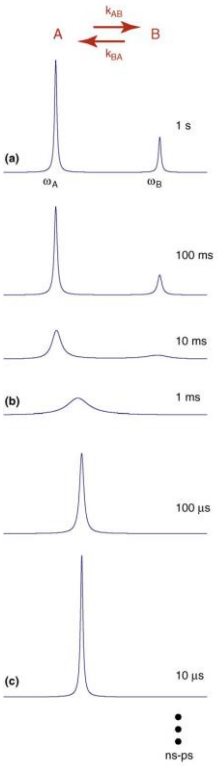

Figure 6 Simulated NMR spectra for a two-side exchange process. The numbers beside the graphs correspond to $(k_{AB}+k_{BA})^{-1}$. *Reprinted with permission from* [11]. *Copyright ©2009 Elsevier Ltd.*

The intensity of each multiplet or more accurate the peak area is proportional to the number of nuclei which produce the signal. Therefore, if one peak can be assigned to a certain number of protons the peak area can be normalization to this value. The peak used for the normalization might be from the investigated compound itself or from an internal or external reference in the coaxial capillary configuration.

Finally, briefly the concept of Pulsed-Field Gradient Spin-Echo (PGSE) technique will be introduced[12]. This kind of experiment allows to measure the diffusion coefficient of a species. Therefore, beside the radio frequency for the spin flip also pulsed-magnetic field gradients are used. Possible sequences of RF pulses and magnetic field gradients are displayed in Figure 7. The time dependent signal decay thereby follows an exponential function which is directly proportional to the diffusion coefficient of interest D and the "b" parameter and the signal intensity without field-gradient I_0. "b" itself depends on the pulsed gradient program i.e. on δ the duration of magnetic field-gradient pulse, G to the amplitude of the field-gradient and Δ the time between the gradient pulses (eq.(7))[12].

In a typical PGSE experiment the intensity I as function of b is recorded. b is thereby scanned only by the alteration of the gradient strength G, while all the other parameters of the pulsed-gradient sequence are kept constant.

$$I(b) = I_0 e^{-bD} \quad \text{With } b = \gamma^2 G^2 \delta^2 (\Delta - \delta/3) \tag{7}$$

By fitting I(b) to equation (7) the diffusion coefficient for each investigated nucleus can be obtained.

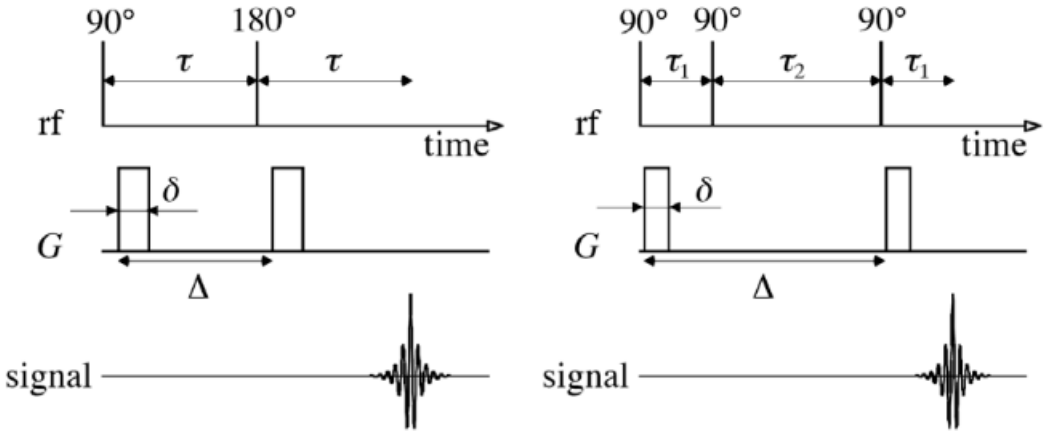

Figure 7 Schematic of a PGSE experiment with 90°-180° Hahn echo sequence or 90°-90°-90° stimulated echo sequence. δ is the duration of the magnetic pulse, Δ the diffusion time between the pulses and G the amplitude of the magnetic pulses. Reprinted with permission from [12] *© 2010 Elsevier B.V.*

1.2 Thermal Analysis

1.2.1 Thermogravimetric Analysis (TGA)

By thermogravimetric analysis (TGA) the mass change of a sample is investigated as function of temperature or exposure time at a constant temperature. This provides information on temperature-dependent alteration of the sample material. Chemical reactions like thermal decomposition or oxidation are examples for typical processes investigated by thermogravimetric (TG) experiments. Beside this TGA is used in some cases to study the sample composition e.g. to determine the amount of inorganic filler or solvent in polymers.

For the measurement a small amount of sample, usually several mg, is filled in a thermally stable crucible. Typical crucible materials are aluminum and ceramics. The crucible with the sample is then placed on the sample holder in the thermogravimetric analyzer. The main parts of a thermogravimetric analyzer are the balance and the furnace (Figure 8)

The balance could be located below or above the furnace. Balances below the oven (Figure 8) could be based on electromagnetic force compensation without a physical reference weight, but all required corrections are applied in post-processing by a computer. For a balance above the oven a balance scale with a reference weight could be used. This type of balance is for example based on the null-balance principle and might use an optoelectrical read-out. Thermal effects from the furnace on the balance are mitigated by a thermal shielding. This is achieved for example with a cooling water circuit between furnace and balance. The sample in the furnace is only connected to the balance by the sample holder. To protect the balance from damage by volatile or gaseous species from the sample e.g. decomposition products, the balance compartment is flushed with a protective gas like N_2. The furnace itself is continuously flushed with another gas stream. The gas stream in the furnace continuously renews the atmosphere and thereby prevents an enrichment of evaporation or decomposition products in the atmosphere. Such enrichment has to be avoided because it might alter the outcome of the measurement i.e. led to a self-inhibition of a decomposition or evaporation process. By the selection of the gas in the furnace different processes can be studied. Typically, inert gases like N_2 or Ar, or oxidizing atmospheres like synthetic air (80 v% N_2 20 v% O_2) or even pure O_2 are used. The type of gas is one factor, which influences the result of a TG experiment.

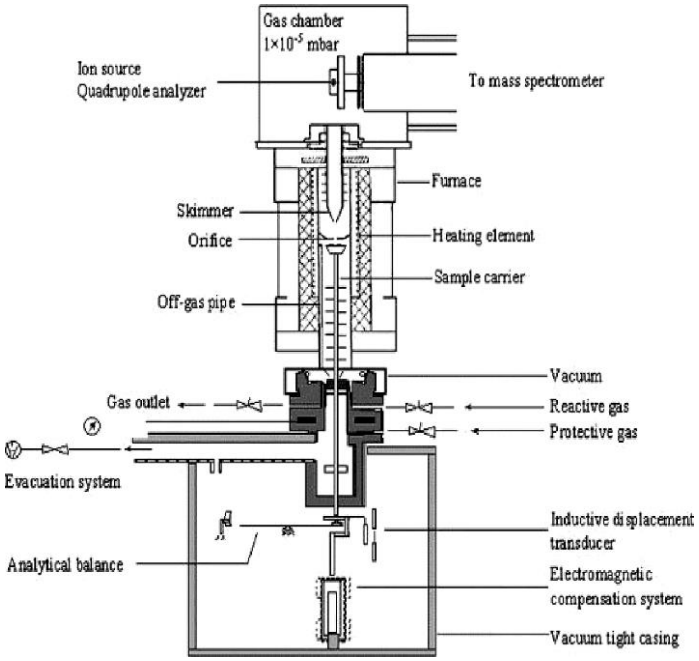

Figure 8 Schematic of a thermogravimetric analyzer. A device with a balance based on electromagnetic force compensation is displayed. Note that also a mass spectrometer for gas analysis is depicted. Reprinted from [13] *licensed under CCBY-NC-ND.*

The two main TG operation modes are dynamic and isothermal measurements. In a dynamic TGA the mass change as function of the temperature is recorded and the temperature is increased with a constant scan rate. Often scan rates of 5 $K \cdot min^{-1}$ or 10 $K \cdot min^{-1}$ are used. In an isothermal TGA experiment the temperature is kept constant for a defined amount of time and mass change over time is recorded. After the isothermal temperature step, temperature is increased to the target temperature of the next isothermal step. Typical parameters for the characterization of the thermal stability by TGA are the onset temperature and temperature at x% mass loss or the peak temperature. The onset temperature is defined according to the ASTM E2550 as the point in the TG curve where a deflection from the established baseline prior to the thermal event is first observed. The onset temperature could be derived from both dynamic and isothermal measurements. The temperature, which corresponds to x% of mass loss, often 5% is a commonly extracted value from dynamic TG experiments. Another important parameter in dynamic TG measurements is the peak temperature. The peak temperature is defined as the temperature at a local maximum of the first derivative of the TG curve. The first derivative of a TG curve is called differential thermogravimetric (DTG) curve. For stepwise reactions the peak temperature of each step can be determined. Physically the peak temperature is the temperature with the most rapid mass change i.e. the fastest reaction rate of the corresponding reaction. Like the onset temperature, the temperature at x% mass loss and the peak temperature are influenced by the temperature scan rate and increases with increasing scan rate.

Beside the scan rate the sample mass and shape influence the dynamic and isothermal TG curve. Larger masses will result in higher onset/peak temperatures. Like mentioned before the crucible material and atmosphere in the furnace are further parameters, which influence the onset/peak temperature.

Beside simple TG analyzers the devices could be coupled with further analytical instruments or could be equipped with additional sensors. For example, the evolving gases could be further characterized by coupling of the exhaust gas from the TG analyzer to a mass/IR spectrometer (Figure 8).

Other combined TGA devices include sensors for simultaneous thermogravimetric and differential thermal analysis (DTA) or have the capability to perform simultaneously TGA and differential scanning calorimetry (DSC). The company Netzsch implemented in some of their TG analyzer the so-called c-DTA (Calculated Differential Thermo Analysis) feature[14]. In DTA the temperatures of a sample and of an inert reference in the furnace are compared. The temperature difference between sample and reference gives insight in the enthalpy of a thermally induced reactions[15]. In Netzsch c-DTA the temperature in vicinity to the sample is compared with temperature in the furnace. One use of this method is for the temperature calibration of the TGA furnace with melting point standards. Beside this, the c-DTA function increases the capability of the TG device to the analysis of exothermic and endothermic phase transitions without mass loss like for example of melting points. For the c-DTA feature a thermocouple is placed in the sample holder right below the sample crucible. It records the temperature T_x during the measurement. The calculated furnace temperature $T_{furnace}$ is derived from the known heating rate β and the heating time t_{heat} and the initial temperature T_{start}. The c-DTA signal is the temperature difference between the calculated furnace temperature and the measured temperature in vicinity of the sample. It is calculated according to equation (8).

$$\mathrm{c-DTA} = (\beta \cdot t_{heat}) + T_{start} - T_x = T_{furnace} - T_x \qquad (8)$$

The c-DTA value is given in K. A negative value is obtained, if the temperature at the sample T_x is higher than the temperature in the furnace $T_{furnace}$. This is the case for exothermic reactions. An endothermic reaction like the melting of the sample results in a positive c-DTA signal. While this feature could provide some useful additional information, DTA is primarily a qualitative method. The DTA signal depends on the bulk density of the sample and its thermal conductivity[15]. Differential scanning calorimetry (DSC) could overcome these limitations and will be introduced in the next subchapter.

1.2.2 Differential Scanning Calorimetry (DSC)

By differential scanning calorimetry (DSC) the thermal induced transitions and reactions could be analyzed. Therefore, it is the state-of-the-art for investigation of melting and crystallization processes. Knowledge about state of aggregation is essential to define the application and process conditions for a material. For semi-crystalline or amorphous materials like polymers or ionic liquids (ILs) often the glass transition point T_g could be observed in DSC experiments. At T_g the vitrification takes place. Therefore, physical processes, which are related to transport phenomena like ionic conductivity decline and the material loses its elasticity and becomes a brittle glass.

DSC is from the experimental set-up similar to the differential thermal analysis (DTA) mentioned in the subchapter 1.2.1. Two generally different DSC set-ups are the power compensated DSC and heat flux DSC. In this work a heat flux DSC was used, therefore only this type will be introduced here. Further information on power compensated DSC and the difference with the heat flux DSC can be found in references [16,17]. For DSC experiments a small quantity of sample, usually a few mg, is filled in an inert and thermal well conducting crucible. Measurements could be performed in open crucibles or for air/moisture sensitive samples in hermetic sealed crucibles. A typical material for single-use DSC crucibles is aluminum, which could be sealed by cold-welding. The sealed-aluminum crucible can only withstand a limited amount of pressure. Therefore, high-pressure crucibles like stainless-steel pans are required, if sealed-samples should be investigated around their boiling point or around the onset of thermal decomposition. Gold or gold-plated crucibles offer high chemical resistance for example for corrosive samples like strong acids. An empty crucible of the same material, and similar weight like the sample crucible is prepared as reference. In heat flux DSC with turret-type measuring system both sample and reference pan are placed on platforms in a single furnace for simultaneous heating/cooling of sample and reference (Figure 9a). For cooling the DSC might be equipped with an air or liquid nitrogen cooler. Thermal induced phase transformations of the sample like melting/crystallization cause a heat flow between the sample and the measurement cell body. The direction of the heat flow thereby depends weather the sample reacts endothermic or exothermic. To measure this heat flow between sample and cell body thermocouple junctions are integrated in the sample and reference platform. For e.g. Chromel discs are mounted underneath the Constantan platform tops to form Chromel-Constantan thermocouples (Figure 9b). The heat flow of the reference pan is then subtracted from the heat flow of the sample to eliminate effects of the crucible and from the device.

In the devices of the Discovery Series (TA Instruments) used in this thesis additional thermocouples at integrated in the base body between the sample and reference platform (Figure 9b).

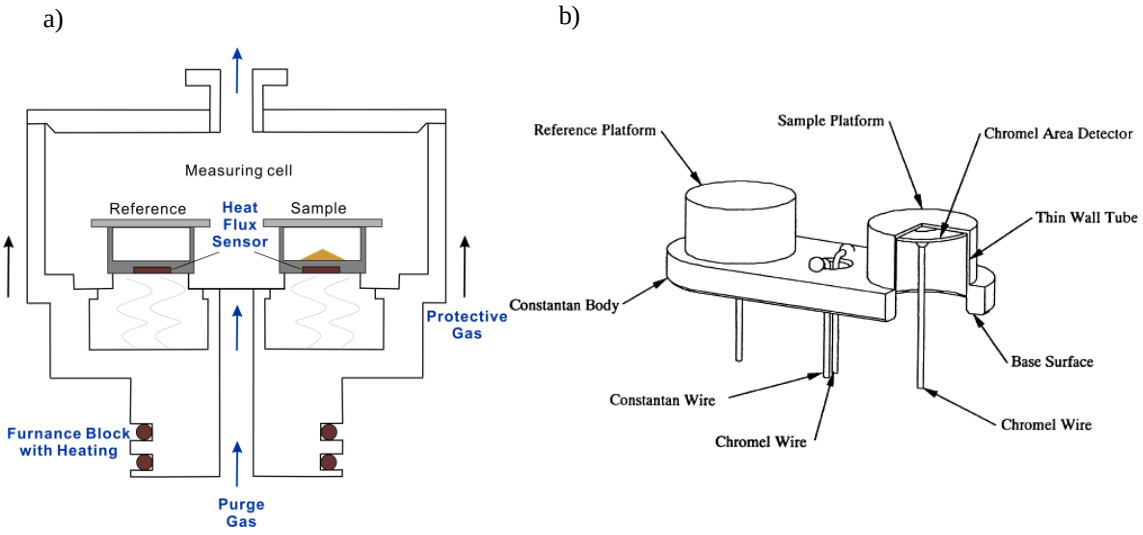

Figure 9 a) Schematic of instrumental set up of a heat flux DSC. b) Details of the turret-type measuring cell with the additional thermocouple developed by TA Instruments. b) is reprinted with permission from [18]. © 2002 Elsevier Science B.V.

These sensors are used for online corrections and baseline-calculations with the Tzero Technology. The basic idea is to determine the heat capacity and thermal resistance on the sample and reference side separately to suppresses imbalances between the sample and reference side of the instrument for enhanced measurement accuracy and increased baseline-flatness. A detailed discussion on this technique is beyond the scope of this thesis. Further information can be found in the patent U.S. 6,431,747 B1[19] and chapter 3 of reference[16].

In a heat-flux DSC the sample heat-flow i.e. the temporal change of enthalpy H can be expressed according to equation (9). Here c_p is the heat capacity of the sample, (dT/dt) the (constant) heating/cooling rate and f(T,t) the temperature and time dependent kinetic response of the sample[17].

$$\frac{dH}{dt} = c_p \cdot \left(\frac{dT}{dt}\right) + f(T,t) \tag{9}$$

Equation (9) shows that the heat flow and therefore the DSC signal is influenced by both the heat capacity and the kinetic response function of the sample.

When a liquid is cooled the kinetic energy and mobility of the molecules decreases. Therefore, the effect of the attractive interactions increases more and more and the volume of the liquid contracts. If a dense and well-ordered arrangement is reached the liquid crystalizes. Volume change and enthalpy change are related to each other. Therefore, a similar curve is obtained for the enthalpy.

The change of the sample enthalpy (dH/dT) i.e. the heat flow thereby results in a peak for a crystallization process. Such phase transition is of 1st order[20]. Melting as the reverse process can be described in the same way.

If steric prevents closely and well-ordered structures and the intermolecular interactions are only weak, crystallization is hindered and an undercooled melt is obtained. With ongoing cooling, the kinetic energy decreases continuously and the effect of the frictional forces between the molecules becomes more and more important. This will hinder the viscous flow i.e. lead to a higher viscosity. At some point, the viscosity becomes so high that the motions of the molecules are "frozen" and the material vitrifies to an amorphous glass. In the glass state, similar to the crystalline state, molecules are mainly displaced from their position by vibrations or rotations, but translational motions hardly occur.
The temperature at which this transition from liquid to glass state occurs is called glass-transition temperature T_g. In the Gold Book by the IUPAC the T_g is defined as temperature at which the viscosity reaches 10^{13} dPa·s [4]. In liquid and glass state the heat capacity is different. This change in heat capacity at T_g influences the first term of the heat-flow formula (eq. (9)) and causes a step-like shape in the DSC curve. The glass transition shows some characteristics of a 2nd order phase transition, however it is no real thermodynamic phase transition, because there is no equilibrium state on both side of T_g and the glass transition is influenced by the thermal history of the sample[20].

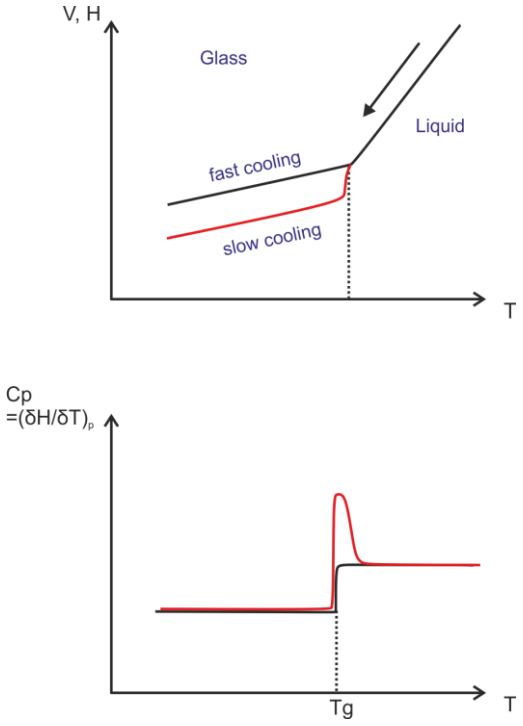

Figure 10 Volume and enthalpy change at the glass transition and the related change in c_p.

So, the volume in the glass state depends on the cooling speed. With faster cooling a larger volume in the glass state is reached than with the slower cooling (Figure 10). As a consequence, the thermal history of a glass is important. If a glass formed by slow cooling or annealed below the T_g, is heated with a faster rate, the volume and enthalpy suddenly increase when the T_g is crossed and the glass becomes liquid. This sudden increase in enthalpy leads to a peak in the DSC curve, which overlays the step-shape of the glass transition and is the so-called enthalpy relaxation peak (Figure 10). The peak shape is plausible when keeping in mind that c_p is the derivative of the H vs. T curve. Often the enthalpy relaxation peak is a drawback for a precise determination of T_g, but in some cases of polymer-blends with overlapping T_g values of each compound it might be used to characterize the amount of each compound in amorphous state, because the enthalpy relaxation peaks are often better resolved than the step-like shape of the T_g.

1.3 Physical Characterization

1.3.1 Karl Fischer Titration

K. R. Seddon et al. demonstrated already in the year 2000 in a systematic study the impact of water on physical properties like viscosity, ionic conductivity etc. in ionic liquids[21]. Therefore, precise control of the water content is crucial for experimental investigations and applications of ionic liquid-based electrolytes in energy storage and conversion devices.

A standard method for the determination of the water content down to the ppmw (parts per million by weight) level is the Karl Fischer (KF) titration[22].

In a Karl Fischer titration the titrant is iodine (I_2) and the converted analyte is sulfur dioxide (SO_2), or in some cases a sulfur dioxide adduct (eq.(11)). Karl Fischer uncovered that this reaction only takes place in the presence of water. This makes it suitable for the determination of the water content of a wide variety of chemicals[23]. In methanolic solution two water molecules are consumed for each iodine molecule which reacts with sulfur dioxide (eq.(10)).

$$\begin{aligned} I_2 + 2e^- &\rightarrow 2I^- && \text{(reduction)} \\ SO_2 + 2H_2O &\rightarrow SO_4^{2-} + 2e^- + 4H^+ && \text{(oxidation)} \\ I_2 + SO_2 + 2H_2O &\rightarrow 2HI + H_2SO_4 && \text{(sum)} \end{aligned} \qquad (10)$$

In alcohol-free medium the stoichiometry is different. In some cases, special alcohol-free reagents have to be used to avoid falsification of the result be side reactions of the sample with the alcohol. An example for analytes that require alcohol-free reagents are aldehydes and ketones. With methanol these class of compounds would undergo acetal and ketal formation. By both reactions water is formed and therefore a too high (wrong) water content would be found. In this thesis all experiments could be performed with methanol-based reagent, therefore the following description only focuses on these reaction conditions.

In methanolic solution the methyl sulfite ion is proposed as the reactive species instead of SO_2. It forms by a chemical reaction between the sulfur dioxide and methanol according to equation (11).

$$CH_3OH + SO_2 \rightleftharpoons CH_3OSO_2^- + H^+ \qquad (11)$$

This reaction could be one explanation for the pH-dependency of the Karl Fischer titration[b]. On the one hand, at high pH (low H^+ concentration) the equilibrium is shifted on the side of the reactive methyl sulfite. This causes an increase of the rate constant of the Karl Fischer reaction. On the other hand, a high hydronium concentration at low pH values hinders the formation of methyl sulfite, and therefore leads to a decrease of the rate constant. For reliable and reproducible measurements therefore, the pH has to be constant within the titrations. This is achieved by addition of a buffer like an amine to the reaction solution. In his original work Karl Fischer used pyridine for this purpose[23]. Nowadays, pyridine gets often substituted by non/less carcinogenic amine buffers with a less disturbing odor. For example, in some commercial Karl Fischer reagents the buffer system consists of imidazole derivates or a guanidine/benzoic acid mixtures[24]. In addition to the use of a buffer in the reagent/solution an acidic sample like a protic acidic ionic liquid can be diluted, for example with absolute methanol, prior to the injection in the titrator – the so-called external dilution method. By external dilution of an acidic sample the challenges related to the pH are bypassed or at least minimized, however the water content in the methanol and the dilution factor have to be considered for a correct calculation of the water content in the sample. In addition, by dilution the limit of detection increases. A positive side effect of the external dilution for ionic liquids, is their improved processability i.e. more reproducible sample injection with a syringe, due to the decrease of viscosity, by the dilution.

In practice the titration can be performed with the volumetric or coulometric method. In his original work Karl Fischer used the volumetric method. There the sample is diluted in an anhydrous solvent and the titrant with SO_2/I_2 is added in small increments by a burette or an automatic dispenser. The color change from slightly yellow to brown by excess I_2 served for the visual endpoint determination[23]. Nowadays visual endpoint determination is replaced by the state-of-the-art 2-electrode potentiometry. The volumetric method can be applied for solutions containing 0.01 wt% to 100 wt% of water, because the titrant is simply added and a higher water content will only require the addition of a larger amount of titrant. The lower limit of about 0.01 wt% (100 ppmw) is related to the smallest volume of titrant, that can be added in a reproducible and reliable way with an automatic dispenser[22].

For lower water contents, down to 10 ppmw (0.001 wt%), coloumetric titration has to be applied. In this method the I_2/SO_2 titrant is not added to the solution in small increments but the iodine I_2 is generated *in-situ* by electrochemical oxidation of iodide I^- at the so-called generator electrode (Figure 11 left side).

[b] The pH is only defined for aqueous solutions. In case of a low water content this condition is not fulfilled for Karl Fischer titrations and hydronium activity should be used instead of pH. For improved readability a case-by-case analysis is omitted and only the expression pH is used in this chapter.

Reduction of hydronium i.e. hydrogen evolution occurs at the counter electrode. The amount of iodine generated is calculated from the current and reaction time with Faraday's laws of electrolysis. Considering the stoichiometry of the Karl Fischer reaction (eq.(10)) 10.712 C of electrical charge are required for the generation of iodine, which is equal to 1 mg of water in the sample[22].

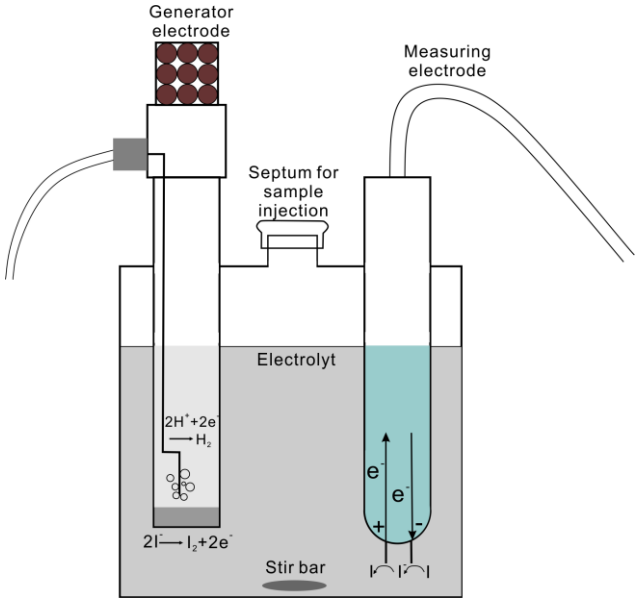

Figure 11 Schematic of a coulometric Karl Fischer titrator. On the left side a generator electrode without a diaphragm is displayed. On the right side the working principle of the measuring electrode is illustrated.

Backreaction of the iodine to iodide at the counter electrode would lead to an experimental overestimation of the water content. Both the design and operation of the generator electrode are optimized to limit this backreaction of the iodine. First, current pulses are used at the generator electrode instead of a constant current to minimize the chance, that iodine diffuses to the counter electrode before it reacts with the methyl sulfite ion and water. To achieve high current densities often pulses with a fixed height are applied for the iodine generation and the titration rate, i.e. the amount of iodine generated in a defined time period is controlled by the pulse duration[25]. Second, the distance between the working and counter electrode of the generator electrode is maximized, to limit the probability of the diffusion of the I_2 to the counter before the reaction with water and the SO_2 species occurs. In addition, the formation of hydrogen gas bubbles at the counter hinders contact of the iodine with the counter electrode. However, for very accurate determination of samples with less than 50 µg water/sample a separation of anode and cathode of the generator electrode with a diaphragm is required. Also, some samples that can be readily reduced by the hydrogen *in statu nascendi* like unsaturated hydrocarbons or nitro compounds like nitrobenzene can only be measured with a generator electrode with a diaphragm.

Originally the endpoint was visual determined by the color change due to the iodine excess after the endpoint is reached. The accuracy of the visual detection of the end-point is limited by the slow and gradual color change of the solution. In addition this approach fails with colored samples[25]. Nowadays, the more universal applicable und more reliable bipotentiometric indication, also called 2-electrode potentiometry, is the state-of-the-art method for the end-point determination in both volumetric and coulometric Karl Fischer titrations. A small AC polarization current is applied to the two platin pins of the measuring electrode. The corresponding voltage between the two electrodes is recorded. This voltage is governed by the simultaneous reduction and oxidation of the iodine/iodide couple (Figure 11 right side). The rather large amount of iodide in the coulometric Karl Fischer reagent stays approximately constant during the titration. In contrast the iodine concentration strongly varies in course of the titration. Therefore, the potential is a sensitive measure for the iodine concentration. Before and after the sample injection a constant iodine concentration forms by the equilibrium between generation at the generator electrode and consumption by reaction with atmospheric moisture. This constant initial iodine concentration results in a low constant electric potential at the measuring electrode. When a water containing sample is added, the iodine gets consumed according to the Karl Fischer reaction. The decrease of iodine in the solution causes a potential jump (Figure 12). After sample injection the reaction solution is homogenized by stirring for a defined time period (Mixing time in Figure 12). With the start of the titration the increased generation of iodine lead to a consumption of the water and a restoration of the initial higher iodine level. Consequently, the measured potential drops to its initial level. One criterion for the termination of the titration is the measured potential at the measuring electrode.

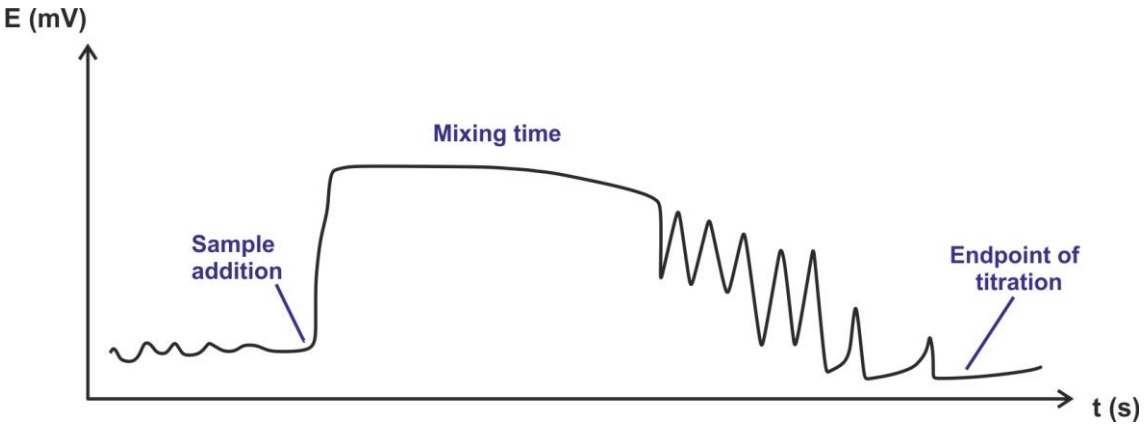

Figure 12 Schematic curve of the measuring potential during a coulometric KF titration.

Beside the role of the potential for the endpoint determination, the potential and potential change over time are used in automatic Karl Fischer titration stands to control the titration rate i.e. the iodine generation rate. Therefore, generator electrode and measuring electrode are connected by a feedback loop. With a potential close to the set endpoint and a small change of the potential over time (dE/dt) iodine is generated slower.

State-of-the-art microcontrollers enables online-monitoring of the amount of water which gets titrated per time. This value is called drift and often given in µg(H_2O)/min. Before and after the titration the drift should be small i.e. only a little amount of environmental humidity enters the titration cell. A small drift is realized with a glass titration cell with a septum for sample injection and the only possible gas exchange through a drying funnel on top of the generator electrode. For accurate results the contamination by environmental humidity is subtracted from the measured water content. For this calculation the drift before the sample injection and the titration time are used. Beside for baseline correction, the drift is applied together with the measured voltage at the measuring electrode for the endpoint determination. If the drift drops below a set drift value the titration is terminated. An absolute or relative drift value, which is recorded before the sample injection, could be used for the drift as termination criterion of the titration.

Liquid samples or solids, which are soluble in solvents compatible with Karl Fischer titration, can be directly injected into the titration cell. Other solid samples can be measured with the oven methode. Thereby the sample is heated in an oven and the released water is transported in a stream of dry gas in the titration cell and then titrated.

1.3.2 Density Measurement

The density ρ is a material specific physical parameter. It states the mass m of a defined volume V. The SI unit for the volume is m^3, but the density is usually reported in g per cm^3 or ml.

$$\rho = \frac{m}{V} \tag{12}$$

Due to the dependency of the volume on temperature and pressure the density has a temperature and pressure dependency, too. Beside the general use of the density for the calculation of required volumes for a certain mass or vice versa, ρ plays an important role for the calculation of concentrations. Therefore, the density is required for the calculation of the molar equivalent conductivity of ionic liquids (subchapter 1.4.1).

Density measurements with a pycnometer according to the definition in equation (12), require relatively large amount of sample like 50 mL or more, are time consuming and suffer from the challenge of precise temperature control and possible alteration of the sample, like water uptake or solvent evaporation, during the weighing process. A more sophisticate approach is the oscillating U-tube method. The liquid sample is loaded in U-shaped tube of borosilicated glass or stainless steel. An oscillator stimulates the vibration of the tube. A sensor e.g. an array of a laser and a photodiode, records the oscillation of the tube (see Figure 13). This oscillation is damped by the liquid sample inside the tube. A feedback loop between the oscillator and the sensor is used to find the resonance frequency of the filled tube (resonance of energy mode). In a less common measuring mode the feedback loop adjusts the frequency until the excitation and the oscillation of the tube have the same amplitude, but a phase shift of π (resonance of amplitude mode)[26].

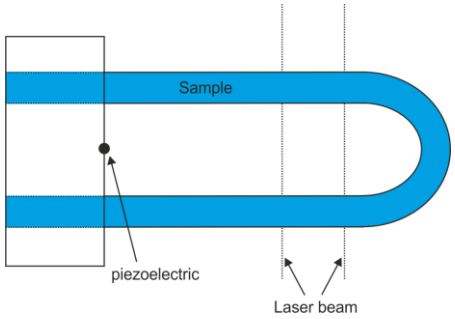

Figure 13 Schematic set-up of the oscillating U-tube density meter.

The vibrating tube could be described by the mechanical model of a damped spring-mass system, that is stimulated to oscillation by an external force. For the resonance frequency ω_0 a relationship between the density of the sample and the period of the oscillation τ_{osc} of the filled tube can be established (eq.(13)).

There K is the force constant in the theoretical spring in the model. V is the sample volume and m_0 the mass of the empty tube. However, all this parameter can be merged to the parameters A and B, which are obtained from calibration experiments[26].

$$\rho = \frac{K}{4\pi^2 V} \cdot \tau_{osc}^2 - \frac{m_0}{V} = A \cdot \tau_{osc}^2 + B \tag{13}$$

In an Anton Paar DMA 4100 M vibrating tube density meter, a second reference oscillator measures the oscillation period τ_{Ref} of an empty reference tube, to consider the aging effect of the borosilicated glass tube and thereby further improves the reliability and accuracy of the measurement data (eq.(14)). In addition, by the factors f_1 and f_2 the effects by temperature, sample viscosity and non-linearity on the instrumental constants A′ and B′ are corrected[27].

$$\rho = A' \cdot f_1 \cdot \left(\frac{\tau_{osc}}{\tau_{Ref}}\right)^2 - B' \cdot f_2 \tag{14}$$

From the density the isobaric thermal expansivity α_p could be calculated by equation (15). α_p is a measure for the degree of volume expansion upon temperature increase[28].

$$\alpha_p \equiv \frac{1}{V}\left(\frac{\partial V}{\partial T}\right)_p = -\frac{1}{\rho}\left(\frac{\partial \rho}{\partial T}\right)_p = -\frac{b}{\rho} \tag{15}$$

With

$$\rho = a + b \cdot T$$

The origin why α_p can be determined from the density is the independency of the mass from temperature. This approximation is valid for temperatures far from the Planck temperature (about 10^{32} K)[29]. A stepwise mathematical derivation, which includes this approximation is given in the appendix in equation (49). For ionic liquids usually a linear relationship between temperature and density could be observed. In this case α_p could simply be calculated from the slope b of a linear regression line in a temperature-density plot. In contrast to the common linear relationship Costa et al.[30] proposed a second-order polynomial dependency of the density on the temperature. In the opinion of the author of this thesis this equation by Costa et al. is an overparameterization compared to the simple linear relationship, but for completeness it is printed in the appendix in equation (50).
On the one hand, the isobaric thermal expansivity α_p, has to be considered for the application of a material in an environment with significant temperature fluctuations. The thermal expansion of the material might cause damage to a part of a device. In the context of electrochemical energy storage devices, the thermal expansion might lead to loss of electric contact. On the other hand, from scientific point of view α_p gives insight in the interaction between atoms or molecules in solids or liquids. Especially in case of protic ionic liquids (PILs) this could be used for qualitative comparison of the H-bond network strength between different PILs.

1.3.3 Viscosity Determination and Rheometry

Liquids have different consistencies. This could be experienced in daily life for example during the preparation of a meal. When honey is stirred the cutlery experiences a larger resistance compare to stirring a cup of coffee. In addition, the honey flows down much slower from the spoon compared to the water-based coffee beverage. These observations illustrate three fundamental properties of liquids.

First, intuitively we characterize liquids according to their flow behavior as viscous (honey) or thin (coffee beverage). The scientific and also quantitative measure for the property of a liquid related to its consistency is the viscosity.

Second, to stir a liquid, or more general generate a liquid flow, energy is required. This supplied deformation energy gets completely dissipated i.e., after the load is removed a fluid with ideal viscous behavior stays in its deformed state and no energy can be recovered. To understand this energy dissipation in a flowing fluid, processes on molecular level have to be considered. The friction between molecules in a flowing fluid generates heat – the so-called viscous heating. The generated heat might change the temperature of the fluid itself or is released to its surrounding. To display an ideal-viscous behavior with a complete dissipation of the deformation energy, there should be only weak interactions between the molecules like it is often the case in liquids of small and asymmetric molecules. Stronger molecular/atomic interaction forces like in a metal spring lead to elastic behavior for small deformations and nearly the complete deformation energy can be recovered.

Third, there are two different types of viscosity, which can be observed from the different kinds of experiments. Either a moving external body (the stirring spoon) stimulates the flow by its dragging force or the flow is only driven by the gravity of the fluid itself (the honey flowing down the spoon). In the first case the so-called dynamic viscosity η is obtained, in the second one the kinematic viscosity η_{kin}[c]. The dynamic viscosity is usually measured in Pa·s. A historical unit for η, which is still used in the context of the Walden plot (subchapter1.4.2), is the Poise (unit symbol P). Thereby 1 P=0.1 Pa·s and accordingly 1 cP ("centi-Poise"10^{-2} P)=1 mPa·s. Ultra-pure water a common reference liquid for test and calibration of viscosimeters and rheometers displays a viscosity of 1 cP or 1 mPa·s at 20 °C [31]. The unit of the kinematic viscosity is usually $mm^2 \cdot s^{-1}$.

[c] The IUPAC recommends the symbol ν for the kinematic viscosity[4]. However, in this thesis η with the index "kin" will be used to avoid confusion of the symbol ν with its other uses for frequency etc. η without indice stands for the dynamic viscosity.

From unit analysis it can be seen, that the kinematic viscosity and the dynamic viscosity are linked by the density ρ (subchapter 1.3.2) of the liquid[4] . However, the relationship between η_{kin} and η (eq.(16)) only holds true for Newtonian liquids. A definition of Newtonian liquids will be given later in this subchapter (eq.(20) and Figure 15).

$$\eta_{kin} = \frac{\eta}{\rho} \tag{16}$$

Kinematic viscosity is on the one hand of historical relevance, on the other hand still measured in industry e.g., for testing of coatings, inks, ceramic suspensions, drilling fluids or petrochemicals for quality control[32]. It can be determined with flow cups or capillaries.

A body, which moves through a liquid experience a retarding frictional force. For a rigid and smooth sphere with radius R, which moves with a speed v in an infinite extended fluid of homogeneous composition this frictional force F_d can be calculated with the Stokes law (eq.(17)). Important assumptions are a laminar flow and no-slip condition between the sphere and the fluid. The frictional force F_d is directly proportional to the dynamic viscosity η

$$F_d = -6\pi\eta R\mathrm{v} \tag{17}$$

Therefore, η is relevant for transport processes in liquids and related properties like the ionic conductivity (subchapter 1.4.1). The dynamic viscosity can be measured with rotational or falling ball viscosimeters or with a rheometer.

Before continuing the discussion of the dynamic viscosity, the terms rheology and rheometry will be introduced. The word “rheology” originates from the Greek “rhein”, which means “to flow”. So, rheology could be literally translated as “flow science”. Its aim is to understand the structure-property relationship in flowing liquids and deformable solids. These results support the development and optimization of industrial processes, processing conditions and equipment and design of materials with the required properties for their final application. Rheometry is the generic term for the instruments, tests and analysis methods used in rheology[32].

To define the dynamic viscosity and related parameters a two-plate model will be used. In this model two parallel plates sandwich a liquid film. The thickness of the film e.g. the gap between the two plates has a dimension h (Figure 14). The lower plate is static (speed $v=0\ m\cdot s^{-1}$). A constant shear force F, gets applied to the upper plate, which leads to a shear stress τ_{Stress} [d] in the liquid film.

[d] In this thesis the index “stress” is used for the shear stress to avoid mix up with other uses of τ as time constant or period of oscillation etc.

Obviously, the same force will generate a larger shear stress, if it acts on a smaller area. Therefore, the shear stress τ_{Stress} is defined as the shear force F normalized to its contact area A.

$$\tau_{Stress} = \frac{F}{A} \tag{18}$$

By the stress the liquid film gets deformed. If a constant shear stress is applied the top plate is set to motion and the liquid starts to flow. For the description of this flow, it is assumed that, the liquid sticks to both plates (no wall-slip effect) and flows laminar[32].

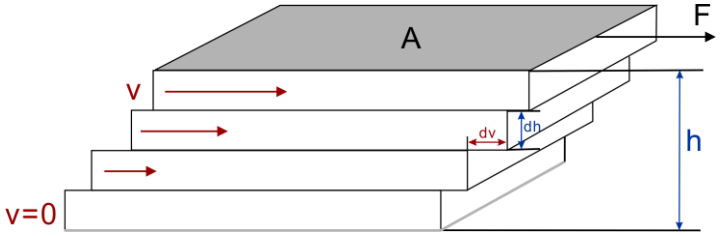

Figure 14 Schematic of the liquid flow in the two-plate model.

In the laminar flow regime, the liquid has a layered structure, which could be depicted like a stack of playing cards (Figure 14). Between the different liquid layers, no vertical mixing occurs. Assuming no slip, the top layer follows the motion of the top plate with its speed v and the bottom layer stays static (speed v=0 $m \cdot s^{-1}$). The velocity drops linear and continuously between these two extreme values across the gap. In a snap shot taken at a time t (like in Figure 14) the deformation of the liquid film γ can be simply calculated from the displacement x of the mobile top plate divided by the film thickness h (eq. (19)). The dynamic of the deformation or flow process is described by the rate of deformation, which is for a shear deformation called shear rate. Mathematically, the change of the deformation with the time corresponds to the temporal derivative. With the assumption of a constant gap the shear rate is simply the (constant) speed of the top plate divided by the gap height (eq.(19)).

$$\gamma = \frac{x}{h}$$
$$\frac{\partial \gamma}{\partial t} \equiv \dot{\gamma} = \frac{\partial}{\partial t}\left(\frac{x}{h}\right) = \frac{\mathrm{v}}{h} \tag{19}$$

The shear rate $\dot{\gamma}$ has the unit of reciprocal seconds s^{-1}. The unit Hertz Hz shouldn't be used for the shear rate in this case, since it is exclusively used for periodical oscillating processes and not for linear motion.

The analysis of the relation between the applied shear stress and resulting shear rate (stress-controlled experiment) or the resulting stress for an applied shear rate (strain-controlled experiment) is a fundamental subject in rheology. For ideal flow behavior the shear stress and shear rate are directly proportional. This proportionality between shear stress and shear rate is stated in the Newton's law (for fluids) in equation (20). The proportionality factor between the shear rate and shear stress is thereby the dynamic viscosity η. Phenomenological this law simply states that if the same shear stress gets applied to different liquids i.e., different pastes are stirred with the same stirrer, the liquid with the lower dynamic viscosity will flow faster (higher shear rate)

$$\tau_{Stress} = \eta \cdot \dot{\gamma}$$
$$\eta = \frac{\tau_{Stress}}{\dot{\gamma}} \tag{20}$$

In a plot of the shear stress over the shear rate (flow curve) the measurement data of a fluid which follows the Newton's law can be fitted by a straight line. The slope of this line corresponds to the dynamic viscosity η (Figure 15).
The dynamic viscosity is therefore independent of the applied shear rate or the applied shear stress. Such fluids are called Newtonian liquids. Pure organic solvents with small molecules without any pronounced solvent structure often are Newtonian liquids, at least in a limited shear rates range. For a shear-thinning liquid the dynamic viscosity decreases with increasing shear rate i.e., the slope in the flow curve is not constant and the shear-stress values for higher shear rate are lower than expected according to the Newton's law (Figure 15). This behavior is for example typical for polymer melts or solutions. Under the shear stress the polymer coils start to orient in the shear gradient and partially disentangle. This leads to a reduction of the friction between the molecules and therefore a decrease in the stress under shear. Consequently, the dynamic viscosity according to definition in equation (20) decreases with the decreasing shear stress. Other examples of shear-thinning materials are suspensions and emulsions. In suspensions the shear-thinning is caused by orientation of non-spherical partials in the shear gradient and rupture of particle agglomerates. In emulsions the deformation of the droplets along the shear-gradient causes the shear-thinning effect. The opposite to shear-thinning liquids are shear-thickening liquids. For this class of materials, the flow curve is bend upwards with increasing shear rate e.g., the dynamic viscosity increases with increasing shear rate (Figure 15). Well-known shear-thickening systems are concentrated dispersions, like concentrated aqueous starch dispersions. Shear-thickening materials are less common and some measurement effects related to the used measurement geometry and the shear rate range, like Taylor vortices or turbulent instead of laminar flow cause an increase in shear stress for higher shear rates, which might erroneously be interpreted as shear-thickening behavior[33].

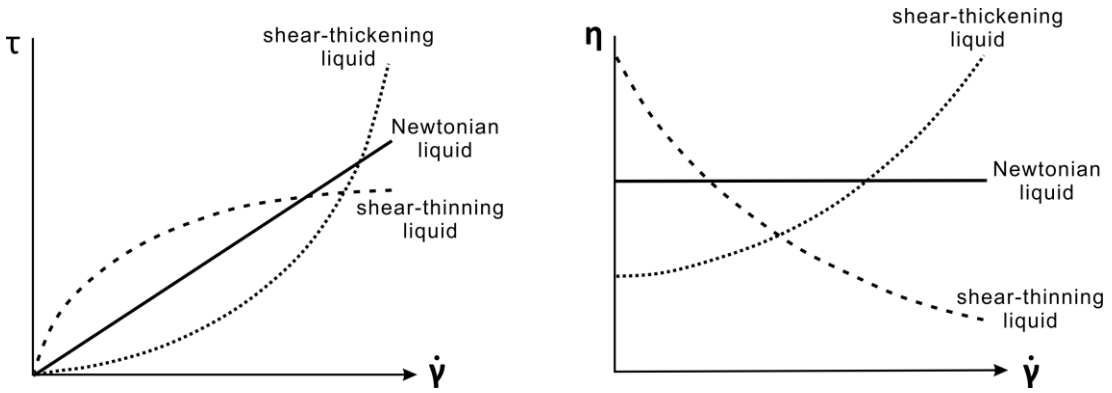

Figure 15 Illustration of Newtonian and non-Newtonian flow behavior.

Obviously, for non-Newtonian shear-thinning/thickening liquids the flow curves cannot be fitted by the Newton's law and always the dynamic viscosity $\eta(\dot{\gamma})$ for a specified shear rate $\dot{\gamma}$ has be given. Because $\eta(\dot{\gamma})$ in non-Newtonian fluids is the observed dynamic viscosity for special conditions it is often called apparent viscosity. Simple flow curves of shear-thinning/thickening materials like in Figure 15 could be fitted to power-law equations like for example the Ostwald-De Waele model[32]. In experiments shear-thinning is often only observed for the medium shear rate range. For low and high shear rates Newtonian plateaus with a constant and shear-rate independent dynamic viscosity $\eta(0)$ and $\eta(\infty)$, respectively, are obtained. For low shear rates the shear forces are not sufficient to induce rearrangement and orientation processes on a molecular/particle level in the liquid and therefore Newtonian behavior with a shear rate independent dynamic viscosity $\eta(0)$ is measured. Starting from a critical shear rate $\dot{\gamma}_C$ the reorientation processes start, and the shear-thinning phenomena occurs. At some point the maximal degree of molecular/particle reorientation is reached and the dynamic viscosity reaches its high shear rate threshold value $\eta(\infty)$. The shape of the curve with the low and high shear rate Newtonian plateau, is not represented by the Ostwald-De Waele model. Instead other models like for example a Carreau model might be used to explain data with high and low shear rate Newtonian plateaus.

Various measurement geometries exist. Common ones are the plate-plate and cone-plate. In the plate-plate geometry the sample is placed in the gap (100 µm to about 1 mm) between a rotating and a fixed plate. A benefit is the adjustable gap height, a drawback is the non-constant shear rate in the gap. This originates from the faster angular velocity of the edges of the plate compared to the center of the plate. To compensate this disadvantage the cone-plate set up was developed. There the rotor has the shape of a truncated cone with a very flat angle. Therefore, the gap is smaller in the center and increases to the edges. By this design the different angular velocities are compensated and the shear rate (v/h) is constant within the gap.

Precise temperature control is crucial as the viscosity might change for 15 decades in the accessible temperature range[e].

In 1923 C.V. Raman suggested an Arrhenius-type temperature dependency of the viscosity similar to equation (21a). His theory was based on the interpretation of a liquid as mixture of vapor and solid phase. In such a mixture some unassociated molecules display a gas-like mobility, while molecules in clusters behave in a more solid-like manner. Raman demonstrated the validity of this concept by the good agreement between experimental viscosity data and values he calculated from vapor viscosity data of benzene[34].

E. N. DA C. Andrade rediscovered the Arrhenius-type temperature dependency of the dynamic viscosity η like in equation (21a) in 1930[35]. He tested the equation for several liquids with different properties like butanol and octane and found, that it can correctly reproduce the viscosity over a wide temperature range from 0-120 °C. A and b in the formula are constants and T is the absolute temperature. A is the preexponential factor, which is in the original form temperature independent[f]. b the activation temperature, which might be converted to the activation energy E_A of viscose flow according to equation (22). With the result of equation (22) the equation (21a) can be rearranged to contain the activation energy E_A (eq.(21b)). In all this equations R is the gas constant. Beside the exponential shape a linearized plot according to equation (23) is possible, which yields the activation temperature b as the slope of the linear fit. If ln(η) is plotted vs. 1/RT the slope directly corresponds to the activation energy E_A.

$$\begin{aligned} a)\ \eta &= A exp\left[\frac{b}{T}\right] \\ \text{b)}\ \eta &= A exp\left[\frac{E_A}{RT}\right] \end{aligned} \tag{21}$$

$$E_A = -RT^2 \frac{d\ln(\eta)}{dT} = \frac{b}{T^2} \cdot RT^2 = b \cdot R \tag{22}$$

$$ln(\eta) = b \cdot \frac{1}{T} + ln(A) \tag{23}$$

[e] Liquid like water ~1 mPa·s (20 °C)[31], undercooled melts at glass-transition temperature T_g ~10^{15} mPa·s [4]

[f] In the original formulation by Andrade the preexponential factor is temperature independent. The temperature dependency might be introduced to the preexponential factor by multiplication with a term T^n (see entry "modified Arrhenius equation" in [4]). For η sometimes n=1/2 i.e. a square root temperature dependency of the preexponential factor is used like in [173]. Such a square root temperature dependency of A leads to a change in the equation for E_A, too.

In honor of E. N. DA C. Andrade this equation is sometimes called Arrhenius-Andrade or simply Andrade equation or law.

While the Arrhenius-Andrade equation usually appropriately describes the temperature dependency of the viscosity in fluids above their melting points it fails to reproduce the behavior in undercooled melts, especially in vicinity of the glass-transition temperature. The reason for this different behavior of fluids in the liquid and undercooled melt state could be explained on a microscopic level. In a simplified picture a liquid might be described by an arrangement of particles (molecules, ions or atoms) without long-range order and a low density. Due to the relatively large amount of free space between the particles their movement is approximately uncorrelated. To move a particle has to detach from its surrounding and occupy free volume in vicinity. To detach from other particles the jumping particle has to overcome an energy barrier. Such a process can be modeled by an Arrhenius type equation. Thereby the ratio between this energy barrier to the thermal energy determine how easy a particle can move i.e. how high the macroscopic viscosity is. At the melting point the liquid reaches a dense structure with only a small amount of free volume. With decreasing temperature, the density increases further and if no crystallization occurs a metastable undercooled melt forms. Here the available void space i.e. the free volume is limited. Therefore, not the activated jump of the moving particle into the free space, but correlated statistical redistribution (heat movements) of free volume(s) within the fluid becomes the determining process. This process can't be described by the Arrhenius type equation and the viscosity increases more rapid with decreasing temperature than in the liquid state. Figure 16 illustrates this different temperature dependency in the liquid and undercooled melt state. Ionic liquids usually fall in the category of undercooled melts, therefore the viscosity in this state will be described in more details.

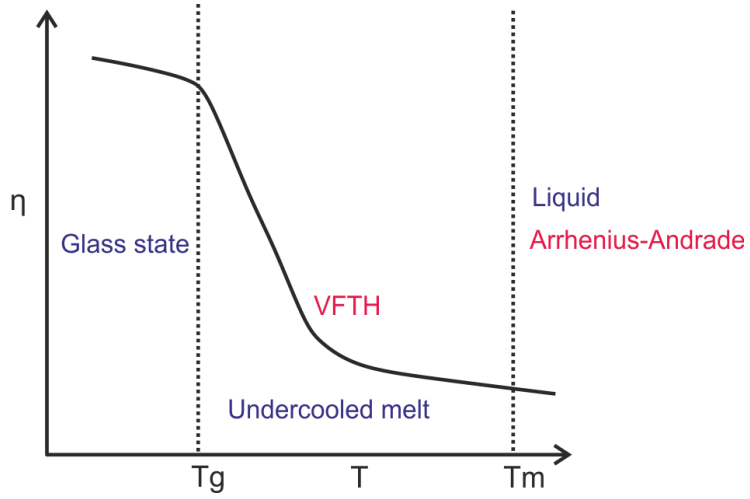

Figure 16 Schematic of the temperature dependency of the viscosity. T_m is the melting point and T_g the glass-transition temperature. The regions where the Arrhenius-Andrade and Vogel-Fulcher-Tammann-Hesse (VFTH) theory are valid are marked (inspired by[36])

H. Vogel studied the temperature-dependent viscosity of water, mercury and oil in the liquid state and found an exponential function as the best description for his data. Thereby some of his main achievements were the introduction of a constant high-temperature viscosity limit η_∞ as base in his exponential function and the temperature T_0 where the viscosity becomes infinite in the exponential term[37]. While Vogel investigated only substances in the liquid state, G. S. Fulcher pioneered the analysis of undercooled melts and presented an empirical equation for melts of glass. In his analysis of literature data he discovered that the temperature dependency of the decadic logarithm of the viscosity can be described by equation (24) with the 3 fitting parameters A', B' and T_0[38]. Independent of Fulcher's study G. Tammann and W. Hesse confirmed equation (24) for the viscosity of the undercooled melts of several organic substances[36]. In recognition of the discoverers, equation (24) is called the Vogel-Fulcher-Tammann-Hesse (VFTH) equation.

$$log_{10}(\eta) = -\mathrm{A}' + \frac{\mathrm{B}' \cdot 10^3}{T - \mathrm{T_0}} \tag{24}$$

The curve shape corresponds to a hyperbola without a classical vertex point. Instead it has the vertical asymptote T_0, where it tends to infinity, and the horizontal asymptote -A.

The origin of the VFTH equation is that of an empirical equation, however after its discovery the shape of the equation was justified theoretically for example by the free-volume theory of M. H. Cohen and D. Turnbull[39]. In addition, the Williams–Landel–Ferry equation[40] can be obtained from the VFTH equation for special conditions. All these finding demonstrate the physical meaning behind the VFTH equation.

In the VFTH equation (24) the decadic logarithm of the viscosity is shown. The viscosity itself might by displayed according to VFTH equation (25). That both forms are the representation of the same law is demonstrated in the mathematical appendix. There in equation (51) and (52) the conversion factors between the different parameters of both forms are printed.

$$\eta = \eta_\infty exp\left[\frac{B_\eta}{T - T_0}\right] \tag{25}$$

With B_η the activation temperature of viscose flow, which is usually called pseudo-activation energy in literature. T_0 is the temperature of zero configuration entropy or zero free volume.

The final volume in glass state i.e. the amount of free volume depends on the cooling speed (Figure 10). Therefore, with infinite slow cooling a maximum density in the glass state i.e. zero free volume might be reached. Following this line of interpretation T_0 might be understood as equilibrium glass-transition temperature[41]. T_0 often lies about 10-50 K below the (kinetic) glass-transition temperature T_g[41–43], from DSC experiments. η_∞ is the hypothetical high-temperature limit i.e. the viscosity at infinite temperature, even G. Tammann and W. Hesse already emphasized in their original work, that the VFTH equation is limited to the range between glass-transition temperature T_g and melting point T_m, so to the region where the fluid is in the state of an undercooled melt.

For B_η and especially its conversion to an activation energy of viscous flow different interpretations exist, that are sometimes mixed up in literature. B_η might be converted to an Arrhenius-like activation energy of viscous flow E_η according to equation (26). In contrast to the Arrhenius-Andrade theory E_η is temperature dependent. Therefore, data which follow the VFTH equation not give a straight line in the plot of ln(η) vs. 1/T but have a curved shape due to the variation of the slope with the temperature. If the investigated temperature range is significantly above T_0, which at the same time means significantly above T_g, the temperature-dependent factor in equation (26) vanishes and the temperature independent activation energy E_η' of the viscous flow is obtained. Equation (27) for the conversion of B_η to E_η' under the boundary condition $T>>T_0$ corresponds from the form the conversion of the activation temperature b to E_A in the Arrhenius-Andrade equation (22).

$$E_\eta = -RT^2\frac{d\ln(\eta)}{dT} = -RT^2\left(\frac{d\left(\ln(\eta_\infty)+\frac{B_\eta}{T-T_0}\right)}{dT}\right) = -RT^2\cdot\frac{-B_\eta}{(T-T_0)^2} \qquad (26)$$

$$E_\eta = R\left(\frac{T}{T-T_0}\right)^2 B_\eta$$

$$\text{For} \quad T \gg T_0 \quad E'_\eta \approx R\cdot B_\eta \qquad (27)$$

1.4 Electrochemical Characterization

1.4.1 Ionic Conductivity

If two electrodes are immersed in an electrolyte and an alternating electric voltage is applied a charge flow due to ion movement is observed (Figure 17).

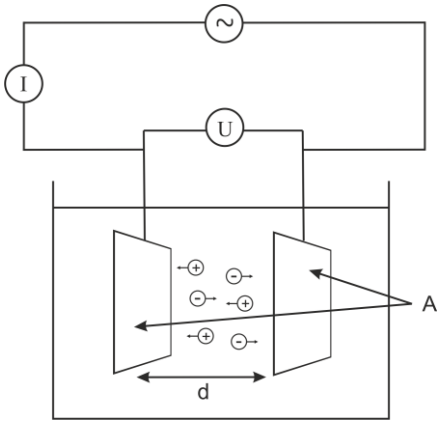

Figure 17 Schematic set-up for the measurement of the conductivity of an electrolyte.

The driving forces for the ion movement are thereby diffusion, advection and electromigration. In case of a static liquid no advection occurs. By the use of an alternating voltage the formation of a concentration gradient and thereby diffusion is suppressed. Then the only driving force is electromigration F_{el}. This driving force is opposed by the frictional force F_d between the moving ion and the surrounding medium. If the ion j is assumed as a solid sphere the frictional force can be calculated with the Stokes law (eq. (17)). The ion reaches a constant drift speed v_j if both forces F_{el} and F_d are in an equilibrium (eq. (28)-(30)).

$$F_{el} = -F_d \tag{28}$$

$$z_j e E = 6\pi r_j \eta \, v_j \tag{29}$$

$$v_j = \frac{z_j e}{6\pi r_j \eta} E \tag{30}$$

Here z_j is the charge number and r_j the radius of the solvated ion i.e. the sum of the ionic radius and the radius of the solvation shell, e is the elementary charge, E the electric field strength and η the dynamic viscosity of the fluid.

This drift speed could be used to calculate the current density j which flows between the two electrodes. The current density j is defined as the charge Q i.e. the number of ions multiplied by their charge number, which flows in a defined time t through the cross-section A between the two electrodes (eq.(31)).

$$j = \frac{Q}{A \cdot t} = \sum_n z_i F c_i v_i = \underbrace{\sum_n \frac{(z_i e)^2 N_A c_i}{6\pi r_i \eta}}_{\sigma} E \tag{31}$$

$$\sigma = \sum_n \frac{(z_i e)^2 N_A c_i}{6\pi r_i \eta} = \sum_n \frac{(z_i e)^2 N_A c_i}{6\pi r_i} \cdot \phi \tag{32}$$

Here F and N_A are the Faraday and Avogadro constant, respectively. c_i is the concentration of the ion sort *i* in the fluid and the sum runs over all sorts of ions in the fluid. ϕ is the fluidity, the reciprocal of the dynamic viscosity η.

The current density j is proportional to the electric field strength E with the ionic conductivity σ as the proportionality constant (eq.(31)). The ionic conductivity σ is the reciprocal of the specific resistivity ρ of the electrolyte (eq.(33)) and is usually expressed in $S \cdot m^{-1}$ or $mS \cdot cm^{-1}$. The unit S is called Siemens and is the reciprocal of an Ohm.

$$\sigma = \frac{1}{\rho} \tag{33}$$

For the measurement of the ionic conductivity a cell like in Figure 17 is used. The electrodes have to be non-polarizable electrodes like platinized platinum, to prevent false results due to an additional polarization current at the electrodes, beside the desired current by the ion flow. While the specific resistivity ρ and thereby the ionic conductivity is not directly accessible it can be calculated from the solution resistance R_{sol} and the geometry factor of the measurement cell (eq.(34)).

$$R_{sol} = \rho \cdot \frac{d}{A} = \rho \cdot k_c \tag{34}$$

The geometry factor, the so-called cell constant k_c is the quotient of the distance d of the two electrodes and the surface area A. k_c is usually not retrieved from the less precise geometrical dimensions of the measurement cell, but is determined in a calibration experiment with a standard solution of known ionic conductivity i.e. an aqueous KCl solution.

The solution resistance R_{sol} is measured by impedance spectroscopy. Therefore, the sample is perturbated from equilibrium state with a small alternating voltage like 50 mV-150 mV amplitude and the frequency of the alternating voltage is ramped e.g. between 100 Hz-50 kHz. The solution resistance R_{sol} is obtained from the system response i.e. the impedance of the sample by fitting the experimental data to an equivalent circuit.

The frequency analyzer (FRA) based Multiplexed Conductivity Meter MCM 10 (Material Mates/BioLogic) used in this thesis, extracts the solvent resistance R_{sol} from the impedance data by a slightly different approach. The frequency with the smallest modulus of the phase angle is selected for evaluation. There the modulus of the impedance is taken as an approximation for the solvent resistance R_{sol}[44].

As obvious from equation (32) the ionic conductivity σ depends on the concentration of the ionic species in the sample. An attempt to eliminate the concentration-dependency and to obtain a material specific quantity is the introduction of the molar conductivity Λ (eq. (35)). For a fully dissociated 1:1 electrolyte ($c_{Anion}=c_{Cation}=c$) it is calculated by dividing the ionic conductivity by the concentration c of the ionic species. The concentration itself is calculated from the density ρ and the molecular weight M_w.

$$\Lambda = \frac{\sigma}{c} = \sigma \cdot \frac{M_w}{\rho} \tag{35}$$

However, from experimental results it is known, that Λ is not truly concentration independent. For example, for diluted fully dissociated electrolytes the concentration dependency of Λ is described by the Debye–Hückel–Onsager theory.

1.4.2 Walden Plot

An important approach for qualitative evaluate of the molar conductivity Λ and discussion of conduction mechanisms in polymers, glasses and especially in ILs is the so-called Walden plot. In 1906 P. Walden published a systematic study on viscosity and molar conductivity for the limiting case of infinite dilution of tetraethylammonium iodide in different organic solvents. Thereby he discovered, that the product of the molar conductivity at infinite dilution and the viscosity of the neat solvent is a temperature and solvent independent constant. P. Walden explained this by the invers proportionality between molar conductivity and viscosity i.e. with a higher viscosity a lower molar conductivity is observed and vice versa[45]. In 1914 P. Walden performed a similar study with ammonium nitrates melts, which are now known as protic ionic liquids (PILs). This study confirmed the finding of constant product of molar conductivity and viscosity for concentrated ionic fluids, too[46].

Mathematically the so-called Walden product rule or simply Walden rule is given in equation (36). For a fully dissociated 1:1 electrolyte ($c_{Anion}=c_{Cation}=c$) the Walden product has a constant value C at a given temperature, which theoretically only depends on the charge numbers z_i and ionic radii r_i of the cation and anion.

$$\Lambda \cdot \eta = constant\ "C"\ = \frac{e^2 N_A}{6\pi} \sum_n \frac{z_i^2}{r_i} \tag{36}$$

In equation (36) the molar conductivity and viscosity are directly proportional i.e. an increase of the viscosity by a factor of two will decrease the molar conductivity to ½. This proportionality is "fractured" in the equation (37), the so-called fractional Walden rule. α[g] is a constant between zero and unity. Its physical meaning will be explained in detail in the next paragraph about the Walden plot.

$$\Lambda \cdot \eta^{\alpha} = C \tag{37}$$

Nearly a century after P. Walden published his work, C. A. Angell and Coworkers realized the significance of Walden plot, the graphical representation of the Walden rule, for the classification and analysis of conductivity in polymers[47] and ILs, especially in PILs[48–51].

For the so-called Walden plot the fractional Walden rule in equation (37) is mathematically rearranged and the decadic logarithm of the molar conductivity Λ for different temperatures is plotted over the decadic logarithm of the fluidity ϕ (reciprocal of η). Materials which follow the Walden rule will display in such a Walden plot a linear trend with a slope of α and an intercept of C (eq.(38),Figure 18)[h].

$$log\Lambda = \alpha log\left(\frac{1}{\eta}\right) + log(C) = \alpha log(\phi) + log\left(\frac{e^2 N_A}{6\pi} \sum_n \frac{z_i^2}{r_i}\right) \tag{38}$$

A special line in this Walden plot is the diagonal, which serves as reference line. If the units of reciprocal Poise P^{-1} and $S \cdot cm^2 \cdot mol^{-1}$ are used the diagonal corresponds to a line of origin, i.e. the intercept C is zero, with slope α=1 through the datapoint of 1 M KCl (~2.05/~2.05) at 25 °C. Since the line passes through the data point of 1 M KCl at 25 °C and is also similar to the data points of KCl solutions with other concentrations, (Figure 18b), this reference line is often called KCl line.

[g] α should not be confused with the dissociation degree, for which the same symbol is usually used.
[h] This statement is only valid if the density change with temperature is linear. This is the case for most ILs and many other materials.

However, the selection of the data point of the 1 M KCl solution at 25 °C as the base point of the reference line is an arbitrary definition, which is not based on theoretical principles, but nevertheless has found wide acceptance in the scientific community[52].

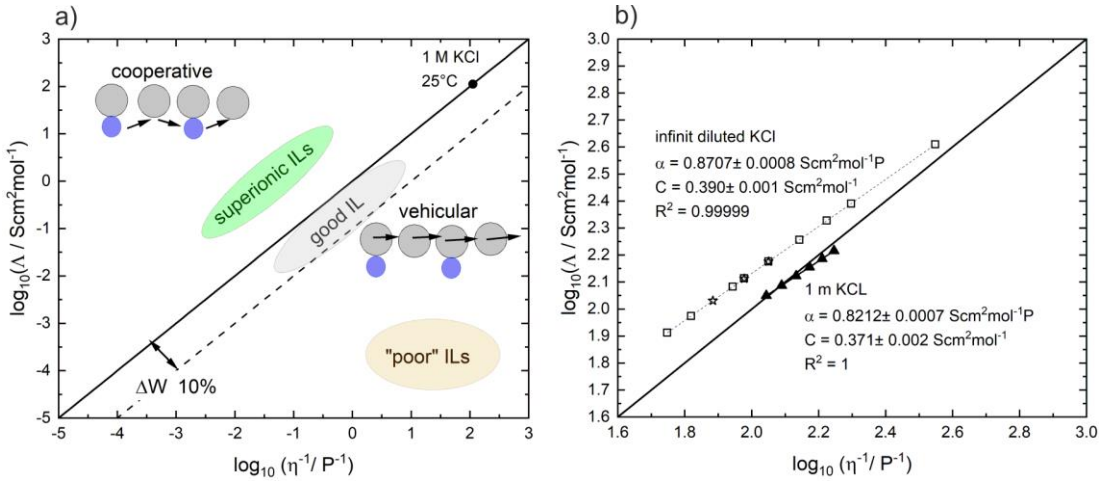

Figure 18 a) Schematic Walden plot. The different areas of „good", „poor" and „superionic" ILs and the different conduction mechanisms are marked. b) Walden plot of aqueous KCl. The solid triangles correspond to 1 m KCl with a solid line as linear fit. Ionic conductivity data from [31] "page 5-72", density from [53] (for 1.0043 m KCl) and viscosity from [54]. The open squares are infinite diluted KCl with a dashed line as linear fit. Data for the open squares are calculated from [55] "Appendix 6.2". The open stars represent data of infinite diluted KCl, from [56] with the viscosity values of pure water given there.

To understand the significance of this reference line the slope α has to be examined in more details.

The slope α depends on the relation between the temperature dependency of the molar conductivity Λ and the fluidity ϕ i.e. on the relation of the temperature dependencies of σ and η. The dynamic viscosity η in supercooled melts and ILs usually can be described by the VFTH equation (eq.(25)). Due to the proportionality between the fluidity ϕ and ionic conductivity σ (eq.(32)), the ionic conductivity in ILs displays usually a VFTH behavior, too (eq.(39)).

$$\sigma = \sigma_\infty exp\left[\frac{-B_\sigma}{T - T_0}\right] \tag{39}$$

$$E_\sigma = RT^2\frac{d\ln(\sigma)}{dT} = \mathrm{R}\left(\frac{T}{T - \mathrm{T_0}}\right)^2 \mathrm{B}_\sigma \tag{40}$$

$$\mathrm{T}>>\mathrm{T_0} \quad E_\sigma{}' = B_\sigma \cdot R \tag{41}$$

B_σ the activation temperature or pseudo-activation energy of ionic conductivity, T_0 the temperature of zero free volume and σ_∞ the conductivity at infinite temperature are fitting constants.

Their physical meanings are similar to B_η, T_0 and η_∞ in subchapter 1.3.3 but here in the context of the ionic conductivity instead of the viscose flow. B_σ can be transformed to an Arrhenius-like activation energy of ionic conductivity E_σ by equation (40). Like for E_η for $T>>T_0$ a temperature independent activation energy of ionic conductivity E_σ' is obtained (eq.(41)).

A different temperature dependency of the viscosity (eq.(25)) and the ionic conductivity (eq.(39)) i.e. fluidity and molar conductivity, only originate from the pseudo-activation energies B_η and B_σ if the preexponential factors η_∞, σ_∞ are assumed temperature independent[i]. Therefore, the slope α in the Walden plot can be interpreted as the ratio of both activation temperatures (or pseudo-activation energies) according to equation (42).

$$\alpha = \frac{B_\sigma}{B_\eta} \tag{42}$$

A slope α=1 therefore could be interpreted by equal pseudo-activation energy of ionic conductivity B_σ and viscos flow B_η. This condition is fulfilled if the charge carriers move without interactions with other ions or solvent molecules by electromigration. Therefore C.A. Angell and Coworkers applied the diagonal as reference line for ideal diffusion dependent conductivity. In context of PILs the proton transport has to be considered. For the diagonal line an ideal vehicular mechanism can be assumed (Figure 18a). Thereby the proton only travels with the anion or cation, which diffuses across the fluid. In contrast results from aprotic ILs and PILs often fall well below the diagonal. This means that the molar conductivity is smaller than for the ideal reference line. C.A. Angell and Coworkers have attributed this deviation from the ideal behavior in aprotic ILs to a restriction of unimpeded ion movement due to ion pair association. For PILs data below the diagonal might indicate beside ion pair association an incomplete proton-transfer and therefore lower number of ions which can contribute to the molar conductivity. To compare and categorize ILs and PILs based on the degree of ion pair association and amount of proton transfer in PILs, the parameter ΔW is introduced. ΔW states the distance of the experimental data to the reference line. A deviation of 10% below the ideal line is often taken as boarder to separate "good" and "poor" ILs (Figure 18a). In case of aprotic ILs "good" might be understood as high conducting electrolyte due to low degree of ion pairing. For PILs beside the ion paring incomplete proton-transfer i.e. formation of the PIL, might be another reason for a conductivity well below the ideal line. This behavior will result in a classification as "poor" PIL.

[i] To take the temperature dependency of the preexponential factor in VFTH equation of conductivity or molar conductivity into account σ_∞ is sometimes multiplied by the factor $T^{-1/2}$ [42]. This might be justified from the free volume transport model[174].

Beside the position relative to the ideal reference line the slope α, obtained from a linear fit of the experimental datapoint is another important parameter, which can be determined from the Walden plot.
As explained with equation (42) α depends on the ratio of pseudo-activation energies B_σ of ionic conductivity and B_η of viscose flow. $\alpha=1$ corresponds to equal pseudo-activation energies for ionic conductivity and viscosity and therefore the ideal behavior of unimpeded ion transport in the electric field on the ideal reference line. $\alpha<1$ implies $B_\sigma<B_\eta$. Ion pairing will lead to an increase in the activation-energy of the viscos flow B_η and thereby a reduction of the slope α. Within a dataset the effect of the ion pairing, can often be observed by a decreasing slope with increasing temperature. The increase of the ion pair association with increasing temperature is understandable with the idea that at the (hypothetical) boiling point not single ions but ion pairs enter the gas phase because of the charge neutrality condition[50].

While most ILs lay below the diagonal in the Walden plot, a few examples above the ideal line are known. $LiAlCl_4$ is one example of an aprotic IL which is located above the diagonal in the Walden plot[57]. Among the PILs some examples, mostly with hydrogen sulfate or dihydrogen phosphate anions display a molar conductivity above the value expected for the given fluidity on the diagonal. For instant butylammonium hydrogensulfate and dimethylammonium hydrogensulfate slightly exceed the diagonal for low temperatures[58] or guanidinium dihydrogenphosphate displays a more pronounced position above the diagonal line[59]. The physical meaning of this finding is, that the molar conductivity is larger than obtained by ideal vehicular transport mechanism. The additional conductivity in PILs might be interpreted as an indication for a cooperative conduction mechanism, similar to the Grotthuss mechanism of protons in water[60,61]. In such a cooperative conduction mechanism the proton transport is decoupled from the molecular movements in the electrical field. Instead of motion together with the molecules of the liquid, like in the vehicular mechanism, the proton is transferred from one molecule to another. Therefore, the proton transfer could potentially be faster than the motion of the molecules and higher conductivity is expected. It is important to mention that a proton-transfer reaction changes the charge state of a molecules/ions in a PIL, i.e. a cation becomes neutral after deprotonation or an anion becomes neutral after protonation and a neutral molecule might become an anion or cation after deprotonation or protonation, respectively. Therefore, in a cooperative proton mechanism a cascade of transfer reaction appears, which leads to the motions of the protons through the liquid. ILs above the diagonal are called “superionic”[50].

For superionic PILs with a cooperative conduction mechanism $\alpha<1$ is expected. Here the pseudo-activation energy for the ionic conduction B_σ is smaller than for the viscous flow B_η, due to the decoupling of proton transfer from the ion motion.

This shows, that a slope α<1 might be a sign for ion pairing or for a decoupling of the conduction mechanism from ionic motion. The two effects can be distinguished depending on which side of the ideal reference line (diagonal) the data fall on[50].

This section so far explained the concepts behind the Walden plot in detail and displayed the virtue of this simple approach. However, wrong conclusions might be drawn if only relying on the Walden plot. Therefore, although additional data analysis models and theoretical approaches should be used.

One main critic by C. Schreiner et al. is the general concept of the diagonal as the ideal reference line[52]. The assumption of a slope at unity for ideal behavior is questionable since the slope for the fit in many diluted solutions tends to be found at 0.8±0.1 i.e. well below unity.

Figure 18b illustrates the slope below unity for literature data of infinite diluted aqueous KCl and for data calculated from different sources for 1.0 m aqueous KCl (1 mol KCl per 1 kg water). In addition, the data points for infinite diluted KCl lie above the diagonal. This illustrates that the assumption of an intercept of 0, which was behind Angell et al.'s choice of the diagonal as reference line might not be valid without restrictions.

A modification to tackle the intercept challenge in the Walden plot, was proposed by D. R. MacFarlane et al.[62]. He found that when ILs with significantly different sized ions are compared, ILs with large ions lie further below the diagonal (larger ΔW) than ILs with smaller ions. The ILs with the bulkier ions therefore might be incorrectly considered by the ΔW to have stronger ion pairing than the ILs with smaller ions. The origin of the downward shift of ILs with larger sized ions in the Walden plot can be understood when the intercept C of data displayed in the Walden plot is analyzed. Equation (38) shows that the intercept is inversely proportional to the sum of the ionic radii. Therefore D. R. MacFarlane et al. proposed to multiply the fluidity by a correction term with the radii r_+ and r_- of the cation and the anion. Such shift of the data points to smaller x values corresponds to an upward shift relative to the diagonal in the Walden plot. The formula for the Walden plot with the radii adjustment can be written according to equation (43).

$$log\Lambda = \alpha log\left(\frac{1}{\eta}\cdot\left(\frac{1}{r_+}+\frac{1}{r_-}\right)\right) + log(C') \qquad (43)$$

For the correction of the Walden plot according to equation (43) the ''effective'' cation r_+ and anion r_- radii are required.

With the assumption of a spherical shape the radii of the anion and cation can be obtained from the molecular volumes of the anion $V_m(A^-)$ and cation $V_m(C^+)$ according to equation (44).

$$r_+ = \sqrt[3]{\frac{3}{4\pi} \cdot V_m(C^+)} \quad and \quad r_- = \sqrt[3]{\frac{3}{4\pi} \cdot V_m(A^-)} \tag{44}$$

For condensed ionic matter the molecular volumes $V_m(A^-)$ and $V_m(C^+)$ of the anion and cation, respectively, can be estimated from X-ray crystal structures. The exemplary formula for the calculation of the molecular volume of the anion in a crystal with a 1:1 anion-cation ratio is given in equation (45)[63].

$$V_m(A^-) = \frac{V_{cell}}{Z} - V_m(C^+) \tag{45}$$

Here V_{cell} is the volume of the unit cell. Z is the number of formula units i.e. anion-cation pairs, in the unit cell. For the calculation a volume has to be assigned to the counter-ion in the formula unit i.e. the $V_m(C^+)$ in equation (45). Values for the molecular volume for some common ions can be found for example in the work of L. Glasser and H. Jenkins[64]. There the values were obtained by least-square optimization of the single ion volumes for an experimental set of 237 ionic solids. By this method the void space in the unit cell is equally distributed between the cations and anions. Molecular volumes calculated by this approach from the unit cell volume include portions of the void space in the crystal structure and are therefore in some cases larger than the values obtained by other methods.

D. W. M. Hofmann studied the averaged atomic volume in crystal structures by splitting the unit cell volume into the volumes of the individual atoms, which constitute the crystal structure[65]. By an iterative multi-linear least-square regression process the atomic volumes for the first 100 elements in the periodic table were obtained. For this process calculated unit cell volumes were optimized by least-square regression against 20 training sets of each 9112 experimental cell volumes from the Cambridge Structural Data base. The molecular volume can be obtained from Hofmann's averaged atomic volumes V_{atom}(Hoffmann) according to equation (46).

$$V_m(\text{Hofmann}) = \sum V_{atom}\,(Hofmann) \tag{46}$$

Alternative approaches for the determination of the molecular volume are based on summation of group or single atom contributions. In 1964, A. Bondi derived the still widely used set of van der Waals radii and molecular volumes of selected functional groups[66].

These calculations are based on experimental densities and a geometric model in which the atoms under consideration are represented by two overlapping spheres. The distance between the centers of the spheres corresponds to the covalent bond distance and the radii of the overlapping spheres to the van der Waals radii. Bondi's results for the main group elements are still in use today and have also been confirmed by more recent studies.

S. Alvarez determined the van der Waals radii in his 2013 study using bond length distributions mapping[67]. His results are in good agreement with Bondi's van der Waals radii for most of the main group elements. However, for the main group elements nitrogen, sulfur and phosphorus, Alvarez found significantly larger radii than Bondi, because Alvarez excluded in contrast to Bondi crystal structures in which hydrogen bonds can occur. A comparison of the different van der Waals radii and molecular volumes obtained by the cited studies for the elements relevant in this thesis is given in Table S 1 on page 149.

Despite the good agreement with experimental crystal densities, which is achievable with molecular volume values for functional groups, such an approach is limited to groups with published volume contributions. Y. H. Zhao et al.[68] calculation from Bondi's data single atom contributions for common elements in organic molecules. They could demonstrate, that by the addition of several correction terms, the molecular volume can be calculated with this small set of single atom contributions with comparable accuracy to quantum chemical methods. The required correction terms for the calculation of the molecular volume (in $Å^3$) are displayed in equation (47).

$$V_m(\text{Zhao}) = \sum V_{atom}(Zhao) - 5.92\ B - 14.7\ R_A - 3.8\ R_{NA} \qquad (47)$$

Here V_{atom}(Zhao) are the volumes from the individual atoms in the molecule according refence[68]. These values are also printed Table S 1 on page 149 in the appendix. B is the number of bonds in the molecule and includes all bond orders i.e. single, double and triple bonds. R_A and R_{NA} are the number of aromatic and non-aromatic rings in the molecule, respectively.

2. Experimental Part: Materials & Methods

2.1 Chemicals and Materials

Table 1 Chemicals and Materials.

Use	Material	Supplier	Specification Part-Number
Synthesis DESPA&DEMSPA zwitterion	1,3-Propane sultone	Alfa Aesar	99%,
	Diethylamine	Sigma Aldrich	≥99.5%
	N,N-Diethyl-N-methylamine	ACROS Organics	98%
Synthesis of PIL	Trifluoromethanesulfonic acid	Sigma Aldrich	98%
	2-Aminoethanesulfonic acid (Taurine), SEA zwitterion	Merck	Taurine for synthesis ≥ 99.0 % 808616
	2-Aminoethyl dihydrogen phosphate, PEA zwitterion	Sigma Aldrich	≥98.0%
	2-Aminoethyl hydrogen sulfate, SOEA zwitterion	Sigma Aldrich	≥98.0%
	Methanedisulfonic acid, H2MDS	abcr	95% AB336890
Synthesis of H2MDS	Methanedisulfonic acid Dipotassium salt	Sigma Aldrich	≥99.0% 94589-50G-F
	Barium chloride $BaCl_2$(anhydrous)	Alpha Aeser	99.998% (metal basis) 10995
	Sulfuric acid	Merck	96% supra pure 1.00714.100
Calibration standard ICP-OES	ICP multi-element standard solution IV	Merck	111355
IL samples	$[DESPA^+][TfO^-]$ 99%	IoLiTec	Batch T001x88.1-FR 1326
	Propylammoniumnitrate	Synthesized by Dr. Alessandro Mariani	-
	Ethylammoniumnitrat	Synthesized by Dr. Alessandro Mariani	-
Viscosity standard for Rheometer tests	Ethylenglycol high purity Grade	VWR chemicals	-
	Viscosity and Density Standard N1400	Paragon Scientific Ltd	-

Continuation Table 1 Chemicals and Materials

Use	Material	Supplier	Specification Part-Number
General lab chemical, KF titration	Aquastar CombiCoulomat fritless Karl Fischer reagent	Merck	Supelco 109257
	Karl Fischer water calibration standard, 100 ppmw in anisole	VWR chemicals	-
	Absolute ethanol	Merck	Ethanol absolute EMPLURA sulpleco 8.18760.1000
	Methanol anhydrous	VWR chemicals	83679.290
NMR spectroscopy	DMSO-d_6 (99.9%D) + TMS 0.1 v% for NMR	Merck	Magni solv 1.03587.0025
	DMSO-d_6 (99.80% D) +0.03% TMS(v/v)	VWR chemicals	84113.0025
	Heavy water D_2O	Alfa Aesar	99.8% (D)
Calibration standard conductometer	KCl Standard (0.01 $mol \cdot L^{-1}$) with a conductivity of 1.413 $mS \cdot cm^{-1}$ (25 °C)	VWR chemicals	83607.180

2.2 Methods

Ultrapure water (>18 MΩ·cm at 25 °C) from a MilliQ device was used for the preparation of all aqueous solutions. All commercial chemicals were used as received.

Synthesis of DESPA and DEMSPA zwitterion
The zwitterions were provided by Dr. Xinpei Gao. The synthesis is published in[69]. Briefly, diethylamine for DESPA or *N*, *N*-diethyl-*N*-methylamine for DEMSPA and 1,3-propane sultone were dissolved separately in acetone. The amine/acetone mixture was added slowly under ice cooling to the 1,3-propane sultone/acetone mixture. After complete addition stirring on ice was continued for further 3 h. Continued by stirring at room temperature for 3 days. During this time the zwitterion precipitates. It was collected by filtration, washed with acetone and dried at 80 °C under vacuum.

Synthesis of [DESPA$^+$][TfO$^-$], [DEMSPA$^+$][TfO$^-$],[SEA$^+$][TfO$^-$], [SOEA$^+$][TfO$^-$], [PEA$^+$][TfO$^-$]
The protic acidic ionic liquids (PAcILs) were prepared by addition of the stochiometric amount of trifluoromethanesulfonic acid to the zwitterions. After the addition the mixture was heated for 1 h to 80 °C to achieve a complete dissolution of the zwitterion. Transparent colorless to slightly yellow PAcILs were obtained. Due to the high hygroscopicity the PAcILs were stored in a vacuum desiccator in a dryroom (dew point <-60 °C).

Synthesis of H2MDS
The synthesis followed the route by H. J. Backer[70] and the patent U.S. 9,440,915 B2[71]. An illustration of the synthesis route can be found in Figure 33.

1. Step: Preparation of BaMDS
All glass vessels were cleaned with sulfuric acid and then rinsed with MilliQ water. 15.617 g anhydrous $BaCl_2$ (75 mmol) was dissolved in 50 ml water. To remove some insoluble (dust) particles the solution was filtered through a 0.2 µm syringe filter. 19.999 g (79 mmol) of dipotassium methanedisulfonate (K2MDS) was dissolved in 350 ml water. To support the dissolution of K2MDS the solution was heated to 60 °C. Afterwards the temperature was increased to 80 °C and the $BaCl_2$ solution was added. Directly after addition of the $BaCl_2$ the solution some fine precipitate was visible. The solution was stirred for another hour at 80 °C and then kept for about 41 h at room temperature (without stirring) to allow the growth of larger crystals. The aging should ease the workup by filtration. After filtration and washing with about 175 ml of water the product was dried for 20 h at 80 °C in vacuum. 21.862 g (63 mmol) of the barium methanedisulfonate ($BaMDS \cdot 2H_2O$) were obtained. This corresponds to a yield of about 84 % related to the $BaCl_2$.

2. Step: Conversion of BaMDS to the free acid

20 g (58 mmol) BaMDS·2H_2O were loaded in a 1 L round flask with 500 ml of water. 27.6 ml 20% H_2SO_4 (64 mmol) were added. After completion of the addition of the acid the solution was heated for 14.5 h to 120 °C. During the reaction time no significant optical change was observed and a solid, most probably $BaSO_4$, remains in the reaction mixture. By centrifugation (6000 rpm, 30 min) the liquid phase was separated from the solid. The liquid phase was completely dried with a rotary evaporator and a membrane pump. The total drying time was 189 h, and the temperature did not exceed 40 °C during the process. About 11 g of the final product after the drying was obtained. Assuming a structure of H2MDS·2H_2O this corresponds to a yield of about 52 mmol or about 90%.

Synthesis of [$DESPA^+$][$HMDS^-$]

Here the synthesis with the commercial H2MDS is described. However, the synthesis can be performed analogues with the self-synthesized H2MDS.

The batch of [$DESPA^+$][$HMDS^-$] used for all experiments except the Pulsed-Field Gradient Spin-Echo (PGSE) NMR experiments was synthesized according to the following description. 10000 mg of DESPA zwitterion (M_w:195.28 g/mol, n:51.2 mmol) was weighted in a 100 ml round flask and dissolved in about 15 ml water. 9020 mg of the commercial methanedisulfonic acid H2MDS (abcr, nominal M_w:176.16 g/mol, n:51.2 mmol) was added to 20 ml water under ice cooling. The aqueous H2MDS solution was added slowly (about 1 drop per second) to the ice-cooled aqueous solution of the DESPA zwitterion. After completion of the addition of the acid to the zwitterion the ice bath was removed and the solution was stirred over night at ambient temperature. About 28 ml of water (pH 5 by pH paper) were removed with a rotary evaporator at 50 °C and the vacuum set to 1 mbar. On the next day another 263 mg of the H2MDS was dissolved in about 5 ml water and slowly added to the ice-cooled reaction mixture. This further addition of acid was done because the initial ratio did not consider the crystal water in the commercial H2MDS. Based on the intense studies (subchapter 4.2) a structure of H2MDS·0.28 H_2O (M_w: 181.29 g/mol) is proposed for the used batch of the commercial H2MDS. With this formula the total amount of about 9283 mg are the equimolar amount of the DESPA zwitterion i.e. 51.2 mmol. Again, the mixture was stirred over night at ambient temperature. Remaining water was first removed at the rotary evaporator at 60 °C and a vacuum of 40 mbar before the sample was dried in oil pump vacuum. The protocol for the drying was: 40 °C 12 h, 50 °C 3.5 h, 60 °C 5.5 h, 80 °C 60 h. After this procedure a final vacuum of $1 \cdot 10^{-3}$ mbar was reached. During the drying in the oil pump vacuum a total amount of about 2.3 g of water was removed.

The batch for the PGSE-NMR experiments was synthesized slightly different. 5.00056 g (M_w:195.28 g/mol, n: 25.6 mmol) was dissolved in 20 ml water in a round flask. 4.64200 g (M_w: 181.29 g/mol, n: 25.6 mmol) of the commercial H2MDS was added to the ice-cooled solution of the zwitterion.

The mixture was stirred for 30 minutes on ice after the addition. The water was removed at the rotary evaporator at 60 °C over night. A final vacuum of about 70 mbar was reached. The removed water had a pH of 5-6 by pH paper. The drying was continued as for the other sample in oil pump vacuum:50 °C 5 h, 60 °C 5 h, 80 °C 40 h, 90 °C 21 h. After this drying process the water content was still about 1.1 wt%. Therefore, the drying was continued with a turbopump at 80 °C for 46.5 h. At the end of the drying process a final pressure $4 \cdot 10^{-6}$ mbar was reached. After the drying process the averaged water content (with maximum error) from four Karl Fischer titrations was 5483±189 ppmw.

NMR experiments

Monodimensional ^{1}H-NMR at Institute of Organic Chemistry I of Ulm University

^{1}H-NMR of the PAcILs were performed on a Bruker Avance III or on a Bruker Avance Neo 400 spectrometer, both working at a 9.4 T magnetic field (^{1}H-NMR operating frequency 400 MHz). Usually zg50 or zg30 pulses were applied. Apodization, phase correction and baseline subtraction were done manually in MestReNova14.2.0. Standard NMR tubes of "Economy" Quality (Hilberg) with outer diameter 4.95±0.05 mm and inner diameter 4.19±0.05 mm were used.

Preparation of neat samples for experiments in coaxial configuration:

A coaxial capillary configuration was used to study the neat PAcILs. In case of the experiments in Figure 24 the locking-solvent D_2O+maleic acid was flame sealed inside a capillary (Hilgenberg NMR tube "Economy" quality 2.95±0.03 mm, inner diameter: 2.36±0.03 mm) and the PAcILs [SOEA$^+$][TfO$^-$] and [DESPA$^+$][TfO$^-$] were added into the gap to a 5mm diameter NMR tube("Economy" quality, Hilberg). For the other experiments with neat sample the PAcILs were flame-sealed into the capillary. The sealing process took place in a dryroom (dew point <-60 °C). To fill the highly-viscous PIL in the capillaries the samples were pre-heated to 80 °C. Then the PAcIL was injected into the capillaries through a cannula fitted by luer-lock connection to a syringe. The needle was inserted in the capillary through a glass Pasteur pipette. This allowed the retraction of the needle from the capillary without contamination of the capillary walls in the later flame-sealed part. During the process, all devices were heated with a heat-gun. Air bubbles were removed from the capillaries by cycles of centrifugation and cautious heating in vacuum to 80 °C. Some D_2O (Alfa Aesar 99.8% D) or DMSO-d_6 (Merck, 99.9% D or VWR Chemicals 99.80% D) was then added as locking solvent in the space between the capillary and the NMR tube's walls, until solvent level reached the same level of the PAcILs inside the inner capillary, thus minimizing the inhomogeneity of the magnetic field.

PGSE ^{1}H-NMR at University of Turino

PGSE ^{1}H-NMR analysis was performed on a Jeol ECZR600 spectrometer, working at a 14.1 T magnetic field (^{1}H-NMR operating frequency: 600 MHz). The spectra were

recorded in a coaxial capillary configuration, with the ionic liquid sample inside a flame-sealed capillary (Hilgenberg NMR tube "Economy" quality, inner diameter: 2.36±0.03 mm). Some DMSO-d_6 (Merck, 99.9% D) was then added as locking solvent in the space between the capillary and the NMR tube's walls, until solvent level reached the same level of the ILs inside the inner capillary, thus minimizing the inhomogeneity of the magnetic field. Monodimensional ^{1}H-NMR spectra were acquired without sample spinning, and with a relaxation delay of 1 s. PGSE experiments were performed at 358 K, 370 K, 382 K and 393 K, applying 32 gradient amplitudes (from 0.05 to 800 mT/m), with a gradient pulse duration of 3.5 ms and a diffusion time of 0.3 s. Parameters were optimized at the higher temperature and then they were kept constant. The modification of these parameters at the lower temperature values does not improve the quality of the spectra due to the extreme viscosity of the sample.

ICP-OES

ICP-OES analysis was performed on a Spectro Arcos spectrometer (Spectro Analytical Instruments). A multi-element standard with Al, B, Ba, Bi, Ca, Co, Cu, Fe, K, Li, Mg, Mn, Na, Ni, Pb, Tl, Zn was used for the calibration. Typically, 50-70 mg of PAcIL sample were dissolved in aqua regia. The measurement sequence consisted of the following steps: calibration measurement with the standard, blank measurement with ultra-pure water (MilliQ, Merck) and measurement of the sample. The blank measurements were periodically repeated between the sample measurements.

CHNS analysis

CHNS analysis was performed by Institute of Analytical and Bioanalytical Chemistry (IABC) of University Ulm with a vario Micro cube from Elementar.

Determination of the water content

The water content of the samples was determined by Karl Fischer titrations with a C30 coulometric Karl Fischer titrator (Mettler Toledo). The device was checked before each measurement series with a water standard (Karl Fischer water calibration standard, 100 ppmw in anisole, VWR). The IL was directly injected in Karl Fischer reagent (Aquastar CombiCoulomat fritless Karl Fischer reagent, Merck). To assure complete dissolution of the IL the reagent solution was stirred 300 s between the injection and start of the titration. The device was installed inside a dryroom (dew point <-60 °C) to minimize the drift and allow direct sample injection in the titrator without a septum.

The water content of the samples for the electrochemical experiments was measured with a 825 KF Titrando (Metrohm). To inject the highly viscous samples with a needle through a septum the samples were diluted with glacial acetic acid. The water content of the acid was determined before the experiment and considered in the calculation of the water content.

Thermogravimetric measurements

TGA experiments of all fluorinated PAcILs were performed with a TG 209 F1 Libra (Netzsch) in synthetic air (7-8 ml·min^{-1} O_2 (AIR LIQUIDE, 99.9999%) and 32-33 ml·min^{-1} N_2 (house supply)). The balance was protected during the experiments by a 20 ml·min^{-1} N_2 flow. Each sample was prepared directly before the TGA measurement to exclude alterations during storage. About 2-3 mg of specimen was sealed in a hermetic aluminum crucible (DSC-crucibles, 25 µL Netzsch) inside a dry-room (dew point: <-60 °C) to prevent water uptake from the environment. After the insertion of the crucible in the TGA furnace, the lid was pierced by the autosampler (Netzsch). An automatic baseline correction, considering the thermal buoyancies, heat rate, gas flow etc., was performed with the TG-BeFlat algorithm (Netzsch). To precisely control the sample temperature the sample temperature calibration (STC) function of the device was used. With the STC the heat release or consumption by chemical reactions of the sample is monitored with a thermal sensor in the sample holder and the heating rate gets adjusted accordingly. This sensor was used for the temperature calibration of the oven with melting point standards (Netzsch Calibration Kit), as well. The measurements and calibrations were performed with the Netzsch measurement software (Version 6.1.0, 11.07.2014). In dynamic experiments, after 30 min equilibration at 30 °C the samples were heated with 5 °C·min^{-1} up to a maximum temperature of 600 °C. In isothermal experiments a constant temperature was held for defined time in between the 5 °C·min^{-1} heating steps.

Isothermal TGA of [DESPA$^+$][HMDS$^-$] was performed with a Discovery TGA (TA Instruments). The sample was sealed in a hermetic aluminum crucible (Discovery TGA & Q5000 IR, 80 µL) inside a dryroom (dew point: <-60 °C) to avoid any water uptake. The lid of the crucible was perforated by the autosampler prior to the measurement. An empty crucible (nominally identical to the sample one) was used as counterweight on the balance scale. An atmosphere of 20 v% O_2 (AIR LIQUIDE, 99.9999%) and 80 v% N_2 (house supply) inside the furnace was set with the Trios software (v3.2.0.3887).

Differential Scanning Calorimetry measurements

DSC experiments were performed with a Discovery DSC (TA Instruments). The samples were sealed into hermetic aluminum crucibles (Tzero crucibles) inside a dryroom (dew point: <-60 °C). The headspace in the crucibles therefore were filled with dry air, and the results refer to the thermal behavior of the samples in dry air. To avoid contaminations i.e. by atmospheric moisture, the measurement cell was always kept at 40 °C between the experiments and was flushed with N_2 (house supply), when performing a DSC run. The standard measurement procedure consisted of an initial equilibration step at 40 °C for 30 min, followed by a cooling-heating cycles with 5 K·min^{-1}. The evaluation of the T_g was done with an inhouse developed variation of the mid-point method.

A linear baseline was fitted before and after the step by the glass transition. The intersection of the bisector of these two baselines with the DSC trace is defined as T_g.

Density measurements

The density was recorded with an DMA 4100 M density meter (Anton Paar). Due to the high viscosity of [$DESPA^+$][$HMDS^-$] trapped air bubbles were removed in oil pump vacuum at 80 °C (about 17 h) before the measurements. The sample was then directly injected into the pre-heated device (80 °C). [$DESPA^+$][TfO^-] was injected without overnight evacuation. The density values were acquired in 5 °C steps between 80 °C and 20 °C. Each step was hold until the instrumental stability criteria was reached. The maximum difference between a cooling and a consecutive heating cycle was 0.0001 $g \cdot cm^{-3}$. This proves the bubble-free injection and high reproducibility of the measurements.

Measurements of ionic conductivity

For the conductivity measurement the PAcILs were sealed inside a dryroom (dew point: <-60 °C) in High Temperature Conductivity Cells (HTCC) from Materials Mates. The cells consist of two parallel platinized platinum electrodes on a borosilicated glass holder. The cell constants were determined before each experiment with a 0.01 M KCl standard solution with a conductivity of 1.41±0.02 $mS \cdot cm^{-1}$ (25 °C). The conductivity was obtained from electrical impedance recorded for 27 frequencies in the range from 50 kHz to 100 Hz with a MCM 10 Multichannel Conductivity Meter (Materials Mates & BioLogic). The frequency with the smallest modulus of the phase angle is selected by the MultyC software (Materials Mates). The modulus of the impedance corresponds in good approximation to the electric resistance R of the investigated system. With the resistance R and the cell constant K the MultyC software calculates the specific conductivity κ of the sample in $mS \cdot cm^{-1}$. This set-up of HTCC and MCM10 allows according to the manufacturer measurements between 2 $\mu S \cdot cm^{-1}$ to 200 $mS \cdot cm^{-1}$. The nominal inaccuracy is less than 4% for the conductivity range of 2-20 $\mu S \cdot cm^{-1}$ and less than 2% for the 20-200 $mS \cdot cm^{-1}$ range. The temperature of the samples is controlled with a WTSH 10 Peltier based temperature control unit (Materials Mates). The WTSH 10 unit operates between -40 °C to +150 °C and has a nominal accuracy according to the technical datasheet of ±0.1 °C. In a typical measurement the sample is heated from 25 °C to 120 °C in 5 °C or 10 °C steps. Each temperature step was hold for 1 h and all conductivity values, where the temperature was within ±0.1 °C of the target temperature were accepted and averaged for the reported values.

Viscosity measurements

To avoid water uptake, the ionic liquids (ILs) were only handled in a dryroom (dew point < -60 °C, < 10 ppmw H_2O). Viscosity measurements were performed with an MCR 102 Rheometer (Anton Paar). Experiments with [$DESPA^+$][TfO^-] were performed with a

cone-plate geometry (diameter 25.026 mm; α=1.986° gap 0.108 mm) from Anton Paar. To protect the geometry against the strong acidic ILs it was coated with a Teflon layer. Unfortunately, this coating got mechanically damaged. Therefore, the experiments with [$DESPA^+$][$HMDS^-$] had to be performed with a different plate-plate geometry (diameter 25 mm) with a 100 µm gap. This geometry is made of titanium and therefore could resist the strong acidic ILs, too. A comparison between the values from the two different geometries didn't show a significant difference. Precise temperature control was achieved using a Peltier-heated P-PTD200/DI base plate and an H-PTD200 actively-heated geometry housing. In a typically experiment the temperature was ramped in 5 °C steps from the loading to the final temperature and back. At each step 100 points at a constant shear rate (often 10 s^{-1}) were recorded. For each point the signal was average for 3 s. Usually the change between the first and last measurement was within 10%. These changes confirm a negligible drying effect and the stability of the samples in the investigated temperature range.

Raman and IR spectroscopy:
The IR and Raman measurements were performed with a Bruker Vertex70 FT-IR spectrometer with a RAM II FT-Raman module with a laser wavelength of 1064 nm and a maximum laser power of 1000 mW.

For the IR measurements of the zwitterions and the precipitate, obtained after the reaction of [$SOEA^+$][TfO^-] with water, a diamond ATR unit was applied. During the experiment the sample was in vacuum, therefore the hygroscopic material could be analysed without water uptake.

For the temperature dependent Raman measurements, the samples were filled in 5 mm diameter economy NMR tubes (Wilmad). The temperature was controlled with a Linkam stage. Typically, 500 scans with 600 mW laserpower were accumulated for one spectrum.

Electrochemical experiments

For all electrochemical experiments the set-up developed by Wippermann et al. and described in detail in [72] was used. The measurements cell consists of a Pt crucible with a diameter of 20 mm and height of about 30 mm (volume 3–4 ml). The Pt crucible thereby serves both a vessel and counter electrode. The working electrode for the linear sweep voltammetry experiments was a Pt wire (1 mm diameter), which is molten into a glass capillary and protrudes for about 6.42 mm from the glass. The tip was round polished with 1200-4000 SiC abrasive papers and 1 µm diamond polish. The active surface area was determined before each experimental series by the H_2-desorption peak. Therefore, cyclic voltammograms at a scan rate of 100 $mV \cdot s^{-1}$ were recorded at 25 °C in 0.5 M H_2SO_4 in N_2 atmosphere (10 ml/min N_2, 1 h purged before the experiments).

A self-prepared palladium-hydrogen electrode was used as reference.

For the Chronoamperometric measurements for the determination of the oxygen saturation concentration and oxygen diffusion coefficient a Pt disc electrode with a diameter of 250 µm was used. The active surface area was determined in the same way like described above. Before the experiments the sample was purged for at least 2 h at 120 °C with O_2.

3. Development of Cation Structures for IT-PEMFC

3.1 Introduction

To mitigate the impact of climate change, greenhouse gas emissions must be reduced in all areas of life. In the mobility sector on the one hand the replacement of private cars with internal combustion engines to fully electrical vehicles (EVs) seems a possible route for drastically reduction in CO_2 emission. On the other hand, the replacement of internal combustion engines with electric motors and batteries in the public and goods transport sectors presents a challenge. Here alternative approaches which rely on chemical energy carriers like green-hydrogen or green synthetic fuels might be promising alternatives to fossil fuels. While green synthetic fuels might be used in combustion engines similar to state-of-the-art devices, for green-hydrogen a system consisting of a fuel cell (FC) and an electric engine is required.

The transition from coal and gas-powered electric energy generation to renewable production of electricity by wind and solar technology also brings the challenge of energy storage. To solve this challenge, energy storage strategies are required both to buffer short-term production peaks and to compensate seasonal variation in the solar power. In the so-called power-to-gas approach excess electric energy is used for the production of green hydrogen via electrolysis. The hydrogen could be stored, and when required is converted back to electric energy with fuel cells.

Fuel cells suitable for the conversion of hydrogen to electric energy are mainly the alkaline fuel cell (AFC) and the currently technical more relevant proton-exchange membrane fuel cell (PEMFC). The schematic of a PEMFC is displayed in Figure 19a).

The working principle of an FC is to divide the "Knallgas" reaction into spatially separated steps. Instead of directly transferring electrons from hydrogen to oxygen, the first step involves the oxidation of hydrogen to H^+ at the surface of the anode. The electrons transferred to the anode must take the path of least electrical resistance through the cables outside the cell, while the protons can directly pass through the electrolyte, i.e. the proton-exchange membrane, to reach the cathode. In the oxygen reduction reaction (ORR) at the cathode, protons and electrons react with oxygen to form water. This water must be removed from the cell. The electrons, on their path through the cables outside the cell, can be used to perform electrical work.

Due to the crucial function of the proton-exchange membrane such type of cell is sometimes called polymer electrolyte membrane fuel cell (PEMFC), too.

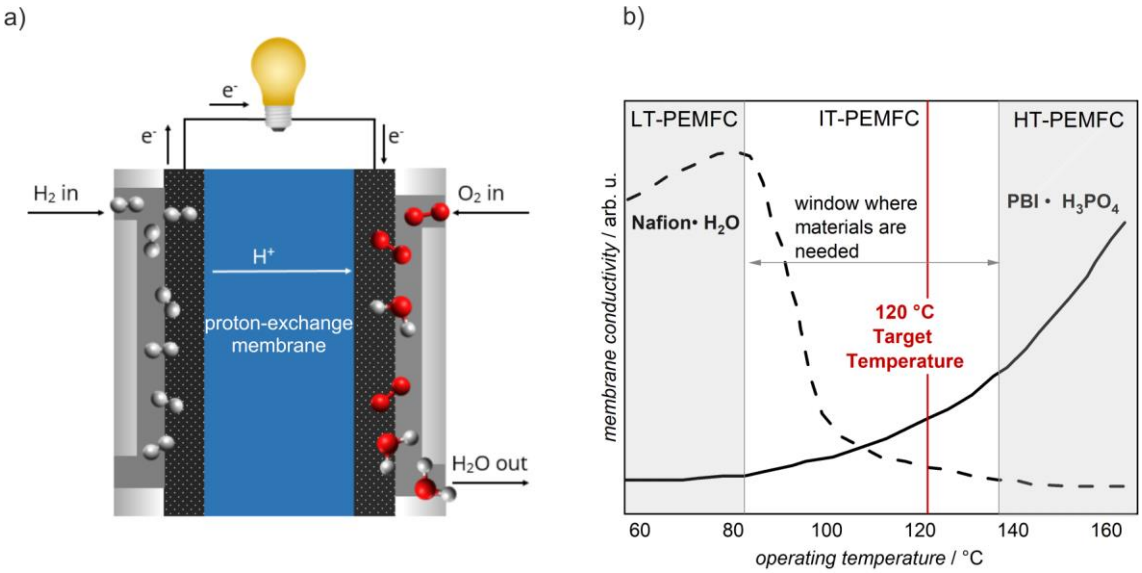

Figure 19 a) Schematic of a PEMFC. b) Specific conductivity of different membrane systems vs. temperature. The gap at the intermediate temperature of 120 °C is highlighted. Inspired by [73].

Common membrane systems are perfluorosulfonic-acid membranes (PFSA) like Nafion or Aquivion. In these systems the sulfonic acid groups in the side-chains of the polymer dissociate in the presents of water and thereby form the proton-conducting hydronium ions. Therefore, the conductivity rapidly drops when the membrane gets dehydrate (Figure 19b). However, increasing the temperature would provide five main advantages[73–75]:

I. A higher quality of the waste heat, i.e. more efficient use of waste heat.
II. Easier thermal management due to higher temperature difference between the surrounding and the cell. A precise temperature control is important for efficient PEMFC operation.
III. Easier water management or even the complete elimination of the need for water management if the membrane is conductive (for protons) under anhydrous conditions.
IV. Increased tolerance of the platinum (Pt) catalyst to fuel impurities, in particular CO. For example, at 80 °C already 0.002% of CO in the feed gas lead to a significant loss of performance of the Pt catalyst, but at 160 °C concentrations up to 0.5–1 % have only a minor effect[75].
V. Higher catalytic efficiency and therefore requirement of smaller quantities of the expensive and precious Pt catalyst. Eventually the Pt catalyst can be even replaced by alloys or non-noble metals which could reach a sufficient high catalytic activity at higher temperatures.

To realize the same required relative humidity for operation of PFSA membranes at elevated temperatures, a significant higher gas pressure would be required i.e. 3 bar instead of 1 bar[73]. Additionally, the mechanical stability of PFSA membranes at higher temperatures is limited due to the low glass-transition temperature of such systems.
Both limits the operating temperature of cells with PFSA membranes to below 80 °C. Therefore, this cell type is called low-temperature PEMFC (LT-PEMFC).

In 1995 J.S. Wainright et al. proposed phosphoric acid doped polybenzimidazole (PBI) as new electrolyte for operation at elevated temperatures[76]. Membranes from this class of materials display an appropriate conductivity for high-temperature PEMFC (HT-PEMFC) applications in a broad temperature range between about 140-200 °C[75] (Figure 19b). Beside the conductivity also the kinetic of the hydrogen oxidation reaction and of the oxygen reduction reaction (ORR) are crucial for the cell performance. While the H_2-oxidation is little influenced by the presents of H_3PO_4, it shows especially at lower temperatures a significant influence on the ORR by both blocking the active centers of the Pt catalyst[77] and by reduction of the oxygen diffusion[78]. At 120-150 °C, were Nafion already exhibits a low conductivity due to dehydration, the exchange current density for the H_3PO_4·PBI system is still 1-2 orders lower. To solve this issue only the loading with the Pt catalyst can be increased[79]. While the higher Pt loading can improve the performance at temperatures of about 120 °C, a H_3PO_4·PBI based HT-PEMFC is intrinsically limited by the sluggish ORR kinetic. Additional H_3PO_4 might be washed out of the cell during operation, especially by water, which is not sufficiently removed at lower temperatures[80]. The acid loss limits the performance and life cycle both by decreasing membrane conductivity and by corrosion of components like flow fields.

The advantages of operation at 120 °C i.e. in the intermediate temperature (IT) range between LT-PEMFC and HT-PEMFC are that there is no liquid water present, and all the aforementioned benefits of higher operation temperature can be utilized. At the same time, the moderate temperature limits the demands on the thermal resistance of the materials, which is why a longer life cycle might be expected. In addition, intermediate temperature PEMFC (IT-PEMFC) systems can be designed more compactly due to the lower operating temperature, which is particularly attractive for automotive applications[73].

To achieve this goal there are, on the one hand, ongoing efforts to extend the application range of LT-PEMFC with established membrane materials like Nafion towards 120 °C, for example by increasing the humidity and the oxygen back-pressure, however, the durability of the membranes limits these approaches[81]. On the other hand, the properties of the H_3PO_4 prevent an efficient operation of HT-PEMFC systems at lower temperatures. Therefore, currently no suitable membrane system for the intermediate temperature (IT)

range exists (Figure 19b). To close the intermediate temperature gap by the development of a suitable membrane system is a crucial task to reach for PEMFC market penetration.

A promising approach towards a membrane material, that can be used at 120 °C under anhydrous conditions is to replace the proton-conductor H_3PO_4 in membranes like PBI by protic ionic liquids (PILs)[82,83].

PILs and aprotic ionic liquids (AILs) constituted together the large family of ionic liquids (ILs). ILs are according to the generally adopted definition by Walden from 1914 "water-free salts that are in liquid form below 100 °C"[46]. However, the melting temperature of 100 °C is an arbitrary limit and they might be more rigorous defined as water-free organic salts showing a melting point below their decomposition temperature. In these salts crystallization is prevented by a low lattice energy[a] of the crystalline state caused by the low charge density and the bulky and asymmetric shape of the usually organic ions[84].
ILs consist solely of unsolvated “bare” ions, which is why they possess several useful properties such as typically negligible vapor pressure, nonflammability, good thermal and electrochemical stability, and relatively high ionic conductivities. These properties make ILs well-suited for applications as environmentally friendly and safe industrial reaction media[85,86] or in electrolytes in electrochemical energy storage devices[87]. For the subgroup of PILs, additionally their acidity should also be mentioned, which can be utilized for acid catalysis as well as in proton-conductive membranes, as proposed for the application in IT-PEMFC[51,57]. Additionally, the properties of ILs can be readily tuned for the target application. This gave ILs the nickname “designer solvents”. Like all salts an IL consists of both cations and anions, which balance each other’s charge. Therefore, already by combining different existing cation and anion structures a countless number of different ILs can be prepared. Furthermore, both the cation and anion structures can be functionalized as desired. In this thesis for the investigation in chapter 3. ILs got functionalized with different groups, while in chapter 4. a new combination of a cation and anion structure is examined.

In aprotic ILs the cation charge usually originates from a quaternization at a nitrogen or phosphorus atom via alkylation for example with haloalkanes (Figure 20). The resulting halide salt is commonly a (high melting) solid. Via ion exchange of the halide ion to an anion with more pronounced charge delocalization and higher sterically demand an IL is obtained. Due to the low lattice energy the melting point (T_m) of an IL is low and additional often undercooling below T_m to a metastable liquid is possible. These properties lead to a wide liquid range in ILs of often more than 100 °C. ILs, which are liquid at room temperature are often called room temperature ILs. Due to the irreversible

[a] For the lattice energy no universal definition exists and it might be calculated for the formation of an ionic solid or its splitting into individual (gas phase) ions. Here it is understood for the splitting into individual ions.

nature of the alkylation reaction in the first synthesis step the charge is locked at the heteroatom in the cation of the AIL and only degradation can lead to the formation of uncharged species.

Purified AILs i.e. after the removal of halide ions, process solvents, remaining reactants or water, are binary "mixtures", which purely consist of cations and anions in a stoichiometry ratio.

In protic ILs in contrast the cation charge center is formed by protonation. This formation mechanism also serves as the definition of the term PIL and the differentiation between PILs and AILs. The formation mechanism of a PIL by the neutralization reaction between a Brønsted acid and base is illustrated in (Figure 20). It only consists of a single step, therefore the PIL synthesis is simpler compared to the preparation of AILs.

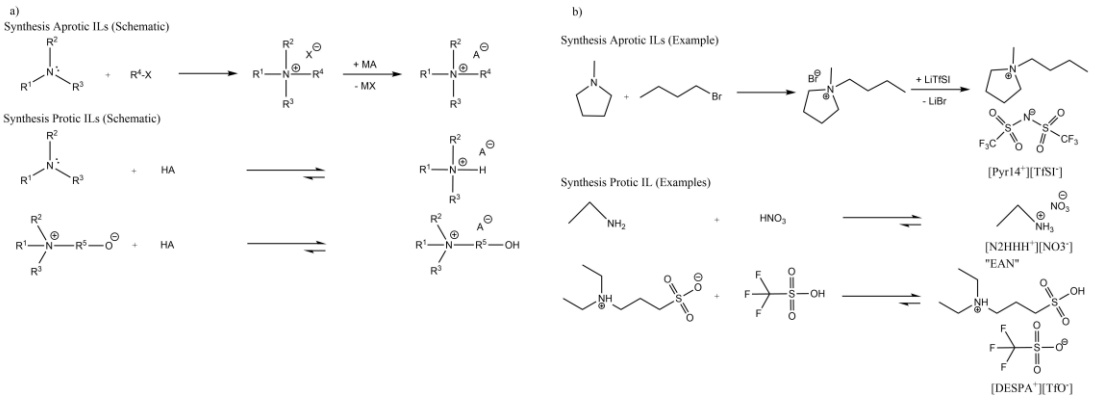

Figure 20 a) Schematic of the synthesis of aprotic ILs (AILs) and protic ILs (PILs) together with b) examples for each type of reaction.

Obviously, a protonation is an equilibrium reaction. Therefore, in contrast to the binary anion and cation "mixture" in AILs, PILs inherent contain some "free" acid and base. Based on the position of the protonation equilibrium the formation degree of the PIL can be defined. To obtain high formation degrees, i.e. complete proton transfer, correspondingly strong (super)acids like Trifluoroacetic acid (HTFAc), Methanesulfonic acid (HMS), Trifluoromethanesulfonimide (HTFSI), Trifluoromethanesulfonic acid (TfOH) have to be applied in the synthesis of the PILs. M. Yoshizawa et al. introduced the concept of the Δpka i.e. the pka difference between the acid and base (in water), to estimate which acid-base pairs might form PILs with a high formation degree[48].

Only if the system in equilibrium lies nearly completely on the product i.e. PIL, side a behavior like for AILs is observed. Otherwise the PIL might not display the aforementioned useful properties of negligible vapor pressure, high thermal and electrochemical stability and relatively high ionic conductivity.

The literature-known PILs, that were proposed for IT-PEMFC applications, are typically prepared from strong acid trifluoromethanesulfonic and amines. The use of this strong acids leads to nearly complete formation of the PIL, which is important as remaining amines significantly reduce thermal stability of the PIL. Additionally, the adsorption of the corresponding triflate anion on the Pt catalyst is only weakly pronounced [88]. Additional fluorocarbons are known to increase the oxygen adsorption[89], therefore triflate might be beneficial to achieve higher oxygen saturation concentrations and thereby higher limit currents for the ORR.

The physical properties of Triethylammonium triflate and mesylate and blends with Nafion are reported by C. Iojoiu et al. They reported a sufficient thermal stability and observed a vehicular proton transport independent from the type of anion in the PIL[90].

J. Thomson et al. presented the highly fluorinated PIL 2-fluoropyridinium triflate as fuel cell electrolyte. At 80 °C an ORR onset potential close to the thermodynamic limit of 1.2 V vs. RHE was observed. At 80 °C under load a significantly higher voltage was measured for 2-fluoropyridinium triflate compared to H_3PO_4. A maximum current density of about 100 $mA \cdot cm^{-2}$ could be reached. However, 2-fluoropyridinium triflate thermally decompose below 120 °C in O_2 atmosphere and is therefore not suitable for an IT-PEMFC application. It was proposed that further fluorination of the pyridine structure might improve the thermal stability[91].

In an extensive screening by the group of M. Watanabe diethylmethylammonium trifluoromethanesulfonate $[N221H^+][TfO^-]$[b], was identified as a promising candidate for fuel cell operation. At 150 °C in $[N221H^+][TfO^-]$ an OCP above 1 V was observed and a maximum current density of 0.8 $mA \cdot cm^{-2}$ could be reached in the H_2/O_2 fuel cell polarization curve. Both the OCP and maximum current density of $[N221H^+][TfO^-]$ are superior to anhydrous H_3PO_4 [92,93].

However, the ammonium groups in these PILs are only weak acids. Therefore, the proton remains on the cation structure and a proton transport predominantly occurs in the stoichiometry PIL by a vehicular mechanism, i.e. by motion of the proton together with the cation core structure[93]. By preparation of more acidic cation structures it might be possible to unlock a significant faster proton transport via a Grotthuss-like cooperative proton transfer mechanism, were the proton jumps between donor-acceptor groups. Additionally, a high acidic cation will be able to protonate the water, which is absorbed in the PIL or released by the ORR. The inclusion of residual water in the proton transfer would significant enhance the number of proton acceptor groups and thereby probably enable a cooperative proton transfer like excess Brønsted base in non-stoichiometric PILs[93]. Beside the influence on the proton transfer the acidity of the PIL also influences

[b] Often abbreviated in literature as “DEMA TfO”

the ORR kinetic. Water shifts the ORR onset potential towards lower values as it enhances platinum oxide (Pt-O) formation.

Only after the Pt-O is reduced the O_2 adsorption on the Pt-O free surface and thereby the ORR takes place. If the water activity is reduced by protonation the Pt surface stays oxide-free and ORR starts at higher potentials[94]. Furthermore, higher acidity of the PIL can lead to increased O_2 solubility. However, this is not always the case, as oxygen saturation depends on various factors.

A first prove-of-principle for such a protic acidic ionic liquid (PAcIL) was reported by K. Wippermann et al. with 2-Sulfoethylammonium triflate [SEA^+][TfO^-][72].

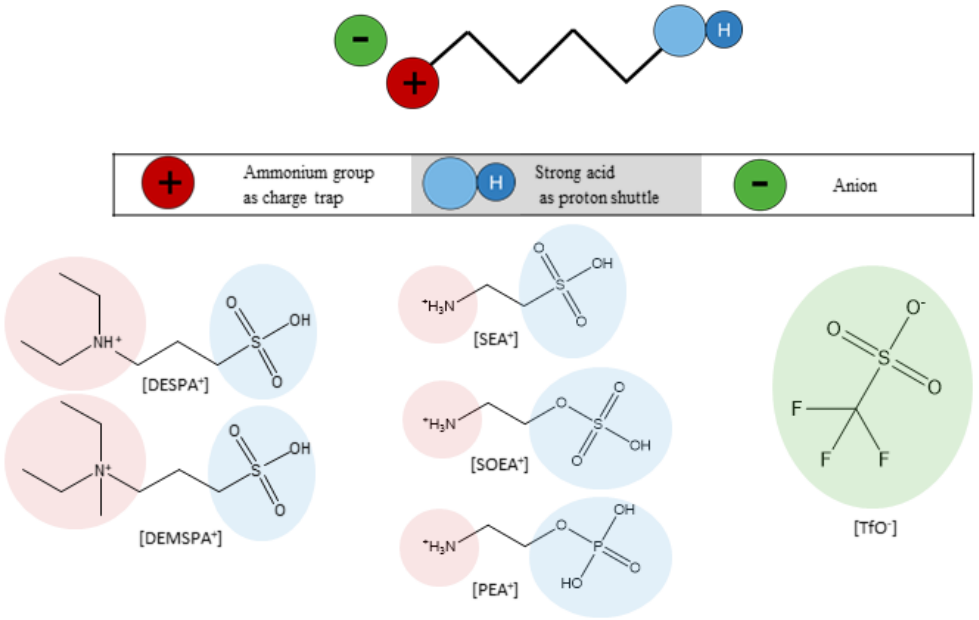

Figure 21 Schematic of the general structure motive of the PAcILs and chemical structure formula of the different cations and of the triflate anion used in this thesis.

The [SEA^+] cation structure (Figure 21) corresponds to protonated taurine (2-Aminoethanesulfonic acid). Electrochemical results of 95 wt% aqueous solution of the PAcILs demonstrated comparable ORR kinetic to 95 wt% H_3PO_4. Under certain conditions the ORR kinetic of [SEA^+][TfO^-] might be superior to the reaction in H_3PO_4. However, already in the original publication it is stressed that [SEA^+][TfO^-] is a prototype and further optimization in the structure are required for example to improve the thermal stability and ionic conduct.

In contrast to other medium to low acidic PILs, which were proposed for IT-PEMFC applications, the alkyl group in the [SEA^+] cation structure is further functionalized with a sulfonic acid group. This sulfonic acid group is the origin of the expected high acidity of [SEA^+][TfO^-].

From this structure, an entire family of acidic cations can be derived in which the positive charge is "trapped" on the ammonium group and one alkyl side chain is further functionalized with an additional acid group. A sketch of this cation design is displayed in Figure 21.
In this thesis the impact on the physical properties of both functional groups in the cation i.e. the ammonium group and the acid group in the sidechain is studied. Thereby special focus is placed on the criteria for IT-PEMFC application namely:

I. Low melting point
II. Thermal stability above the designated operation temperature
III. Stability in the presence of water, especially at the *operando*-conditions of 120 °C
IV. High proton conductivity
V. Wide electrochemical stability window at least between 0.0-1.3 V vs. RHE
VI. Weak interactions of the PAcIL with the Pt catalyst
VII. High oxygen permeability i.e. oxygen saturation concentration c_{O2} and diffusion coefficient D_{O2}

While the properties I.-III. were tested for all compounds, a detailed study on the proton conductivity and the performance in context of ORR was only performed for the most promising PAcILs and is reported in the chapter 4.2.5 & 4.2.6 .

The anion used was the well-established triflate. To separate the influence of both functional groups in the cation two sets of PAcILs were prepared.

In the first set the functionalization at the ammonium group was varied. *N*,*N*-**d**i**e**thyl-3-**s**ulfo**p**ropan-1-**a**mmonium triflate [DESPA$^+$][TfO$^-$] and *N*,*N*-**d**i**e**thyl-*N*-**m**ethyl-3-**s**ulfo**p**ropan-1-**a**mmonium triflate [DEMSPA$^+$][TfO$^-$] with a ternary and quaternary ammonium group belong both to this set (Figure 21). Originally also *N*-**m**ethyl-3-**s**ulfo**p**ropan-1-**a**mmonium triflate [MSPA$^+$][TfO$^-$] with a secondary ammonium group should be included. However, this component was discarded from the investigation, as previous studies by Dr. Xinpei Gao and Dr. Sangsik Jeong have shown that this cation structure cannot be obtained with the required purity and is not thermally stable enough for the intended use in the IT-PEMFC.

In the second set of PAcILs different acid functionalizations of the alkyl group, i.e. with sulfonic, sulfuric and phosphoric acid, were tested. Cations from this set always contained a primary ammonium group. 2-**S**ulfo**e**thyl**a**mmonium triflate [SEA$^+$][TfO$^-$], 2-(**S**ulfo**o**xy)**e**than-1-**a**mmonium triflate [SOEA$^+$][TfO$^-$] and 2-(**P**hosphonooxy)**e**than-1-**a**mmonium triflate [PEA$^+$][TfO$^-$] are the three compounds of this set (Figure 21).

3.2 Results and Discussions

3.2.1 Synthesis and NMR Spectroscopy of Triflate-based PAcILs

The different PAcILs with the triflate anion were prepared by mixing equimolar amount of the corresponding zwitterion with trifluoromethanesulfonic acid. The 3-(diethylammonio)propane-1-sulfonate (DESPA) and 3-(diethyl(methyl)ammonio)propane-1-sulfonate (DEMSPA) zwitterion were prepared as described in [69]. 2-Aminoethanesulfonic acid (trivial name taurine, CAS: 107-35-7), 2-Aminoethylhydrogensulfate (CAS: 926-39-6) and 2-Aminoethyldihydrogenphosphate (CAS: 1071-23-4) are the commercial available "zwitterions"[c] for the synthesis of the PAcILs 2-Sulfoethylammonium triflate [SEA^+][TfO^-], 2-(Sulfooxy)ethan-1-ammonium triflate [$SOEA^+$][TfO^-] and 2-(Phosphonooxy)ethan-1-ammonium triflate [PEA^+][TfO^-], respectively. For the characterization in this chapter the PAcILs are analyzed as synthesized. The samples might contain depending on the water content of the starting materials, especially trifluoromethanesulfonic acid, different amount of water. Additionally, during storage of the hygroscopic materials, even in a dryroom (dew point <-60 °C) samples might accumulate some water. By vacuum drying, a common strategy for aprotic ILs, the water content can be reduced in some cases, however depending on the PIL water contents below 0.4-1 wt% might often not be reached with this strategy, due to strong hydrogen bonded or ionized (H_3O^+) residual water. Moreover, treating PILs with vacuum poses the risk of removing volatile components, thereby shifting the acid-base equilibrium. This may even lead to a reverse reaction of the PILs to the reactants[95]. Therefore, drying steps were mostly omitted, and the water content was determined using coulometric Karl Fischer (KF) titrations (chapter 1.3.1). The water content is specified in the figure/table captions where relevant. The uncertainties given represent the maximum deviation of repeated measurements. The indication (n=...) behind the value, denotes the number of repeated KF titrations for the obtained average value and the uncertainty.

First coupling patterns and peak integrals in one-dimensional ^{1}H-NMR measurements of diluted samples in deuterated solvents are evaluated to confirm the successful synthesis of the PAcILs. In the second part of this subchapter neat PAcILs are investigated to estimate the degree of protonation and acidity.

In the ^{1}H-NMR spectra of the studied PAcILs with the fully fluorinated triflate anion only signals of the cation structures are observable.

[c] For crystalline taurine the zwitterion form was experimentally confirmed[175]. For consistency all starting materials with similar structure are called ''zwitterions", also when their charge distribution is not known in solid state.

The ^{1}H-NMR spectrum of *N*,*N*-diethyl-3-sulfopropan-1-ammonium triflate [DESPA^{+}][TfO^{-}], *N*,*N*-diethyl-*N*-methyl-3-sulfopropan-1-ammonium triflate [DEMSPA^{+}][TfO^{-}], [SEA^{+}][TfO^{-}], [SOEA^{+}][TfO^{-}] and [PEA^{+}][TfO^{-}] are displayed in Figure 22.

The coupling patterns and integrals are highlighted in the insets. This information is used for the assignment of the signals, which is indicated by the numbers in the chemical structures. Integrals of non-exchanging protons and coupling patterns show a good agreement with the theoretical predictions, and thereby confirm the molecular structures.

For the methyl groups in the backbone of [DESPA^{+}][TfO^{-}] (signal 2,2',4,6) small side peaks are visible. These signals are not symmetrical and too intense for ^{13}C satellites. Therefore, the first guess would be an impurity. However, identical signals were observed in a commercial [DESPA^{+}][TfO^{-}] sample from IoLiTec Ionic Liquids Technologies GmbH (Figure 23 a)). Finding the identical impurity in samples from two different sources (self-synthesized and commercial) is possible, but less probable. Another explanation could be that these small peaks originate from a 7-membered cyclic form of the [DESPA^{+}] cation with an intra-molecular hydrogen bond between the $NH^{+\cdots}SO_3H$ group, which coexists in equilibrium as minor species while the major species is the "linear" form of the [DESPA^{+}] cation[96].

[DESPA^{+}][TfO^{-}] in contrast to [DEMSPA^{+}][TfO^{-}] is soluble in DMSO-d_6. This allows the measurement of [DESPA^{+}][TfO^{-}] in a solvent without proton-deuterium exchange capability. In Figure 22 a) therefore the exchangeable protons of the sulfonic acid (signal 7) and of the ammonium group (signal 3) are visible at about 11 ppm and 9 ppm, respectively. The small peak at about 8.2 ppm (signal 3*) might be assigned to the ammonium group of the cyclic [DESPA^{+}] species. The peaks width of exchangeable protons i.e. the full width at half maximum (FWHM) is influenced by the proton exchange rate, among other factors[97]. The peak width from the tertiary ammonium proton (signal 3) is with about 19 Hz significant smaller than of the sulfonic acid proton (signal 7) with about 51 Hz[d]. This might indicate a slower proton exchange (on the NMR timescale) for the ammonium group compared to the sulfonic acid group. Therefore in [DESPA^{+}][TfO^{-}] the proton of the sulfonic acid group might be more mobile, while the proton of the ammonium group might be trapped there for a longer time period.

[d] The peak width was obtained from peak fitting in MestReNova Version 14.2.0-26256 with Lorentzian-Gaussian peaks (width constrain 0.1-100.00 Hz, position constrain ±5%, 500 coarse iterations, 100 fine iterations)

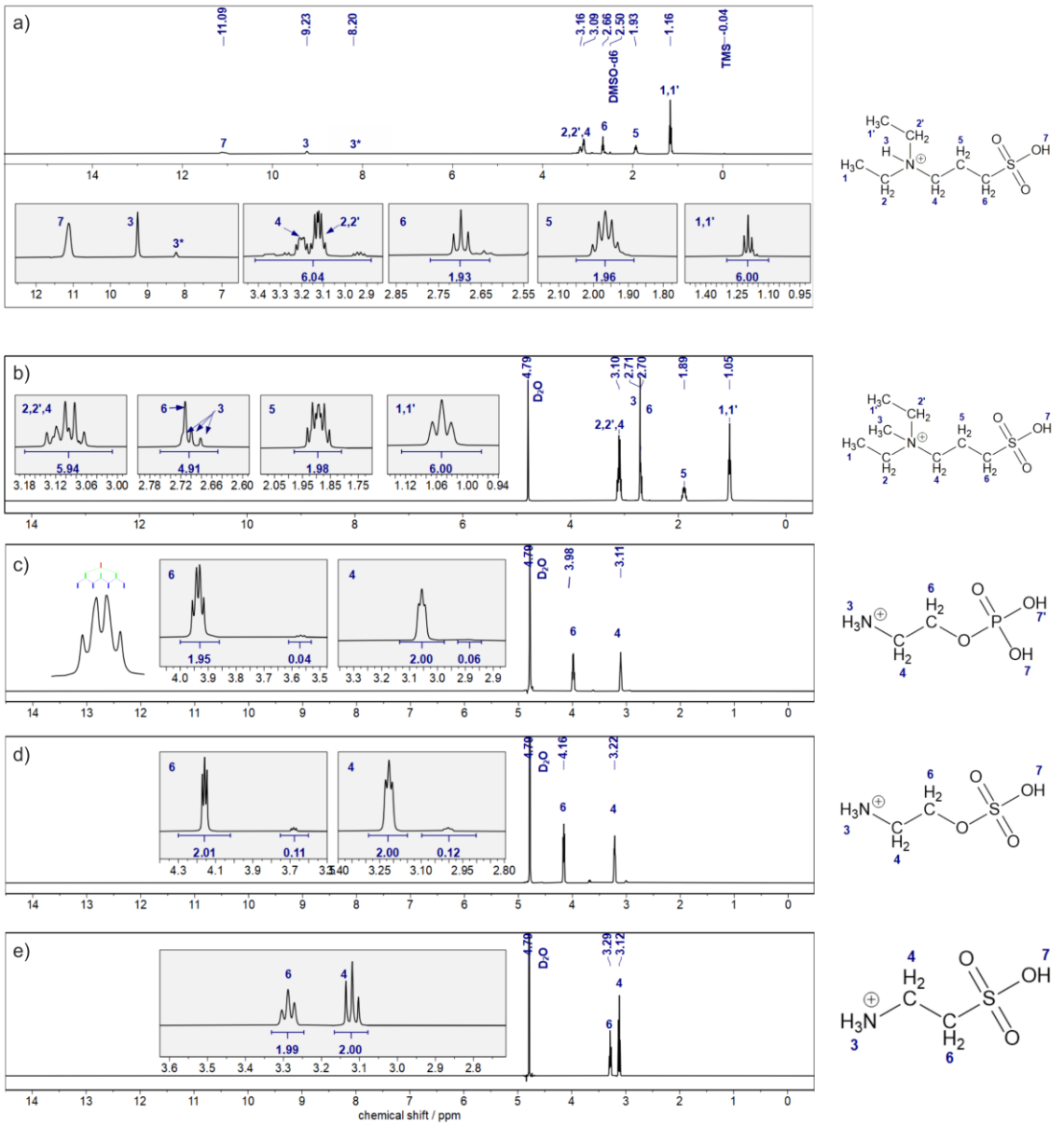

Figure 22 ^{1}H-NMR spectra and cation structures with peak assignment of a) [DESPA^{+}][TfO^{-}] with a water content of 12302±146 ppmw in DMSO-d$_6$, b) [DEMSPA^{+}][TfO^{-}]c) [PEA^{+}][TfO^{-}],d),[SOEA^{+}][TfO^{-}] and e) [SEA^{+}][TfO^{-}] in D$_2$O. All spectra are referenced to the solvent residual peak. Labels for the peak assignment in the chemical structures are not in a strict order of sequence but similar functional groups in the different PAcILs are labeled with the same numbers. The integrals in a), b) of 1,1' and in c)-e) of 4 were normalized to a value of 6 and 2, respectively.

The ^{1}H-NMR spectra of the PAcILs [PEA^+][TfO^-], [$SOEA^+$][TfO^-] and [SEA^+][TfO^-] with phosphoric, sulfuric and sulfonic acid group, respectively, are displayed in Figure 22 c)-e). Again, the coupling patterns are beneficial for the peak assignment in the diluted PAcILs. The solubility of this PAcILs is a challenge and only D_2O could be used for NMR experiments. With the ethyl group in the cation backbone of [PEA^+][TfO^-],[$SOEA^+$][TfO^-] and [SEA^+][TfO^-] a pair of triplets from the coupling between the two CH_2 groups is expectable. For [$SOEA^+$][TfO^-] and [SEA^+][TfO^-] indeed triplets at 3.22 ppm, 4.16 ppm and 3.12 ppm, 3.29 ppm, respectively, were observed. In contrast in [PEA^+][TfO^-] the signal at 3.98 ppm is a quartet.

This unexpected coupling pattern is explained by the sketch in Figure 22 c). The CH_2OP protons couple via the three-bond spin-spin couplings with the two protons from the adjacent methylene group and with the ^{31}P nuclei. As a consequence, each peak of the triplet from the coupling with the methylene groups (green labels) is further split into doublets by the coupling with ^{31}P nuclei (blue labels). With similar $^{3}J_{HH}$ and $^{3}J_{HP}$ coupling constants of about 6 Hz the resulting doublet of a triplet looks like a quartet. This phenomenon is known in literature for the deprotonated form of [PEA^+] 2-Aminoethyl phosphate[9,98] and similar compounds like 3-Aminopropylphosphate and homologs with longer alkyl chains[99,100]. Moreover, it is a general feature for the α-methylene group of Phosphor-esters like Triethyl phosphite[101].

Therefore the quartet in [PEA^+][TfO^-] at 3.98 ppm can be assigned to the methylene group attached to the phosphorous acid group. In the spectra of [$SOEA^+$][TfO^-] and [SEA^+][TfO^-] only triplets are observable. Based on the literature report of ^{1}H-NMR with deuterium-labeled taurine-d_3[102] the triplet at about 3.29 ppm can be assigned to the methylene group attached to the sulfonic acid group. In analogy the peak at about 4.16 ppm in [$SOEA^+$][TfO^-] was assigned to the methylene group attached to the sulfuric acid group. The similarity in the spectra of [PEA^+][TfO^-] and [$SOEA^+$][TfO^-] with a separation of about 1 ppm between both triplets is expected to arises from the structural similarity of the phosphoric and sulfuric acid ester in [PEA^+][TfO^-] and [$SOEA^+$][TfO^-], respectively.

The comparison of the ^{1}H-NMR spectra of the cation structures in the PAcILs with the unprotonated starting materials from own experiments and literature reports[9,98,102] show, that the protonation of the phosphoric, sulfonic and sulfuric acid group has no significant effect on the chemical shift of the methylene protons i.e. differences are smaller than ±0.5 ppm. Figure 23b) and c) show this comparison as an example for the DESPA zwitterion and [$DESPA^+$][TfO^-]. There the differences in the chemical shift are below 0.3 ppm, even the experiment with the zwitterion and the PAcILs were made in different deuterated solvent, due to solubility of the compounds.

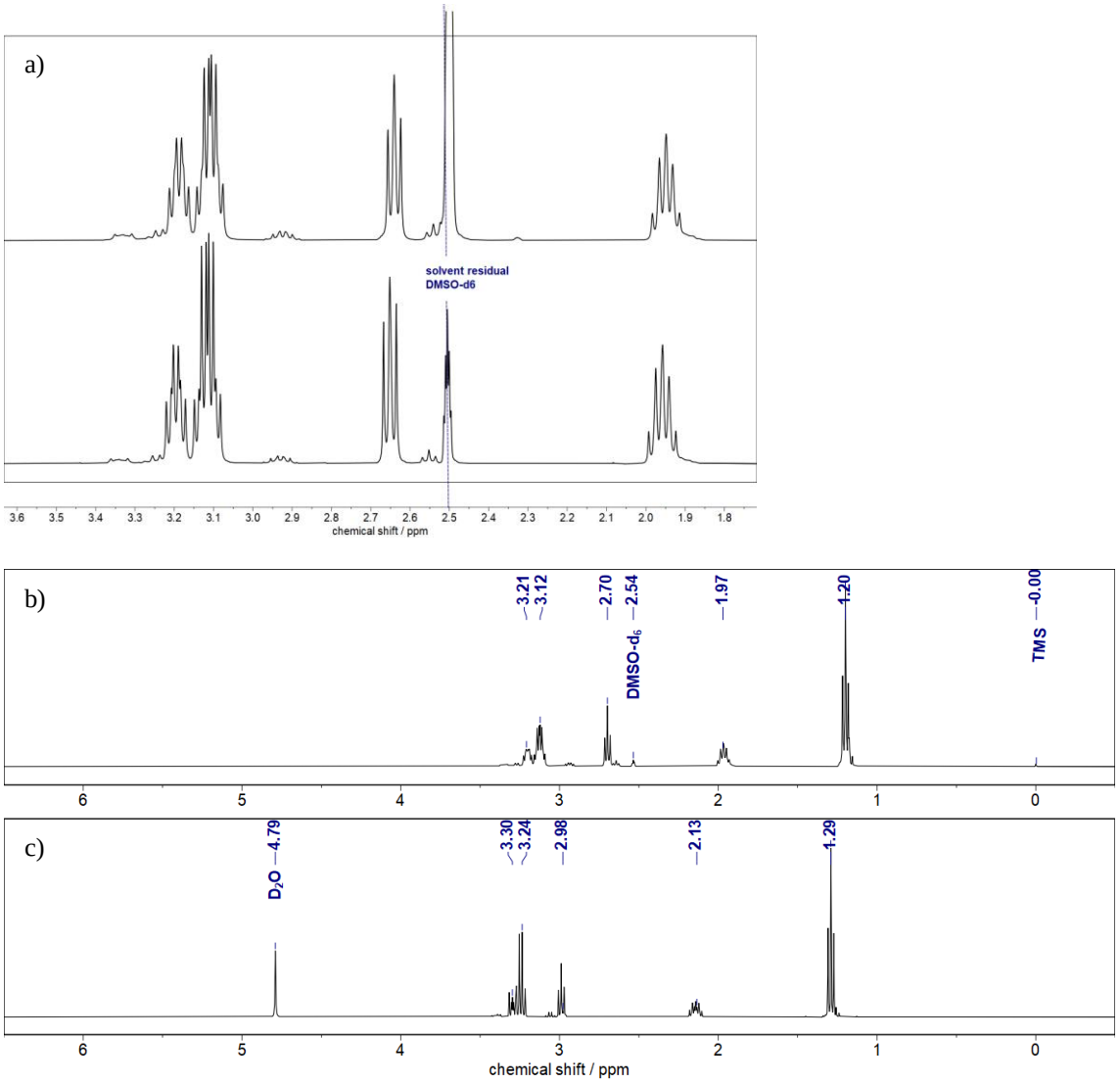

Figure 23 ^{1}H-NMR of a) self-synthesized [DESPA^{+}][TfO^{-}] (top) and a commercial sample from IoLiTec Ionic Liquids Technologies GmbH (bottom) in DMSO-d_6.b) [DESPA^{+}][TfO^{-}] in DMSO-d_6., c) DESPA zwitterion in D_2O. All chemical shifts are referenced to the solvent residual peak.

While the study of the diluted samples with well resolved peaks and coupling patterns can help to identify the chemical structure NMR measurements of pure PAcILs are required to estimate the degree of protonation and acidity of the PAcILs. In such kind of experiments a coaxial capillary configuration is used. The PAcIL is flame-sealed in a capillary and the deuterated locking-solvent is added in the space between the capillary and the NMR tube. In addition, flame-sealing the PAcIL in the capillary in the moister free atmosphere of a dryroom or glove box is a way to protect the PAcIL from water uptake during the NMR experiments. However, the viscosity of the PAcILs might be a challenge for the filling of the narrow capillary. To overcome this challenge a preparation method was developed, which is described in detail in the experimental section.

To avoid this challenge the usually less viscous locking solvent might be filled in the flame-sealed capillary and the PAcIL in the wider NMR tube itself. While this approach might be simpler from a preparative viewpoint the drawback is the possible water uptake of strongly hygroscopic PAcILs during NMR measurements.

Figure 24 shows the ^{1}H-NMR of the neat PAcILs measured with the coaxial capillary configuration. In contrast to the measurements with the diluted samples the acidic protons are visible, too. To achieve a decent resolution of the peaks some of the high viscose samples were measured at 70 °C instead of room temperature to reduce the peak broadening due to the high viscosity. The chemical shift of the protons of the ammonium group (signal 3 in Figure 24, except in [DEMSPA^{+}][TfO^{-}]) ranges between 6.29-7.17 ppm. These values lie in the typical range for ammonium protons for example in PILs with protonated 1,8-diazabicyclo[5.4.0]-undec-7-ene [DBU^{+}] (6.96-7.96 ppm)[103] or di- and trialkylammonium cation structures (6.05-7.90 ppm)[58]. A downfield shift of the signal for the NH proton (to higher ppm values) would indicate that the proton is bond longer time on the experimental timescale to the trifluoromethanesulfonic acid[104]. This not seems the case for the studied PAcILs. The high formation degree of stochiometric PAcILs is also confirmed for [PEA^{+}][TfO^{-}] and [SEA^{+}][TfO^{-}] by the integral of the ammonium protons, which is close to 3 i.e. the theoretical value for the R-NH_3^{+} group. The integral of the signals 7 of the protons at the oxoacid (RO-H) in the cation is at the same time close to 1 or 2 for [PEA^{+}][TfO^{-}] . For [SOEA^{+}][TfO^{-}] the broad and overlapping peaks hinders an integration. [DEMSPA^{+}][TfO^{-}] contains a quaternary ammonium group, therefore no NH proton is visible. For the ratio 6:1.15 of the CH_3 protons (signal 1,1') to SO_3H proton (signal 7) could be an indication for a stochiometric PAcIL within the measurement accuracy of the NMR spectroscopy. In [DESPA^{+}][TfO^{-}] the ammonium group contains one proton, therefore an integral of about 1 would be expected. However, only a value of approximately 0.68 is actually found. The integral for the proton, which might be assigned to the sulfonic acid in the cation (signal 7 in Figure 24), is significantly larger than expected, with a value of approximately 1.51. The sum of the integrals of the two signals is around 2.2, which is within the expected range of 2 for the sum of the two NH and SO_3H protons. Due to the broad and overlapping signals of the CH_2 and CH_3 groups in the ^{1}H-NMR spectrum of neat [DESPA^{+}][TfO^{-}], the integration is subject to some uncertainty. However, this only partially explains the deviation of the NH (signal 3) and SO_3H (signal 7) integrals from unity and the observation suggests, that there might be a significant proportion of non-protonated nitrogen in equilibrium. The proton, on the other hand, appears to be temporary bound to an acid group (like SO_3H, H_3O^{+}) or at least strongly interacts with the acid group to become part of signal 7, due to the population averaged chemical shift observed for fast exchanging protons.

The signals 7 of the protons at the oxoacid (RO-H) in the cation in Figure 24 i.e. sulfonic, sulfuric and phosphoric acid protons are found for the different PILs at chemical shift range of 10.83-12.90 ppm. This range corresponds to strong acidic protons. For example the chemical shift of the acidic protons in neat trifluoromethanesulfonic acid, trifluoroacetic acid and methanesulfonic acid, which are among the strongest known acids, are in the same ppm range (10-12 ppm)[10].

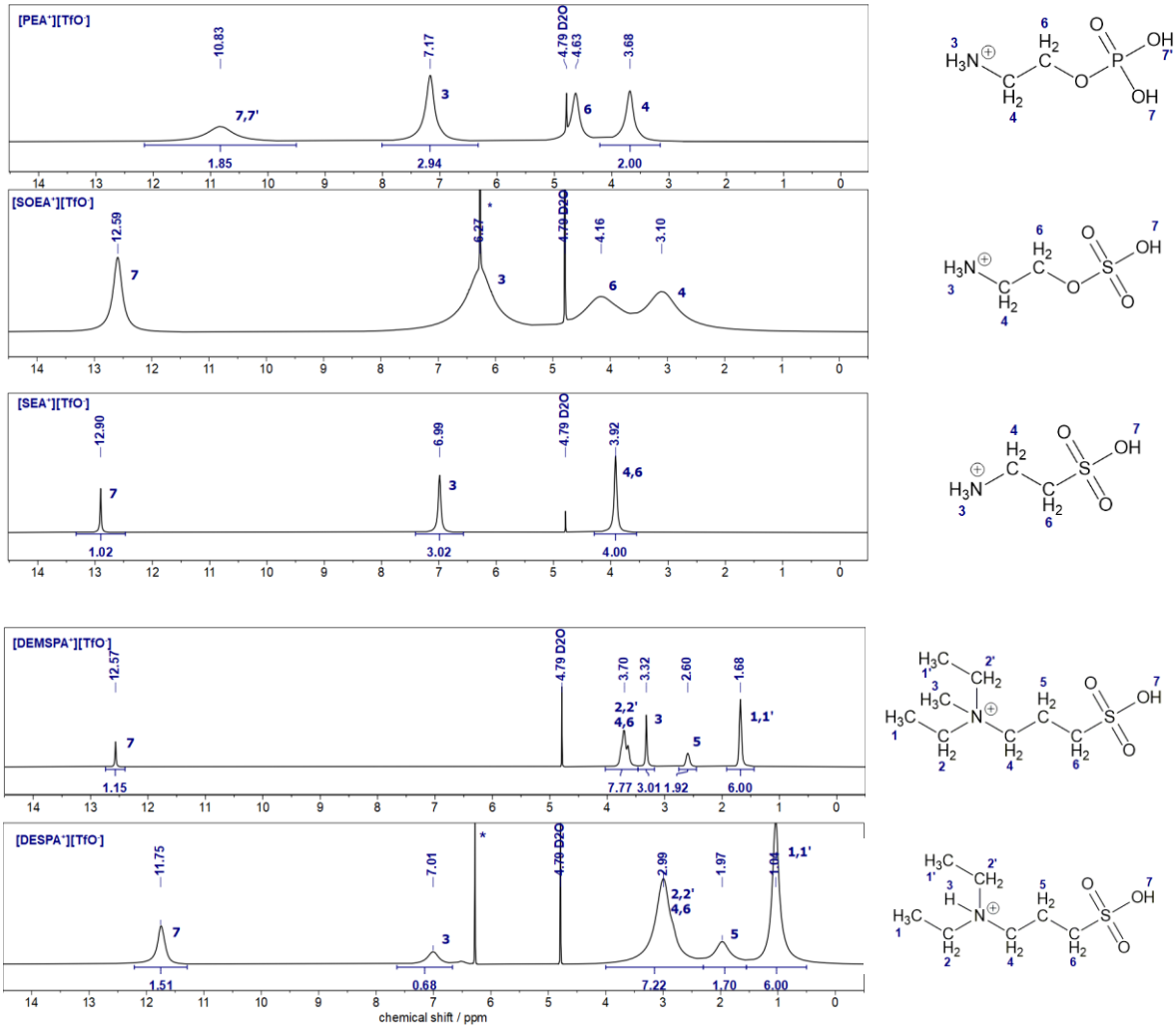

*Figure 24 ^{1}H-NMR spectra of pure PAcILs measured with the coaxial capillary configuration. The numbers beside the peaks indicate the assignment of the signals to the corresponding cation structure. Spectra of [PEA$^+$][TfO$^-$],[SEA$^+$][TfO$^-$] and [DEMSPA$^+$][TfO$^-$] are acquired at 70 °C and the PAcILs were flame-sealed in the capillary. Spectra of [SOEA$^+$][TfO$^-$] and [DESPA$^+$][TfO$^-$] were measured at about 22 °C with D_2O and maleic acid as reference for quantifications in the capillary and the PAcILs in the space between the capillary and the outer-NMR tube. *marks the signal of the maleic acid. All spectra are referenced to the chemical shift of the locking-solvent D_2O.*

From the chemical shift of the protons at the oxoacid (signal 7) the following order could be derived:

$[PEA^+][TfO^-]<[DESPA^+][TfO^-]<[DEMSPA^+][TfO^-]<[SOEA^+][TfO^-]<[SEA^+][TfO^-]$

This might be an indication for the acidity of the oxoacid group in the PAcILs. However, the different chemical shift values are only spread over a range of about 2 ppm, therefore are quite similar. In addition, several other factors influence the position of the acidic proton in the ^{1}H-NMR, beside the acidity of the proton. Here exchange with protons from residual water should be mentioned. The observed chemical shift is the population averaged value of the chemical shift of the different species. Therefore, residual water will cause an upfield shift of the OH signal (to lower ppm values). This effect might be one reason why the OH (signal 7) in $[DESPA^+][TfO^-]$ (12302±153 ppmw H_2O) is about 0.82 ppm upfield shifted (to lower ppm) in comparison with $[DEMSPA^+][TfO^-]$ (578±15 ppmw H_2O). Therefore, the proton NMR gives an estimation on the expected acidity, but should not be overinterpreted.

The $[DESPA^+][TfO^-]$ as example of a PAcIL with self-synthesized zwitterion was analyzed with inductively coupled plasma optical emission spectroscopy (ICP-OES). The results are summarized in Table 4 on page 97. From the tested elements (see caption of the table) 400 ppmw of potassium were the largest inorganic impurity detected.

The ^{1}H-NMR investigation and ICP-OES measurements demonstrate, that the different PAcILs were successfully prepared. In the ^{1}H-NMR spectra no organic impurity was detected. In the ICP-OES of $[DESPA^+][TfO^-]$ no significant inorganic impurity was found. By the coupling pattern and integrals the structures of the different self-synthesized and commercial zwitterions were confirmed. The ^{1}H-NMR in the neat state shows that the proton transfer took place and in the most cases high formation degrees were achieved. Based on the comparison of the NH and SO_3H proton integrals a 1:1 stoichiometry is suggested within the measurement accuracy of NMR spectroscopy. Only for $[DESPA^+][TfO^-]$ it seems according to the experiments that about 1/3 of the nitrogen atoms are unprotonated in the dynamic equilibrium. On the one hand this indicates a lower formation degree, on the other hand a higher mobility of the proton could be beneficial for example for the conductivity.

3.2.2 Thermal Stability of Different Functionalized PAcILs

For the application in intermediate temperature PEMFC the thermal stability beyond the designated operation temperature of 120 °C is crucial. Therefore, dynamic and isothermal thermogravimetric analysis (TGA) of [SEA^+][TfO^-], [$SOEA^+$][TfO^-] and [PEA^+][TfO^-] in synthetic air-like atmosphere (17.5 v% O_2 82.5 v% N_2) was performed (Figure 25). The same analysis for [$DESPA^+$][TfO^-] under comparable conditions is presented in Figure 38 on page 106.

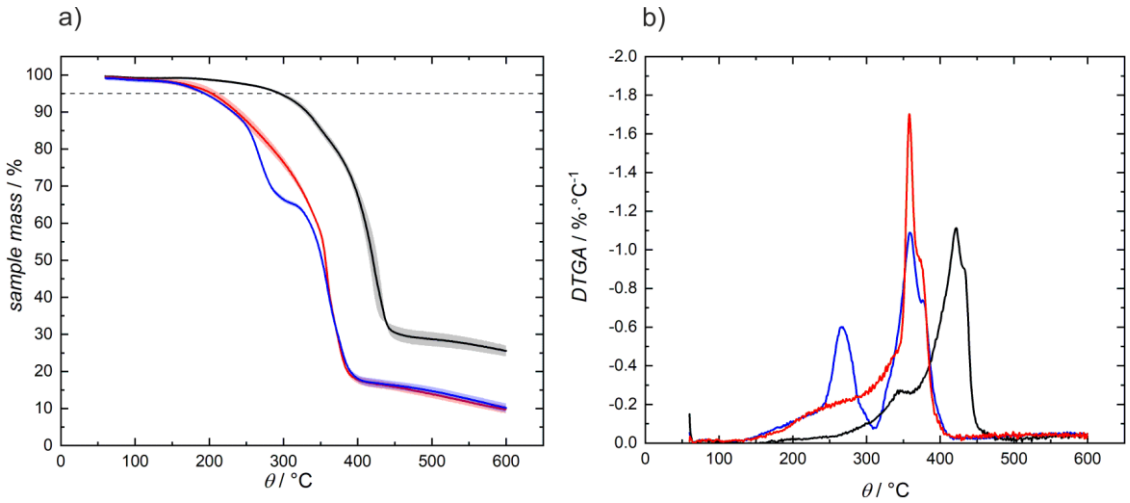

Figure 25 a) dynamic TGA curves of [PEA^+][TfO^-] (black), [SEA^+][TfO^-] (red) and [$SOEA^+$][TfO^-] (blue). Each curve is the average of at least 3 measurements. The shaded areas represent the averag±standard deviation. The measurements were performed with a scan rate of 5 K·min^{-1} in a synthetic air-like atmosphere (17.5 v% O_2 82.5 v% N_2). Aluminum crucibles were used and the sample mass was between 2.0-2.4 mg. The temperature was hold at 60 °C for 1 h before each experiment for thermal equilibration and the sample mass is normalized to the final mass after the equilibration. The dashed-line is the reference line for 5% mass loss. b) the corresponding DTG curves, smoothed by a 10 point average.

[SEA^+][TfO^-] and [$SOEA^+$][TfO^-] contain a sulfonic and a sulfuric acid group, respectively. Despite this different structure their TGA curves in Figure 25 are quite similar (red and blue). The curve of [$SOEA^+$][TfO^-] in contrast to [SEA^+][TfO^-] displays an additional step, which corresponds to about 33-37 % weight loss. Theoreticaly the loss of about 31 wt% is expected for the loss of sulfuric acid. Also the position would fit to the boiling point of sulfuric acid at 337 °C[31]. Therefore this step in the TGA curve might be related to the loss of the sulfuric acid from the [$SOEA^+$] cation. The TGA curve of [PEA^+][TfO^-] lies much appart from the ones of [SEA^+][TfO^-] and [$SOEA^+$][TfO^-] and therefore this PAcIL seems visually more stable. For the determination of the thermal stability no universal criteria exist. Commonly the temperature at 5% mass loss T(5%) or the temperature which correspond to the peak maximum T_{peak} in the first derivative of the TG curve (DTG) is used. In Table 2 both values are summarized for the PAcILs. According to the T(5%) the thermal stability increases in the order [$SOEA^+$][TfO^-]<[SEA^+][TfO^-]<[$DESPA^+$][TfO^-]<[PEA^+][TfO^-].

With the T_{peak} the same order of thermal stability is obtained for the different PAcILs. The DTG curve in Figure 25b or the corresponding Table 2 reveals, that for [$SOEA^+$][TfO^-] and [SEA^+][TfO^-] already before the main peak at respectively 359 °C and 358 °C, i.e. the temperature where the thermal decomposition has reached its fastest rate, significant decomposition processes take place, which already start slightly above 100 °C.

Table 2 Evaluation of the TGA and DTG curves displayed in Figure 25. T(5%): temperature at 5% mass loss. T_{Peak}: temperature at the peak maxima in DTG curves. Bold numbers indicate the most intense DTG peak for each sample. Peak maxima for the T_{Peak} values were determined with the peak analyzer function in the OriginPro 2019b software. [(a)] *Broad peaks without pronounced maxima and the given values are only approximations.* [(b)] *See Figure 38 and Table 6.*

Sample name	T(5%) / °C	T_{Peak} / °C
[SEA^+][TfO^-]	203	150-300[(a)],**358,**371[(a)]
[$SOEA^+$][TfO^-]	194	266, **359,**376
[PEA^+][TfO^-]	295	346[(a)],**422,**431[(a)]
[$DESPA^+$][TfO^-]	271[(b)]	**378[(b)]**

Dynamic TGA measurements tend to overestimate thermal stability and simulate a rapid heating scenario, such as in the case of thermal runaway. To test thermal stability for long-term operation at elevated temperatures, isothermal TGA measurements are necessary.

For both [SEA^+][TfO^-] and [$SOEA^+$][TfO^-] isothermal TGA measurements (Figure 26) show already at 100 °C a significant mass loss. By dynamic TGA measurements K. Wippermann et al. observed a thermal stability of [SEA^+][TfO^-] up to 140 °C, so sufficient for a suggested IT-PEMFC application[72]. The main difference of the experiments here and by K. Wippermann et al. is, that K. Wippermann et al. "dehydrated" the sample by heating prior to the experiment. Therefore, the mass loss in Figure 26 at 100-120 °C might be partially from dehydration. However, a water content of 7 wt% or 10 wt% for [SEA^+][TfO^-] and [$SOEA^+$][TfO^-], respectively, is in the opinion of the author of this thesis rather unlikely, especially when considering the behavior with water described in subchapter 3.2.4. A final clarification of the question could be achieved through further experiments, such as a long isothermal test at 120 °C. If the mass would reach a constant value after a certain time, this could be an indication that only water is evaporating. However, based on the current data such a behavior is not expected by the author of the thesis.

[PEA^+][TfO^-] shows in the isothermal measurements in the beginning at 100 °C a mass loss of about 2%, but then the mass stabilizes (Figure 26c-d). This mass loss might be related to dehydration. After this initial mass loss the mass of [PEA^+][TfO^-] is stable up to at least 130 °C. Even at 220 °C the decomposition rate i.e. the change of the mass with time, is still moderate. Then between 250-350 °C [PEA^+][TfO^-] decomposes almost completely.

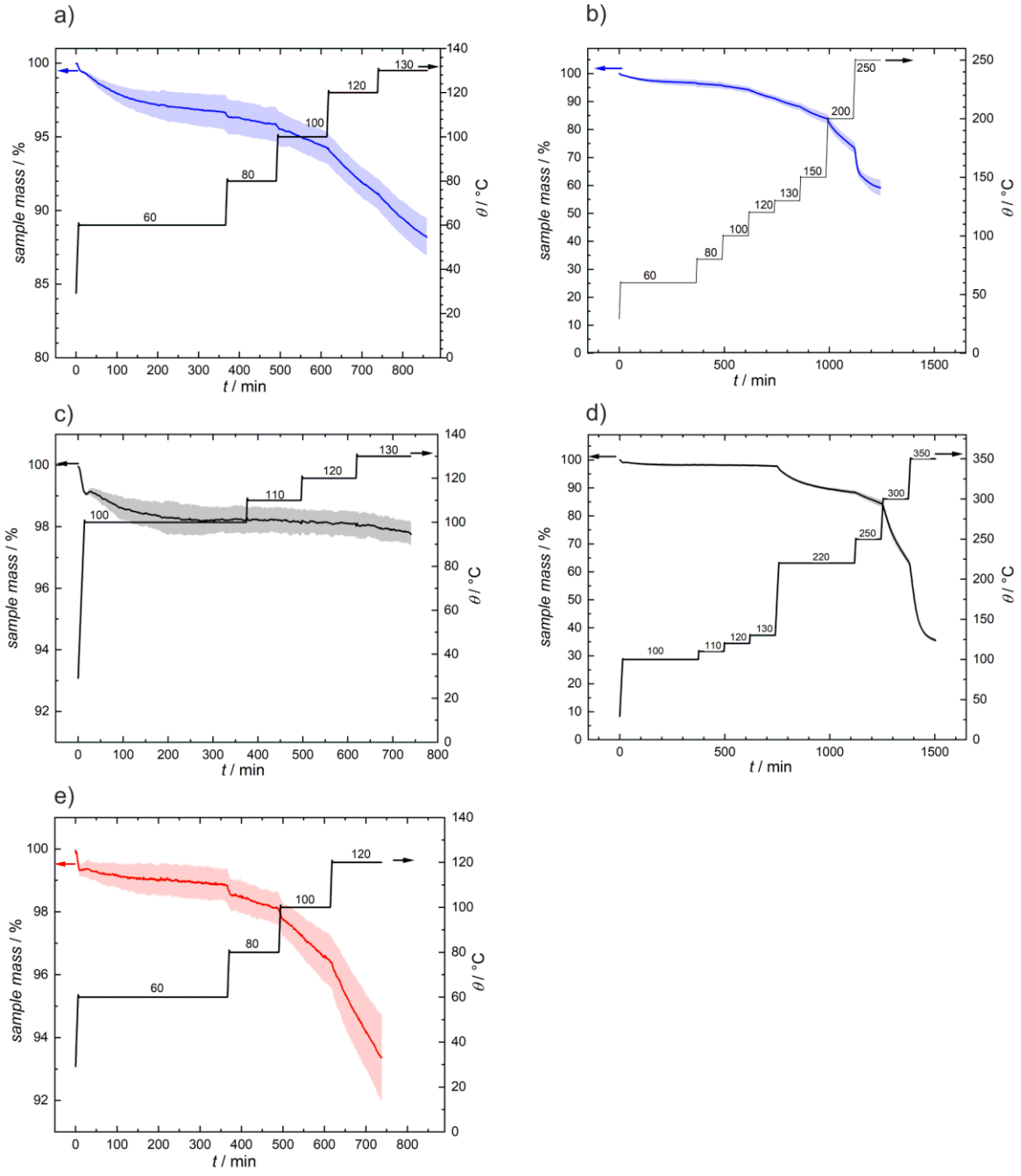

Figure 26 Isothermal TGA of a)-b) [SOEA⁺][TfO⁻], c)-d) [PEA⁺][TfO⁻], e)[SEA⁺][TfO⁻] in a synthetic air-like atmosphere (17.5 v% O_2 82.5 v% N_2). Aluminum crucibles were used and the sample mass was between 1.9-2.2 mg. Each experiment was performed at least as triplet. The TGA curves correspond to the average and the shaded areas to the average±standard deviation. The numbers highlight the temperatures in each step. a) and c) are zooms of the corresponding curves in b) and d), respectivly.

The isothermal TG curve for [DESPA$^+$][TfO$^-$] and [DEMSPA$^+$][TfO$^-$] is displayed in Figure 27. We published these data previously in[69]. After an initial mass loss [DESPA$^+$][TfO$^-$] and [DEMSPA$^+$][TfO$^-$] display curves with a constant slope over a wide temperature range. The independency of the slope from the temperature might indicate that this slope is related to an instrumental drift and not to the sample. The slope of the TG curves, i.e. the decomposition rate, of [DESPA$^+$][TfO$^-$] increases at about 150 °C and for [DEMSPA$^+$][TfO$^-$] at about 240 °C. This demonstrates that both PAcILs are stable above 120 °C and [DEMSPA$^+$][TfO$^-$] is even more stable then [DESPA$^+$][TfO$^-$]. This might be related to the higher thermal stability of the quaternized ammonium group compared to the tertiary one.

The inital mass loss of [DESPA$^+$][TfO$^-$] and [DEMSPA$^+$][TfO$^-$] of about 4 wt % at 100 °C exceed the initial water content in the samples of about 2 wt%. Therefore, it was assumed that eventually a volatile species froms from the PAcIL-water mixtures. To test this hypothethis an isothermal run of [DEMSPA$^+$][TfO$^-$] with 16.7 wt% of water was performed. A stable value at about 80 % of the initial mass was observed at 150 °C. The observed 20 % mass loss is larger than the inital water content of 16.7 wt% in the PAcIL, but in a very similar order of magnitude. This demonstrates, that water not forms volatile species with the PAcIL, because otherwise a much larger mass loss would be expected. The deviation in the observed mass loss and water content could be, at least partial be related to the thermal drift observed in these experiments. While all measurements with the [TfO$^-$] anions were made with a TG 209 F1 Libra (Netzsch), for halogen-free samples a Discovery TGA (TA Instruments) was available, too. Both devices are technically different because the TG 209 F1 Libra has a balance below the sample (like in Figure 8) and no physical reference while the Discovery TGA uses a balance above with an empty crucible as physical reference. Interestingly in the experiments in this thesis the TG 209 F1 Libra outperformed the Discovery TGA in dynamic experiments, but in isothermal experiments the Discovery TGA displayed significant lower drifts (Figure S 2). However, the Discovery TGA is not stable toward HCl, HBr, HI and HF, substances which form in the combustion process of halogenated compounds and could therefore not be used for experiments with the triflate-based PAcILs.

From the data of dynamic and isothermal TGA experiments some trends can be derived. First it seems like higher functionalized ammonium-based cations i.e. [DESPA$^+$], [DEMSPA$^+$] are more stable than cations with primary ammonium groups. Second the organosulfate in the [SOEA$^+$] cation seems less stable and appears to cleave sulfuric acid. The PAcILs [DESPA$^+$][TfO$^-$], [DEMSPA$^+$][TfO$^-$] and [PEA$^+$][TfO$^-$] display a thermal stability above 120 °C and therefore are regarding the thermal stability suitable for an IT-PEMFC application at 120 °C. All three PAcILs outperform the baseline compound [SEA$^+$][TFO$^-$].

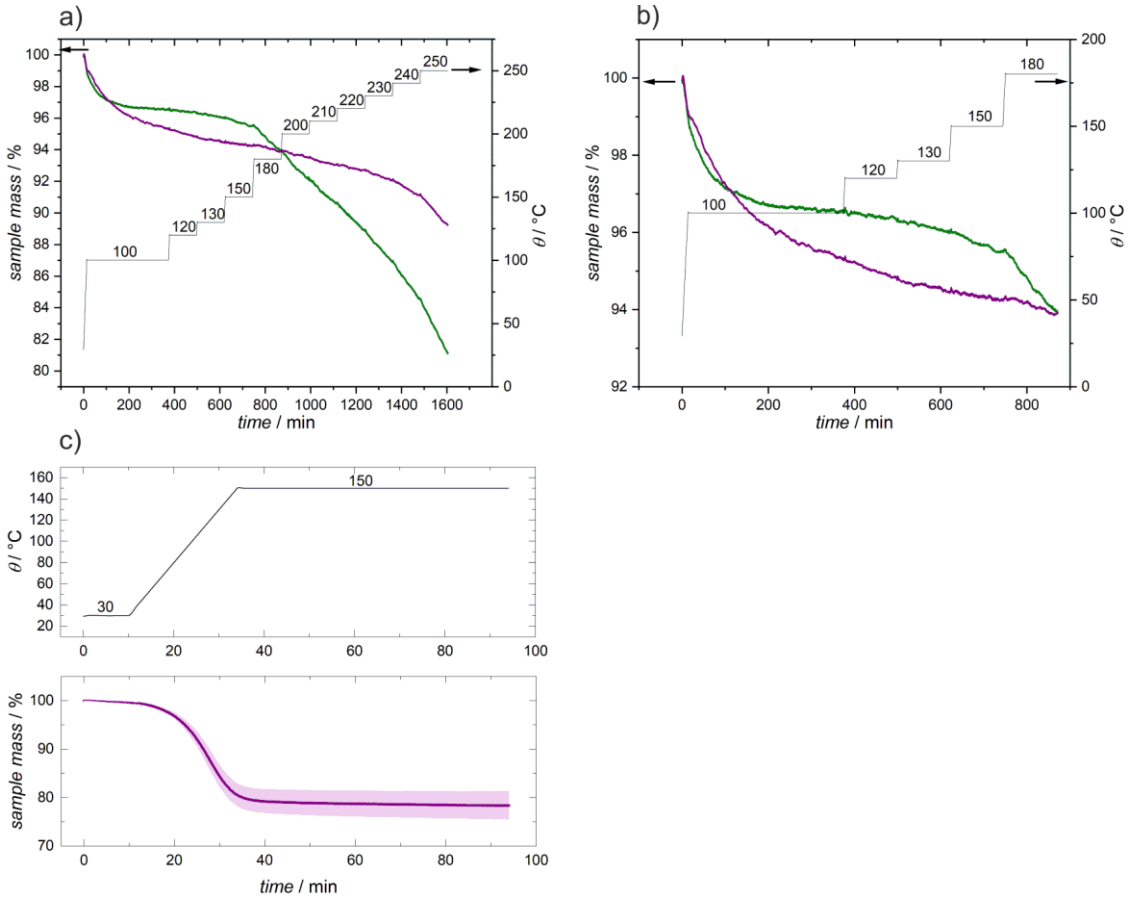

Figure 27 a) Isothermal TGA of [DESPA⁺][TfO⁻] with 1.89 wt% H_2O (green) and [DEMSPA⁺][TfO⁻] with 2.0 wt% H_2O (purple) in a synthetic air-like atmosphere (17.5 v% O_2 82.5 v% N_2). b) is a zoom of a). c) Isothermal TGA of [DEMSPA⁺][TfO⁻] with 16.7 wt% H_2O. Aluminum crucibles were used. The experiments were performed as triplets. The shaded area in c) corresponds to the standard deviation of the 3 experiments. The numbers in the temperature graphs indicate the temperatures of each step.

3.2.3 Phase Transitions of Different Functionalized PAcILs

During storage of the PAcILs in a dryroom (dew point <-60 °C) at about 20 °C the solidification of $[PEA^+][TfO^-]$ and $[SEA^+][TfO^-]$ was observed. Interestingly the 3rd PAcIL from the group with the primary ammonium function $[SOEA^+][TfO^-]$ stayed liquid during storage. However, like discussed in the next subchapter the determination of the water content in $[SEA^+][TfO^-]$, $[SOEA^+][TfO^-]$ and $[PEA^+][TfO^-]$ was impossible. Therefore the different behavior of $[SOEA^+][TfO^-]$ compared to the other two PAcILs might be related to a different water content. One hint for this hypothesis could be that the SOEA zwitterion is very hygroscopic and by vacuum drying at 60 °C a weight loss of about 14% was observed.

Both $[DESPA^+][TfO^-]$ and $[DEMSPA^+][TfO^-]$ didn't show any sign of solidification. Therefore, as overall trend it might be concluded, that the alkylation of the nitrogen in the cation suppresses solidification of the PAcILs. By alkylation on the one hand the positive charge is screened and on the other hand the cation becomes bulkier. Both effects reduce the coulombic interactions and therefore contribute to the suppression of solidification.

The differential scanning calorimetry curves of $[SEA^+][TfO^-]$, $[SOEA^+][TfO^-]$ and $[PEA^+][TfO^-]$ are displayed in Figure 28. For the first heating $[SEA^+][TfO^-]$ shows two reproducible endothermic peaks at about 40 °C and 50 °C. In $[PEA^+][TfO^-]$ a single endothermic peak at about 52 °C is visible in the first heating. After the melting in the first heating scan up to 60 °C no recrystallisation was observed at a scan rate of 5 $K \cdot min^{-1}$. In the liquid state the PAcILs only show a glass transition at the temperature T_g. With the modified mid-point method, which is described in subchapter 4.2.4 and the methods subchapter 2.2, T_g of the PAcILs were determined. Thereby the following order $[SOEA^+][TfO^-]<[SEA^+][TfO^-]<[PEA^+][TfO^-]$ i.e. -37.9°C, -30.6°C, -26.2°C, are obtained from the heating trace of the second cycle (Figure 28c). Both $[SEA^+][TfO^-]$ and $[PEA^+][TfO^-]$ have higher T_g's than $[SOEA^+][TfO^-]$. This is an indication for stronger interactions in $[SEA^+][TfO^-]$ and $[PEA^+][TfO^-]$ compared to $[SOEA^+][TfO^-]$ and fits to the observation that only the first two substances crystallize during storage.

In $[DESPA^+][TfO^-]$ a T_g between -54.5 °C to -59.2 °C was obtained with different water contents (see Figure 41 on page 114 and Table 8 on page 115). For $[DEMSPA^+][TfO^-]$ a T_g of about -52.6 °C was extracted from the heating trace of the second cycle (Figure 28d). These measurements demonstrate that the T_g for both PAcILs with the higher functionalized ammonium groups i.e. $[DESPA^+][TfO^-]$ and $[DEMSPA^+][TfO^-]$ is significant lower than for $[SEA^+][TfO^-]$, $[SOEA^+][TfO^-]$, $[PEA^+][TfO^-]$ with the primary ammonium. Considering the maximum shift of T_g of approximately 5 °C for the $[DESPA^+][TfO^-]$ samples with different water content, it seems unlikely that the difference of >10 °C between the PAcILs with a higher functionalized ammonium group

i.e. [DESPA$^+$][TfO$^-$], [DEMSPA$^+$][TfO$^-$] and with the primary ammonium group i.e. [SEA$^+$][TfO$^-$], [SOEA$^+$][TfO$^-$], [PEA$^+$][TfO$^-$] is due to varying water content.

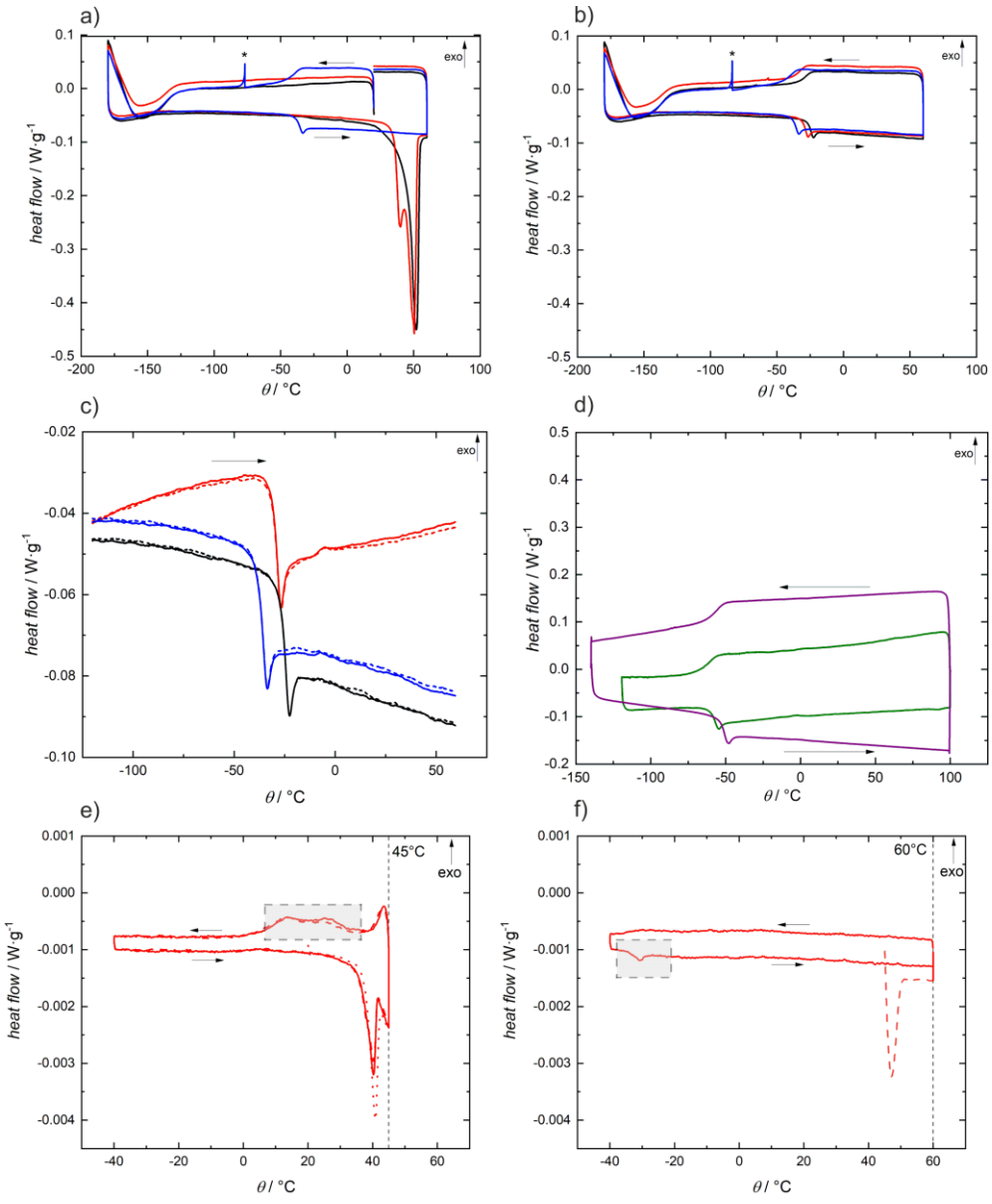

*Figure 28 a)-c) DSC of [SEA$^+$][TfO$^-$](red),[SOEA$^+$][TfO$^-$](blue) and [PEA$^+$][TfO$^-$](black). a) 1st cycle b)2nd cycle. c) a zoom of the heating trace of the 2nd cycle (solid line) and 3rd cycle (dashed line). d) DSC of [DESPA$^+$][TfO$^-$](green, 12599±187 ppmw H_2O) and [DEMSPA$^+$][TfO$^-$] (purple, 578±15 ppmw H_2O). Only the second cycles are displayed. a)-d) Experiments were performed with a scan rate of 5 K·min^{-1} in hermetically sealed aluminum crucibles with dry air inside the crucibles (from a dryroom with dew point <-60 °C). *mark thermal spikes, which are artefacts by the detector. The bump at about 150 °C is an artefact, which originates from the baseline calibration. e) [SEA$^+$][TfO$^-$] with a scan rate of 0.5 K·min^{-1}, 1st heating (red dotted-line), 1st complete cycle (red solid-line),2nd cycle (red dashed-line). The other conditions are equal like in the other panels. The vertical dashed line at 45 °C marks the upper boarder of the scan. The gray box highlights the crystallization peaks. f) continuation of the experiment in e). Therefore [SEA$^+$][TfO$^-$]is heated with 0.5 K·min^{-1} to 60 °C (indicated by dashed-vertical line). The gray box highlights the T_g. Internal IDs in a)-c) for [SEA$^+$][TfO$^-$] 20200525, [SOEA$^+$][TfO$^-$] 20200529,[PEA$^+$][TfO$^-$] 20200528, in d) for [DESPA$^+$][TfO$^-$] 20211115 and for[DEMSPA$^+$][TfO$^-$] 20190207. e)-f) 20200619.*

However the water content of [SEA^+][TfO^-], [$SOEA^+$][TfO^-], [PEA^+][TfO^-] could not be determined as described in next subchapter 3.2.4 and this line of reasoning is only based on the analogy to [$DESPA^+$][TfO^-].

For the endothermic peaks in [SEA^+][TfO^-] and [PEA^+][TfO^-], which are assigned as melting peaks, it was challenging to observe an exothermic counterpart for the recrystallisation. Several different experimental procedures like cycling around the T_g etc. didn't show any significant effect on the DSC curves. Only when [SEA^+][TfO^-] was measured with a low scan rate of 0.5 $K \cdot min^{-1}$ and the upper vertex temperature did not exceed the maximum of the second endothermic peak at 50 °C, a quite broad endothermic double peak is visible between about 10-30 °C in the cooling trace (Figure 28e). If the upper temperature is increased to 60 °C, so above the second endothermic peak no exothermic recrystallisation peak was visible any more, but instead the T_g of [SEA^+][TfO^-] was observed (Figure 28f).

To further investigate this behavior and get more inside in the phase transitions temperature-dependent Raman spectroscopy of both [SEA^+][TfO^-] and [PEA^+][TfO^-] was performed. Therefore, the solidified samples were crushed into powder and filled in an NMR tube as measurement cell. The temperature-dependent Raman spectra of [SEA^+][TfO^-] and [PEA^+][TfO^-] are displayed in Figure 29. Both from the 2D color plot and from the selected trace of the most intense peak at a Raman shift of about 1034 cm^{-1} it can be seen, that the scattering intensity decreases, when the temperature approaches the temperature of the exothermic peak in the DSC of [SEA^+][TfO^-] (Figure 29a) and [PEA^+][TfO^-] (Figure 29b), at 50 °C or 52 °C, respectively. The intensity minimum is thereby for [PEA^+][TfO^-] slightly shifted to a higher temperature compared to [SEA^+][TfO^-]. This agrees well with the minor difference in the position of the endothermic peaks in the DSC of both PAcIL. The decrease of the scattering intensity might be related to the change of the sample volume during the transition from powder to liquid form and to a change in the scattering cross section. Based on these experiments it can be assumed that the endothermic peaks of [SEA^+][TfO^-] and [PEA^+][TfO^-] at 50 °C and 52 °C indeed correspond to the melting points of the solidified PAcILs. The sharp peaks in the Raman spectra indicates that both PAcILs actually are crystalline materials in the solid state. In the Raman spectrum of solid [SEA^+][TfO^-] at 20 °C (Figure 29a) additional peaks are visible, which cannot be observed for the solid [PEA^+][TfO^-]. This finding suggests, that [SEA^+][TfO^-] eventually crystallized in two different phases and therefore in the DSC measurement two melting points are visible. If the heating run in DSC is stopped before completely melting both phases, the remaining crystallites are seeds for the recrystallisation during a slow cooling ramp.

Both DSC and temperature-dependent Raman experiments demonstrate the crystallization of [SEA$^+$][TfO$^-$] and [PEA$^+$][TfO$^-$]. The melting points of 50 °C and 52 °C are a drawback of these two PAcILs for a possible IT-PEMFC application. Crystallization inside the device could lead to a damage of the membrane or other parts of the fuel cell stack.

[SOEA$^+$][TfO$^-$], [DESPA$^+$][TfO$^-$] and [DEMSPA$^+$][TfO$^-$] remain liquid during storage at room temperature for more than one year and also in the DSC experiments no indication for a crystallization was found. Therefore, regarding the liquidus range and phase behavior [SOEA$^+$][TfO$^-$], [DESPA$^+$][TfO$^-$] and [DEMSPA$^+$][TfO$^-$] are promising for the planed IT-PEMFC application.

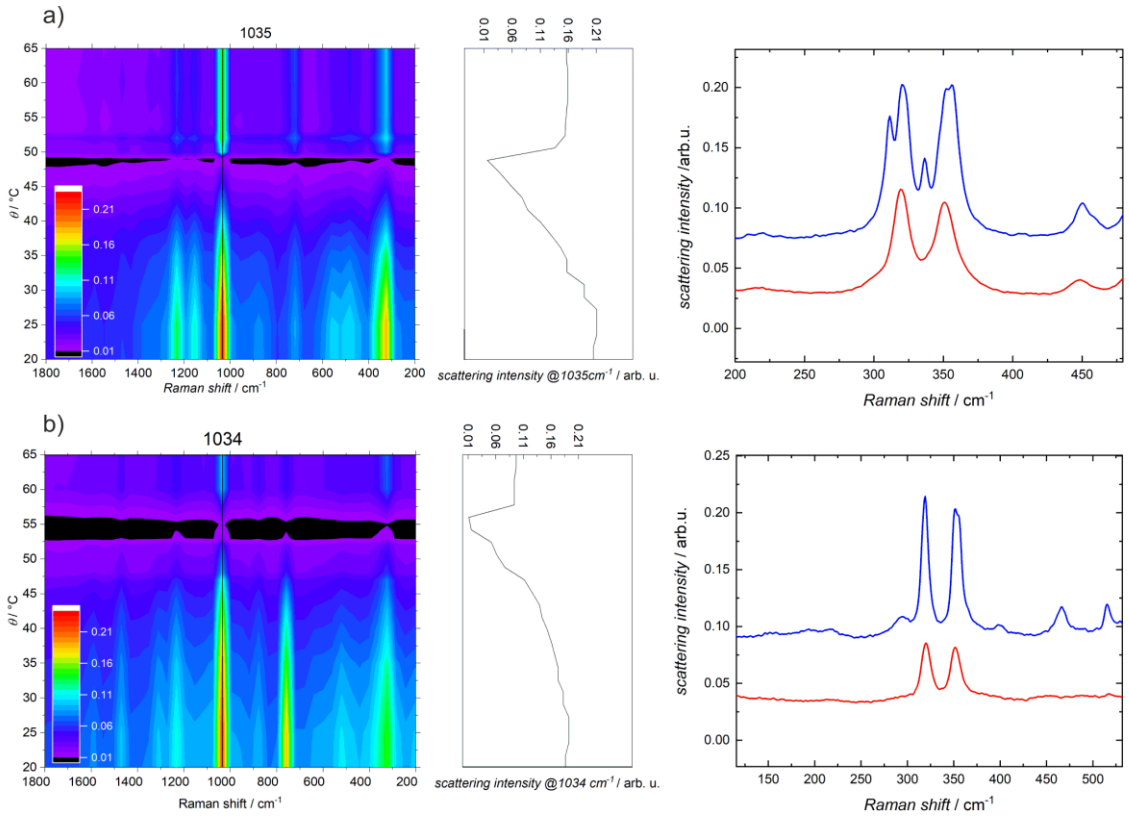

Figure 29 Temperature-dependent Raman spectra of a) [SEA$^+$][TfO$^-$] and b) [PEA$^+$][TfO$^-$]. In the beginning of the experiments the samples were in the solid state and the temperature was increased from 20-65 °C. Thereby spectra were recorded at 20 °C, 25 °C, 30 °C, between 35-55 °C in 1 °C steps and at 60 °C and 65 °C. Color-coded 2D plots of the scattering intensity (in arbitrary units) vs. the Raman shift and the temperature are shown. Additionally, the temperature-dependent line profile for the most intense peak (at ~1034 cm^{-1}) and the segments of the spectra for the vibrations of the CF_3 group at 20 °C (blue) and 65 °C (red) are displayed.

3.2.4 Water-PAcIL Interactions at Room Temperature and 120 °C

For a PAcIL intended for use in a PEMFC, the interaction with water plays a crucial role. While at temperatures >100 °C, the water formed during the reaction in the PEMFC is released as water vapor, there can be an accumulation of water in the cell, especially during start-stop processes. Two aspects are particularly relevant here: (I) the miscibility of the PAcIL with water within the *operando*-temperature range and (II) the stability of the PAcIL at elevated temperatures (e.g., 120 °C) with high water content.

The miscibility of the investigated PAcILs $[DESPA^+][TfO^-]$,$[DEMSPA^+][TfO^-]$, $[SEA^+][TfO^-]$,$[SOEA^+][TfO^-]$ and $[PEA^+][TfO^-]$ at room temperature was investigated. When $[DESPA^+][TfO^-]$ or $[DEMSPA^+][TfO^-]$ are overlaid with water the PAcILs remain optically unchanged at the water interface. With time and vigorous shaking of the vessel $[DESPA^+][TfO^-]$ or $[DEMSPA^+][TfO^-]$ get dissolved. No peculiar visible observation was made when preparing mixtures up to 1:1 (wt:wt), which corresponds to 1:19 and 1:20 molar ratios of $[DESPA^+][TfO^-]$ and $[DEMSPA^+][TfO^-]$ to H_2O respectively.

With the primary ammonium-based PAcILs $[SEA^+][TfO^-]$,$[SOEA^+][TfO^-]$ and $[PEA^+][TfO^-]$ the situation is completely different compared to the tertiary ammonium-based $[DESPA^+][TfO^-]$ and quaternary ammonium-based $[DEMSPA^+][TfO^-]$. When $[SEA^+][TfO^-]$,$[SOEA^+][TfO^-]$ and $[PEA^+][TfO^-]$ are exposed to water, at the interface immediately the formation of a white precipitate is observed. The formation of a white precipitate in contact with water was already described for $[SEA^+][TFO^-]$ by K. Wippermann et al. He assumed that the particles are hydrates[72]. To determine the chemical composition of the white precipitate in this work, the precipitate was analyzed by Attenuated Total Reflectance Fourier Transform Infrared Spectroscopy (ATR-FTIR). The ATR-FTIR spectrum from the C-H/O-H region of the precipitate of $[SOEA^+][TfO^-]$ in Figure 30a) clearly indicate, that the precipitate is the backreacted zwitterion. For the $[SEA^+][TfO^-]$ and $[PEA^+][TfO^-]$ similar results for the ATR-FTIR measurements were obtained. Therefore, it is suggested that in all three cases of the primary ammonium-based PAcILs the precipitate consists of the backreacted zwitterion. This backreaction is sketched in Figure 30. A possible driving force for the backreaction of the PILs in contact with water might be according to the Le Chatelier's principle the limited solubility of the SEA, SOEA and PEA zwitterions. While for SEA and SOEA zwitterion i.e. taurine and 2-Aminoethyl hydrogen sulfate, the solubility in water is reported in literature, for PEA, DESPA and DEMSPA theses values are not available. Therefore, the saturation concentration of the zwitterions in water were estimated experimentally. Briefly, the liquid phase from a saturated aqueous solution of the investigated zwitterion with precipitate on the bottom, was decanted and filtered through a syringe filter. A defined volume from an Eppendorf pipette was dried in an oven at 80 °C.

However, it's important to note the described approach is only an estimation, since precise temperature control during the handling of the liquid is limited. Exact measurements could be achieved, for example, by examining the solution's light transmittance as a function of temperature.

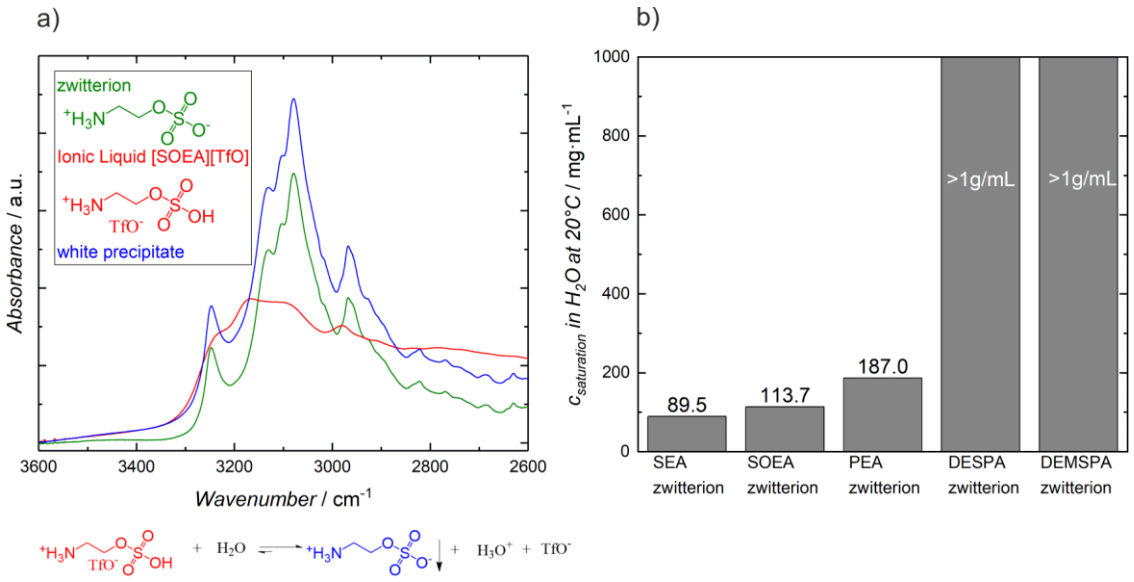

Figure 30 a) ATR-FTIR spectra of [SOEA$^+$][TfO$^-$](red), the SOEA zwitterion i.e. 2-Aminoethyl hydrogen sulfate. (green) and the white precipitate (blue). The proposed reaction equation for the formation of the white precipitate is sketched below the spectra. b) The experimental estimation of the saturation concentrations in H_2O at about 20 °C of the different zwitterionic precursors. For DESPA and DEMSPA zwitterion the investigation was stopped when the dissolved concentration exceeded 1 g·ml^{-1}.

The results from the above described experiments to estimate the aqueous saturation concentration of the different zwitterions at about 20 °C are displayed in Figure 30b). Despite the simple approach used, the experimental data obtained for SEA and SOEA display a good agreement with literature values (Figure S 1). The water solubility increases from SEA<SOEA<PEA<<<DESPA, DEMSPA zwitterion. While the water solubility SEA, SOEA and PEA zwitterion ranges between about 90-190 mg·ml^{-1}, it is by at least more than a factor of 5-10 higher for the DESPA and DEMSPA zwitterions. Indeed, for both DESPA, DEMSPA zwitterions the solubility limit determination was stopped after the solubility exceeded 1 g·ml^{-1}. The significant higher water solubility for the DESPA and DEMSPA zwitterion is probably based on the more stable ionic form. In DESPA the positive charge at the ammonium nitrogen is probably stabilized by the +I effect of the two attached ethyl groups. In DEMSPA the charge is even locked at the ammonium nitrogen atom by quaternization in an irreversible alkylation reaction. In contrast in the SEA, SOEA and PEA zwitterion the positive charge at the ammonium is not stabilized by any alkyl substituent. Therefore, it can be expected that a substantial amount of SEA, SOEA and PEA zwitterion are in the neutral form. This difference in the ratio of neutral and zwitterionic form in water might be the origin for the much higher solubility of DESPA and DEMSPA zwitterions compared to SEA, SOEA and PEA.

Ultimately this significant different water solubility of the zwitterions leads to a water miscibility of [DESPA$^+$][TfO$^-$] and [DEMSPA$^+$][TfO$^-$] over the complete window of mixing ratios. In contrast the low solubility of the zwitterions of SEA, SOEA and PEA cause a precipitation of this compound which leads according to the Le Chatelier's principle to a continuous decomposition of [SEA$^+$], [SOEA$^+$] or [PEA$^+$] to a charge neutral form, both as zwitterion and in the uncharged state.

The immiscibility of [SEA$^+$][TfO$^-$], [SOEA$^+$][TfO$^-$] and [PEA$^+$][TfO$^-$] with water at room temperature i.e. decomposition in the zwitterionic starting material is a significant drawback for PEMFC application. Additionally, the immiscibility is not only limited to water but the same effect was observed for organic solvents like absolute ethanol, absolute methanol, glacial acidic acid, DMSO, DMF etc., too. This challenge to mix the PAcIL with any solvent impedes further processing for example solvent casting, application as an electrolyte additive in batteries etc. In addition due to the immiscibility with methanol or other suitable solvents the water content in [SEA$^+$][TfO$^-$], [SOEA$^+$][TfO$^-$] and [PEA$^+$][TfO$^-$] cannot be determined by Karl Fischer titration (see chapter 1.3). Like for example reported by G. L. Burrell and observed by the author of the thesis from PILs the water can often not be removed by heating even in vacuum due to strong water-PIL bonds [95]. Therefore, the application of Karl Fischer titration with the oven method didn't yield realistic values. Attempts to determine the water content in these PILs in the neat state by ^{1}H-NMR spectroscopy were unfortunately not successful because no water signal is visible (Figure 24). TGA with according to the experience of the author an uncertainty of at least 0.3 wt% is not suited for the measuring the water content in samples with expected amount of water ≤1 wt%. Therefore the determination of the water content in [SEA$^+$][TfO$^-$], [SOEA$^+$][TfO$^-$] and [PEA$^+$][TfO$^-$] was impossible. Therefore, also quantities of [SEA$^+$][TfO$^-$], [SOEA$^+$][TfO$^-$] and [PEA$^+$][TfO$^-$], which depend on the water content like the ionic conductivity and viscosity will not be discussed here. For [DESPA$^+$][TfO$^-$] and [DEMSPA$^+$][TfO$^-$] were the water content can be determined by KF titration, values on the ionic conductivity and viscosity are published in [69]. Additionally for [DESPA$^+$][TfO$^-$] a detailed discussion of the ionic conductivity and viscosity is presented in chapter 4.2.5 in comparison to the fluorine-free PAcIL [DESPA$^+$][HMDS$^-$].

While [SEA$^+$][TfO$^-$], [SOEA$^+$][TfO$^-$] and [PEA$^+$][TfO$^-$] are not soluble in water at room temperature, at elevated temperature (>60 °C) an aqueous 1:1 solution (by mass) could be prepared. Under these harsh conditions of high water content, strong acidity and high temperature PAcILs especially with organic sulfate groups like [SOEA$^+$][TfO$^-$] might hydrolyze.

Therefore, the stability of selected PAcILs vs. hydrolysis was studied by temperature-dependent Fourier transform Raman spectroscopy (FT-Raman).

A set-up, which allows experiments in the NPT ensemble (constant temperature, pressure and composition) was constructed to mimic the *operando* conditions in a PEMFC. By the connection of a balloon to an NMR tube a measurement cell with a pressure exchange reservoir was prepared (inset Figure 31a). The sample was heated with a Linkam temperature-controlled stage to 120 °C and a time series of Raman spectra with one spectrum per hour was acquired. The spectra of 1:1 mixture (by mass) of water and [$DEMSPA^+$][TfO^-], [$DESPA^+$][TfO^-] and [$SOEA^+$][TfO^-] are displayed in Figure 31a)-c). The intensity of each spectrum was normalized to the peak at 316 cm^{-1}, which is assigned to a vibration of the CF_3 group. This normalization assumes that the high thermal and chemical stable CF_3 group will remain unaltered during the experiments. In the spectra of [$DEMSPA^+$][TfO^-] in Figure 31a) it can be seen that the intensities of some bands are increased or decreased in the hydrated state (orange) compared to the pristine one (blue). This might be related to the change in dielectric constant in aqueous solution and/or to water-PAcIL H-bond interactions. However, beside these intensity differences the spectra in hydrated and pristine state are identical. Also, during the 24 h at 120 °C the spectra hardly changes and the spectrum recorded after 24 h (red) nearly completely overlaps with the initial one (orange). This demonstrates the [$DEMSPA^+$][TfO^-] is not affected by the water and is stable in the highly hydrated state at elevated temperature of 120 °C for at least 24 h. For [$DESPA^+$][TfO^-] Figure 31b) similar changes in peak intensities of the pristine and hydrated sample like for [$DEMSPA^+$][TfO^-] are observed. In contrast to [$DEMSPA^+$][TfO^-] the intensities of some peaks in [$DESPA^+$][TfO^-] changed during the 24 h at 120 °C and approached the intensities in the pristine sample. This might be interpreted as dehydration of the sample during the 24 h at 120 °C. Like [$DEMSPA^+$][TfO^-] the spectra of [$DESPA^+$][TfO^-] in Figure 31b do not display any other changes beside the intensity changes related to hydration/dehydration during 24 h under IT-PEMFC *operando* conditions. The spectra of [$SOEA^+$][TfO^-] in contrast to [$DEMSPA^+$][TfO^-] and [$DESPA^+$][TfO^-] show some significant changes after heating of the hydrated sample in the 900 cm^{-1} region (Figure 31c). The peak at 873 cm^{-1} shifts for 9 cm^{-1} towards a lower value and at 834 cm^{-1} a new peak appears (inset Figure 31c). Both the peak shift and the appearance of the new peak indicate the cleavage of the HSO_4-group. The obtained double peak pattern is similar to sulfuric acid (inset Figure 31c). Interestingly this change is already visible in the first spectrum. Within the time series no progression could be observed between the first and last spectrum.

Therefore, it seems like the decomposition of the [$SOEA^+$] cation already takes place during the heating step to dissolve the PAcIL in the water during sample preparation or during the heating towards 120 °C.

However, according to the Raman spectroscopic investigation [$DESPA^+$][TfO^-] and [$DEMSPA^+$][TfO^-] are inert under the strongly hydrolyzing IT-PEMFC *operando* conditions while [$SOEA^+$][TfO^-] seems to be highly labile and the sulfuric acid group is split from the organic rest quickly.

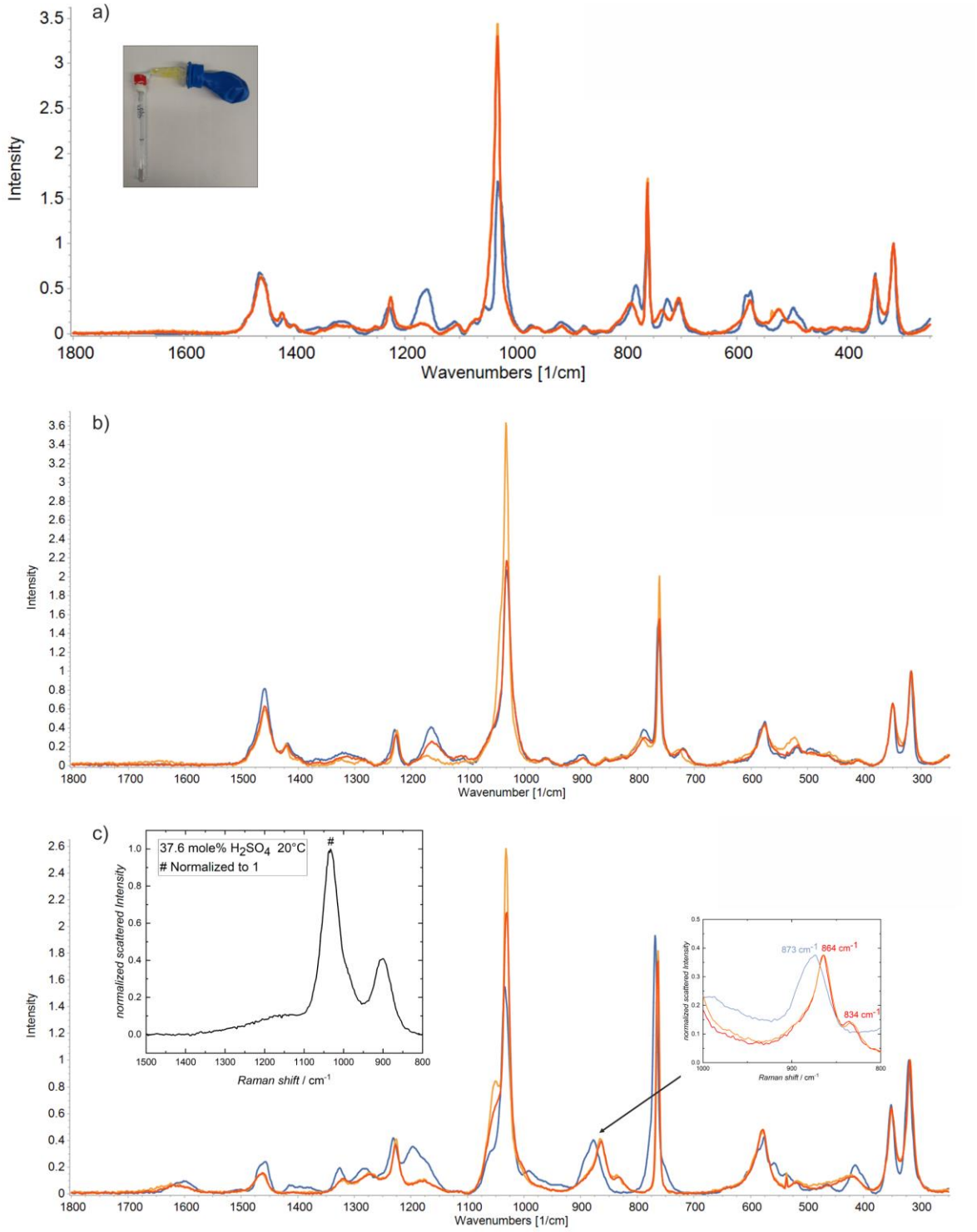

Figure 31 In situ *Raman spectroscopy of 1:1 (wt:wt) mixtures of PAcILs with water at 120 °C. The spectra are normalized to the peak at 318 cm^{-1}. a) [DEMSPA$^+$][TfO$^-$] b)[DESPA$^+$][TfO$^-$] and c)[SOEA$^+$][TfO$^-$]. The blue curves correspond to the water-free PAcILs. The orange ones were obtained after 1 h at 120 °C and the red ones after 24 h at 120 °C. In a) a photograph of the setup for the experiments under constant pressure is shown. In c) a zoom of the region at about 900 cm^{-1} and a reference spectrum from 37.6 mol% H_2SO_4 are displayed.*

3.3 Conclusion: Most Promising Cation Structure for IT-PEMFC Application

In this chapter five protic acidic ionic liquids (PAcILs) with different functionalized cation structures and the triflate anion were synthesized and tested for their applicability in intermediate temperature proton-exchange membrane fuel cell (IT-PEMFC), with a target operation temperature of 120 °C. The different PAcILs can be grouped into two set:

a) with primary ammonium group and sulfonic, sulfuric and phosphoric acid group:
2-Sulfoethylammonium triflate [SEA^+][TfO^-]
2-(Sulfooxy)ethan-1-ammonium triflate [$SOEA^+$][TfO^-],
2-(Phosphonooxy)ethan-1-ammonium triflate [PEA^+][TfO^-]

b) with a sulfonic acid group and a different functionalized ammonium group:
N,*N*-diethyl-3-sulfopropan-1-ammonium triflate [$DESPA^+$][TfO^-],
N,*N*-diethyl-*N*-methyl-3-sulfopropan-1-ammonium triflate [$DEMSPA^+$][TfO^-]

[SEA^+][TfO^-] is the only of the 5 PAcILs which was reported before in literature[72]. Parts of this chapter were published in [69].

^{1}H-NMR spectroscopy was used to verify the successful synthesis. By measurements in the neat state the signals of the acidic protons are visible. These experiments confirmed within the detection limit of the NMR the complete protonation of the zwitterion i.e. high formation degree of the PAcILs. Additionally, the protonation state of the ammonium group on the NMR timescale can be analyzed. All PAcILs displayed a large protonation degree at the ammonium function. Only in [$DESPA^+$][TfO^-] about 1/3 of unprotonated N groups (in the time average) were observed. This finding might correlate with the relatively high water content of about 1.2 wt% and therefore large number of additional proton acceptor groups. For the PAcILs of group (a) with the primary ammonium the water content was not accessible by Karl Fischer titration and could not be estimated from the NMR experiments. Therefore, no general trend that relates the protonation degree of the ammonium group to the water content can be formulated.

In both dynamic and isothermal thermogravimetric experiments, a thermal stability of [PEA^+][TfO^-], [$DESPA^+$][TfO^-] and [$DEMSPA^+$][TfO^-] beyond 120 °C in synthetic air was observed. For the baseline compound [SEA^+][TfO^-] and [$SOEA^+$][TfO^-] in the isothermal TG measurement already a significant mass loss was observed below 120 °C. A step in dynamic TG curves of [$SOEA^+$][TfO^-] might be interpreted by the cleavage of the sulfuric acid group.

During storage at room temperature [SEA^+][TfO^-] and [PEA^+][TfO^-] crystalized. With DSC a melting point of 50 °C and 52 °C was measured for the two PAcILs, respectively. The other PAcILs didn't display any sign of crystallization, both during storage and in the DSC measurements. For the glass-transition temperature T_g values of -37.9 °C, -30.6 °C, -26.2 °C were determined for [$SOEA^+$][TfO^-], [SEA^+][TfO^-], [PEA^+][TfO^-], respectively. For [$DESPA^+$][TfO^-] with different water contents T_g values between -54.5 °C to -59.2 °C and for [$DEMSPA^+$][TfO^-] of about -52.6 °C were observed. The more than 10 °C higher T_g and the crystallization of the PAcILs with the primary ammonium demonstrate the stronger ionic interactions of [$SOEA^+$][TfO^-], [SEA^+][TfO^-] and [PEA^+][TfO^-] compared to [$DESPA^+$][TfO^-] and [$DEMSPA^+$][TfO^-] with the higher functionalized ammonium groups. This trend can be rationalized by the better screening of the positive charge in the sterically more demanding PAcILs [$DESPA^+$][TfO^-] and [$DEMSPA^+$][TfO^-].

The different behavior of the two sets of investigated PAcILs is also obvious for the contact with water. While for [$SOEA^+$][TfO^-], [SEA^+][TfO^-] and [PEA^+][TfO^-] in contact with water the zwitterionic precursor precipitate, [$DESPA^+$][TfO^-] and [$DEMSPA^+$][TfO^-] are miscible with water up to at least a 1:1 (wt:wt) ratio. One reason for the different reactions with water are the significantly different saturation concentrations of the corresponding zwitterions in water. While the DESPA and DEMSPA zwitterion is soluble up to at least 1g·ml^{-1} at 20 °C, the precursors of SEA, SOEA, PEA have at least 10 times lower solubility in water. For 1:1 (wt:wt) ratios with water and at elevated temperatures the PAcILs can be dissolved in water. By temperature-dependent Raman spectroscopy of these water-PAcIL mixtures it was found that [$DESPA^+$][TfO^-] and [$DEMSPA^+$][TfO^-] are stable against hydrolysis for at least 24 h at 120 °C. [$SOEA^+$][TfO^-], in contrast shows a rapid hydrolysis under these conditions.

Based on all these tests the PAcILs with the primary ammonium are found less suitable for the planed IT-PEMFC application. [SEA^+][TfO^-], [$SOEA^+$][TfO^-]and [PEA^+][TfO^-] are not compatible with water and form a solid precipitate. Additional [SEA^+][TfO^-] and [PEA^+][TfO^-] crystalizes at room temperature. [$SOEA^+$][TfO^-] does not crystalizes but is labile to hydrolysis.

[$DESPA^+$][TfO^-] and [$DEMSPA^+$][TfO^-] are thermally stable far above 120 °C, do not crystalize, are miscible with water, and are stable to hydrolysis under *operando* conditions. Therefore, [$DESPA^+$][TfO^-] and [$DEMSPA^+$][TfO^-] are the most promising candidates for IT-PEMFC application. [$DESPA^+$][TfO^-] is in contrast to [$DEMSPA^+$][TfO^-] soluble in DMSO, which is beneficial for membrane casting. And it displays a lower viscosity. Therefore, despite the better thermal stability of [$DEMSPA^+$][TfO^-], the [$DESPA^+$] cation was selected for the investigation of an optimized fluorine-free anion structure presented in the next chapter.

4. Development of a Fluorine-free PAcIL for IT-PEMFC

4.1 Introduction

In the previous chapter *N*,*N*-diethyl-3-sulfopropan-1-ammonium triflate [$DESPA^+$][TfO^-] was identified as a promising candidate for intermediate temperature PEMFC application. Triflate belongs to the widely used group of fluorinated anions such as bis(trifluoromethanesulfonyl)imide [$TFSI^-$], bis(fluorosulfonyl)imide [FSI^-], and trifluoroacetate [$TFAc^-$]. But why are fluorinated anions so common in ILs?

First, each strongly electronegative fluorine atom in the anion attracts the negative anionic charge and thereby contributes to the charge delocalization in the molecule. Obviously by charge delocalization the coulombic interactions in the IL are weakened. This leads to a beneficial suppression of crystallization and also a reduction of viscosity. Furthermore, the charge delocalization improves the electrochemical stability of the anion towards oxidation.

Second, fluorine carbon bonds are among the strongest bonds in organic chemistry with bond dissociation energies (BDEs) of 413-547 kJ/mol[31,105]. For comparison in alkanes the BDEs for an H abstraction range between 396-439 kJ/mol[31]. Therefore, by fluorination usually the thermal, chemical and electrochemical stability of the molecule gets increased.

Third, fluorine has a low polarizability, which results in a low surface energy and therefor only weak cohesive forces between fluorocarbons[105]. Hence fluorination is an effective strategy to reduce the viscosity of ILs.

In context of PILs fluorination serves an additional purpose. As described in chapter 3.1 PILs are prepared by a reversible acid base reaction. To nearly quantitatively protonate medium to weak bases strong acids are required. Due to its large electronegativity fluorine atoms draw electrons away from the bond to the acidic proton and thereby weaken the bond and stabilize the negative charge of the deprotonated anionic form. These effects lead to a drastic increase in acidic strength (in aqueous medium), which is illustrated by the comparison of acetic acid (pK_a 4.76[31]) to trifluoroacetic acid (pK_a 0.52[31]) or methanesulfonic acid (pK_a -1.92[106]) to trifluoromethanesulfonic acid (pK_a -5.9[106], ~-14[107]).

Despite the beneficial effects of fluorine, the serious economic and ecological disadvantages of fluorinated ILs cannot be ignored.

While fluorine-free cations can usually be synthesized at low cost, fluorinated anions are more expensive to produce and thus push up the manufacturing costs of the corresponding ILs. The higher cost of fluorinated compounds is evident, for example, by the average selling price of 40 US$/kg for trifluoromethanesulfonic acid compared to 14 US$/kg for methanesulfonic acid on the bulk sales platform "Made-in-China"[a]. The selling price is, of course, determined not only by production costs but also by supply/demand etc. Nevertheless, the high cost of fluorination is for sure reflected in the costs for fluorinated compounds. High production costs of fluorinated ILs are an obstacle for market penetration and hinder the widespread use in intermediate temperature fuel cells. In contrast it is expected that fluorine-free ILs can be synthesized to significant lower costs, which would be highly desirable from an economical point of view.

Though the high stability of the C-F bond is an advantage for the application of fluorinated compounds, it becomes a severe issue when fluorinated compounds are released in the environment. Due to the stability of the C-F bond many per and polyfluoroalkyl substances (PFAS) are hardly biodegradable and therefore have a long half live in the environment. This persistency leads to an accumulation in the nature and even in the human body i.e. so-called bioaccumulation[108]. The detailed effects of the PFAS on the human health and the nature are not fully disclosed yet, but some compounds are suspected to be toxic for human reproduction. To limit further bioaccumulation and thereby protect both human health and the environment the European Chemicals Agency (ECHA) has already issued regulations/banns for some fluorinated carbonic and sulfonic acids in the legal framework of REACH[109,110]. On 13.01.2023 public authorities of Germany, Netherland, Denmark, Norway and Sweden proposed a nearly complete ban of all PFAS[111]. If this measure will be realized also trifluoromethanesulfonic acid, which falls under the current PFAS definition[112], might be regulated or banned in the European economic area. Such a regulation will have a strong impact on the application of $[DESPA^+][TfO^-]$ in IT-PEMFC.

Due to the impact of fluorinated compounds on the environment, the human health and ecological considerations described above, obviously a fluorine-free PAcIL is required as alternative for $[DESPA^+][TfO^-]$ in the planned intermediate temperature fuel cell application.

Important aspects that must be considered in the development of a fluorine-free anion include (I) the need to maintain high thermal and electrochemical stability and (II) the requirement for high acidity despite the absence of the strongly electron-withdrawing

[a] https://www.made-in-china.com . Data retrieved on 23.09.2023 15 o'clock. Averaged prices are calculated from 19 offers for each compound with a minimum order quantity (MOQ) of 1 kg. The nominal purities specified by the sellers were in both cases technical qualities between 70-99%. For trifluoromethanesulfonic acid and methanesulfonic acid the price ranges were 1-150 US$/kg and 1-120 US$/kg, respectively.

fluorine. Due to (I), organic sulfates are excluded as candidates, as they are prone to hydrolysis in the presence of water (see chapter 3.2.4) and also exhibit strong adsorption on the catalyst surface, thereby diminishing catalytic activity. The effect of sulfate on the catalytic activity is for example discussed for [DESPA$^+$][HSO_4^-] in reference [69].

Within the HiFi-PEFC project[b], several fluorine-free acids were tested as precursors for PAcILs. However, it was observed, that methanesulfonic acid was too weak to form a stable PAcIL. Sulfonic acids containing an aromatic ring, such as p-toluenesulfonic acid, were capable of protonating the DESPA zwitterion; however, they were unsuitable for mid temperature fuel cells at 120°C due to their high melting points[113].

In an extensive literature search for sulfonic acids, the diprotic methanedisulfonic acid H2MDS was discovered. As diprotic acid it possesses the two deprotonation stages of hydrogen methanedisulfonate [$HMDS^-$] and methanedisulfonate [MDS^{2-}] (Figure 32a). A study by T. L. Smith and J. H. Elliot revealed, that for a 0.5-5 mM solution in glacial acetic acid the Hammett acidity parameter H_0 of H2MDS with -0.26 to -1.33 is significantly lower than methanesulfonic acid (+1.19 to +0.27) and even lower than sulfuric acid (+0.65 to -0.29)[114]. This suggests that in a non-aqueous system, methanedisulfonic acid is considerably stronger than methanesulfonic acid and is likely capable of protonating the DESPA zwitterion. In an acid-base titration of aqueous solution of methanedisulfonic acid P. M. Brewster and G. L. Jenkins, only observed one equivalence point. This observation is similar to that of sulfuric acid and indicates high acidity strength of H2MDS in an aqueous environment[115].

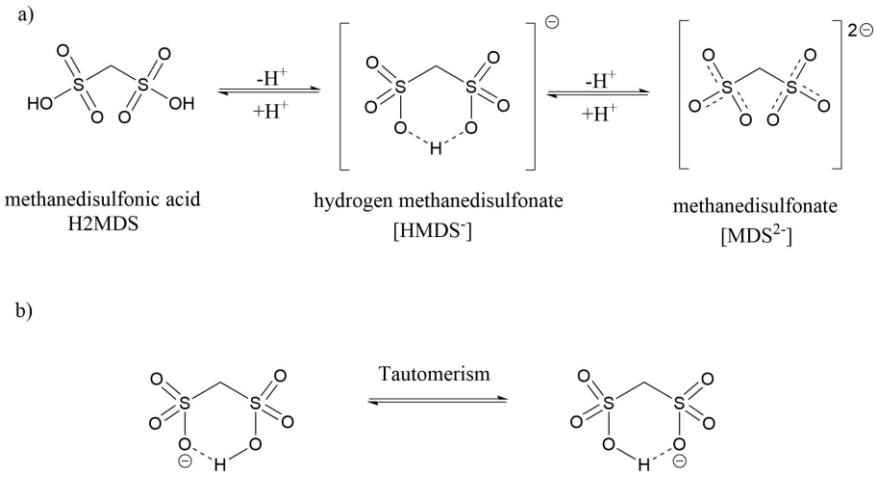

Figure 32 a) Chemical structure of methanedisulfonic acid H2MDS and its two deprotonation stages hydrogen methanedisulfonate [$HMDS^-$] and methanedisulfonate [MDS^{2-}]. b) Illustration of the tautomerism in the cyclic form of [$HMDS^-$].

[b] **Hi**gh-temperature stable **F**unctionalized **I**onic Liquids for Mid to High-temperature **P**olymer **E**lectrolyte **F**uel **C**ell application (HiFi-PEFC) funded by German BMWE 2017-2021 (funding number 03ETB003A + B)

The high acidity of H2MDS derived from experimental observations, both in non-aqueous and aqueous media, can potentially be explained by the expected cyclic structure of the first deprotonation stage [$HMDS^-$], as depicted in Figure 32. Usually such 6-membered ring structures are energetically favored. The formation of this 6-membered state could be a driving force for the deprotonation of H2MDS and thus contribute to its high acidity.

Additionally, the rotations around the single bonds are frozen in the cyclic form and a tautomerism exist (Figure 32b). These tautomers transform into each other by passing the bridging hydrogen atom of the intramolecular hydrogen bond from one sulfonic acid group to the other. At the same time this leads to the formation of a negative charge at the oxygen atom which is not covalently bond to the hydrogen. This mechanism therefore transfers both the H-atom and the negative charge from one sulfonic acid group to the other and thereby will contribute to the charge delocalization.

Both the expected high acidity and the delocalization of the negative charge would be beneficial for the formation and the physical properties of a methanedisulfonic-acid-based PAcIL.

In addition, [$HMDS^-$] is an amphoteric compound i.e. while it is deprotonated (Brønsted base) it still retains an “acidic” proton (Brønsted acid). In literature only a few PILs with anions containing “acidic" protons like [HSO_4^-], [$H_2PO_4^-$] or maleate and fumarate are described[116]. The uniqueness of an anion with an extra proton is that it can act both as a hydrogen acceptor and as a donor. This potentially fulfills the prerequisites for proton transfer through a cooperative mechanism. The partially unexpectedly high conductivity of PILs with such anions is therefore interpreted as being due in part to a Grotthuss-like proton transport mechanism[59,95,117,118].

When considering proton transfer in protic ionic liquids, however, there is a fundamental challenge. For strong Brønsted acid–base pairs the protolysis equilibrium heavily favors the ionic liquid side. This is on the one hand beneficial to achieve a high formation degree of the PIL, and therefore minimize the amount of usually more volatile and less thermal stable neutral species. But on the other hand, in such an IL the acidic proton is strongly bound to the former base, making it unavailable for proton transfer. This is where the proposed structure of a cation with a sulfonic acid group like [$DESPA^+$] and [$HMDS^-$] present an interesting combination. The very similar acidic groups in the cation and anion could result in a low energy barrier for proton transfer, thereby facilitate proton transfer between species and ultimately enable a decoupling of the proton mobility from the slower motion of the bulky cations and anions.

Despite these interesting properties, both from scientific and application point of view methanedisulfonic acid is a surprisingly unknown, especially considering its relatively simple molecular structure is considered. In Google Scholar only about 595 items could be retrieved for the exact match "methanedisulfonic acid" (including citations and patents). For comparison "methanesulfonic acid" yields about 89,200 items [c]. Among these publications about methanedisulfonic acid are to the author's knowledge only two reports on PILs with the [$HMDS^-$] or [MDS^{2-}] anion.

D. Song et al. investigated the catalysis of the Pechmann reaction of phenols with ethyl acetoacetate by hydrogen N-methylimidazolium hydrogen methanedisulfonate [$HMIM^+$][$HMDS^-$][119]. ^{1}H-NMR in DMSO-d_6 and high-resolution mass spectrometry (HRMS) results are provided to demonstrated the successful preparation of the PIL. However, the assignment of the ^{1}H-NMR spectrum in the paper, not fits to the chemical structure. A closer look to the original data in the supporting information reveals that the spectrum contains two additional unassigned peaks at 7.80 ppm and 14.05 ppm. These peaks are tentatively assigned by the author of this thesis to the NH in [$HMIM^+$] and the proton of [$HMDS^-$], respectively. Calculated and measured HRMS results fit to each other. For the Hammett acidity function H_0 of 80 mM [$HMIM^+$][$HMDS^-$] in methanol a value of 0.43 is reported. This value is similar to diluted aqueous H_2SO_4 (2.26 wt%) with 0.48[120].

G. Wang et al. explored 1-(4-butylsulfonic acid)-3-hexylimidazolium methanedisulfonate [$BSHexIM^+$]$_2$[MDS^{2-}] as catalyst for the oligomerization of olefins[121]. Neither the presented ^{1}H-NMR nor the IR results provide conclusive information about the degree of formation of the PIL because in the NMR experiments D_2O, in which H-D exchange occurs, was used as the solvent. Additionally, distinguishing between the SO_3H groups of the product and the reactant using IR spectroscopy is challenging. A H_0 value of 0.14 for [$BSHexIM^+$]$_2$[MDS^{2-}] in ethanol was determined in the publication.

Both literature examples are a first prove-of-principle for H2MDS-based PILs. A high acidity of PILs with the [$HMDS^-$] anion can also be assumed from the cited studies. However, the proposal in this thesis to apply the fluorine-free [$DESPA^+$][$HMDS^-$] in a PEMFC represents a novelty.

The chapter begins with the synthesis of H2MDS and the detailed characterization of the relatively unknown acid. Subsequently, the synthesis of [$DESPA^+$][$HMDS^-$] is described, and the formation of the PAcIL is confirmed by NMR spectroscopy. The required thermal stability for use in a PEMFC at 120°C is examined, always with a comparison to the fluorinated [$DESPA^+$][TfO^-].

[c] Retrieved on 17.09.2023 17:43 o'clock.

To gain more information about the interactions in the PAcILs, density, isobaric thermal expansivity, and the glass-transition temperatures are investigated.

The crucial proton transport mechanism for use as a proton conductor is extensively analyzed through the activation energy for ionic conductivity and viscous flow. By combining the results from the various experimental methods, the Walden plot is created. The thereby gained insights into vehicular and cooperative proton transport mechanisms are verified through Pulsed-Field Gradient Spin-Echo (PGSE) NMR measurements. Finally, in electrochemical proof-of-principle experiments, the compatibility of $[DESPA^+][HMDS^-]$ with a Pt catalyst is tested under intermediate temperature PEMFC *operando* conditions.

4.2 Results and Discussions

Parts of this chapter has been published in:

[96] **Schütz, H. M**., Nejrotti, S., Adenusi, H., Mariani, A., Bodo, E., Bonomo, M., Innocenti, A., Barolo, C., Gao, X. & Passerini, S. Superionicity by design: high proton conductivity in a fluorine-free protic ionic liquid. J. Mater. Chem. A 12, 18412–18422 (2024)

4.2.1 Synthesis and Properties of Methanedisulfonic Acid as Precursor for [HMDS$^-$]-based PAcILs

This subchapter will introduce the synthesis of methanedisulfonic acid (H2MDS) as the precursor for PAcILs and gives an overview on its physical properties.

On lab scale methanedisulfonic acid is mainly prepared by sulfonation of acetylene or halomethanes. Historically the sulfonation of acetylene was studied by S. Zeisel, G. Schroeter and W. Muthmann[122–124]. Sulfonation of trihalomethane and dihalomethane was described by A. Strecker[125] and H. J. Backer[70], respectively. Beside these two main routes also different approaches, such as the hydrolysis of the corresponding sulfonyl chloride[126] or the reaction of chlorosulfonic acid with methanesulfonic acid[127] are reported.

An early description of the synthesis of H2MDS by sulfonation of acetylene with concentrated sulfuric acid was provided by S. Zeisel in 1878. Based on some preliminary tests he has concluded, that the reaction product is a thermally stable disulfonic acid. However, because of the low yield, he described the reaction product without further tests wrongly as ethane-1,2-disulphonic acid, which was known by that time[122].
G. Schroeter reported his own analysis on this reaction in 1897. Opposite to the assumption of S. Zeisel G. Schroeter demonstrated, that not the ethane-1,2-disulphonic acid but methanedisulfonic acid is formed. He suggested a reaction mechanism with the inter-mediate 2-oxoethane-1,1-disulfonic acid (Figure 33a)[123].
Independent of Schroeter's work W. Muthmann synthesized the barium, potassium and ammonium salt of the methanedisulfonic acid from acetylene and sulfuric acid in 1898. Based on elementary analyses he proposed the correct chemical structure of the methanedisulfonates[124].

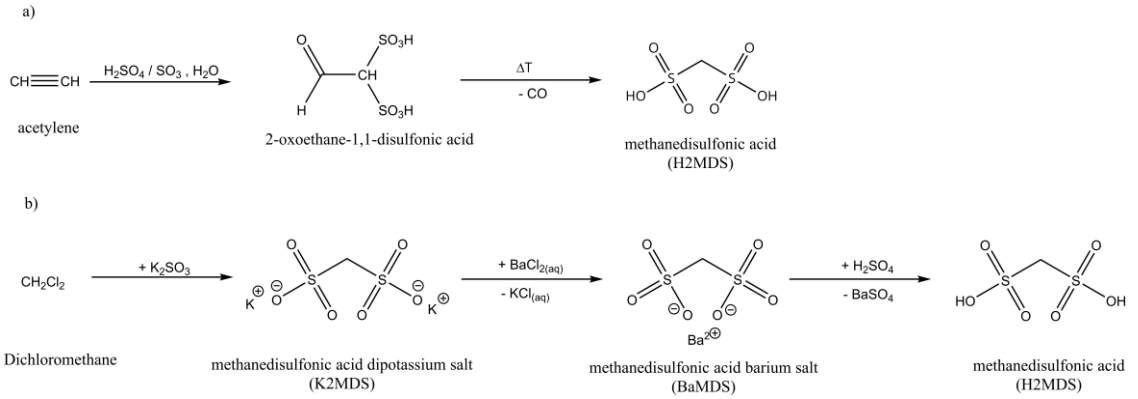

Figure 33 Reaction schemes of the synthesis of methanedisulfonic acid. a) Synthesis from acetylene and sulfuric acid according to G. Schroeter. b) multistep reaction according to H. J. Backer.

While the reaction of acetylene with sulfuric acid gave access to methanedisulfonic acid, it suffers from some drawbacks. Mainly, the large required excess of sulfuric acid causes several issues. First, unreacted sulfuric acid has to be removed after the reaction. This distillation process is time consuming and traces of the sulfuric acid may remain in the product. Second, several side products are formed. Therefore, the yield is reduced and complete removal of these impurities might be challenging.

Parallel to the development of the synthesis from acetylene and sulfuric acid a second synthesis route by the sulfonation of halomethane was invented.

A. Strecker described in 1868 the synthesis of H2MDS by sulfonation of chloroform and iodoform with potassium sulfite[125]. For the mechanism he proposed, that initially the trihalomethane is reduced to the dihalomethane i.e. dichloromethane and diiodomethane.

Therefore, it is not surprising, that 1928 H. J. Backer was able to obtain H2MDS from dichloromethane in a multi-step reaction (Figure 33b). First he prepared barium methanedisulfonate and in a second step it was converted to the acid with sulfuric acid[70]. The reaction equilibrium for the conversion of the barium salt to the acid is strongly on the product side due to the low water solubility of the barium sulfate formed in the process. A quite similar route is subject of the US American patent US 9,440,915 B2 from 2016[71].

Barium methanedisulfonate can be prepared by the reaction of dichloromethane and barium sulfite at 150-160 °C in a pressurized autoclave. The purification process of the barium methanedisulfonate benefits from the low boiling point of the dichloromethane and the possibilities to separate the low-water soluble barium salt from impurities by i.e. filtration, washing and crystallization.

A low-temperature and low-pressure version, which only requires 60-90 °C and (near-) atmospheric pressure is claimed in the patent US 2006/0155142 A1. There a combination of alkali metal iodide and tetraalkylammonium salt is proposed as catalyst[128].

Alternatively, the barium methanedisulfonate can be prepared by an ion exchange from alkaline/alkaline earth salts of methanedisulfonic acid. These salts could be prepared by the same route like the barium salt in the previous paragraph. For this conversion the big difference in the water solubility of the alkaline/alkaline earth methanedisulfonates and the barium methanedisulfonate is used. Addition of an aqueous solution of a barium salt like $BaCl_2$ to an aqueous solution of alkaline/alkaline earth methanedisulfonate leads to an immediate precipitation of the barium methanedisulfonate. The barium methanedisulfonate could then be converted with sulfuric acid to the H2MDS (Figure 33b).

In this thesis methanedisulfonic acid was synthesized applying the previously described method by H. J. Backer[70] and the patent US 9,440,915 B2[71]. As starting material commercially available dipotassium methanedisulfonate (K2MDS) was used. Therefore, the first step in the reaction scheme in Figure 33b) could be omitted. After a proof of principle with the self-synthesized H2MDS additionally a commercial methanedisulfonic acid sample from abcr GmbH Deutschland was purchased for comparison.

An in-depth study of the purity and composition of the self-synthesized and commercial methanedisulfonic acid was performed. Organic compounds were analyzed by CHNS analysis and ^{1}H-NMR spectroscopy. Traces of inorganic species, especially alkaline/ alkaline earth metals, barium and transition metals were determined by inductively coupled plasma optical emission spectroscopy (ICP-OES).

Table 3 CHNS analysis of self-synthesized and commercial methanedisulfonic acid. The values are the average of two measurements. The uncertainty is the maximum error from the two measurements. [(a)] Oxygen was not measured. The mass difference to 100% is considered to be oxygen. [(b)] For the calculation of the chemical formula, all substance quantities were related to the amount of carbon. Therefore, no uncertainty for the number of carbon atoms is given.

	self-synthesized H2MDS			commercial H2MDS (abcr)		
	m / wt%	n in 100 g / mol	formula	m / wt%	n in 100 g / mol	formula
C	5.49±0.03	0.46±0.00	1.00[(b)]	6.90±0.05	0.57±0.00	1.00[(b)]
H	3.71±0.10	3.68±0.10	8.06±0.18	3.37±0.08	3.34±0.08	5.82±0.10
S	30.74±0.07	0.96±0.00	2.10±0.00	33.62±0.09	1.05±0.00	1.83±0.01
O[(a)]	60.07±0.20	3.75±0.01	8.22±0.06	56.11±0.22	3.51±0.01	6.10±0.07

From the CHNS analysis of the self-synthesized H2MDS a sum formula of $CH_8S_2O_8$ was calculated (Table 3). The “additional” H and O atoms compared to the expected structure of $CH_4S_2O_6$ can be explained by an average of two crystal waters per methanedisulfonic acid molecule. Such kind of structure is more accurate described as an acid hydrate.

For other strong acids like trifluoromethanesulfonic acid the tendency to form solid hydrates is well known[129]. This result from the CHNS analysis fits well to the elementary analysis published by H. J. Backer in his original work on the synthesis route. There he already described the methanedisulfonic acid as dihydrate[70]. In 1994 P. Sartori et al. were able to resolve the crystal structure of H2MDS, which was prepared in a similar manner. From these results it can be deducted, that the methanedisulfonic acid dihydrate in its solid state is actually a salt of methanedisulfonate and hydronium, which might be described as $[CH_2(SO_3^-)_2][H_3O^+]_2$ [126].

In the CHNS analysis of the commercial H2MDS sample only about 6 hydrogen atoms per molecular unit were found. This stoichiometry could be represented by the formula $[CH_2(SO_3^-)_2][H_3O^+]_{1.33}$.

However, this formula is not supported by the calculated amount of oxygen. This could be partly explained by the fact, that in the CHNS analysis oxygen is not measured, but the residual mass is assumed to be the oxygen fraction. Therefore, the deviations in all other elements effect the calculated amount of oxygen. Nevertheless, this cannot be the only reason for the relatively large deviation. Although the quantitative statement of the elemental analysis of the commercial H2MDS sample must be treated with caution, it can be stated that the commercial sample contains a significantly lower amount of crystal water compared to the self-synthesized sample. This may be due to a different synthesis route.

The ^{1}H-NMR spectra of the self-synthesized and commercial H2MDS in DMSO-d_6 are shown in Figure 34.

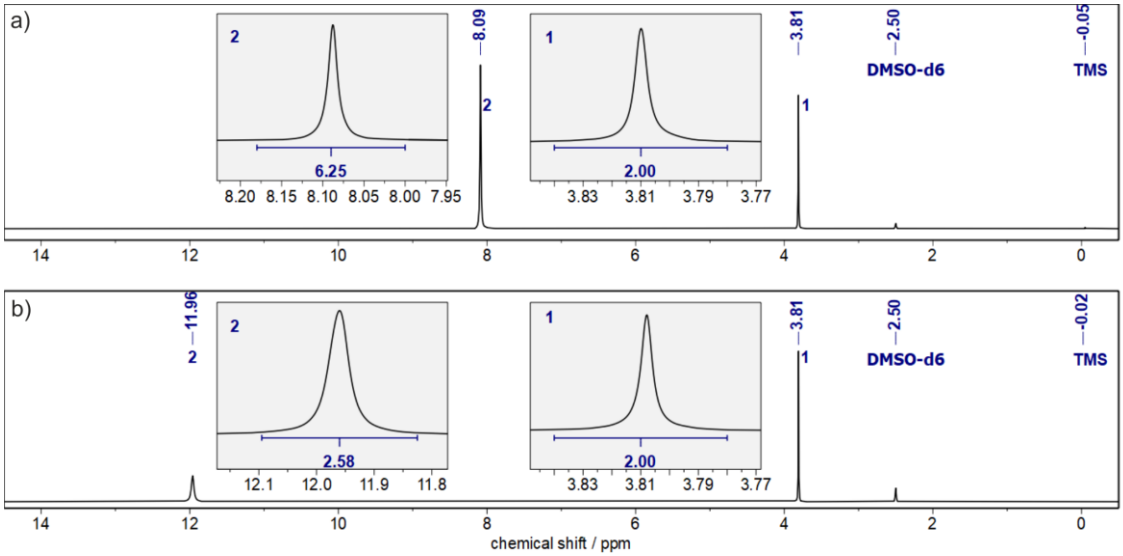

Figure 34 ^{1}H-NMR spectrum of a) self-synthesized H2MDS and b) commercial H2MDS. Both measurements are performed in DMSO-d_6 and the chemical shifts are referenced to the solvent residual peaks. The integral of signal 1 in both spectra is normalized to 2.00.

Only two singlets are visible. The signal at 3.81 ppm in both samples was assigned to the methylene protons in the backbone. The peak position fits to the chemical shift of 3.82 ppm for the methylene group of barium methanedisulfonate in DMSO-d_6 reported by G. Opitz et al. [130].

In the self-synthesized sample, the deshielding of the second signal with a chemical shift of 8.09 ppm is rather small for a sulfonic acid (Figure 34a). The integral has a value of about 6, if the methylene signal is normalized to 2. This does not fit to the expected 2 SO_3H protons but agrees well with the 6 protons from two hydronium ions per acid molecule derived from the elementary analysis. The chemical shift, therefore probably corresponds to the population-weighted averages of chemical shift of the individual species SO_3H, H_3O^+ and H_2O, which are in a fast-dynamic equilibrium. Further details about the phenomenon can be found in the theory part in chapter 1.1

In the ^{1}H-NMR spectra of the commercial H2MDS sample the singlet 2 appears at 11.96 ppm (Figure 34b). Compared to the self-synthesized sample this is signal is much more downfield shifted. If it is assumed that the SO_3H protons have a larger chemical shift than the H_3O^+/H_2O protons, this could be interpreted according to a population-weighted averages of the chemical shifts with a smaller amount of H_3O^+/H_2O i.e. less crystal water in the commercial sample. Indeed, the integral of this signal has only a value of 2.59. If the "additional" portion of the integral (about 0.6) is ascribed to the crystal water this would correspond to about 0.3 water molecules per formula unit. This NMR result of 0.3 water per molecule is quite close to the maximum water content of 0.25 water molecules per acid molecule from the certificate of analysis of the commercial H2MDS sample. The difference between elementary analysis (about 1.33 water molecules per H2MDS) and ^{1}H-NMR (0.3 water molecules per H2MDS) maybe originate from the different experimental conditions. For the NMR measurement the sample was filled in the sample tube inside a dryroom (dew point ≤-60 °C), while the elementary analysis was performed without specific precautions to exclude ambient moisture in the analytical department of Ulm University. So, water uptake during sample preparation and measurement of the elementary analysis cannot be excluded. Also, because of the information in the analysis certificate, the NMR result is weighted more heavily, even though it must be emphasized here that the performed routine NMR experiment without special measurement procedure e.g. ^{13}C decoupling, optimization of delay time etc. is subject to significant measurement uncertainties for quantitative experiments. However, all further calculations in this thesis will be done with the assumption of 2 crystal water per molecule in the self-synthesized sample and 0.25 molecules of crystal water for the commercial H2MDS sample, derived from elementary analysis and/or ^{1}H-NMR spectroscopy.

The ICP-OES results of both self-synthesized and commercial H2MDS are summarized in Table 4. By calibration with a multi-element standard a big variety of main and side group elements were tested (see caption Table 4), but only elements with ≥100 ppmw in at least one material and barium are included in Table 4.

Table 4 Summary of ICP-OES results. A multi-element standard with Al, B, Ba, Bi, Ca, Co, Cu, Fe, K, Li, Mg, Mn, Na, Ni, Pb, TI, Zn was used for the experiments. All elements ≥100 ppmw are reported in the table. Elements with the label n.d. were not detectable. The values are the average of two individual measurement series (each 4 determinations). The uncertainty is the maximum error of the two measurement series. Measurement ID20211104 for the measurement of the commercial and self-synthesized H2MDS and ID20211123 for both PILs

sample	Ca / ppmw	K / ppmw	Na / ppmw	Ba / ppmw
self-synthesized H2MDS	43±12	185±82	78±27	54±39
commercial H2MDS	309±7	n.d.	1185±11	12±4
[$DESPA^+$][$HMDS^-$]	157±5	378±24	583±2	n.d.
[$DESPA^+$][TfO^-]	27±2	400±6	34±1	n.d.

In the self-synthesized H2MDS the largest inorganic impurity from the investigated elements is potassium with 185 ppmw. The potassium probably originates from the starting material dipotassium methanedisulfonate, which was transformed to barium methanedisulfonate in the first synthesis step (Figure 33b). In the commercial H2MDS sample no potassium was detected, and the main impurities are Ca and Na with 309 ppmw and 1185 ppmw, respectively. A special focus is on barium from the intermediate barium methanedisulfonate. Barium ions are particularly undesirable in the final PAcIL not only because of their toxic effect on humans but also because of their possible poisoning effect on the fuel cell catalysts. In both H2MDS samples, only small traces 54 ppmw and 12 ppmw were detected. In the PAcILs synthesized with H2MDS barium was undetectable by ICP-OES.

In summary, the CHNS analysis, ^{1}H-NMR and ICP-OES confirm the successful synthesis of methanedisulfonic acid, with a high purity. The main impurity is water bond as crystal water. For the comparison of self-synthesized and commercial H2MDS sample similar analysis results were obtained. However, the commercial sample contains less crystal water, which might indicate a different synthesis route under anhydrous conditions. The amount of crystal water in the acid was determined, which is important for the synthesis of a stochiometric PAcIL, described in the next subchapter. To complete the physical characterization of the methanedisulfonic acid the melting point will be investigated in the following paragraph.

Methanedisulfonic acid is in comparison to trifluoromethanesulfonic and methanesulfonic acid at room temperature solid. This property offers some benefits for the handling on lab scale, for example when mixing in precise stochiometric amount with a base in the PAcIL synthesis.

Also, some benefits might arise for transport and handling of large amounts on industrial scale. Interestingly for K2MDS and BaMDS no melting points are reported in literature and only for H2MDS values are given, but no further experimental details are provided on the melting point determination of H2MDS in literature. Therefore here, to the authors knowledge, the first differential scanning calorimetry (DSC) study on H2MDS and its precursors the potassium and the barium salt is presented (Figure 35).

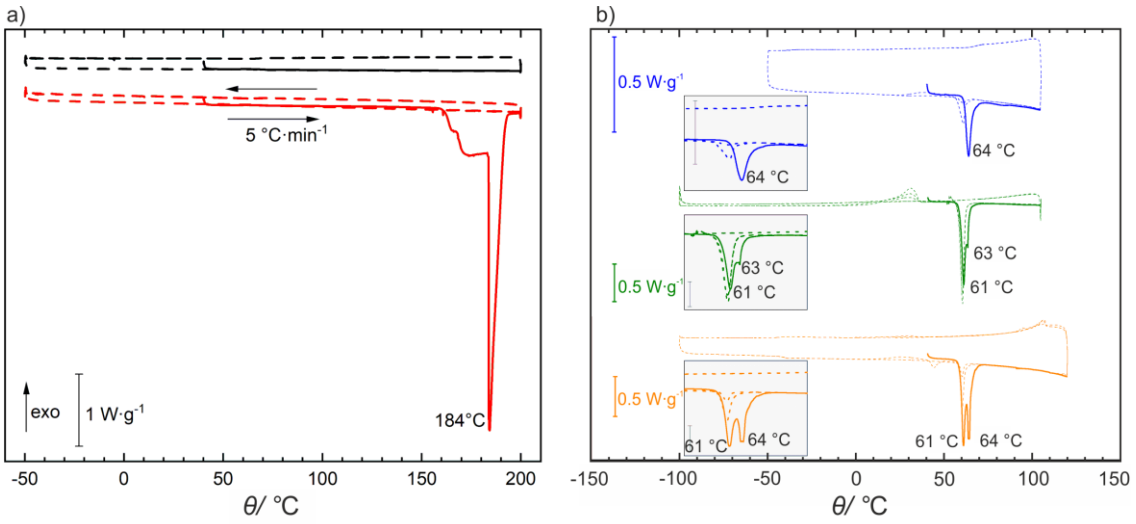

Figure 35 DSC curves of a) K2MDS (black) and BaMDS (red) b) self-synthesized H2MDS (blue), commercial H2MDS (green) and commercial H2MDS measured in a crucible with 50 nm Au-coating (orange). Measurements were performed in aluminum crucibles in a dry air atmosphere, if not otherwise stated. The temperature was ramped with 5 K·min^{-1}. An offset is applied to the curves for clarity. The first heating trace is printed as solid line. Consecutive cycles are displayed as dashed lines. The scale bares in the inserts correspond to 0.5 W·g^{-1}. The peak maxima of the melting peaks were determined with the peak analyzer function in the OriginPro 2019b software.

For K2MDS, the starting material of the synthesis, no melting point was observed in DSC experiments up to 200 °C (Figure 35a). Even for temperatures up to 600 °C no melting point was found for the K2MDS in the Calculated Differential Thermo Analysis (c-DTA), which is presented in Figure 39c). In literature, G. Opitz mentioned that the melting point of BaMDS·2H_2O is >250 °C, but no further details on this statement are provided[130]. For barium methanedisulfonate (BaMDS) a melting point between 179-184 °C was extracted for the first heating ramp in the DSC of different batches. In the consecutive cooling-heating cycles no crystallization or further melting peak was observed. For DSC measurements a difference of about 5 °C between the melting points of different batches is relatively large. It might originate from different water content of the different BaMDS samples. A different water content of the two analyzed BaMDS batches is also supported by the different pronounced first mass loss step at about 160 °C in TGA.

This mass loss might be the dehydration of strong bond water (Figure S 3). In DSC this drying process is not visible, maybe due to suppression of the evaporation in the hermetic sealed DSC crucibles, while the DSC melting peak is not observed in the TGA/c-DTA curves. For the self-synthesized H2MDS a melting point of 64 °C was found in the first heating (top trace Figure 35b). In the commercial H2MDS sample a melting peak at 61 °C with a shoulder at 63 °C was observed (middle trace Figure 35b). In the DSC measurements of the commercial H2MDS with a gold-coated crucible these two melting peaks at 61 °C and 64 °C are even more obvious (bottom trace Figure 35b).

With two molecules of crystal water per formula unit in the self-synthesized sample and about 0.25 in the commercial sample, the two melting peaks might be assigned to the different hydrates. According to this reasoning, the peak at about 64 °C corresponds to the dihydrate and the peak at 61 °C to a specie with lower amount of crystal water. However, all these values are significantly lower than the melting points reported in literature. H. J. Backer determined a melting point of 90.5 °C [70] for H2MDS·2H_2O. A similar value of 100 °C was observed P. Sartori et al.[126]. H. Goldwhite et al. found a much higher melting point of 138-140 °C, but used $SOCl_2$ in DMF for a chemical drying of the sample. Based on base equivalent he claimed, that the melting point corresponds to the water-free H2MDS[131].

Impurities, which might reduce the melting point by their colligative properties, can be ruled out due to the in-depth analysis of the composition of the H2MDS samples presented in the previous section. Another hypothesis for the reduced melting point compared to the literature was a reaction of the strong acid with the aluminum crucible. This might be the difference to melting point measurements with glass capillaries usually performed in organic synthesis and most likely applied in the above cited literature. To test this hypothesis of a reaction between the acid and the aluminum crucible, a 50 nm gold layer was sputter-coated on the aluminum crucible. The quality of the gold layer was analyzed by the lateral distribution of Au Mα1 signal with EDX-SEM and by optical microscopy. Both analytical techniques demonstrated a uniform and defect-free gold layer. In the DSC measurement of the commercial H2MDS with the gold-coated crucible no higher melting point was found and the results obtained with the aluminum crucibles were confirmed (bottom trace Figure 35b).

To further confirm the compared to the literature lower melting point of H2MDS in this thesis, measurements with melting point capillaries were performed. Therefore, samples of the commercial H2MDS were flame-sealed inside a dryroom in glass capillaries. The melting process was then monitored with an optical microscope equipped with a Linkam-heating stage. Between 68-72 °C most crystals were molten (Figure S 4). However, some larger crystals were not completely molten until 113 °C. This first confirms the in comparison to literature lower melting temperature of H2MDS observed in DSC. Second the incongruent melting might justify, why the melting point from melting capillary

experiments could be significantly higher than the DSC measurements and was found in literature at about 100 °C, when the sample is fully molten. Third, the incongruent melting might be related to the different hydrate species in the sample and their distribution.
To complete the study of the melting point of H2MDS an attempt to fully remove the crystal water was made. Crystal water-free H2MDS would not only be relevant from a scientific point of view, but would also allow to prepare completely water-free PAcILs from the acid. During vacuum drying experiments a sublimation process was observed. Inspired from this finding, sublimation was systematic studied with self-synthesized H2MDS and a sublimation apparatus. To exclude any water uptake all operations with open apparatus/sample vials were performed inside a dryroom (dew point ≤-60 °C). At temperatures of 100 °C and a vacuum down to 0.15 mbar sublimation was observed. In addition, the initially melted H2MDS crystallized again under these conditions (Figure 36a). Afterwards different fractions of the sample were collected with a ceramic knife under humidity exclusion and analyzed by ^{1}H-NMR and DSC. For the remaining H2MDS after removal of sublimed compounds (bottom fraction) the ^{1}H-NMR chemical shift of the acidic protons (signal 2) in DMSO-d_6 is 13.64 ppm (Figure 36b bottom). The integral of this peak is 2.13. Both the peak position and the integral value would fit to a nearly water-free H2MDS. By DSC a melting point of 159 °C was found (Figure 36c). This value is much higher than the melting point of the H2MDS before the sublimation experiment. It is similar to the result from H. Goldwhite et al. of 138-140 °C, after chemical drying with $SOCl_2$ in DMF[131]. However, DMF is challenging to remove and therefore might be trapped in the sample prepared by Goldwhite et al. Therefore, it is assumed that the melting point of 159 °C represents the melting point of "pure" H2MDS with only traces of crystal water. Like already discussed in the previous section the NMR chemical shift of the acidic protons (peak 2) is probably the population-weighted average of individual signals from SO_3H, H_3O^+ and H_2O. H_2O and H_3O^+ protons have probably much lower chemical shifts than SO_3H protons. Therefore, a downfield shift of the signal of the acidic protons in this type of sample might correlated with a higher amount of crystal water in the sample. Based on this reasoning it can be assumed that the amount of crystal water increases from the fraction at the rim of the cooling finger with a chemical shift of 11.39 ppm for signal 2 towards the specimen collected at the top of the sublimation devices with a chemical shift of 7.56 ppm. The integral of signal 2 of the H2MDS specimen from the rim of the cooling finger is 3.20. Together with the chemical shift the structure of H2MDS·0.5H_2O is proposed, which would be the hemihydrate. A melting point of 60 °C was determined for H2MDS·0.5H_2O the by DSC (Figure 36d). Together with the DSC measurements from the pristine samples it can be concluded that, H2MDS xH_2O with 0.25≤ x≤2 has a melting point between 60-64 °C. For the sample from the top of the cooling finger the integral value of the acidic protons at 7.56 ppm is 5.60. Both the integral and the chemical shift are similar to the pristine self-synthesized H2MDS in Figure 34a). Therefore, the already described structure with H2MDS·2H_2O can be assumed.

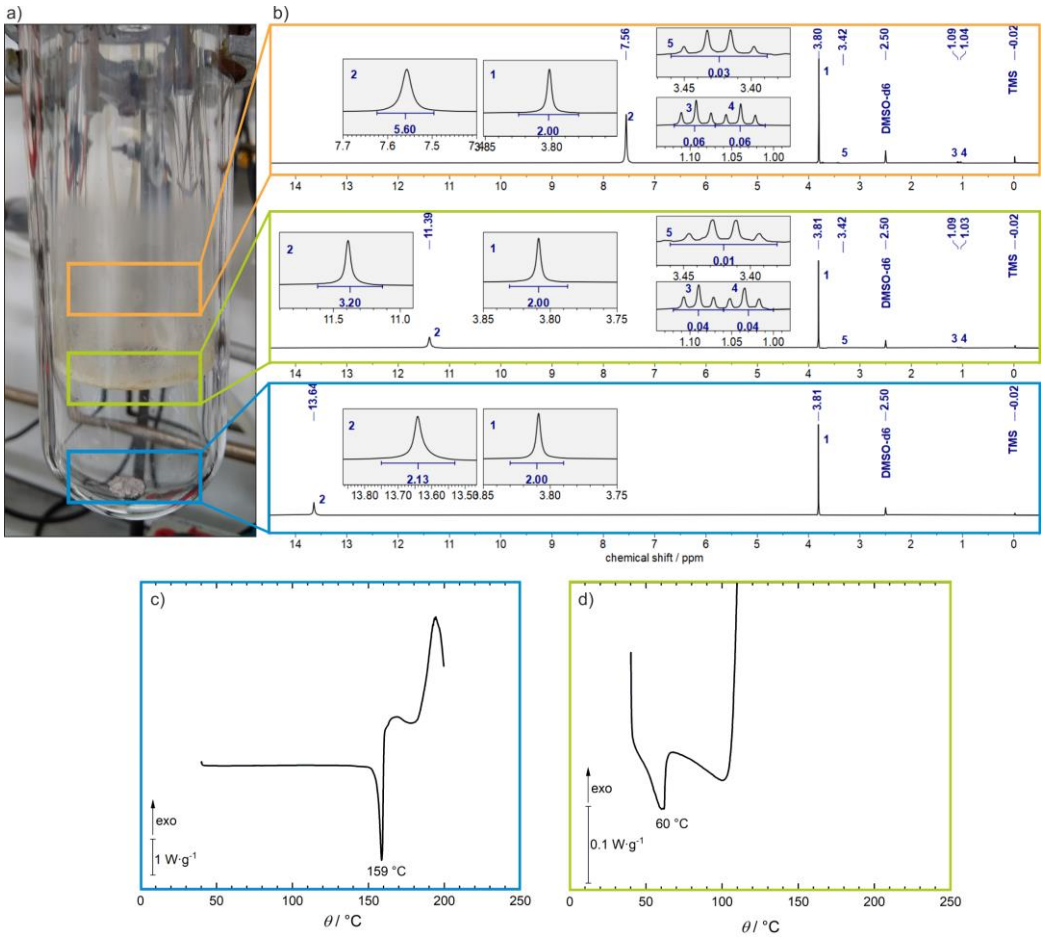

Figure 36 Sublimation experiment of self-synthesized H2MDS. a) Foto of H2MDS in the sublimation device at the end of the sublimation process. b) Displays the ^{1}H-NMR spectra of the corresponding samples in DMSO-d_6. The spectra are referenced to the solvent residual peaks, and the signal 1 of the methylene protons is normalized to 2.00. DSC heating trace of c) the bottom fraction and d) of a sample from the rim of the cooling finger. Samples were heated with 5 K·min^{-1} in a dry air atmosphere in aluminum crucibles. In d) the strong exothermic reaction at about 110 °C is a measurement artefact by a blow up of the crucibel. The peak maxima of the melting peaks were determined with the peak analyzer function in the OriginPro 2019b software.

The sublimation experiment is a successful proof of concept for a potential way to prepare "water-free" H2MDS with a melting point of 159 °C, however, during the process also a partial decomposition of the sample was observed. This can already be seen from the yellowish to brown coloration of the sample at the rim of the cooling finger and some black particles in the unsublimated bottom fraction (Figure 36a). In the ^{1}H-NMR measurements the additional multiplets 3, 4 and 5 in the rim and top fraction indicate the decomposition products (Figure 36b). Therefore, removal of the crystal water under the tested sublimation condition seems to cause partial decomposition of the H2MDS sample. Condition screening or further optimization for the sublimation is beyond the scope of this thesis and was not performed. Therefore, all further experiments were performed with the neat self-synthesized and commercial H2MDS with the corresponding amount of crystal water.

In the last part of this section the molecular volume V_m of methanedisulfonate [MDS^{2-}] and hydrogen methanedisulfonate [$HMDS^-$] will be discussed and compared to the molecular volume of triflate [TfO^-]. The V_m influences many physical properties in solid and liquid state for example the density, melting point and molar conductivity and is therefore useful for the discussion of these properties in ILs and PILs[49,63]. Table 5 summarizes V_m values for the different ions calculated with equation (45) from crystallographic data and with different atom contribution-based theories.

Table 5 Comparison of the molecular volume V_m of hydrogen methanedisulfonate [$HMDS^-$], methanedisulfonate [MDS^{2-}], triflate [TfO^-] anion and [$DESPA^+$] cation. Calculations from crystal structures were performed according to equation (45). All relevant parameters and the references to the publications with the crystal structures can be found in Table S 2. The molecular volume V_m (Hofmann) and V_m (Zhao) were calculated with equation (46) and equation (47), respectively. The single atom contributions used for V_m (Hofmann) and V_m (Zhao) type calculations are summarized in Table S 1.

	[$HMDS^-$]	[MDS^{2-}]	[TfO^-]	[$DESPA^+$]
V_m (crystal structures)/ Å^3	-	119-126	119-140[63]	-
V_m (Hofmann)/ Å^3	148	143	107	260
V_m (Zhao)/ Å^3	114	113	88	187

In the theoretical calculations based on single-atom contributions with the formula of Zhao and Hoffmann, the [$HMDS^-$] anion is larger than [MDS^{2-}] by the value for the additional H-atom. The calculated volume of triflate is significantly smaller than the volume for [$HMDS^-$] or [MDS^{2-}]. This can be explained by the different number of atoms, which contribute to the volume calculations. Triflate consists of 8 atoms, while [$HMDS^-$] and [MDS^{2-}] contain 12 and 11 atoms, respectively. The molecular geometry and effect of the electron cloud in the anions are not taken into consideration by both calculation schemes. The calculation scheme by Zhao et al. is based on the van der Waals volumes for uncharged atoms. The van der Waals volumes for the individual atoms obtained by Hofmann are an average for the different charge states in the crystal structures included in his calculation of the single atom contributions.

Both geometry and charge distribution influence the volume derived from crystal structures. The more striking is the similar volumes of the double charged [MDS^{2-}] and single charged triflate obtained from the crystal structures. For the [$HMDS^-$] anion used in the PAcILs in this thesis no crystal structure is known. However, it is reasonable to assume, that the molecular volume of [$HMDS^-$] is smaller than the volume of [MDS^{2-}]. On the one hand, this can be argued by the general trend, that the size of an anion decreases with decreasing charge. On the other hand, it can be assumed that [$HMDS^-$] in contrast to [MDS^{2-}] can form the intramolecular hydrogen bond shown in Figure 32 and has therefore a more compact structure. Based on the investigation of published crystal structures and the theoretical considerations mentioned above the assumption, that the molecular volume of [$HMDS^-$] is similar to [TfO^-], eventually even slightly smaller, is justified.

4.2.2 Synthesis of [DESPA$^+$][HMDS$^-$]

N,N-diethyl-3-sulfopropan-1-ammonium hydrogen methanedisulfonate [DESPA$^+$][HMDS$^-$] was synthesized in a similar way like the triflate-based PAcILs. Therefore, the strong methanedisulfonic acid (H2MDS) was mixed with the DESPA zwitterion. In contrast to the synthesis with the liquid trifluoromethanesulfonic acid a suitable solvent is required to mix the solid H2MDS with the solid DESPA zwitterion. This solvent should have a high polarity, should be easy to remove after the synthesis i.e. should have a low boiling point and has to be chemical inert under the strong acidic conditions. In the initial try a 1:2 mixture of absolute methanol and ethanol and was used. However, the ^{1}H-NMR spectrum of the reaction product in Figure S 5 shows some traces of impurities. These impurities might originate from an esterification reaction. Such reaction is likely to happen under the strong acidic conditions, especially during the vacuum drying step at temperatures up to 100 °C.

To circumvent this problem finally water was used as solvent. The disadvantage of an aqueous synthesis is the unavoidable relative high amount of residual water in the final PAcIL[95]. However, as discussed in details in the previous subchapter 4.2.1 the self-synthesized H2MDS contains 2 crystal water per unit i.e. about 17 wt% H_2O and the commercial sample with a formula of H2MDS·0.25H_2O still 2.5 wt%. Therefore, a real anhydrous synthesis is not possible and drying steps are required in any case. A common problem for the drying of PILs is the loss of volatile species like amines which are formed by the backreaction from the PIL[95]. In case of [DESPA$^+$][HMDS$^-$] with alkyl groups in both cation and anion the ratio of acid and base can be estimated after the drying process from ^{1}H-NMR spectroscopy. Here it should be clarified, that only the total ratio of the DESPA zwitterion/[DESPA$^+$] to [HMDS$^-$]/H2MDS/[MDS^{2-}] can be estimated by this approach and the different individual species are not distinguishable. The ^{1}H-NMR of the [DESPA$^+$][HMDS$^-$] from aqueous synthesis is displayed in Figure 37a). In the NMR no signals from impurities are detectable. The small sidebands of the peak 2,2', 4 and 6 were already discussed in chapter 3.2.1 together with the peak assignment for the [DESPA$^+$] cation. The 2:6 ratio of the integrals of signal 8 and 1,1' shows that within the limit of detection of ^{1}H-NMR a stochiometric PAcIL was obtained. To achieve a stochiometric PAcIL it is important to consider the amount of crystal water in the H2MDS in the calculation of the required amount of acid.

The signal of the acidic protons at 11.6 ppm is actually a superposition of the peaks of the sulfonic acid in the cation (Proton 7) and in the anion (Proton 9). This is illustrated in the insert by the good agreement of the fit with two Gaussians (green lines, sum pink and residual red). These peaks of the acidic protons will play a major role in chapter 4.2.5 in the study of the proton transfer mechanism by PGSE-NMR measurements.

The ^{1}H-NMR of the neat [DESPA^{+}][HMDS^{-}] sample in a coaxial geometry is displayed in Figure 37b). Here the signal of the protons from the sulfonic acid groups (Peak 7&9) is visible at ~12 ppm. The similar chemical shift of the acidic protons in [DESPA^{+}][HMDS^{-}] and the triflate based-PAcILs with 11-13 ppm (Figure 24) demonstrates that the acidity is comparable. Again, the peak of the acidic protons is a superposition of the two signals from cation and anion. The integral of the ^{1}H signal of the ammonium group (Peak 3) is ~0.8. The small peak 3* at 8.15 ppm in DMSO-d_6 and 5.88 ppm in neat state could be assigned like in subchapter 3.2.1 to the N-H of the 7-membered cyclic form of the [DESPA^{+}] cation[96]. The sum of the integrals of 3 and 3* is >0.8. This show that the majority of the ammonium groups is protonated at 120 °C. The difference is partly related to the uncertainty of the quantitative NMR determination, but might be interpreted by some free amine groups (unprotonated N-atoms) in the thermal equilibrium, too.

In the ICP-OES measurements no significant amount of inorganic impurities, which might affect physical properties like ionic conductivity etc., was found (Table 4). Both NMR and ICP-OES results confirm the successful synthesis of [DESPA^{+}][HMDS^{-}] with sufficient high purity.

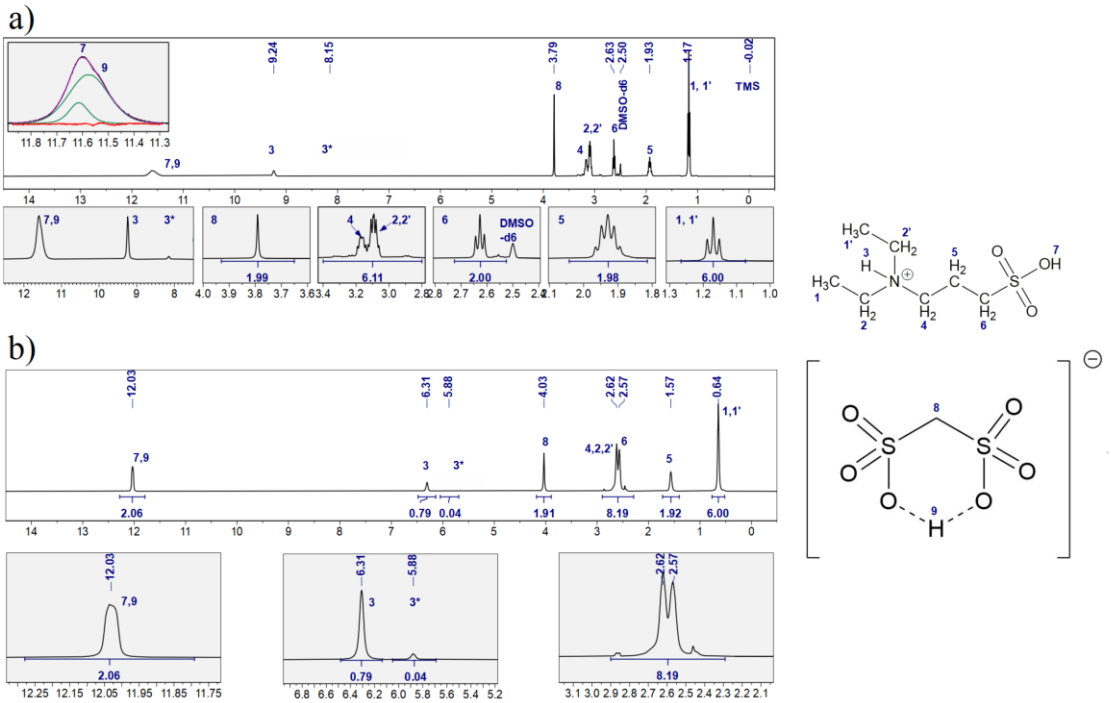

Figure 37 a) ^{1}H-NMR (400 Hz, 295 K) of [DESPA^{+}][HMDS^{-}] in DMSO-d_6 with commercial H2MDS. The spectrum is from the aqueous-synthesized, batch which was used for conductivity, viscosity and density measurement. b) ^{1}H-NMR spectrum (600 Hz, 393 K) of neat [DESPA^{+}][HMDS^{-}] in coaxial geometry with DMSO-d_6 between the capillary and the NMR tube wall. The sample is from an aqueous-synthesized, batch with commercial H2MDS, which was used for the PGSE-NMR measurements. The water content by KF titration is 5483±189 ppmw (n=4). The signal 1,1' is normalized to 6. The spectra are referenced to the solvent residual peak.

4.2.3 Thermal Stability of [DESPA$^+$][HMDS$^-$] and [DESPA$^+$][TfO$^-$]

For the application of PAcILs in an intermediate temperature PEMFC the thermal stability above the designated operation temperature i.e. 120 °C, is crucial. In subchapter 3.2.2 the influence of the cation structure on the thermal stability was study. [DESPA$^+$] and [DEMSPA$^+$] were identified as sufficient thermal stable cation structures for long term operation at 120 °C. In this chapter it will be tested, if the fully fluorinated triflate anion [TfO$^-$] in [DESPA$^+$][TfO$^-$] can be replaced by the fluorine-free hydrogen methanedisulfonate anion [HMDS$^-$] without loss of the thermal stability.

Air is an economical oxygen source for fuel cell operation. Therefore, all thermogravimetric (TG) tests were performed in synthetic air. For dynamic measurements typically, a scan rate of 5 K·min^{-1} was used. The results for [DESPA$^+$][TfO$^-$] and [DESPA$^+$][HMDS$^-$] obtained under these conditions are displayed in Figure 38 a). One common criterion to compare the thermal stability is the temperature, which corresponds to 5% loss of the initial mass (T(5%)). Another criterion is the temperature, which corresponds to the peak maximum (T_{Peak}) in the 1st derivative of the TG (DTG) curve i.e. the temperature with the fasted decomposition rate. Both quantities are summarized in Table 6. For [DESPA$^+$][TfO$^-$] 5% mass loss is reached at about 271 °C. [DESPA$^+$][HMDS$^-$] can be heated to an about 40 °C higher temperature of 311 °C before reaching the T(5%) threshold. In the DTG curve of [DESPA$^+$][TfO$^-$] a peak at about 378 °C is visible. For [DESPA$^+$][HMDS$^-$] two peaks were observed in the DTG curve. The first side-peak appears at 377 °C and the main peak at about 447 °C. Two conclusions can be drawn from these results. First, [DESPA$^+$][HMDS$^-$] seems to be thermally slightly more stable than [DESPA$^+$][TfO$^-$]. Second, the similar peak in DTG curves of the different PAcILs could be an indication that not the anions but the shared [DESPA$^+$] cation structure is the limiting factor for the thermal stability.

Table 6 Evaluation of the TGA and DTG curves displayed in Figure 38 and Figure 39. T(5%): temperature at 5% mass loss. T_{Peak}: temperature at the peak maxima in DTG curves. Bold numbers indicate the most intense DTG peak for each sample. Peak maxima for the T_{Peak} values were determined with the peak analyzer function in the OriginPro 2019b software. [(a)] Broad peaks without pronounced maxima and the given values are only approximations.

Sample name	T(5%) / °C	T_{Peak} / °C
[DESPA$^+$][HMDS$^-$]	311	377, **447**
[DESPA$^+$][TfO$^-$]	271	**378**

Sample name	T(5%) / °C	T_{Peak} / °C
H2MDS	270	290, 299, 491, **539**
K2MDS	396	**404**, 450[(a)]
KTfO	449	**478**
KMS	445	**479**[(a)]
[DESPA] zwitterion	288	**301**, 330[(a)]

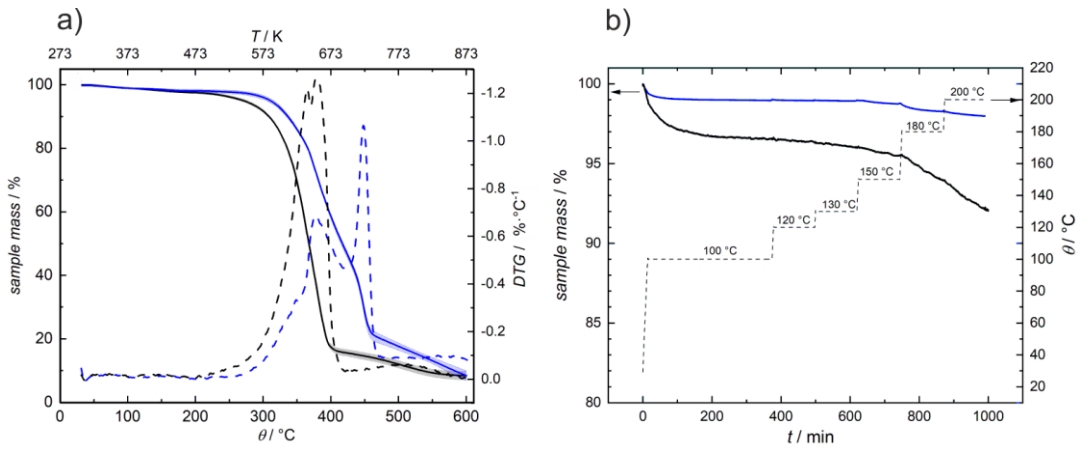

Figure 38 a) dynamic TGA measurements (sold lines) and DTG curves (dashed lines) for [DESPA$^+$][HMDS$^-$](blue) and [DESPA$^+$][TfO$^-$](black). The experiments were performed in synthetic air with a scan rate of 5 K·min^{-1}. Each curve is the average of at least three experiments and the shaded area indicates the maximum error. The water content of [DESPA$^+$][HMDS$^-$] was 8123±546 ppmw and of [DESPA$^+$][TfO$^-$] 12302±153 ppmw by KF titration b) Isothermal TGA of [DESPA$^+$][HMDS$^-$] (blue) and [DESPA$^+$][TfO$^-$] (black) in synthetic air. The experiment with [DESPA$^+$][TfO$^-$] was performed with a TG 209 F1 Libra (Netzsch) and [DESPA$^+$][HMDS$^-$] with a Discovery TGA (TA Instruments).The data of [DESPA$^+$][TfO$^-$] are published in [69]. The water content of [DESPA$^+$][HMDS$^-$] is the same like in a) and of [DESPA$^+$][TfO$^-$]1.89 wt%.

To further investigate if the cation or anion structure is the limiting factor TGA measurements of different precursors and of the potassium salts of the anion structures were performed. Potassium salts were selected due to the commercial availability for all studied anions.

First dipotassium methanedisulfonate (K2MDS), potassium triflate (KTfO) and for completeness potassium mesylate (KMS) were compared. 5% mass loss occurs for the three compounds in the temperature range between 396 – 449 °C i.e. at quite similar temperatures (Table 6). KMS and KTfO show a similar thermal stability with T(5%) of 445 °C and 449 °C, respectively. This similarity is also visualized in the DTG curves in Figure 39 a) where the peak positions for KMS and KTfO are visually identical. The similar thermal stability of the mesylate and triflate illustrates that the fluorination of the methyl group in such structures does not influences the thermal stability significantly. K2MDS has with 396 °C the lowest T(5%) value among the three potassium salts.

However, [DESPA$^+$][HMDS$^-$] not contains the fully deprotonated methanedisulfonate, but the hydrogen methanedisulfonate [HMDS$^-$]. To prepare this compound equimolar amount of aqueous solutions of H2MDS and K2MDS were mixed and the water was evaporated. The DSC curves in Figure S 6 a) and b) show, that a mixed material with heterogeneous composition in the different crystals is obtained. Recrystallisation from water led to needle-shaped crystals of K2MDS (Figure S 6 c). Therefore, TGA measurements of the potassium hydrogen methanedisulfonate (KHMDS) are not possible because KHMDS was synthetically not accessible.

The thermal stability of the [$HMDS^-$] anion can only be estimated from the comparison of the methanedisulfonic acid (H2MDS) and the fully deprotonated dipotassium methanedisulfonate (K2MDS). DTG and TGA curve in Figure 39 a)-c) show, that the stability increases with the deprotonation of the methanedisulfonic acid. It can be assumed that the thermal stability of [$HMDS^-$] lies between the two limiting cases of the fully protonated and deprotonated species. Based on the possible stabilization of [$HMDS^-$] by an intramolecular hydrogen bond and the high charge delocalization (see Figure 32), the thermal stability is postulated similar to the more stable fully deprotonated form.

All the investigated potassium salts of the anions show in comparison with the DESPA zwitterion i.e. the precursor of the cation structure a higher thermal stability (Table 6 and Figure 39). This indicates that the limiting factor for the thermal stability in [$DESPA^+$][$HMDS^-$] might be the cation structure and not the [$HMDS^-$] anion.

The Calculated Differential Thermo Analysis (c-DTA) data in Figure 39 are interesting additional information obtained from the TGA investigation of the potassium salts and DESPA zwitterion. Details on this method are given in theory part about TGA (chapter 1.2.1). Briefly a positive c-DTA signal is generated by an endothermic reaction and a negative signal by an exothermic reaction. By the c-DTA signal processes without mass loss, such as melting processes, which cannot be measured using TGA, can also be observed. The oscillation in the c-DTA signal is cause by the feed-back loop of TGA device, which will adjust the furnace temperature according to the c-DTA signal, to keep the set temperature value. In the c-DTA of the DESPA zwitterion (Figure 39 f) and K2MDS (Figure 39 c) no significant peaks are visible before the main decomposition step. The small signal fluctuation for the DESPA zwitterion between 100-150 °C might be caused by drying of the sample, therefore in the TGA curve a small mass loss step is visible, too. For KTFO and KMS sharp endothermic peaks at 233 °C and 396 °C are visible (Figure 39 d) and e). The c-DTA curves in Figure 39 are the average of three independent measurements, therefore the sharp peaks are probable real features of the samples and no measurement artefacts. The peaks at 233 °C and 396 °C are assigned to the melting points of the potassium triflate and potassium mesylate, respectively. For potassium triflate a melting point between 230-238 °C is reported in literature[132,133], the 233 °C found in this work agree well with the literature values.

For potassium mesylate currently[d] no melting point is given in the Reaxys database or in other publications known to the author of this thesis. Therefore, the report of the melting point of potassium mesylate at 396 °C is worth mentioning here.

[d] retrieved on 29.05.2023 18:00 o‘clock

For H2MDS two peaks are visible in the c-DTA curve before the first decomposition step. The first peak at 68 °C fits to the melting point of the hydrate H2MDS·2H_2O (Figure 35b), while the second peak at 154 °C corresponds to the DSC results for the "water-free" H2MDS (Figure 36c).

The origin of the negative sign of the peak at 154°C in the c-DTA curve, which would correspond to an exothermic reaction, is not yet fully understood. ^{1}H-NMR (Figure 36b) of the sublimated "water-free" H2MDS sample shows some traces from decomposition products. Together with the c-DTA curves this might be a hint, that the melting of H2MDS in absence of water at 154 °C is accompanied by decomposition reactions.

Dynamic TGA experiments, on the one hand, simulate the fast heating of the sample to high end temperatures, which might be the case for an overheating emergency situation. Isothermal experiments on the other hand, can simulate long-term operation. Figure 38b) show the isothermal TGA experiments of [$DESPA^+$][$HMDS^-$] and [$DESPA^+$][TfO^-]. During the heating to 100 °C [$DESPA^+$][$HMDS^-$] losses 1% of its initial mass. This effect is probably the dehydration of the sample with a water content of 8123 ppmw. After the initial mass loss [$DESPA^+$][$HMDS^-$] is stable up to at least 130 °C, which is demonstrated by the flat TG curve. At 150 °C the slope of the TG curve increases. This indicates the onset of the thermal decomposition reaction. With higher temperature the enhanced thermal decomposition rate becomes more obvious by the more pronounced slope of the measurement curve. [$DESPA^+$][TfO^-] losses in the first heating step at 100 °C about 3.4 wt% of its initial mass. This is larger than the water content of 1.89 wt% and could maybe similar to the discussion in subchapter 3.2.2 be explained by the instrumental drift. Afterwards no significant mass loss was observed up to 150 °C. These results demonstrate, the necessity of isothermal measurements for realistic assessment of the thermal stability of ionic liquids. While T5% values of 311 °C and 271 °C for [$DESPA^+$][$HMDS^-$] and [$DESPA^+$][TfO^-], respectively, and T_{Peak} values of about 380 °C from both PAcILs could lead to an overestimation of the thermal stability, the isothermal measurements show the onset of the thermal decomposition for both PAcILs already at 150 °C. However, the value of 150 °C is still 30 °C above the target temperature of 120 °C. Although the safety range for long-term operation is only approx. 30°C, it can be deduced from the dynamic TGA measurements that a short-term thermal load up to over 200°C does not cause decomposition of a larger proportion of the PAcILs. Therefore the thermal stability of the non-fluorinated [$DESPA^+$][$HMDS^-$] like the fluorinated [$DESPA^+$][TfO^-] is sufficient for the application in 120 °C IT-PEMFC.

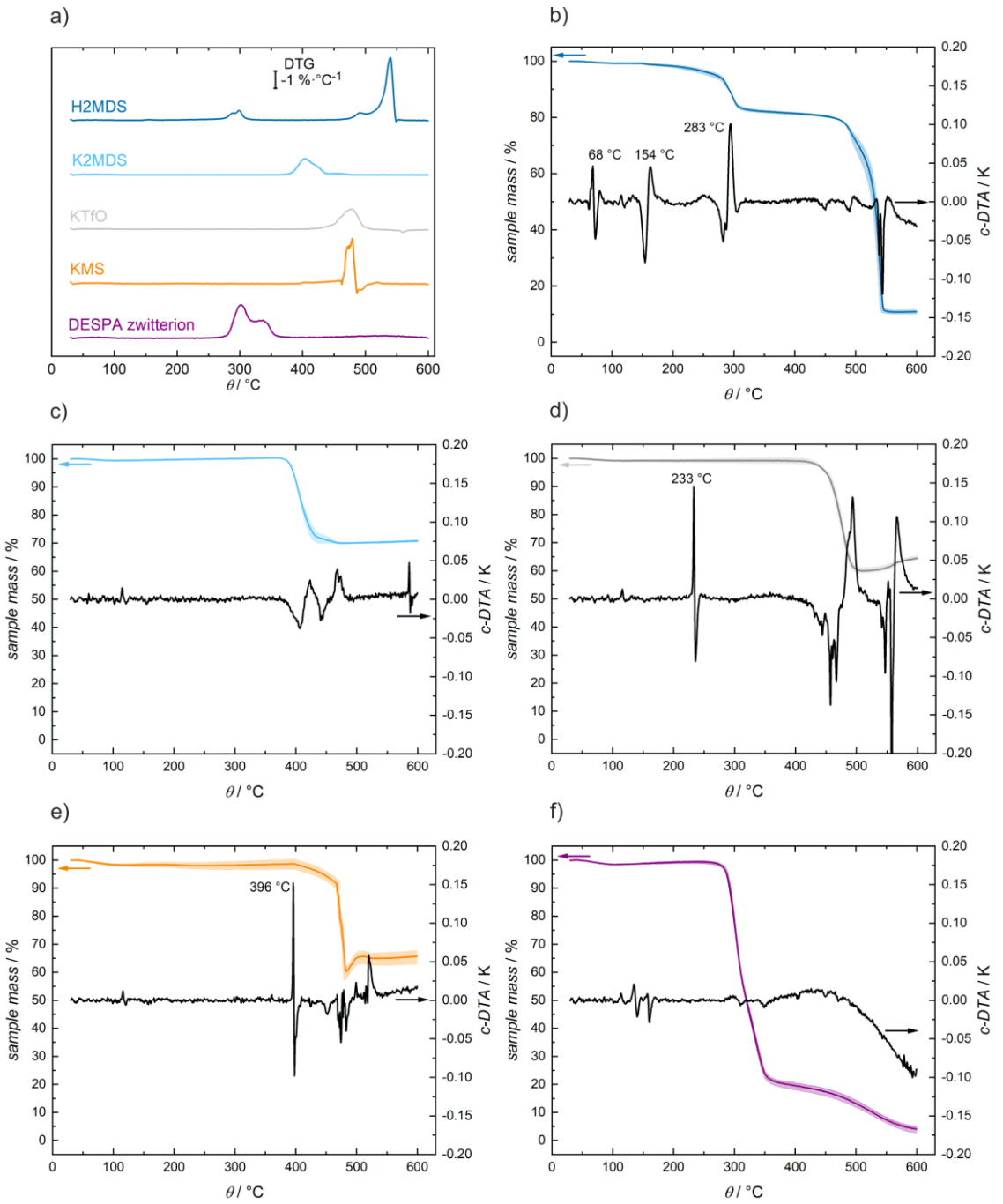

Figure 39 a) DTG traces of methanedisulfonic acid (H2MDS), dipotassium methanedisulfonate (K2MDS), potassium triflate (KTfO), potassium mesylate (KMS) and [DESPA] zwitterion. Figure 39a) is reproduced from Ref. [96] licensed under CC BY 3.0. Dynamic TGA and c-DTA of b) H2MDS, c) K2MDS, d) KTfO, e) KMS and f) [DESPA] zwitterion. All experiments are performed in synthetic air with a scan rate of 5 K·min^{-1} in aluminum crucibles. All DTG, TG and c-DTA curves are an average of three measurements. The maximum error of the TG measurements is indicated by the transparent colored trend channels.

4.2.4 Molecular Interactions and Phase Transitions in [DESPA⁺][HMDS⁻] and [DESPA⁺][TfO⁻]

The density and isobaric thermal expansivity of [DESPA$^+$][TfO$^-$] and [DESPA$^+$][HMDS$^-$] are depicted in Figure 40. The density was measured with the oscillating U-Tube method, which got introduced in subchapter 1.3.2 Density Measurement. The water content of the samples was 0.8 wt% and 1.2 wt% for [DESPA$^+$][HMDS$^-$] and [DESPA$^+$][TfO$^-$], respectively. From literature it is known, that a water content of several weight percent has only a minor impact on the density. For example the density of the ethylammonium nitrate (EAN) with 3 wt% of water is only 0.42% lower than the extrapolated density for the water-free-state[134]. Therefore, it is assumed, that the observed density differences are intrinsic properties of the different PAcILs themselves and are hardly affected by the water content.

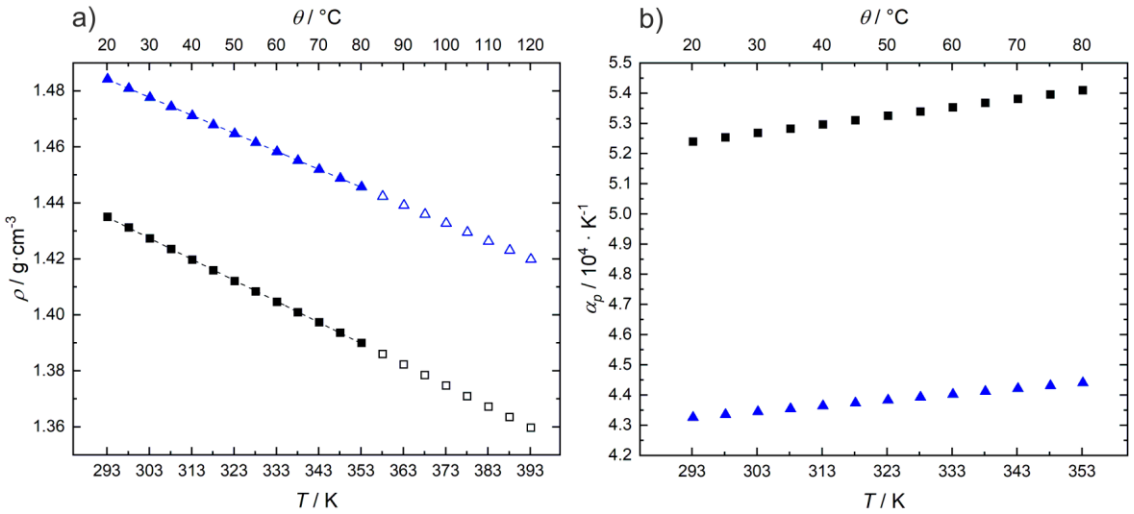

Figure 40 a) Density ρ and b) isobaric thermal expansivity α_P of [DESPA$^+$][HMDS$^-$] (blue triangles) and of [DESPA$^+$][TfO$^-$] (black squares). The dashed lines in a) are linear fits with the parameters in Table 7. The open symbols are extrapolated values based on the linear fits. A water content of 8123±546 ppmw and 12302±153 ppmw was found for [DESPA$^+$][HMDS$^-$]and [DESPA$^+$][TfO$^-$], respectively. The water content is an average of 3 to 4 individual Karl Fischer titrations. The density/ isobaric thermal expansivity values for heating and cooling overlap. The averaged atmospheric pressure during the experiments of [DESPA$^+$][HMDS$^-$] and [DESPA$^+$][TfO$^-$] was 962 hPa. The pressure values are taken from the observation station 232 of the "Deutscher Wetterdienst". The internal measurement identifications for [DESPA$^+$][HMDS$^-$] and [DESPA$^+$][TfO$^-$] are ID20210623 and ID20190708, respectively.

For both [DESPA$^+$][TfO$^-$] and [DESPA$^+$][HMDS$^-$] the density drops linearly with increasing temperature. This decrease of density could be understood in terms of the thermal volume expansion upon heating. The parameters for a linear fit of the data are summarized in Table 7. Based on this linear fit the density of both PAcILs can be extrapolated beyond the maximum temperature of the experimental set up of 80 °C to 120 °C, the target temperature for the IT-PEMFC application. The extrapolated values are displayed as open symbols in Figure 40a).

Table 7 Parameters of the linear fit of the temperature dependency of the density ρ for [DESPA$^+$][HMDS$^-$] and [DESPA$^+$][TfO$^-$] in Figure 40. The fitting equation is $\rho=a+b\cdot T$ with the intercept a and slope b and the thermodynamic temperature T in K.

	Slope + uncertainty of the fit / g·cm^{-3}·K^{-1}	Intercept + uncertainty of the fit / g·cm^{-3}	Adjusted R^2
[DESPA$^+$][HMDS$^-$]	(-6.42±0.01)·10^{-4}	1.6722±0.0005	0.99994
[DESPA$^+$][TfO$^-$]	(-7.52±0.02)·10^{-4}	1.6552±0.0007	0.99999

At 120 °C the extrapolated density of [DESPA$^+$][TfO$^-$] is 1.36 g·cm^{-3} and for [DESPA$^+$][HMDS$^-$] 1.42 g·cm^{-3}. Therefore the density of [DESPA$^+$][HMDS$^-$] is about 4% larger than of [DESPA$^+$][TfO$^-$]. This difference is quite constant over the whole investigated temperature range. On explanation for the larger density of [DESPA$^+$][HMDS$^-$] could be the about 15% larger molecular mass of the [HMDS$^-$] anion (175.15 g·mol^{-1})[e] compared to the [TfO$^-$] anion (149.06 g·mol^{-1}). However, this is only valid, if the molecular volumes of the two types of ions are comparable. Different calculated values for the molecular volume of [HMDS$^-$] and [TfO$^-$] are displayed in Table 5 und were discussed in the corresponding section. Based on these data it can be assumed that both ions have comparable molecular volumes, and that the density differences originate from the different molecular weight of the anions and different packing densities in the PAcILs.

To get further inside in the intermolecular interactions in the PAcILs the isobaric thermal expansivity α_P was calculated with equation (15) from the temperature-dependent density data (Figure 40b). For [DESPA$^+$][HMDS$^-$] and [DESPA$^+$][TfO$^-$] α_P values between 4.3-4.4·10^{-4} K^{-1} and 5.2-5.4·10^{-4} K^{-1} were observed between 20-80 °C, respectively. These α_P values are more similar to melts of simple inorganic salts (~2-5·10^{-4} K^{-1})[135], than to common aprotic ILs like imidazolium/ pyrrolidinium-based ones (~6-8·10^{-4} K^{-1})[f]. This similarity indicates rather strong interactions in [DESPA$^+$][HMDS$^-$] and [DESPA$^+$][TfO$^-$]. In the whole investigated temperature range α_P of [DESPA$^+$][HMDS$^-$] is of about 1·10^{-4} K^{-1} smaller than of [DESPA$^+$][TfO$^-$]. This difference is significant[g] and might originate from different molecular interactions in the two PAcILs. The [HMDS$^-$] anion has in contrast to the [TfO$^-$] anion a hydrogen atom, which could contribute to the hydrogen bonds. This might lead to a more pronounced hydrogen-bond network in [DESPA$^+$][HMDS$^-$] compared to [DESPA$^+$][TfO$^-$]. The more ridged hydrogen-bond network counteracts the thermal expansion i.e. leads to a smaller isobaric thermal expansivity. A similar effect was observed by us before for the comparison of the hydrogensulfate [HSO$_4^-$] and [TfO$^-$] anion. Like the [HMDS$^-$] anion [HSO$_4^-$] could donate a hydrogen bond.

[e] The molecular weight was calculated with "ChemDraw Professional Version 16.0.1.4 (77)".
[f] For some imidazolium and pyrrolidinium-based ILs α_P values were calculated by the author of this thesis and are displayed in Table S 3 and Table S 4 on page 153-154 in the appendix.
[g] See gaussian error propagation in the appendix page 155 in equation (53).

For both ILs with the N,N-Diethyl-N-methyl-3-sulfopropan-1-ammonium [DEMSPA$^+$] and [DESPA$^+$] cation the isobaric thermal expansivity is significantly smaller for the [HSO_4^-] based PAcILs compared to the [TfO^-]-based ones [69]. Interestingly the α_P values for [DESPA$^+$][$HMDS^-$] are similar to the values of about $4.3 \cdot 10^{-4}$ K^{-1} for [DESPA$^+$][HSO_4^-] of our previous study.

In general, the formation of different solid/liquid phases are directly related with the density and the molecular interactions in an IL. Strong interactions between the ions might result in crystallization. Such a liquid-solid transition would be unfavorable for the fuel cell applications and therefore would limit the possible range of operation temperatures. ILs, in which crystallization is prevented by steric demanding building blocks and charge delocalization, might vitrify in the temperature range of the experimental glass-transition temperature T_g. For ILs the glass transition is often observed at temperature below -40 °C[49].

The change in mechanical and transport properties at such low temperatures might not influence common applications. However, the investigation of the glass transition is a tool to probe the interactions in ILs and helps to enhance the fundamental understanding of their liquid structure. In addition, by considering the T_g the conductivity and viscosity of ILs can be compared according to the principle of corresponding states, which will be discussed in subchapter 4.2.5.

In Figure 41a) the differential scanning calorimetry (DSC) curves of [DESPA$^+$][$HMDS^-$] and [DESPA$^+$][TfO^-] are displayed. The flatness of the heating trace of [DESPA$^+$][$HMDS^-$], when it approaches the high-temperature end at 100 °C shows that the PAcIL is like [DESPA$^+$][TfO^-] thermally stable under the experimental conditions. This is further demonstrated by the overlap of the 2^{end} and 3rd cycle displayed in Figure 41b). In this context it should stressed, that the DSC samples are measured in an atmosphere of dry air. The air inside the hermetic-sealed aluminum crucible originates from the DSC sample preparation in a dryroom (dew point ≤-60 °C). Both findings about the thermal stability agree well with the TGA results of subchapter 4.2.3.

For both PAcILs no crystallization or melting peak is visible within the whole temperature range from -120 °C to 100° C. The steps in in the heating and cooling traces of [DESPA$^+$][$HMDS^-$] and [DESPA$^+$][TfO^-] originate from the transfer of the samples from the liquid state to an amorphous glass. The heat capacity C_p[h] drops significantly when the translational motions freeze during this liquid-solid transition, causing the above-mentioned step-like feature in the DSC curve.

[h] Here the heat capacity for constant pressure C_P is used. The same is true for the heat capacity at constant volume C_v.

In contrast to melting and crystallization processes, which occur at well-defined temperatures the formation of the glass, i.e. vitrification, is a more gradual process. Despite the relative broad temperature range covered by a glass transition, different widely accepted evaluation schemes exist to assign the single temperature T_g to the glass transition. Popular among these methods is the so-called mid-point method according to DIN 51007. In this method the glass-transition temperature is defined as the temperature for which the measured curve is equidistant between the upper and lower tangents i.e. the tangents before and after the step in the DSC curve. The application of this method is impeded by the well-pronounced enthalpy relaxation peak in [$DESPA^+$][$HMDS^-$] (Figure 41c).

The enthalpy relaxation peak depends on the thermal history of the sample, especially on the ratio of the heating and cooling rate and the time the sample rests at a temperature below T_g. Therefore, by variation of the experimental procedure the enthalpy relaxation peak can be mitigated. In Figure 41d) the heating trace of [$DESPA^+$][$HMDS^-$] with 10 °C·min^{-1} is displayed. Prior to the heating the sample was cooled with 20 °C·min^{-1} to -80 °C and kept at this temperature for 5 minutes. Due to the faster cooling than heating and the shorter time at temperature below the T_g the enthalpy relaxation peak is suppressed.

However, the altered experimental conditions will result in a different value for the glass-transition temperature (No. 1 and 2 in Table 8 with the modified mid-point method). Therefore, to be consistent with the other experiments in this thesis instead of a change in the experimental method the analysis procedure was adjusted. Deviating from the mid-point method in DIN 51007 linear baselines before and after the glass transition were used, instead of tangents. The results for different [$DESPA^+$][$HMDS^-$] and [$DESPA^+$][TfO^-] samples are summarized in Table 8.

The maximum uncertainty for the T_g determined from the first 3 cycles is better than 0.5 °C. This demonstrates the good reproducibility with one sample at one day. The day to day reproducibility of the T_g determination was tested for the [$DESPA^+$][TfO^-] sample (see No. 3 and 4 in Table 8). Here the T_g values from the heating trace agree within the measurement uncertainty for the different DSC cycles.

For the sake of completeness additionally the T_g values from the cooling traces are listed in Table 8. In general, the T_g values from the cooling traces are lower than from the heating traces. This dependency on the scan direction might originate from the slow thermal equilibration of the samples around the T_g.

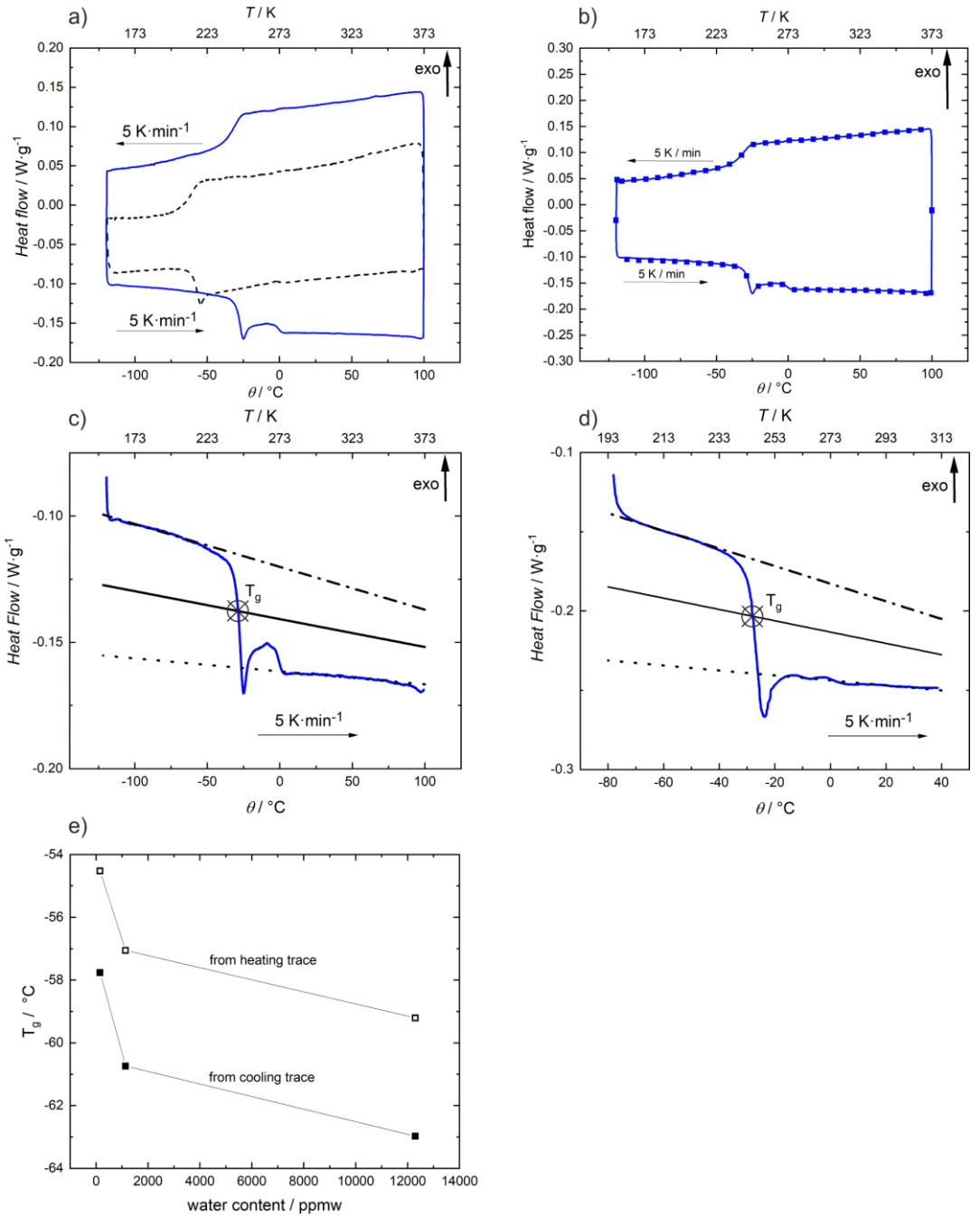

Figure 41 a) 2nd cycle of DSC measurement of [DESPA+][HMDS-] (blue solid line) and [DESPA+][TfO-] (black dashed line). b) Overlay 2nd and 3rd DSC cycle of [DESPA+][HMDS-], line and symbols, respectively. Only every 1000 data points are shown as symbol for clarity. c) Zoom of the heating trace of [DESPA+][HMDS-] (blue solid line) with linear upper (black point-dash line) and lower baseline (black pointed line) of the T_g. The bisector of the two baselines is drawn as black solid line and the intersection with the DSC trace i.e. the T_g is marked by the crosshairs. Figure 41c) is reproduced from Ref. [96] licensed under CC BY 3.0. The experiments a)-c) are performed with 5 K·min-1 heating/cooling rate. The temperature at the reversing points -120 °C and 100 °C was held for 30 min. d) Zoom of the heating trace of [DESPA+][HMDS-] (blue solid line) with 10 K·min-1 heating rate. The cooling rate was 20 K·min-1 and samples was kept for 5 min at the vertex of -80 °C. The lines and marks are the same like in c). e) Plot of the T_g of [DESPA+][TfO-] over the water content of the sample. In e) the lines are just a guide to the eye. The curves of [DESPA+][HMDS-] in a)-c) corresponds to No.1 in Table 8 and in d) to No.2. [DESPA+][TfO-] in a) and e) corresponds to No.3 and No.3, 5, 6 , respectively.

Table 8 Glass-transition temperature T_g and water content of [DESPA$^+$][HMDS$^-$] and [DESPA$^+$][TfO$^-$]. The T_g values were obtained with the modified mid-point method as average of 3 heating and cooling traces as annotated. The water content is the average of "n" individual coulometric Karl Fischer titrations. All uncertainties are the maximum errors. The scan rate in all DSC measurements of the T_g was 5 K·min^{-1} beside No.2. There the cooling and heating was performed with 20 K·min^{-1} and 10 K·min^{-1}, respectively. The temperature at the reversal points of -120 °C and 100 °C was maintained for 30 minutes in all experiments except No.2. In No. 2, the temperatures at the vertex points of -80 °C and 40 °C was maintained for only 5 minutes. The internal identifiers of the experiments from No.1 to No.6 for DSC are ID20211025, ID20211103, ID20211115, ID20211123, ID20220301, ID20220429. For the Karl Fischer titrations the internal identifiers are No.1 ID2021082, No. 2 ID20210827, No.3&4 top ID20190404, No.3&4 bottom ID20220112, No.5 ID20220208, No.6 ID20220413.

No.	Sample name	$T_g \pm \Delta_{max}$ / °C (Heating trace)	$T_g \pm \Delta_{max}$ / °C (Cooling trace)	$H_2O \pm \Delta_{max}$ / ppmw
1	[DESPA$^+$][HMDS$^-$]	-28.8±0.1	-33.0±0.4	4634±1 (n=2)
2	[DESPA$^+$][HMDS$^-$]	-27.8±0.2	-29.9±0.2	4634±1 (n=2)
3	[DESPA$^+$][TfO$^-$]	-58.9±0.3	-64.2±0.2	12302±153 (n=4) 12599± 187 (n=2)
4	[DESPA$^+$][TfO$^-$] repetition	-59.2±0.1	-63.0±0.2	12302±153 (n=4) 12599± 187 (n=2)
5	[DESPA$^+$][TfO$^-$] IoLiTec	-57.1±0.04	-60.7±0.2	1140.3 (n=3)
6	[DESPA$^+$][TfO$^-$] 3. batch	-54.5±0.1	-57.8±0.04	155±4 (n=2)

The T_g of [DESPA$^+$][HMDS$^-$] at about -29 °C is significant higher than the T_g of [DESPA$^+$][TfO$^-$] at about -59 °C. To exclude that this large difference of about 30 °C originates from the slightly different water content (see the water content in Table 8) [DESPA$^+$][TfO$^-$] with a water content between 160 to 12000 ppmw was investigated. Despite the 2 orders of magnitudes different water content the glass-transition temperature T_g in the [DESPA$^+$][TfO$^-$] samples is only lowered by less than 6 °C (see Figure 41e) and Table 8 No. 3-6). This finding agrees with published results[136] and confirms, that the difference in T_g of [DESPA$^+$][HMDS$^-$] and [DESPA$^+$][TfO$^-$] is related to the different anions in the PAcILs and not to the water content. In agreement with the smaller isobaric thermal expansivity α_P the much higher T_g in [DESPA$^+$][HMDS$^-$] compared to [DESPA$^+$][TfO$^-$] might be interpreted as another indication for a more pronounced hydrogen-bond network in [DESPA$^+$][HMDS$^-$].

Based on the DSC results it can be expected that [DESPA$^+$][HMDS$^-$] stays liquid inside a fuel cell, if the temperature not drops below -28 °C. A temperature of -28 °C is reached in the moderate climatic zones with high population density only in exceptional weather conditions. To buffer these temperature peaks, the fuel cell can be enclosed by an insulation layer, for example. Therefore, based on the thermal stability window and the liquid range [DESPA$^+$][HMDS$^-$] seems suitable for IT-PEMFC application with a storage and operation between ambient conditions and 120 °C.

4.2.5 Transport Properties and Proton Conductivity in [DESPA$^+$][HMDS$^-$] and [DESPA$^+$][TfO$^-$]

For a possible application of the PAcILs in the membrane of a PEM fuel cell as proton conducting medium the transport properties and here especially the proton transfer is of crucial importance. Therefore, in this chapter first the viscous flow (theory subchapter 1.3.3) and ionic conductivity (theory subchapter 1.4.1) are discussed, before the transport properties are analyzed in details with the formalism of the Walden plot (theory subchapter 1.4.2). Finally, in cooperation with Dr. S. Nejrotti and M. Bonomo from the MOF group at the University of Turin, the diffusion coefficients are measured with Pulsed-Field Gradient Spin-Echo (PGSE) NMR experiments (theory subchapter 1.1) to verify the conclusions drawn from the Vogel-Fulcher-Tammann-Hesse (VFTH) fittings (theory subchapter 1.3.3) and analysis of the Walden plot.

Before measuring the temperature-dependent dynamic viscosity η of [DESPA$^+$][HMDS$^-$] and of [DESPA$^+$][TfO$^-$] it was test if the PAcILs behave under the investigated conditions as Newtonian fluids, i.e. if the dynamic viscosity is independent of the applied shear rate. At 80 °C, the experimental upper limit[i], Newtonian behavior was observed for [DESPA$^+$][HMDS$^-$] within the whole investigated shear rate range from 1-100 s^{-1} (Figure 48e) on page 143. At 20 °C the shear rate limit was 80 s^{-1} due to the high viscosity of the PAcIL and the specifications of the rheometer. Again, the viscosity of the PAcIL was fairly constant and only a change of about 2.6%, which is within the range of estimated measurement uncertainty, occurred when the shear rate was increased step wise from 1-80 s^{-1}. Therefore [DESPA$^+$][HMDS$^-$] is a Newtonian fluid under the investigated conditions and a constant shear rate of 10 s^{-1} was selected for further temperature-dependent experiments. [DESPA$^+$][TfO$^-$] shows a much more complex behavior including shear-thinning, which gets discussed in details in the chapter 6 “Addendum: viscosity and rheology in ionic liquids”. Figure 50 on page 145 displays the shear rate-dependent dynamic viscosity η of [DESPA$^+$][TfO$^-$] obtained both from linear shear rate sweep (solid line) and step wise increase of shear rate with rest periods between the steps (symbols). This graph of [DESPA$^+$][TfO$^-$] displays a Newtonian plateau for low shear rates, where the dynamic viscosity corresponds in good approximation to the hypothetical viscosity at zero shear η(0). Therefore for [DESPA$^+$][TfO$^-$] a shear rate of 10 s^{-1} was selected, too. This shear rate on the one hand lies within the Newtonian plateau and on the other hand it is the same shear rate like for the experiments with [DESPA$^+$][HMDS$^-$].

[i] A specially manufactured Teflon-coated cone-plate measurement geometry from Anton Paar was used for the measurements with some of the strong acidic PAcILs. To connect the Teflon with the stainless steel-base body an interlayer of confidential chemical composition was used. This interlayer was the limiting factor for thermal and chemical stability of the set-up.

The dynamic viscosity of [DESPA$^+$][HMDS$^-$] (blue triangles, 4634 ppmw H_2O) and [DESPA$^+$][TfO$^-$] (black squares, 18388 ppmw H_2O) at a shear rate of 10 s^{-1} are plotted in Figure 42.

The experimental uncertainty between a heating and consecutive cooling is smaller than the symbol size in the figure. At 25 °C [DESPA$^+$][HMDS$^-$] has an about 60 times higher viscosity compared to [DESPA$^+$][TfO$^-$]. The measured viscosity results were extrapolated based on a Vogel-Fulcher-Tammann-Hesse (VFTH) fit to 120° C, the designated target temperature for fuel cell operation. At 120 °C the viscosity of [DESPA$^+$][HMDS$^-$] is only about 4 times the extrapolated viscosity of [DESPA$^+$][TfO$^-$].

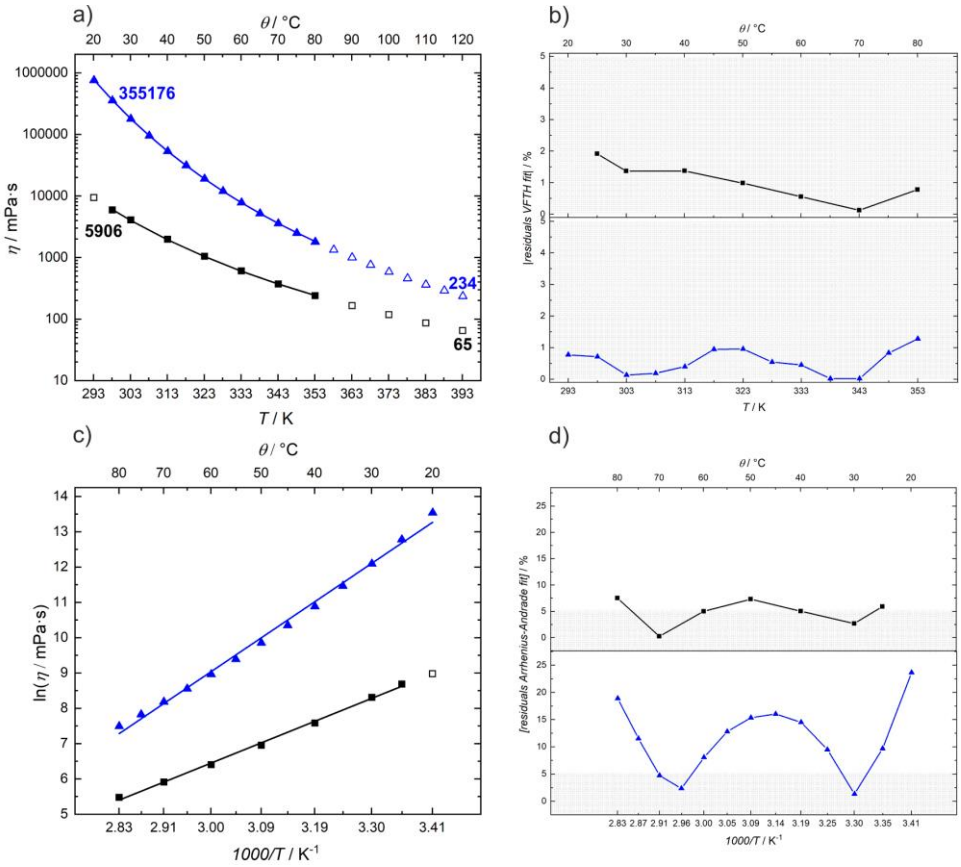

Figure 42 Dynamic viscosity at 10 s^{-1} for[DESPA$^+$][HMDS$^-$] (blue triangles, 4634±1 ppmw H_2O) and [DESPA$^+$][TfO$^-$] (black squares 18388 ppmw H_2O). Each symbol represents the average of at least 30 individual data points. The plot η over the absolute temperture with a logarythmic scaled y-axis is displayed in a). The solid lines are VFTH fits according to equation (25) through the experimental values (solid symbols). The fiting parameters are printed in Table 9. The open symbols are an extrapolation with these VTFH fits. The numbers close to the symbols correspond to the viscosity values at 25 °C and 120 °C. In c) the results are represented in a linearized Arrhenius-Andrade plot. Here the solid lines are a linear fits through the experimental data (solid symbols) according to equation (23). For [DESPA$^+$][TfO$^-$] an extrapolation with this linear fit for 20 °C (open square) is shown to ease the comparison between the two data sets. In b) and d) the absolute residuals in % between the fits and experimental data in a) and c) are displayed, respectivly. The residuals were calculated by ($|value_{exp}$-$value_{fit}|/value_{exp}$)·100. "$value_{exp}$" and "$value_{fit}$" are the experimental values or calculated with the fitting equations, respectivly. The lines connecting the symbols in the residual plots are only guides to the eyes. The 0-5% range in the residual plots is marked by dots (gray color) to ease the comparison between b) and d).

The higher viscosity might be related to stronger intermolecular interactions in [DESPA$^+$][HMDS$^-$] compared to [DESPA$^+$][TfO$^-$], which were already discussed in the context of density and isobaric thermal expansivity α_P in chapter 4.2.4. The Arrhenius-Andrade and Vogel-Fulcher-Tammann-Hesse (VFTH) fits of the viscosity, will be discussed later in this chapter together with the fittings of the conductivity results.

A plot of the ionic conductivity σ of [DESPA$^+$][HMDS$^-$] (blue triangles, 4634 ppmw H_2O), and of [DESPA$^+$][TfO$^-$], one sample from IoLiTec Ionic Liquids Technologies GmbH (black circles, 1140 ppmw H_2O) and one self-synthesized sample (black squares, 12302 ppmw H_2O), are displayed in Figure 43a). The experimental uncertainty of the ionic conductivity values from heating and cooling cycles obtained with different measurement cells of [DESPA$^+$][HMDS$^-$] and [DESPA$^+$][TfO$^-$] is in the range of the symbol size in Figure 43a).

At 20 °C the ionic conductivity of both [DESPA$^+$][TfO$^-$] samples is about one order of magnitude higher than from [DESPA$^+$][HMDS$^-$] i.e. about 34 µS·cm^{-1} / 51 µS·cm^{-1} compare to about 4 µS·cm^{-1}. One explanation for this lower conductivity might be the significant higher viscosity in the fluorine-free [DESPA$^+$][HMDS$^-$] compared to the [DESPA$^+$][TfO$^-$] (see Figure 42). With increasing temperature, the difference in conductivity between the two PAcILs decreases and at 120 °C, the designated operation temperature of the IT-PEMFC application, the values are comparable i.e. 4.41 mS·cm^{-1} / 5.76 mS·cm^{-1} to 2.93 mS·cm^{-1} for the two different [DESPA$^+$][TfO$^-$] and the [DESPA$^+$][HMDS$^-$] samples, respectively.

The effect of the water content is illustrated by the two [DESPA$^+$][TfO$^-$] samples with about 1140 ppmw and 12302 ppmw H_2O. A difference in ionic conductivity of about 45% is observed between the two samples. Considering these data it is unlikely that the slightly different water content between the commercial [DESPA$^+$][TfO$^-$] and the [DESPA$^+$][HMDS$^-$] sample is the main cause for the observed one order of magnitude different ionic conductivity at 20 °C, especially because the water content in the [DESPA$^+$][HMDS$^-$] is slightly higher than in the commercial [DESPA$^+$][TfO$^-$] sample, but its ionic conductivity is significantly lower.

It is a well-known strategy to decrease the glass-transition temperature T_g to obtain higher conductive materials. Therefore the conductivity of [DESPA$^+$][HMDS$^-$] is rather unexpected high, when considering its among ILs high T_g of about -29° C. This is illustrated by the T_g-scaled Arrhenius plot in Figure 43f). Here the ionic conductivity of [DESPA$^+$][HMDS$^-$] is for the same T_g/T ratios about 0.5 decades higher compared to [DESPA$^+$][TfO$^-$]. This unexpected high conductivity for such a viscous liquid might be a weak indication for a conduction mechanism, which is not restricted by the viscous flow,

like a cooperative mechanism. In conclusion the conductivity of [DESPA$^+$][HMDS$^-$] at elevated temperatures like 120 °C look promising from an application point of view.

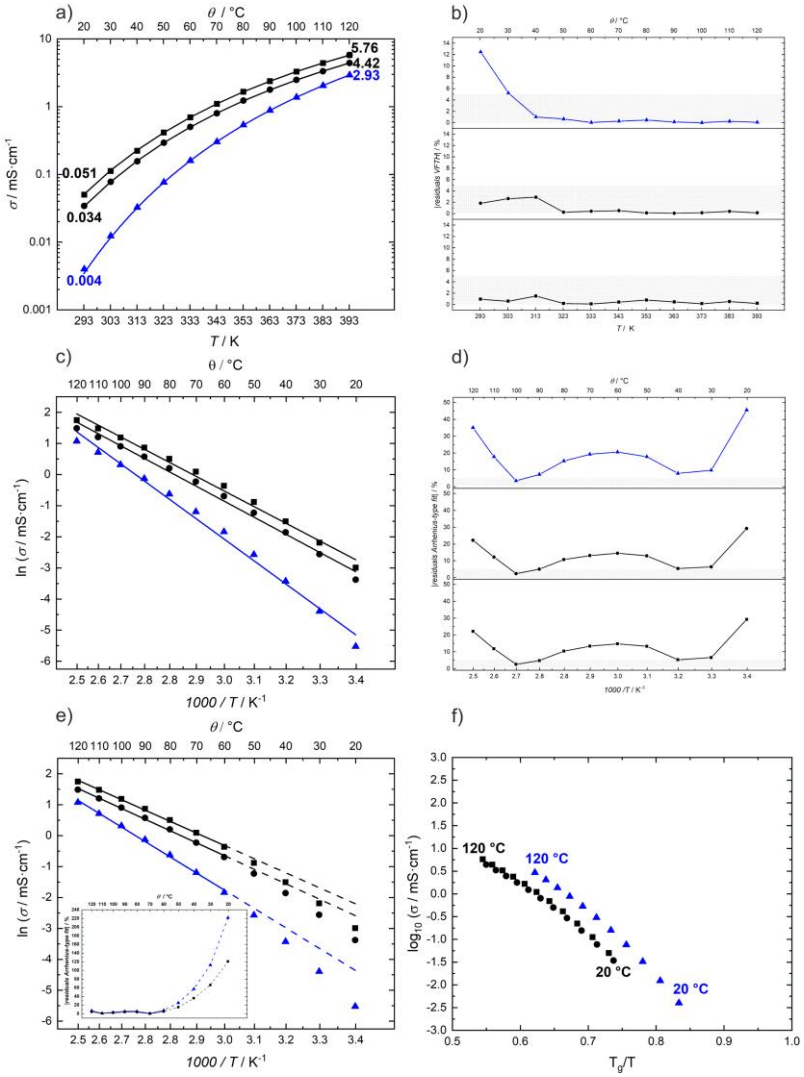

Figure 43 Ionic conductivity of [DESPA$^+$][HMDS$^-$] (blue triangles, 4634±1 ppmw H_2O) and [DESPA$^+$][TfO$^-$] (black symbols). The black squares correspond to the self-synthesized sample (12302±153 ppmw H_2O) and the circles to the commercial [DESPA$^+$][TfO$^-$] sample with 1140 ppmw H_2O. Each symbol is the average of at least 30 measurement values. A plot over the absolute temperature is displayed in a). The ticks on the y-axis have a logarythmic scaling. The solid lines are VTFH fits according to equation (39). The fiting parameters are printed in Table 9. The numbers close to the symbols correspond to the conductivity values at 20 °C and 120 °C. In c) the results are represented in a linearized Arrhenius-type plot with the solid lines correspond linear fits. e) shows the same linearized Arrhenius-type plot with the solid lines correspond linear fits for the values between 60-120 °C and the dashed-lines are an extrapolation of this fits to lower temperatures. In f) another Arrhenius-type plot, scaled by the glass-transition temperature T_g is displayed. For the scaling a T_g of 214.15 K (-59 °C) was used for the self-synthesized [DESPA$^+$][TfO$^-$] (black squares), and of 216.15 K (-57 °C) for the commerical [DESPA$^+$][TfO$^-$] (black cirlces). For the [DESPA$^+$][HMDS$^-$] (blue triangles) a T_g of 244.35 K (-28.8 °C) was applied for the scaling. All the T_g values are taken from Table 8 in chapter 4.2.4. Here the y values are the decadic logarithm of the conductivity. b),d) and the inset in e) depict the absolute residuals in % between the fits and experimental data in a),c) and e), respectivly. The residuals were calculated in the same way like for Figure 42 and described there. The lines connecting the symbols in the residual plots are only guides to the eye. The gray areas in the residual plots b),d) mark the 0-5% range.

To further analyze the transport properties, the temperature dependency of viscosity and ionic conductivity is evaluated. Based on theory a liquid is expected to display an Arrhenius type temperature dependency for both viscosity and conductivity. In the state of an undercooled melt, it is assumed that the temperature dependency of viscosity and conductivity both follow the Vogel-Fulcher-Tammann-Hesse (VFTH) equation (eq. (25) and (39)).

To check which of the two laws the PAcILs follow, the viscosity and conductivity data sets were fitted by a linearized Arrhenius equation and the VFTH equation in Figure 42 and Figure 43. For the VFTH fitting in MATLAB a special procedure was used, because the pseudo-activation energy of ionic conductivity B_σ and the temperature of zero free volume T_0 are no mathematically independent parameters, same as pseudo-activation energy of viscous flow B_η and T_0. Therefore, a comparison between B_σ and B_η, in context of a Walden product-based theory, might be less significant, if different T_0 values are used for the fit of conductivity and viscosity. In the first step of the fitting procedure the viscosity and conductivity data were fitted, with B_η, η_∞, B_σ σ_∞ and T_0 as parameters. All the T_0 values obtained in this way were averaged. In the second step the fits were repeated but now with the T_0 obtained from the first step as fixed value and not a parameter any more. This approach assures that B_σ and B_η are not corrupted by the influence of different T_0 values. The fitting parameters are printed in Table 9. Both the VFTH and linearized Arrhenius fitting curves of [$DESPA^+$][$HMDS^-$] and [$DESPA^+$][TfO^-] are displayed in Figure 42a)&c) and Figure 43a)&c) by the solid lines.

To compare, also in a visual form, which of the two laws represent the data more accurately the residuals i.e. the difference between the experimental data and the fits in percentage of the experimental values[j], is presented for each type of fit in a separate depiction in Figure 42 and Figure 43.

Obviously both the viscosity and conductivity of [$DESPA^+$][$HMDS^-$] and [$DESPA^+$][TfO^-] can be well represented over the whole investigated temperature range by the VFTH equation, with residuals mostly below 5%. In contrast with a linearized Arrhenius plot for the whole temperature range the residuals of some points are nearly 50%.

If only the high-temperature part, like the arbitrary chosen conductivity data between 60 °C and 120 °C, are fitted in a linearized Arrhenius plot the agreement between experimental data and fit is much better (solid line in Figure 43e). However, towards lower temperatures the experimental values notably bend away from the extrapolated high-temperature fit (dashed line in Figure 43e). The residuals of the fit increase for the measurement points at lower temperature to over 200% in some cases (inset Figure 43e).

[j] For this calculation always the absolute values are used, so the natural logarithm in the Arrhenius plot was removed with the natural exponential function.

This change in temperature dependency from high to low temperatures can be understood by the fact, that in the liquid state the viscose flow and thereby the conductivity takes place by activated jumps of the ions. The temperature dependency of such kind of mechanism could be described by the Arrhenius-Andrade equation (eq.(21)). For lower temperatures closer to the T_g, in the state of an undercooled melt the formation of the free-volume becomes the rate determining step for the viscose flow. The temperature dependency of the viscosity and thereby conductivity (eq.(32)), in the free-volume limited regime could be described by VFTH law (eq.(39)). The conductivity data of [$DESPA^+$][$HMDS^-$] and [$DESPA^+$][TfO^-] in Figure 43e) illustrate this change in conductivity from Arrhenius to VFTH behavior.

While an Arrhenius type fit not represents the viscosity and conductivity of [$DESPA^+$][$HMDS^-$] and [$DESPA^+$][TfO^-] over the whole investigated temperature range, the VFTH equation reproduces the experimental results with good accuracy. A temperature dependency according to the VFTH equation is usually observed for ILs.

In the analysis of the VFTH fits (Table 9) first briefly the preexponential factors η_∞, σ_∞ and the temperature of zero-free volume T_0 should be mentioned before the pseudo-activation energies E_η and E_σ which can be calculated from the B_η and B_σ are discussed. η_∞, σ_∞ values of 0.055 mPa·s, 3070 $mS \cdot cm^{-1}$ and 0.195 mPa·s, 1431 $mS \cdot cm^{-1}$ were obtained for [$DESPA^+$][$HMDS^-$] and [$DESPA^+$][TfO^-], respectively. These values are the high-temperature limits of the VFTH fits of the viscosity and conductivity. It can be seen, that the η_∞ of [$DESPA^+$][$HMDS^-$] is smaller than for [$DESPA^+$][TfO^-]. At the same time the conductivity σ_∞ of [$DESPA^+$][$HMDS^-$] is larger than of [$DESPA^+$][TfO^-]. Both can be explained by the more pronounced temperature dependency of viscosity and conductivity of [$DESPA^+$][$HMDS^-$] compared to [$DESPA^+$][TfO^-]. However, these values are mainly fitting parameter and their physical meaning should not be overinterpreted. Already in their original work G. Tammann and W. Hesse emphasized that the VFTH equation is limited to the region where the fluid is in the state of an undercooled melt i.e. temperatures between the glass transition T_g and the melting point T_m[36]. Therefore, this theory is not valid for higher temperatures where the Arrhenius-Andrade theory describes the viscosity and conductivity more accurate. T_0 is the temperature of zero free volume. For [$DESPA^+$][$HMDS^-$] and [$DESPA^+$][TfO^-] values of 190 K and 176 K were found. As explained in chapter 1.3.3 it might be interpreted as equilibrium glass-transition temperature, i.e. obtained by infinite slow cooling. These T_0 values of [$DESPA^+$][$HMDS^-$] and [$DESPA^+$][TfO^-] are about 54 °C and 38 °C below the glass-transition temperature T_g from the DSC experiments. This fits to the general observation, that T_0 lies 10 °C to 60 °C below T_g.

Table 9 VFTH fitting parameters of the viscosity and the conductivity of [DESPA$^+$][HMDS$^-$] and [DESPA$^+$][TfO$^-$] according to equations (25) and (39). For the fitting with MATLAB the 2 step fitting procedure, described in the text was applied. The adjusted R^2 values are generated from MATLAB. All the uncertainties beside the values for T_0 are the uncertainties from the fits for a 95% confidence interval. For T_0 the maximum errors from the 1st fitting cycles with the different conductivity and viscosity datasets are used. E_η , E_η' and E_σ , E_σ' are calculated according to eq.(26),(27) and (40),(41), respectively. For these values no uncertainty is given in the table, because the value which could be calculated from the uncertainty of B_η and B_σ are neglectable. T_0 of [DESPA$^+$][HMDS$^-$] is the average from 5 datasets (4x conductivity measurements, 1x viscosity measurement). T_0 of [DESPA$^+$][TfO$^-$] is the average from the fitting of the two conductivity datasets displayed here. The T_0 from the viscosity fit of [DESPA$^+$][TfO$^-$] in first step was discarded since all coefficients from the fit largely deviate from the other two datasets of [DESPA$^+$][TfO$^-$]. For the fitting in the 2. step the 4 conductivity datasets of [DESPA$^+$][HMDS$^-$] were averaged. [(a)] The viscosity was only measurement between 20-80 °C, so value is calculated with B_η of this range.

PAcIL	η_∞ / mPa·s	B_η / K	E_η / kJ·mol^{-1}	E_η' / kJ·mol^{-1}	T_0 / K	Adjusted R^2
[DESPA$^+$][HMDS$^-$]	0.055±0.002	1699±4	113.76 (20 °C) 66.07 (80 °C) 52.83 (120 °C)[(a)]	14.13	190±5	1.0000
[DESPA$^+$][TfO$^-$] self-synthetized	0.195±0.020	1258±15	26.26 (20 °C) 20.90 (80 °C) 18.97 (120 °C)[(a)]	10.46	176±4	0.9999

PAcIL	σ_∞ / mScm^{-1}	B_σ / K	E_σ / kJ·mol^{-1}	E_σ' / kJ·mol^{-1}	T_0 / K	Adjusted R^2
[DESPA$^+$][HMDS$^-$]	3070±61	1414±4	94.67(20 °C) 54.98 (80 °C) 43.96 (120 °C)	11.75	190±5	1.0000
[DESPA$^+$][TfO$^-$] self-synthesized	1431±24	1195±4	24.95 (20 °C) 19.85 (80 °C) 18.02 (120 °C)	9.94	176±4	1.0000
[DESPA$^+$][TfO$^-$] IoLiTec	1296±4	1232±4	25.72 (20 °C) 20.47 (80 °C) 18.58 (120 °C)	10.24	176±4	1.0000

More relevant than η_∞, σ_∞ and T_0 for the study of the transport properties especially the proton transport mechanism, are the activation energies of viscose flow and ionic conductivity. In Table 9 E_η , E_σ as Arrhenius-like activation energies and E_η', E_σ' for the approximation $T>>T_0$ are printed.

E_η of [DESPA$^+$][TfO$^-$] ranges between 26-19 kJ·mol^{-1} and of [DESPA$^+$][HMDS$^-$] between 114-53 kJ·mol^{-1} for the temperature range 20-120 °C. The activation energy for the viscose flow of [DESPA$^+$][HMDS$^-$] is therefore about 2.9-4.3 times the value of [DESPA$^+$][TfO$^-$]. The higher activation energy is an indication for stronger intermolecular interactions in [DESPA$^+$][HMDS$^-$], which generate a large frictional force and thereby hinder the viscose flow.

These strong intermolecular interactions were already discussed before in the context of the isobaric thermal expansivity α_P and the glass-transition temperature T_g.

E_σ [$DESPA^+$][TfO^-] and [$DESPA^+$][$HMDS^-$] range between 25-18 kJ·mol^{-1} and 95-44 kJ·mol^{-1}, respectively. Like for the viscos flow the activation energy for the ionic conductivity in [$DESPA^+$][$HMDS^-$] is significant higher than in [$DESPA^+$][TfO^-] i.e. 2.4-3.8 times the value of [$DESPA^+$][TfO^-]. For the commercial [$DESPA^+$][TfO^-] the activation energy of ionic conductivity E_σ is about 0.8-0.6 kJ·mol^{-1} higher than in the self-synthesized sample. One reason for the slightly higher activation energy in the commercial [$DESPA^+$][TfO^-] might be the lower water content of about 1140 ppmw compared to 12302 ppmw in the self-synthesized sample. Water thereby might influence the conductivity both by lowering the viscosity and additionally by the formation of H_3O^+ as additional mobile proton shuttle.

The comparison of the activation energies of the viscous flow E_η and the ionic conductivity E_σ in the self-synthesized [$DESPA^+$][TfO^-] yields very similar values for both quantities, i.e. a difference between 1.0-1.3 kJ·mol^{-1} in the investigated temperature range. The temperature independent values E_η' and E_σ' display a small difference of about 0.5 kJ·mol^{-1}. When assessing the difference in the activation energies, it must also be emphasized that the values originate from the fit of datasets obtained with conductivity and viscosity measurements, i.e. completely different methods. Therefore, some deviation could be expected. Based on the very similar activation energies for the viscous flow and the ionic conductivity in [$DESPA^+$][TfO^-], a vehicular conduction and proton transport mechanism is postulated. In contrast for [$DESPA^+$][$HMDS^-$] E_η is between 19-9 kJ·mol^{-1} larger than E_σ. For E_η' and E_σ' a difference of about 2.3 kJ·mol^{-1} is observed. Together with the unexpected high conductivity for the highly viscous [$DESPA^+$][$HMDS^-$] the significant larger activation energy for the viscos flow compared to the ionic conductivity might be an indication that conductivity and ion motion (via electromigration) are partially decoupled. Especially in the context of a PAcIL like [$DESPA^+$][$HMDS^-$] with acidic protons in both the anion and cation structure this decoupling could be realized be a cooperative Grotthuss-like proton transport. In such a mechanism the proton moves by protonation-deprotonation from one proton donor/acceptor to another and can thereby travel faster than the proton donor/acceptor itself.

However, this observation must be properly classified by comparison with literature data. In a previous study the author of this thesis investigated together with cooperation partners the transport properties of several [$DESPA^+$] and [$DEMSPA^+$] based PAcIL with both [TfO^-] and [HSO_4^-] anions. Generally, the activation energies E_η and E_σ were smaller than the data presented here and only lay between 8-17 kJ·mol^{-1}. For PAcILs with [TfO^-] anions E_η was 1.4-1.9 kJ·mol^{-1} larger than E_σ in the temperature range 20-120 °C. In systems with [HSO_4^-] anions E_η was for 1.9-4.1 kJ·mol^{-1} larger than E_σ [69]. For all these systems the difference of E_η and E_σ was significant smaller than for [$DESPA^+$][$HMDS^-$].

Another visual representation of the previously described relation between the temperature dependency of the activation energy of the viscous flow and the ionic conductivity is the so-called Walden plot. Hereby the decadic logarithm of the molar equivalence conductivity is plotted over the decadic logarithm of the fluidity i.e. the reciprocal of the viscosity. Figure 44a) displays the Walden plot for [$DESPA^+$][$HMDS^-$] and [$DESPA^+$][TfO^-] between 20-120 °C.

Only up to 80 °C experimental measurement of the density and viscosity with the applied instrumental set-up were possible. The data from this range are represented in the Walden plot by filled symbols. To estimate the behavior up to 120 °C, the designated target temperature for the IT-PEMFC operation, density and viscosity are extrapolated beyond the experimental limits with the linear equation and the VFTH equation derived before. The extrapolated values are represented in the plot by unfilled symbols.

Both the measured and extrapolated values display a linear trend. The linear fitting parameters for the measured values are summarized in Table 10. The slope α of the linear fits in the Walden plot is interpreted as the ratio B_σ/B_η of the pseudo-activation energy of ionic conductivity B_σ and viscose flow B_η. Both pseudo-activation energies of the VFTH fitting were discussed in details in the beginning of this subchapter.

Table 10 Summerized parameters of the linear fiting (dashed lines) of the Walden plot and adjusted Walden plot in Figure 44 a)&b) of [$DESPA^+$][$HMDS^-$] and [$DESPA^+$][TfO^-]. α, log C and α', log C' correspond to the slope and intercept of the linear fiting in the Walden plot and the adjusted Walden plot with radii correction[62], respectively. The uncertainties are from the linear fits. The radii r^+ and r^- of the cation an anion are calculated from the moleculare volume V_m(Zhao) in Table 5 assuming spherical shape of the ions. For further details on the molecular volumes see subchapter 4.2 (page 102) and subchapter 1.4.2 in the theory part. α from pseudo-activation energies of the VFTH fitting of viscosity and conductivity is given for comparison.

PAcIL	VFTH fitting	Walden Plot			Adjusted Walden Plot				
	$\alpha=B_\sigma/B_\eta$	α=α'	log C	Adjusted R^2	log C'	Adjusted R^2	r_+ / Å	r_- / Å	$r_+^{-1}+r_-^{-1}$/ $Å^{-1}$
[$DESPA^+$] [$HMDS^-$]	0.83	0.817± 0.004	0.15± 0.01	0.9998	0.33± 0.01	0.9998	3.55	3.01	0.6141
[$DESPA^+$] [TfO^-]	0.95	0.963± 0.003	-0.019± 0.003	0.9999	0.164± 0.004	0.9999	3.55	2.76	0.6449

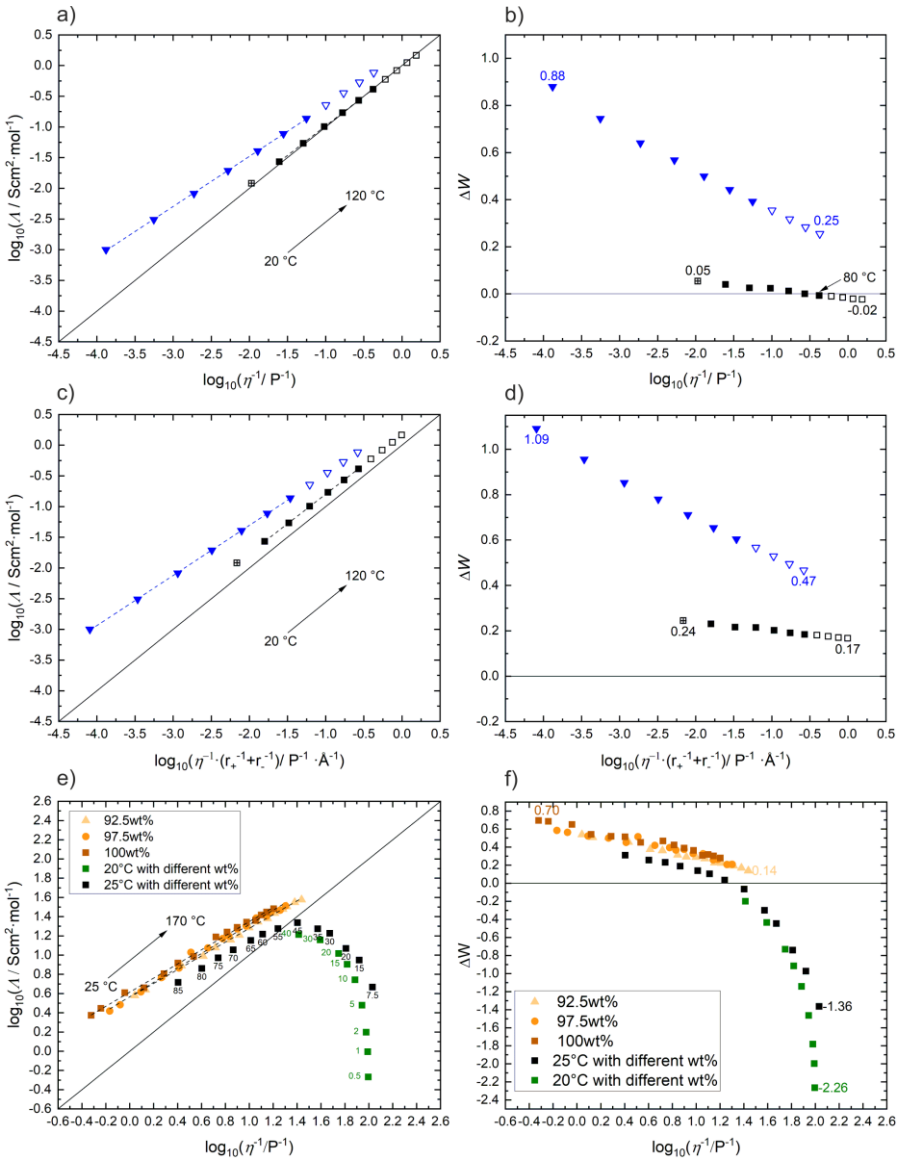

Figure 44 Walden plot a) and the adjusted Walden plot with the radii correction c) of [DESPA⁺][HMDS⁻] (blue triangles) and [DESPA⁺][TfO⁻](black squares). The dashed-lines are linear fits of the filled symbols. The fitting parameters are summerized in Table 10. The solid lines mark the diagonal. For filled symbols σ,ρ and η are measured at the corresponding temperature. Unfilled symbols represent data for which ρ and η are extrapolated beyond the experimental limits of 80 °C. ρ was extrapolated with the linear fits in Table 7, and η by VFTH equation from Table 9. The rectangle with a cross for [DESPA⁺][TfO⁻] at 20 °C has extrapolated η and experimental ρ values. For the calculation of Λ the ρ values from Figure 40 or previous explained extrapolations are used. The molecular weight for a single ionpair of 371.43 g·mol⁻¹ for [DESPA⁺][HMDS⁻] and 345.35 g·mol⁻¹ for [DESPA⁺][TfO⁻] were applied for the calculation of Λ. The adjusted Walden-Plot with the radii correction in c) was performed according to [62]. The ($r_+^{-1} + r_-^{-1}$) adjustment factor from Table 10 was used. In b) and d) the the distance ΔW of the datapoint to the diagonal reference line for the Walden plot and the adjusted Walden plot are displayed, respectivly. A positiv ΔW value corresponds to datapoints above the diagonal and a negativ ΔW value to datapoints below the diagonal. The numbers at the selected data points in b), d) and f) indicate the y values. In e) and f) the Walden plot of aquous phosphoric acid and the corresponding ΔW are displayed. The numbers beside the 20 °C and 25 °C curves in the Walden plot e) denote the weight percent of the acid. For the calculation the following references are used: all 20 °C data[31], all other η and σ values[137], the composition and temperature-dependent ρ for 25 °C and 25-160 °C of 92.5-100 wt% samples were calculated with the formulas given in [138] and [139]. A M_w of 97.99 g·mol⁻¹ was used for the phosphoric acid.

For [DESPA$^+$][TfO$^-$] a ratio B_σ/B_η of 0.95 is obtained from the VFTH fits. This value fits well to the slope α in the Walden plot for [DESPA$^+$][TfO$^-$] of about 0.96. On the one hand, this agreement between both values indicates that the interpretation of the slope α in the Walden plot as the ratio of the pseudo-activation energies might by valid. On the other hand, α is close to unity, which demonstrates that both pseudo-activation energies are quite similar. Therefore, it could be assumed that charge transport in the PAcIL is dominated by simple ion motion by electromigration. For the acid proton a vehicular proton transport mechanism could be suggested, where the proton is bond to the cation structure. This theory is further supported by the report by Schreiner et al. of similar values for α of about 0.92 for aprotic EMIM/BMIM based ILs, which due to their structure most probably only have charge transfer by ion motion[52].

For [DESPA$^+$][HMDS$^-$] the slope α from the Walden plot is 0.82. This is similar to the value of 0.83 calculated from the ratio of the pseudo-activation energies B_σ/B_η from the VFTH fittings. Phosphoric acid is a typical example for proton transport through the Grotthuss mechanism[140]. Here an α value of 0.65[k] was reported by C. Korte for 100 wt% H_3PO_4 (72.4 wt% P_2O_5)[141]. In Figure 44e) Walden plots, which the author of this thesis compiled from literature are displayed. Here α values between 0.72-0.75 were found for 92.5-100 wt% phosphoric acid. These values for the concentrated phosphoric acid are similar to the values [DESPA$^+$][HMDS$^-$], which might be interpreted as another indication for a cooperative proton transport mechanism. However, also for 1 m KCl and infinite diluted one α values of about 0.82 and 0.87 can be obtained (see Figure 18 b). For aqueous KCl solutions a cooperative transport mechanism by the KCl can be ruled out.

Therefore, a slope α<1 might be either a sign for ion pairing or for a decoupling of the conduction mechanism from ionic motion (see chapter 1.4.2). To distinguish the two phenomena the relative position of the data to the diagonal in the Walden plot i.e. ideal reference line has to be analyzed. An α value <1 for data above the diagonal, i.e. with a higher conductivity than predicted from Walden rule (eq.(36)) can be interpreted by the decoupling of ion motion and conductivity. In the subionic region of the Walden plot i.e. below the diagonal an α value <1 indicates ion pairing.

[DESPA$^+$][TfO$^-$] lies close to the diagonal line i.e. has a small ΔW value. The ΔW, which is calculated as difference in ordinate values of the data points and the diagonal is displayed in Figure 44b). For lower temperatures [DESPA$^+$][TfO$^-$] has a small positive ΔW value (~ 0.05). This could be translated to a position of the datapoints slightly above the diagonal i.e. a less pronounced superionic behavior. With increasing temperature, the strength of ionic interactions increases (see explanation of this phenomenon in chapter 1.4.2). Starting from 80 °C ΔW becomes negative, i.e. the datapoints of [DESPA$^+$][TfO$^-$] fall below the diagonal reference line (~ -0.02). This shows [DESPA$^+$][TfO$^-$] is a

[k] In the Walden plot in Ref [141]viscosity values in mPa·s instead of Poise are used. While this influences the position of the data relative to the diagonal it has no impact on the slope α.

"good" IL without strong ionic interactions, which hinder the viscos flow and thereby the transport of charge i.e. the ionic conductivity. Under certain conditions the charge transport might be to a minor extend by a cooperative mechanism. However, the distance to the diagonal or the ΔW values are small (-0.02 to 0.05) and should not be overinterpreted. Therefore, together with the slope α~1 from the Walden plot and the ratio of the pseudo-activation energies, a vehicular proton transport as major mechanism is suggested for [$DESPA^+$][TfO^-].

In [$DESPA^+$][$HMDS^-$] the situation is completely different. This PAcIL shows large positive ΔW values of 0.25-0.88 within the whole temperature range of 20-120 °C (Figure 44b). This demonstrates that [$DESPA^+$][$HMDS^-$] has an exceptional strong pronounced superionic character. Only a few examples of superionic PILs are known from literature, mainly from the research group of C. A. Angell. Alkylammonium sulfates like ethylammonium, dimethylammonium and butylammonium hydrogen sulfate are slightly superionic[58]. Guanidinium dihydrogen phosphate lies in the Walden plot significantly above the diagonal and has therefore a well pronounced superionic character[59]. However, while all these examples are superionic PILs i.e. a higher equivalent conductivity then expectable from the Walden rule, they still lie far below the phosphoric acid and therefore cooperative proton transfer is less pronounced then in H_3PO_4, if it takes place at all. Y. Ansari combined the very weak base pentafluoropyridine (PFP) with strong tetrachloroaluminic acid $H^+[AlCl_4^-]$ to synthesize the PIL [$HPFP^+$][$AlCl_4^-$]. By using a very weak base PFP , i.e., the very strong acidic [$HPFP^+$] cation, a PIL is obtained which superionicity is only slightly lower than that of 98 wt% H_3PO_4[142]. During the study on the pharmaceutical lidocaine di-(dihydrogen phosphate) Z. Wojnarowska uncovered it special proton conductivity, especially around its glass transition. In an extensive study on different lidocaine-based PILs and salts a decoupling of the structural relaxation i.e. the ion motion from the ionic conductivity was found[143]. In the Walden plot lidocaine di-(dihydrogen phosphate) is strongly superionic and even lies above the data of 85 wt% H_3PO_4. The slope α of 0.53 is far below unity. The slope indicates together with the strong superionicity and the relaxation times found by dielectric spectroscopy and temperature modulates DSC a pronounced decoupling of the proton transfer and ion motion in lidocaine di-(dihydrogen phosphate). However, the remarkable properties described in the study have to be relativized. For the doubly charged lidocaine cation with the two negative [$H_2PO_4^-$] ions in a formula unit, a higher molar equivalent conductivity (eq.(32) and eq.(35)) is naturally expected than what the Walden rule predicts for monovalent ILs. Therefore, the observed position wide above the diagonal in the superionic region is not surprising. The slope of lidocaine di-(dihydrogen phosphate) of approximately 0.5 in the Walden plot may also be partly be influenced by the double charged ions[117].

Compared to the cited references [$DESPA^+$][$HMDS^-$] shows a much strongest superiority. The largest ΔW values of 0.88 indicates that for this temperature the molar equivalence conductivity of [$DESPA^+$][$HMDS^-$] exceeds the reference value from the Walden rule by

nearly one decade. In addition, in literature superionicity was only observed for low temperatures, in some cases in vicinity of the glass-transition temperature. [$DESPA^+$][$HMDS^-$] in contrast displays superionicity up to a high temperatures of 80 °C. If no unexpected effect in the viscosity and density appears according to the extrapolated values superionicity might be found even at 120 °C and above (Figure 44a)&b)). Therefore [$DESPA^+$][$HMDS^-$] is to the authors knowledge the PIL with the strongest superionicity especially in the high-temperature regime nearly 100 °C above its T_g. This extraordinary finding was confirmed by multiple viscosity and conductivity measurement series performed with two batches of [$DESPA^+$][$HMDS^-$] with both self-synthesized and commercial H2MDS (Figure S 7).

The slope α of [$DESPA^+$][$HMDS^-$] of ~0.8 should considering its superiority be interpreted by a decoupling of the conduction mechanism and viscose flow. The two other interpretations for $\alpha<1$, a low formation degree or strong ion-pairing can be ruled out. The high formation degree of the PAcIL is proven by the NMR spectra (chapter 4.2.2) and the position far above the diagonal in the superionic regime chancels out the possibility of strong ion-pairing.

The simplicity and elegance of the Walden plot for analyzing transport properties are compelling; however, the approach is not without controversy. D. R. MacFarlane et al. pointed out that the ion sizes are not considered in the classical Walden plot. Especially when comparing bulky organic ions in ILs with atomic ions like K^+ or Cl^-, the effect of the different sizes might not be negligible. Therefore, D. R. MacFarlane et al. proposed an adjusted Walden plot, which is constructed by multiplying the x-value with the sum of the inverse ionic radii (eq.(43))[62]. The accordingly adjusted Walden plot of [$DESPA^+$][TfO^-] and [$DESPA^+$][$HMDS^-$] is shown in Figure 44c). The ionic radii and the corresponding adjustment factors are printed in Table 10. The movement towards smaller abscissas values by the adjustment factor corresponds to an upwards shift relative to the diagonal. Therefore, the ΔW values in Figure 44d) are larger compared to the Walden plot without radii correction. In the adjusted Walden plot, [$DESPA^+$][TfO^-] also clearly falls within the superionic region with ΔW between 0.17-0.24. For [$DESPA^+$][$HMDS^-$] ΔW increases in the adjusted Walden plot to 1.09.

The analysis with the Walden plot suggests that in [$DESPA^+$][$HMDS^-$] the charge i.e. proton transport is decoupled from the viscos flow i.e. the ionic motion. However, as C. Schreiner et al. discussed wrong conclusions might be drawn if the Walden plot is overinterpreted[52]. This is also illustrated in

Figure 18b), were an erroneous decoupling of ion motion and conductivity might be postulated from the Walden plot of infinite diluted KCl. Therefore, always further methods are required to verify the results from the analysis of the Walden plot. A direct way to measure the diffusion coefficients of the individual protons in a liquid is Pulsed-Field Gradient Spin-Echo (PGSE) NMR spectroscopy.

In cooperation with Dr. S. Nejrotti and M. Bonomo from the University of Turin, the diffusion coefficients of the different protons in neat [DESPA$^+$][HMDS$^-$] were measured (Figure 45). Due to the high viscosity of the sample homogenous magnetic fields were only achievable at elevated temperatures above 343 K.

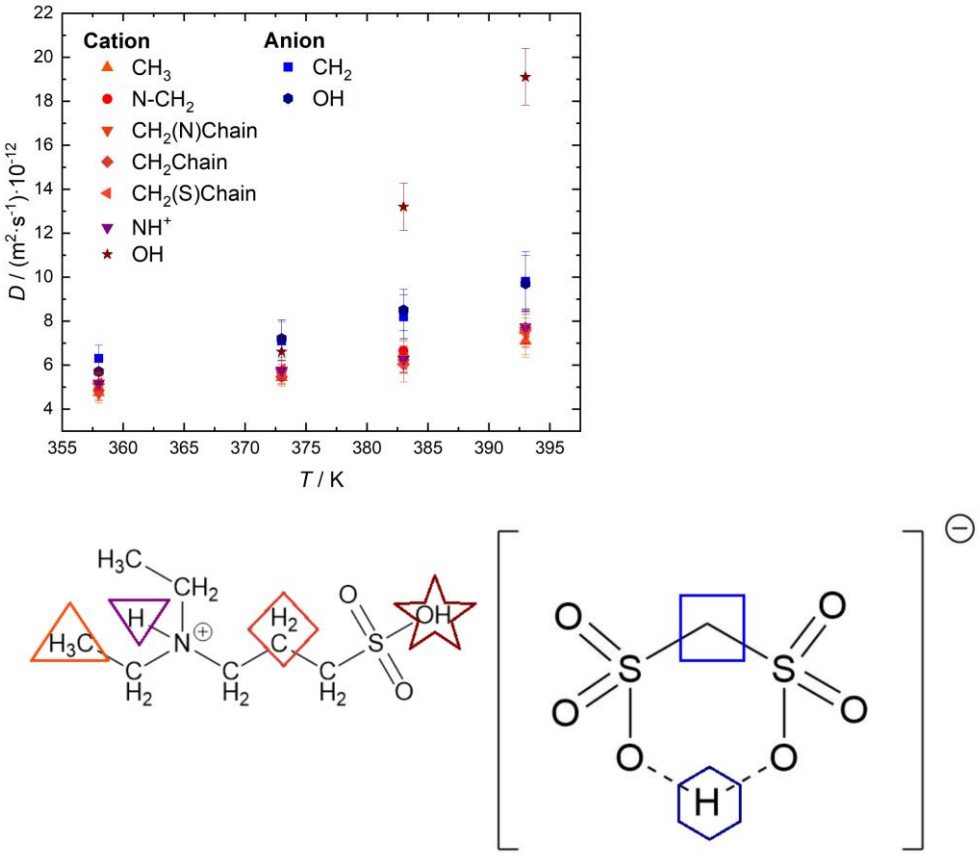

Figure 45 Temperature-dependent diffussion coefficients of neat [DESPA$^+$][HMDS$^-$] obtained from Pulsed-Field Gradient Spin-Echo (PGSE) ^{1}H-NMR spectroscopy. The measurements were performed in coaxial geometry with the PAcIL in a flame-sealed capillary and DMSO-d_6, as locking solvent in the space between the capillary and the NMR tube's walls. The water content of 5483±189 ppmw (n=4) was determined by Karl Fischer titration. The assignment of selected peaks is highlighted by the symbols in the chemical formula. "Chain" in the legend of the graph denotes the CH_2 groups in the propyl chain in the cation. This data set has been published in [96] for a larger temperature range, too.

From Figure 45 it is obvious, that the diffusion coefficients are clustered in two groups. Independent of analyzed proton for the cation diffusion coefficients of about 4.7 to $7.7 \cdot 10^{-12}$ m^2/s were obtained between 358-393 K. Diffusion coefficients for the protons of the anion are at all investigated temperatures higher than of the cation. For example, the measured diffusion coefficients for the methylene proton in the anion are $6.3 \cdot 10^{-12}$ m^2/s or $9.8 \cdot 10^{-12}$ m^2/s at 358 K and 393 K, respectively.

The ratio of D_-/D_+ of the anion/cation diffusion coefficient is rather constant at about 1.2-1.4 within the investigated temperature range. This shows a different mobility of the cation and anion, which was observed for protic and aprotic ILs before[104,144–146]. The higher mobility of the [$HMDS^-$] compared to the [$DESPA^+$] ion might be expected from the different molecular weights of about 175 to 196 g·mol^{-1} and ion sizes (see Table 10 & Table 5).

The diffusion coefficient of the N-H proton is similar to the diffusion coefficient of the cation. This shows that on the experimental timescale the proton is fixed to the nitrogen of the [$DESPA^+$] cation, i.e. the suggested function as charge "trap" for the positive charge is confirmed.

The acidic OH protons require a more detailed discussion. [$DESPA^+$][$HMDS^-$] contains two chemically similar sulfonic acid groups in the anion and cation, which signal at 12.05 and 12.03 ppm overlap to a broad peak at about 12 ppm (peak 7 and 9 of the 1D-spectra in Figure 37). Despite their similar chemical shift, they display quite different diffusion behavior. On the one hand, the diffusion coefficients that can be extracted from the peak at 12.03 ppm of $5.7\cdot10^{-12}$ m^2/s at 358 K and $7.2\cdot10^{-12}$ m^2/s at 373 K are similar to the diffusion coefficient of the methylene protons in the anion. On the other hand, for the peak at 12.05 ppm, similar diffusion coefficients to the cation of $5.7\cdot10^{-12}$ m^2/s at 358 K and $6.6\cdot10^{-12}$ m^2/s at 373 K are obtained. This finding that one acidic proton has a diffusion coefficient similar to the anion and one similar to the cation demonstrates first, once again that the PAcIL was successfully synthesized and the proton transfer from the methanedisulfonic acid H2MDS to the DESPA zwitterion took place in its synthesis. Second the similar diffusion coefficient with the anion and cation with the acid protons is a prove for a vehicular proton transport mechanism. The finding of a vehicular proton transport is surprising. Due to the difference in activation energies for ionic conductivity and viscose flow found in VTFH fitting and the superionicity in the Walden plot a cooperative mechanism was expected.

However, when the temperature is increase above 373 K, the proton transport mechanism changes completely. The diffusion coefficient determined from the peak at 12.03 ppm, which corresponds to the proton of [$HMDS^-$], stays with values around 8.5 and $9.7\cdot10^{-12}$ m^2/s at 383 K and 393 K in the same range like the diffusion coefficients of the anion. While for the peak at 12.05 ppm (star symbol in Figure 45) the extracted values of the diffusion coefficient exceed that of the cation at 383 K 2.1 times ($13.2\cdot10^{-12}$ vs $6.3\cdot10^{-12}$ m^2/s[1]) and at 393 K even 2.5 times ($19.1\cdot10^{-12}$ vs $7.5\cdot10^{-12}$ m^2/s[p]). This enhanced diffusion of the acidic proton compared to the cation, its former vehicular shuttle, indicated a change in the proton transport mechanism.

[1] This value is the error-weighted average from all the CH signals in the cation at the temperature. See also[96].

The most likely explanation for the observed decoupling of the motion of the cation and the acid proton is a cooperative Grotthuss-like proton transfer.

Some examples of Grotthuss-like proton transport have been reported in literature but mainly for non-stochiometric PILs[93,147] or for water-PIL mixtures with a water content of about 6-7 wt%[148,149]. A literature overview of diffusion coefficients from "neat" stochiometric PILs obtained by NMR is given in Table S 5. There the largest ratios of the diffusion coefficients of the acidic proton to the cation for "neat" PILs are 1.4 for triethylammonium acetate [$N222H^+$][Ac^-] at 340 K [m] [145], 1.20 Bis(2-methoxyethyl) ammonium pentafluorobenzenesulfonate [$BMEA^+$][PF^-] and 2.17 for [$N222H^+$][PF^-], both at 373 K [q] [150], 1.98 for [$MSEA^+$][TfO^-] at 363 K (7500-8000 ppmw H_2O)[149] and 2.10 [2-$SEMA^+$][TfO^-] at 343 K (8000 ppmw H_2O)[148]. M. Anouti et al. found for [$PyrHH^+$][HSO_4^-] the largest decoupling of the diffusion of the acidic proton and the cation with values between 3.4-3.7. However, the water content was between 200-30,000 ppmw so might have played a non-negligible effect on the proton transfer[151]. The comparison with these literature data shows, that with the ratio of 2.1-2.5 of the diffusion coefficient of the acidic proton to the cation in [$DESPA^+$][$HMDS^-$], is one of the most significant and reliable examples, which supports the theory of a Grotthuss-like conduction mechanism in protic ionic liquids. The temperature-dependent switch between the vehicular and cooperative conduction mechanism observed for [$DESPA^+$][$HMDS^-$] finds no precedents in the literature. M. Anouti et al. found for [$PyrHH^+$][$TFAc^-$] a switch from cooperative to a vehicular mechanism, however for this sample the change appeared at the melting point[151]. Such a phase transition can clearly be ruled out based on the conductivity measurement of [$DESPA^+$][$HMDS^-$] in Figure 43. In these experiments no deviation from the VFTH curve, which might indicate a phase change, is visible in the relevant region of about 370-382 K.

Further theoretical simulations and spectroscopic measurements are needed to elucidate the exact cause of the transition from vehicular to a cooperative proton transport mechanism in [$DESPA^+$][$HMDS^-$]. Therefore, all current statements can only be educated guesses. One hypothesis is that at temperatures above 373 K, proton transfer occurs from the (protonated) sulfonic acid group of the cation to the (unprotonated) sulfonic acid moiety of the anion. The increasing ion-pair interaction with temperature could be helpful in this process. Additionally, the kinetic energy corresponding to the temperature may play a role as activation energy in the proton transfer cascade.

[m] Water content not specified in the publication.

4.2.6 Electrochemical Stability and ORR in [DESPA$^+$][HMDS$^-$]

After this detailed study on the physical properties and the proton transport in [DESPA$^+$][HMDS$^-$] finally the compatibility with the electrochemistry in an IT-PEMFC at 120°C should be tested. Therefore, the electrochemical stability window (ESW) is measured, the oxygen reduction reaction (ORR) and oxygen diffusion (D_{O2}) and saturation concentration (c_{O2}) are studied. The experiments in this section were performed at the Forschungszentrum Jülich in cooperation with Dr. Hui Hou from PD Dr. Carsten Korte's research team, partially during a one-month research stay of the author of the thesis at this institute.

The experiments are performed with a hydrogen-loaded palladium (Pd-H) reference electrode. A Pd-H electrode has at 25 °C a potential of 50 mV vs. a reversible hydrogen electrode (RHE) in 1 M H_2SO_4. From literature it is known that the potential of Pd-H decreases by about 0.5-0.65 mV·°C^{-1}. Therefore, the deviation of the Pd-H potential from the RHE at 120 °C might be smaller than 50 mV. In the PAcIL [SEA$^+$][TfO$^-$] K. Wippermann et al. observed a difference of the open circuit potential (OCV) of the RHE and Pd-H of 0-20 mV in the temperature range of 30–130 °C[72]. Based on these literature data, it appears reasonable to assume that the potential of Pd-H, even at elevated temperatures, deviates by less than 100 mV from the RHE electrode in a non-aqueous system like a PAcIL. Therefore, potentials against the Pd-H electrode can, in a good approximation, be considered equivalent to the potentials vs. the RHE reference electrode.

The cyclic voltammograms (CVs) of [DESPA$^+$][HMDS$^-$] at 120 °C under N_2 are displayed Figure 46.

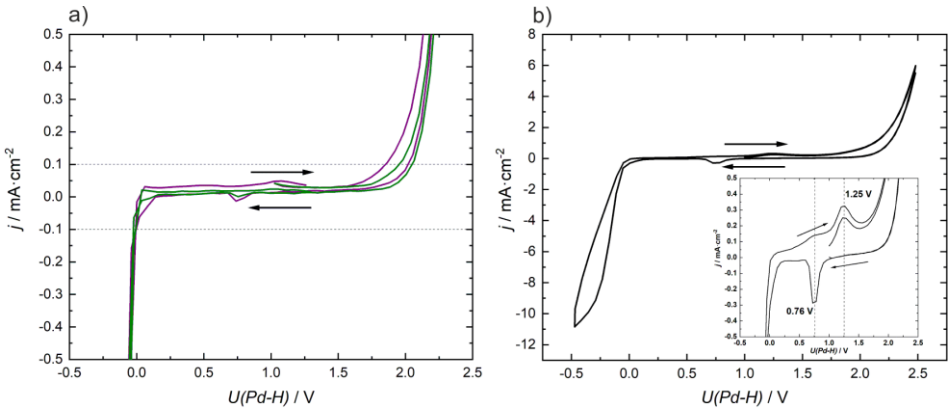

Figure 46 CV of [DESPA$^+$][HMDS$^-$] at 120 °C in N_2 with a cylindrical Pt working electrode (WE), a Pt counter (CE) and a Pd-H reference (RE). The surface area of the Pt WE was 0.27 cm^2, which was determined before the CVs by measurement of H-desorption in 0.5 M H_2SO_4. The initial potential of the scans was 1.025 V. The water content was between 2.75- 3.39 wt%, considering KF titration before and after the experiment. The CVs are plotted according to the IUPAC convention regarding oxidation and reduction. a) Experiments are performed with a scan rate of 2 mV·s^{-1} (green) and 5 mV·s^{-1}(purple) The horizontal dashed lines mark the |100| µA·cm^{-2} threshold for the determination of the ESW. b) A CV with a scan rate of 100 mV·s^{-1}. The insert is a zoom to highlight the peaks at 0.76 V and 1.25 V.

In these CVs no significant current flow is observed between about 0 V and 2 V with the Pt working electrode. There exists no general definition for the electrochemical stability window (ESW) determination. In Table 11 the potential limits, which corresponds to a maximum current of 50 or 100 $\mu A \cdot cm^{-2}$ are summarized. The difference of the anodic and cathodic potential limit, i.e. the ESW, is depending on the scan rate and applied current density limit, between 1.66-1.97 V wide. This shows that the [$HMDS^-$] anion is rather stable to oxidation. The 6-membered ring structure with the intramolecular hydrogen bond (Figure 32) might contribute to the stability of the [$HMDS^-$]. Within the ESW, especially at high scan rate of 100 $mV \cdot s^{-1}$ two minor peaks are visible at 0.76 and 1.25 V (Figure 46b). A similar charge flow of 128 µC for reduction and 112 µC for the oxidation peak indicate that both peaks are related to the same electrochemical reaction. The peak separation of 0.485 V is similar to the theoretical value 0.312 V for a 4-electron process at 120 °C. Due to these observations and the similar positions of the peaks compared to the Pt-O reduction/formation in H_2SO_4 electrolyte, these peaks at 0.76 and 1.25 V are assigned to the platinum oxide reduction and formation, respectively. At the boarders of the ESW the current density rises due to splitting of the water (2.75-3.39 wt%) in the analyzed [$DESPA^+$][$HMDS^-$] sample and probably at some point due to the decomposition of the PAcIL itself. However, the range up to at least 1.70 V is sufficient for the oxygen reduction reaction, with an expected onset below 1 V. In addition, contrary to the initial concern, the CVs do not provide an indication of pronounced adsorption of the [$DESPA^+$][$HMDS^-$], especially of the [$HMDS^-$] anions on the Pt surface.

Table 11 Boarders of the ESW extracted from the measurements in Figure 46. The potentials, which corresponds to an anodic (upper value) and cathodic (lower value) current density of 50 $\mu A \cdot cm^{-2}$ or 100 $\mu A \cdot cm^{-2}$ are given.

Scan rate / $mV \cdot s^{-1}$	U(Pd-H) at |50| $\mu A \cdot cm^{-2}$/ V	U(Pd-H) at |100| $\mu A \cdot cm^{-2}$/ V
2	1.80 0.00	1.95 -0.02
5	1.70 0.04	1.85 0.00

In the next step the oxygen reduction reaction (ORR) in [$DESPA^+$][$HMDS^-$] was investigated. To test if [$DESPA^+$][$HMDS^-$] has an impact on the ORR, for example by blocking the Pt surface, is crucial for the planned PEMFC application. In such a device the PAcIL should form a proton shuttle through the membrane from the anode to the cathode and therefore the PAcIL will wet the Pt catalyst on the cathode surface, where the ORR takes place. To test the ORR the PAcIL was purges with O_2 (20 ml/min) for 2 hours before the experiment. The ORR was investigated by linear sweep voltammetry (LSV) with cathodic scans starting at potentials close to the OCV.

Figure 47 shows two sets of experiments on the ORR in [DESPA$^+$][HMDS$^-$] both at 90 °C and 120 °C. The data in panel b) are a repetition of the experiments in a).

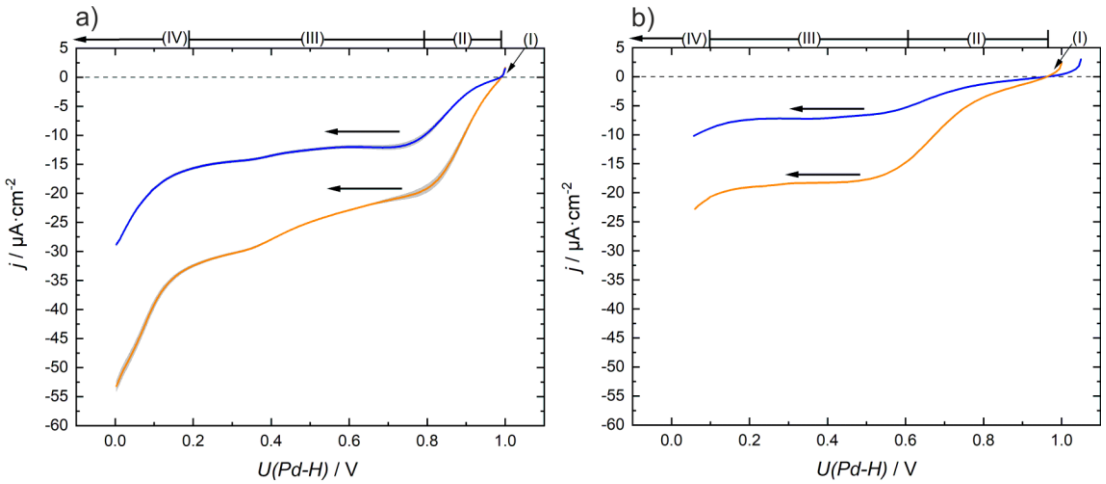

Figure 47 *Study of the ORR in [DESPA$^+$][HMDS$^-$] by LSV. The PAcIL was saturated with O_2 by purging for 2 h before the experiments. During the measurements the electrochemical cell was in O_2 atmosphere. The curves were recorded by a cathodic scan with 5 mV·s^{-1}. The blue curves were recorded at 90 °C and the orange curves at 120 °C. The gray shaded area in a) indicates the standard deviation of 3 measurements. The arrows mark the scan direction and the dashed horizontal lines are reference lines for 0 current density. The roman numbers over the panels refer to the different regions of the ORR in the text. The water content obtained by KF titration was 1.55-2.35 wt% for the data in a) and 1.83-2.31 wt% for the data in b). The active surface area of the Pt working electrode in a) is 0.21 cm^2 and in b) 0.27 cm^2.*

Due to the large quantity of PAcIL required for the experiments (~5 ml) the sample from the experiments in Figure 47a) was recovered and reused for the measurements in b). The characteristic points and regions in the curves are: (I) the OCV i.e. the voltage which corresponds to the current free-state. (II) the kinetic controlled and mixed kinetic and diffusion-controlled regime. Starting from the onset voltage U_{onset} the ORR rate increases. This mainly kinetic controlled region directly transitions into a mixed region in which both kinetic and diffusion processes determine the current density. (III) the diffusion-limited regime, a plateau in the current density j_{lim}, were the reaction rate cannot be enhanced by more cathodic potential because the limiting factor is the supply with O_2 at the Pt surface by diffusion. For the diffusion-limited regime, the onset potential U_{lim} can be defined. And finally (IV) the hydrogen evolution reaction (HER). These different regions are roughly sketched on top of both panels in Figure 47.

Already on the first glance significant differences between the two measurements are visible. The onset potentials in Figure 47b) are shifted to lower values compared to a) and the overall current density is much smaller. Especially in the light of the very similar OCV (maximum difference 3 mV) und similar water content in the two experiments this is surprising.

The most likely explanation for this behavior can be found in the history of the sample. Additional electrochemical experiments, such as the CVs shown in Figure 46, were conducted between the measurements in Figure 47a) and b). Therefore, it cannot be ruled out that at potentials outside the electrochemical stability window, small amounts of [$DESPA^+$][$HMDS^-$] were decomposed. These decomposition products could then have the poisoning effect on the ORR observed in Figure 47b). Nevertheless, the second measurement will not be discarded and should be discussed together with the first one, on the one hand for the sake of completeness and on the other hand in operation there might be conditions where the potential of a cell in the PEMFC stack reaches for a short time values outside the ESW, and therefore the PAcIL might be in a similar state like in Figure 47b).

From both measurement series the onset potentials of the kinetic-controlled region U_{onset} and diffusion-controlled region U_{lim} were determined with the "tangent method". Thereby the onset potential is defined as the intersect of the base line (linear fit) and the tangential line on the midpoint of the step in the current density curve. For some examples this method is depicted in Figure S 8. The onset potentials and corresponding current densities j_{onset} and j_{lim} are summarized in Table 12. For comparison the literature values for [$DESPA^+$][TfO^-] are included, too.

Table 12 Onset potentials in the kinetic-controled region U_{onset} and under diffussional control U_{lim} and current densities at the corresponding points j_{onset} and j_{lim}. The values are extracted from the data in Figure 47. OCV is the open-circuit potential. [(a)] The values are determined by the author of this thesis from the original data of the publication. [(b)] Note the correction of the j values published to the article. [(c)] The range corresponds to the values measured before and after the experiments.

PAcIL	H_2O / wt%[(c)]	θ / °C	OCV (Pd-H) / V	U_{onset} / V	j_{onset} / µA·cm^{-2}	U_{lim} / V	j_{lim} / µA·cm^{-2}	Source
[$DESPA^+$][$HMDS^-$]	1.55-2.35	90 120	0.99 0.99	0.90 n.d.	-3 n.d.	0.77 0.83	-11 -18	Figure 47a)
	1.83-2.31	90 120	0.96 0.96	0.75 0.76	-2 -5	0.52 0.56	-6 -16	Figure 47b)
[$DESPA^+$][TfO^-]	1.75	90 120	0.87[(a)] 0.91[(a)]	0.75[(a)] 0.84	-9[(a)] -12	0.57[(a)] 0.62	-40[(a)] -79	69 (b)

For the first measurement series the onset potentials U_{onset} and U_{lim} are 0.15-0.27 V higher than in the second experimental series, most likely due to the above-mentioned explanations about the electrochemical history of the sample. Interestingly the onset potentials of this first experimental series even exceed the literature value of [$DESPA^+$][TfO^-] by about 0.15-0.21 V. This shows that [$DESPA^+$][$HMDS^-$] does not seems to have a negative effect on the ORR kinetic, however the diffusional limitation is already reached at 0.77 V so in the relevant operation range in PEMFC. In contrast in the second experimental series the onset potentials of [$DESPA^+$][$HMDS^-$] are similar to [$DESPA^+$][TfO^-].

Despite the similar onset-potentials of [DESPA$^+$][HMDS$^-$] and [DESPA$^+$][TfO$^-$] the current densities at both onset potentials are in [DESPA$^+$][HMDS$^-$] significant smaller than in [DESPA$^+$][TfO$^-$].The two measurement series of [DESPA$^+$][HMDS$^-$] agree well for the current density values j_{onset} and j_{lim}, also the current densities were obtained in the first measurement at more positive potentials. The reason for the significant smaller onset current densities in [DESPA$^+$][HMDS$^-$] compared to the TfO-based PAcIL, especially for the diffusion-limited current density, might be related to the oxygen saturation concentration c_{O2} and oxygen diffusion coefficient D_{O2} in the PAcIL.

To test this hypothesis the c_{O2} and D_{O2} were measured by our cooperation partners at Forschungszentrum Jülich in the research team of PD Dr. Carsten Korte. Both c_{O2} and D_{O2} can be obtained from chronoamperometric experiments. Therefore the O_2 saturated [DESPA$^+$][HMDS$^-$] and a disc-shaped Pt microelectrode (radius r_0=125 µm) as working electrode are used. The limiting current density j_{lim} vs. time curve after a potential jump from the OCV (1-1.025 V) to a potential in the diffusion-limited range (0.25-0.425 V) is recorded. From the fit of j_{lim} vs. time t with the Shoup-Szabo equation (eq.(48)) D_{O2} and c_{O2} can be extracted. In equation (48) n corresponds to the number of transferred electrons, r_0 to the radius of the disc-shaped microelectrode. F is the Faraday constant.

$$j_{lim} = \frac{4nFD_{O2}c_{O2}}{\pi r_0} f(\tau)$$

Approximation of Shoup and Szabo

$$f(\tau) = \frac{\pi}{4} + \frac{\pi^{1/2}}{2\tau^{1/2}} + 0.2146e^{-0.7823\tau^{-1/2}} \quad (48)$$

with

$$\tau = \frac{4D_{O2}t}{r_0^2}$$

By this experiment for [DESPA$^+$][HMDS$^-$] c_{O2} of (1.75±0.72)·10^{-6} and (1.74±0.33)·10^{-6} mol·cm^{-3} and D_{O2} of (0.70±0.46)·10^{-7}, (1.86±0.42)·10^{-7} cm^2·s^{-1} were obtained at 90 °C and 120 °C, respectively. The values are the average obtained from the fitting of 12-15 individual j_{lim} vs. time curves. All the values are printed in Table S 6. The uncertainties are the corresponding standard deviations. c_{O2} values of comparable [DESPA$^+$] and [DEMSPA$^+$]-based PAcILs with triflate and hydrogensulfate anion are in the range of 10$^{-5.5}$-10^{-7}·mol·cm^{-3}. 98 wt% H_3PO_4 has between 75-125 °C a relative constant oxygen saturation concentration of 10^{-7}·mol·cm^{-3} [69]. [DESPA$^+$][HMDS$^-$] is situated with a relatively constant c_{O2} of 1.8·10^{-6} mol·cm^{-3} between 90 °C-120 °C, right in the middle of the examples mentioned above.

In the literature, there is a discussion about the correlation between acidity and oxygen saturation concentration. According to this theory, the similar c_{O2} to the examples mentioned above can be explained by the expected similar acidity of [$DESPA^+$][$HMDS^-$] with the other strongly acidic PAcILs.

In contrast D_{O2} values of [$DESPA^+$][$HMDS^-$] are about 1.5-2.5 orders of magnitude smaller than D_{O2} of the above mentioned PAcILs or 98 wt% H_3PO_4. The smaller diffusion coefficient of oxygen is maybe related with the higher viscosity of [$DESPA^+$][$HMDS^-$] compared to the reference substances.

When considering the D_{O2} values of [$DESPA^+$][$HMDS^-$], which are nearly two orders of magnitude smaller than in [$DESPA^+$][TfO^-], it is remarkable that the limiting current density j_{lim} in [$DESPA^+$][$HMDS^-$], is only about 1/5 of j_{lim} in [$DESPA^+$][TfO^-] and not several orders of magnitude smaller. This can be understood when considering that for the ORR, not only oxygen transport but also proton transport is relevant. Proton transport in [$DESPA^+$][$HMDS^-$], is favored by the unusually thermal "on-switch" Grotthuss mechanism uncovered in section 4.2.5. Therefore, the very fast proton transport may partially compensate for the slow oxygen diffusion.

Based on these findings a promising route towards further improvements of the oxygen reduction reaction might be blending [$DESPA^+$][$HMDS^-$] with other PAcILs. With the proper choice of the other PAcIL the viscosity of [$DESPA^+$][$HMDS^-$] can be reduced without losing the beneficial properties for the PEMFC application, namely the proton transport by a cooperative Grotthuss-like mechanism and the high thermal stability. While in a blend, the other PAcIL may not be fluorine-free, a successively increased proportion of fluorine-free [$DESPA^+$][$HMDS^-$] can significantly reduce the fluorine content, which will have a positive impact on the environmental effects and the cost of the PEMFC.

5. Conclusions and Outlook

The aim of this dissertation was to develop protic acidic ionic liquids (PAcILs), which are suitable for a potential application in intermediate temperature proton-exchange membrane fuel cells (IT-PEMFC) at about 120 °C. One key feature of the PAcILs should be their high acidity, which could be beneficial for both the proton transfer and the kinetic of the oxygen reduction reaction (ORR).

A PAcIL in literature, which has been proposed for this task, is 2-sulfoethylammonium triflate [SEA^+][TfO^-][72]. Its high acidity is achieved by the presence of a sulfonic acid group in addition to the ammonium group in the alkyl side chain. However, [SEA^+][TfO^-] exhibits insufficient thermal stability and ionic conductivity. Therefore, in the first part of this dissertation, different analogous cation structures are investigated, with variations in both the degree of substitution at the ammonium group and the type of acid group. Thereby the influence of both structural motifs, i.e., the cationic ammonium group and the acid group, on the physical properties and behavior under IT-PEMFC *operando* conditions should be elucidated. The investigated PAcILs can be divided into the following two sets:

a) with a primary ammonium group and a sulfonic, sulfuric and phosphoric acid group:
2-sulfoethylammonium triflate [SEA^+][TfO^-]
2-(sulfooxy)ethan-1-ammonium triflate [$SOEA^+$][TfO^-],
2-(phosphonooxy)ethan-1-ammonium triflate [PEA^+][TfO^-]

b) with a sulfonic acid group and a different functionalized ammonium group:
N,*N*-diethyl-3-sulfopropan-1-ammonium triflate [$DESPA^+$][TfO^-],
N,*N*-diethyl-*N*-methyl-3-sulfopropan-1-ammonium triflate [$DEMSPA^+$][TfO^-]

From these PAcILs only [PEA^+][TfO^-] [$DESPA^+$][TfO^-], [$DEMSPA^+$][TfO^-] display the required thermal stability beyond 120 °C in synthetic air. These results show that higher thermal stability can be achieved with a higher degree of functionalization at the ammonium group. However, the acid group also seems to have a significant impact on thermal stability, as demonstrated by [PEA^+][TfO^-] and [$SOEA^+$][TfO^-]. While [PEA^+][TfO^-] and [$SOEA^+$][TfO^-] both contain a primary ammonium group [PEA^+][TfO^-] is one of the thermally most stable PAcILs investigated, and [$SOEA^+$][TfO^-] is thermally labile, probably due to the cleavage of the sulfuric acid group.

PAcILs with a primary ammonium displayed a larger tendency to crystalize compared to PAcILs with higher functionalized ammonium groups.

So both [SEA^+][TfO^-] and [PEA^+][TfO^-] crystalized at room temperature and a melting points of 50 °C and 52 °C was measured, respectively.

[$DESPA^+$][TfO^-], [$DEMSPA^+$][TfO^-] and [$SOEA^+$][TfO^-] were reluctant to crystallization. For [$DESPA^+$][TfO^-], [$DEMSPA^+$][TfO^-] the suppression of the crystallization can be rationalized by enhanced charge shielding and sterically demand of the bulky cations. For [$SOEA^+$][TfO^-] the absence of a crystallization might be related to the undeterminable amount of water in the PAcIL. On indication for a higher water content could be the in comparison to [SEA^+][TfO^-] and [PEA^+][TfO^-] lower T_g.

The largest difference between the PAcILs with the primary ammonium and higher functionalized one was observed for the reaction with water. While [$SOEA^+$][TfO^-], [SEA^+][TfO^-], [PEA^+][TfO^-] react with water back to their zwitterionic precursor, which precipitates, [$DESPA^+$][TfO^-] and [$DEMSPA^+$][TfO^-] are miscible with water up to at least a 1:1 (wt:wt) ratio. At 120 °C this aqueous mixtures of [$DESPA^+$][TfO^-] and [$DEMSPA^+$][TfO^-] are stable against hydrolysis for at least 24 h. In contrast [$SOEA^+$][TfO^-] shows a rapid hydrolysis under these conditions.

[PEA^+][TfO^-] displays a high thermal stability, but is due to its crystallization and reaction with water not suitable for the designated IT-PEMFC application. However, it would be interesting to quarternize the ammonium group in [PEA^+][TfO^-] and to reevaluate the properties of this compound to see if the crystallization and reaction with water is successfully suppressed and test the electrochemical performance of the modified [PEA^+][TfO^-].

Due to their thermal stability, reluctance to crystallization and stability in the presence of water, both at room temperature and 120 °C [$DESPA^+$][TfO^-] and [$DEMSPA^+$][TfO^-] were identified as the most promising PAcILs for IT-PEMFC applications

To make the [$DESPA^+$][TfO^-] more environmentally and economically attractive, in the second part of the dissertation , the highly fluorinated triflate anion was replaced with a novel fluorine-free hydrogen methanedisulfonate [$HMDS^-$] anion. An identical thermal stability for [$DESPA^+$][$HMDS^-$] and [$DESPA^+$][TfO^-] was found. By a comparative study with precursors and salts of similar compounds it was demonstrated that the limiting factor for the thermal stability might be the cation structure and not the anion. At 120 °C a similar ionic conductivity was observed for the two PAcILs despite the much higher viscosity of [$DESPA^+$][$HMDS^-$]. This was explained by a decoupling of the viscous flow and the ionic conductivity. The decoupling manifests in the lower pseudo-activation energy for the ionic conductivity compared to the viscous flow obtained from fitting the data to the Vogel-Fulcher-Tammann-Hesse (VFTH) equation and in a strongly pronounced superionic behavior of [$DESPA^+$][$HMDS^-$] in the Walden plot ($\Delta W > 0.8$).

Diffusion coefficients of the different protons from PGSE NMR measurements reveal, that above 100 °C the proton of the sulfonic acid group in the cation structure moves via a cooperative Grotthuss-like proton transfer mechanism.

Thereby probably a proton transfer between the cations and anions takes place. Towards lower temperatures, an unprecedented switch from the cooperative to a vehicular proton transport mechanism was observed. This finding demonstrates the role of the acidic proton in the side chain for an enhance proton conductivity due to a cooperative proton conduction mechanism.

Electrochemical experiments reveal a sufficiently wide electrochemical stability window of [$DESPA^+$][$HMDS^-$] for IT-PEMFC application and an oxygen reduction reaction onset potential comparable to [$DESPA^+$][TfO^-]. While the oxygen saturation concentration in both PAcILs is similar, the oxygen diffusion coefficient in [$DESPA^+$][$HMDS^-$] is significantly lower than in [$DESPA^+$][TfO^-]. The lower O_2 diffusion coefficient might be related to the high viscosity of [$DESPA^+$][$HMDS^-$]. The fact that the diffusion-limited current density in [$DESPA^+$][$HMDS^-$] is in the same order of magnitude compared to [$DESPA^+$][TfO^-], could probably be explained by a compensation of the slower oxygen diffusion by the fast proton transport through the cooperative proton transport mechanism in [$DESPA^+$][$HMDS^-$].

Towards the application of [$DESPA^+$][$HMDS^-$], there are two main tasks. First, to improve the low oxygen diffusion in [$DESPA^+$][$HMDS^-$] based electrolytes, blends with other PAcILs could be tested. The rapid proton transport through the cooperative mechanism might eventually be retained in blends with other PAcILs, while the viscosity could be reduced and thereby the oxygen diffusion coefficient could be enhanced. Second, [$DESPA^+$][$HMDS^-$] has to be incorporated in a membrane. Preliminary experiments with O-PBI have demonstrated that solvent casting from DMSO is not possible because of aggregation/gelation of dissolved O-PBI in the presents of [$DESPA^+$][$HMDS^-$]. Therefore, alternative membrane materials like SPEEK or different membrane fabrication procedures have to be tested.

Nevertheless, [$DESPA^+$][$HMDS^-$] is a highly attractive PAcIL both from a scientific and application perspective. The [$HMDS^-$] anion presented in this work might potentially be used for the synthesis of other ILs with beneficial properties as well.

6. Addendum: Viscosity and Rheology in Ionic Liquids

Part of the results in this section were obtained for the publication:

[103] de Araujo Lima e Souza, G., Di Pietro, M. E., Castiglione, F., Marques Mezencio, P. H., Fazzio Martins Martinez, P., Mariani, A., **Schütz, H. M.**, Passerini, S., Middendorf, M., Schönhoff, M., Triolo, A., Appetecchi, G. B. & Mele, A. Implications of Anion Structure on Physicochemical Properties of DBU-Based Protic Ionic Liquids. J. Phys. Chem. B 126, 7006–7014 (2022)

Despite their many beneficial and promising properties, like low vapor pressure and good thermal and electrochemical stability, the commercial application of ILs and PILs is often limited by their high viscosity. For processing and technical application of ILs not only their viscosity but their behavior under shear is of high relevance for e.g. shear-thinning is a beneficial effect when piping systems and pumps are applied. Beside the relevance in technical applications, the investigations on the behavior under shear might support the fundamental understanding of the liquid structure in ILs for example by uncovering ion-clusters and dynamic heterogeneities. While many papers are related to the viscosity of ILs only a view include rheological experiments of ionic liquids. Some selected papers are discussed together with the experimental results of this thesis in the following paragraphs. One additional highlighted publication and a review are reference [152] and [153].

A basic and widely recognized study on the viscosity of ionic liquids has been published by K. R. Seddon, A. Stark and M-J. Torres. There they describe in detail the influence of the main impurities in aprotic ILs, water and halides such as chloride and organic solvents. Although it is often claimed in citations that this paper is about the question of whether ILs are Newtonian fluids, this aspect is not dealt with in this study and all presented measured values were obtained with a viscometer, i.e. without shear rate control[21].

However, the same authors have present in a conference proceeding the investigation on the flow behavior of different 1-alkyl-3-methylimidazolium-based ILs (entry 1 in Table 13). At 65 °C all investigated ILs displayed a Newtonian behavior. For 40 °C a non-Newtonian shear-thinning was observed in [12MIM$^+$][BF_4^-]. This finding was explained by a liquid crystalline mesophase with a lamellar bilayer structure at this temperature. Under shear the ordered liquid structure gets disrupted and therefore the viscosity drops with increasing shear rate i.e. shear-thinning occurs.

The small hysteresis between increasing and decreasing shear rate ramp was interpreted by an incomplete structure recovery on the time scale of the experiment[154].
Seddon's observation of Newtonian behavior in ILs was confirmed for several common aprotic ILs (Table 13) like tetra-alkylammonium-based (entry 3-4) and pyrrolidinium-based ILs (entry 5-8).

Table 13 Literature review about some ILs with Newtonian or non-Newtonian behavior.

No.	IL	Temperature / °C	Shear rate range / s^{-1}	Newtonian y=yes n=no	Reference
1	$[XMIM^+][BF_4^-]$ X=4-8 $[XMIM^+][PF_6^-]$ X=4-12 $[12MIM^+][BF_4^-]$ $[12MIM^+][BF_4^-]$	65 " " 40	n.d " ~25-200 ~0-0.8	y y y n, shear-thinning	[154]
2	$[N222H^+][TFSI^-]$	20	100-1000	y	[155]
3	$[NX222^+][TFSI^-]$ X=6,8,10,12,14	25	0-12000	y	[156]
4	$[N2222^+]$ $[TFSI^-]$ $[N2222^+]$ $[IM14^-]$ $[N2222^+]$ $[BETI^-]$	>30	100-2000	y	[157]
5	$[PYR1X^+][TFSI^-]$ X=3,4,5,6,7,8,10 $[PYR1iso\text{-}4^+][TFSI^-]$ $[PYR1sec\text{-}4^+][TFSI^-]$	>30 Investigated 20-80	100–2000	y	[158]
6	$[PYR1X^+][TFSI^-]$ X=1,3,4 $[PYR1(2O1)^+]$ $[TFSI^-]$ $[PYR1(2O2)^+][TFSI^-]$ $[PYR1X^+][BETI^-]$ (X=1,3,4), $[PYR1X^+][IM14^-]$ (X=1,3,4)	>30	100-2000	y	[157]
7	$[PYR14^+][TFSI^-]$ $[PYR13^+][FSI^-]$ mixtures of both	20-80	100-2000	y	[159]
8	$[PYR14^+][TFSI^-]$ $[PYR14^+][IM14^-]$ mixtures of both	20-80	100–2000	y	[160]

While most of examples Table 13 are aprotic tetra-alkylammonium and pyrrolidinium-based ILs, Newtonian behavior was also observed for the PIL Triethylammonium bis(tetrafluoromethylsulfonyl)amide $[N222H^+][TFSI^-]$ (entry 2) over the wide shear rate range from 100-1000 s^{-1}.

In this thesis the flow behavior of several 1,8-diazabicyclo[5.4.0]-undec-7-ene $[DBU^+]$-based PILs with the (trifluoromethanesulfonyl)-(nonafluorobutanesulfonyl)imide $[IM14^-]$, $[TFO^-]$, $[TFSI^-]$ and bis(pentafluoroethylsulfonyl)imide $[BETI^-]$ anion was investigated (Figure 48 a)-d)).

All these PILs display Newtonian behavior at room-temperature or close to their melting point. Therefore, the author of this thesis assumes, based on his experience, that the PILs will display Newtonian behavior at higher temperatures in the investigated shear rate range of 1-100 s^{-1}, too.

Similarly Newtonian behavior was observed for [$DESPA^+$][$HMDS^-$] at 80 °C (Figure 48 e)). At 20 °C no linear shear rate sweep with the same rate was possible, because due to the high viscosity the time to reach a constant shear rate was significantly longer. Instead an experiment was performed, where the shear rate was increased stepwise up to the experimental limit for this sample of 80 s^{-1}. The obtained viscosity is rather constant and only a change of about 2.6% was observed, which could be assumed to be within the experimental uncertainty. Therefore also [$DESPA^+$][$HMDS^-$] is a Newtonian liquid under the investigated conditions of 1-100 s^{-1} and temperatures of 20-80 °C and probably above.

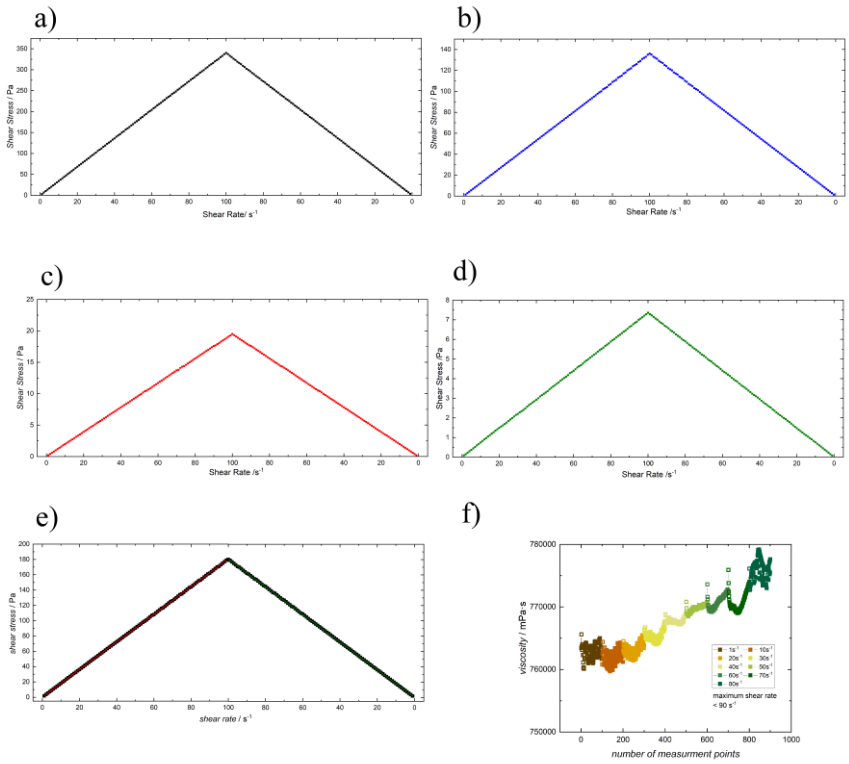

Figure 48 Plot of the shear stress vs. the shear rate of [DBU^+][TfO^-] at 20 °C a), [DBU^+][$IM14^-$] at 20°C b), [DBU^+][$TFSI^-$] at 30 °C c) and [DBU^+][$BETI^-$] at 60 °C d), [$DESPA^+$][$HMDS^-$] at 80 °C with linear fits in red and green e). Plot of the viscosity over the number of measurement points for [$DESPA^+$][$HMDS^-$] at 20° C f). All measurements were performed with an MCR 102 Rheometer (Anton Paar) in a plate-plate geometry (PP25/DI/Ti rotor) with a 100 µm gap. Precise temperature control was achieved using a Peltier-heated P-PTD200/DI base plate and an H-PTD200 actively-heated geometry housing. For the experiments a)-e) a linear shear rate sweep was performed and each shear rate was hold for 3 s. The viscosity in f) was measured by a stepwise increase of the shear rate from 1-100 s^{-1}. However due to the high viscosity the maximum achievable shear rate was 80 s^{-1}. The different shear rates in f) are color-coded and the open symbols correspond to points where a constant shear rate has not been reached. Figure 48e) and 48f) are reproduced from Ref. [96], licensed under CC BY 3.0. In e) the fitting equations and some text on the experimental conditions has been removed from the original image.

While most studies confirm that ILs including PILs behave like Newtonian-fluids, a few reports of non-Newtonian behavior i.e. shear-thinning or shear-thickening are known.

J. A. Smith, G. B. Weber, G. G. Warr and R. Atkins investigated the rheology of different ammonium-based PILs with nitrate and formate anions. In the studied nitrates the water content was below the limit of detection by Karl Fischer titration while the water content in the formates was below 1000 ppmw. At 23 °C both ethanolammonium nitrate $[N(CH_2CH_2OH)HHH^+][NO_3^-]$ and dimethylethylammonium formate $[N112H^+][HCO_2^-]$ display Newtonian-behavior in the whole investigated range up to 4000 s^{-1} or 1000 s^{-1}, respectively. For ethylammonium nitrate $[N2HHH^+][NO_3^-]$, ethylammonium formate $[N2HHH^+][HCO_2^-]$ and propylammonium nitrate $[N3HHH^+][NO_3^-]$ a slightly shear-thinning was observed in this study. J.A. Smith et al. suggest that the shear-thinning is related to the rupture of a sponge-like liquid phase with polar and apolar domains.

In this thesis some of the experiments by J.A. Smith et al. were partially reproduced and the shear rate dependent shear stress and viscosity for ethylammonium nitrate $[N2HHH^+][NO_3^-]$ (green open squares), butylammonium nitrate $[N4HHH^+][NO_3^-]$ (blue open circles) and the reference fluid ethylenglycol (black open squares) are reported in Figure 49. The water content of ethylammonium nitrate $[N2HHH^+][NO_3^-]$, butylammonium nitrate $[N4HHH^+][NO_3^-]$ and ethylenglycol was 16 ppmw, 250 ppmw and about 275 ppmw.

In the shear rate shear stress plot in Figure 49a the experimental datapoints are displayed together with linear fittings (dashed lines). The shear rate and shear stress seem proportional for both PILs and for the reference fluid. However, a closer look reveals that the datapoints drop slightly below the fitting lines for higher shear rates.

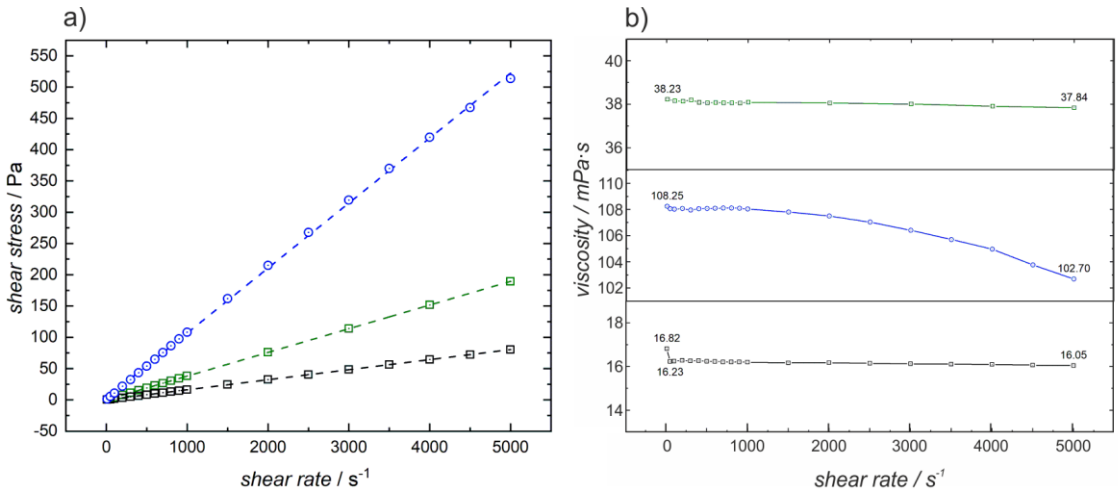

Figure 49 a) Flow curves of butylammonium nitrate (blue), ethylammonium nitrate (green) and ethylengylcol (black). The points correspond to the measurement values and the dashed lines are linear fits. In b) the corresponding viscosity values are displayed. The lines in b) are only a guide to the eye.

The slope in the shear rate shear stress diagram corresponds to the viscosity, which is displayed in Figure 49b. For [N4HHH$^+$][NO_3^-] the viscosity drops for about 6%, when the value at a shear rate of 10 s^{-1} is compared with the value at 5000 s^{-1}. The viscosity in ethylammonium nitrate [N2HHH$^+$][NO_3^-] only slightly drops between 10-5000s^{-1}. The finding that the shear-thinning is more pronounced in [N4HHH$^+$][NO_3^-] compared [N2HHH$^+$][NO_3^-] agrees with the work by J.A. Smith et al. where propylammonium nitrate [N3HHH$^+$][NO_3^-] is stronger shear-thinning than [N2HHH$^+$][NO_3^-]. Longer alkyl chain seems to lead to a more pronounced shear-thinning. The viscosity of [DESPA$^+$][TfO$^-$] and other PAcILs in this work display a quite strong pounced shear rate dependency. In Figure 50a) the flow curve of [DESPA$^+$][TfO$^-$] is shown. Here the results were obtained both from single point measurements with the different shear rates (points) and from a linear shear rate sweep (black line). In Figure 50b) the dynamic response to shear rate jumps is displayed. In the 3rd step of the three periods of the measurement the viscosity recovery can be observed. This shear-thinning is surprising for a pure PAcIL. Usually shear-thinning is related to some structural break down or reorientation of particles. Therefore, it might imply that a certain liquid structure exists in the PAcIL. A. Piednoir et al. studied the flow behavior of [10MIM$^+$][TFSI$^-$] and thereby observed similar apparent shear-thinning. They attributed the decrease in viscosity to shear heating[33]. Considering shear heating as the source for the viscosity drop in [DESPA$^+$][TfO$^-$] a large temperature increase of about 20 °C would have to be assumed.

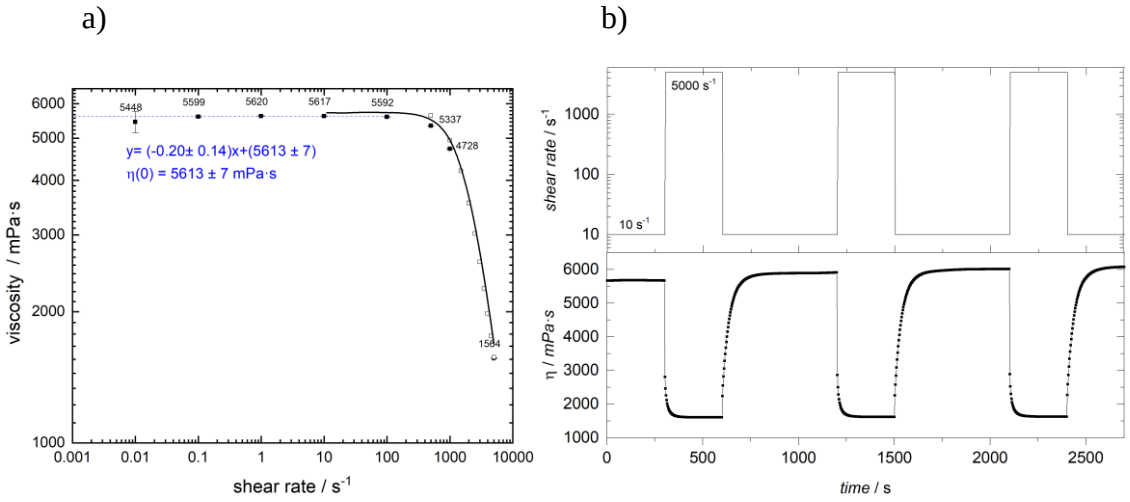

Figure 50 a) Shear rate-dependent viscosity of [DESPA$^+$][TfO$^-$] at 25 °C. The open and filled rectangles represent two different measurement series. Each symbol represents the average of 10-66 measurement points (dependent on the shear rate), which were obtained with a constant shear rate. Between the sampling intervals with constant shear, the shear rate was increased stepwise with a rest period between each step. The labels near by the symbols correspond to the viscosity values. The error bars at the filled symbols correspond to the standard deviation. The solid black line is the results from a linear shear-sweep between 10-5000 s^{-1}. The blue dashed line is a linear fit through the points of the Newtonian plateau to extrapolate the values to the zero-shear viscosity η(0). b) Dynamic response of [DESPA$^+$][TfO$^-$] to variations in the shear rate. All experiments are performed at 25 °C with the Teflon-coated cone-plate geometry.

G. L. Burrell performed a similar investigation on several aprotic and protic ILs. Thereby for some cases also a shear-thinning was observed. For the protic ionic liquids the shear-thinning was explained by IL aggregates due to an intermolecular hydrogen bond network[161].

In summary of this investigation and literature review it can be said, that many ILs behave like Newtonian fluids over wide temperature and shear rate ranges. However, for a few examples, especially for protic ILs shear-thinning (or in some cases shear-thickening) was observed. This behavior was interpreted by shear heating i.e. an experimental artefact or by aggregates due the hydrogen bond network in the PILs.

To further investigate the shear-thinning the author of the thesis tried to perform Rheo-SAXS experiments at the SWING beamline 1 of the Soleil Synchrotron near Paris (France). Unfortunately, the required shear stress conditions could not be reached to observe shear-thinning without spilling the PAcIL out of the geometry. Therefore, further investigations are required both with rheology, spectroscopy etc. to get deeper understanding of the liquid structure in ILs.

7. Appendix

7.1 Additional Mathematical Formulas and Derivations

Isobaric thermal expansion coefficient

$$\alpha_p = \frac{1}{V}\left(\frac{\partial V}{\partial T}\right) = \frac{\rho}{m}\left(\frac{\partial\left(\frac{m}{\rho}\right)}{\partial T}\right)_p = \frac{\rho}{m}\left(\frac{\frac{\partial m}{\partial T}\rho - m\frac{\partial \rho}{\partial T}}{\rho^2}\right)_p$$
$$= \frac{\rho}{m}\left(\frac{-m\frac{\partial \rho}{\partial T}}{\rho^2}\right)_p = -\frac{\rho \cdot m}{m \cdot \rho^2}\left(\frac{\partial \rho}{\partial T}\right)_p = -\frac{1}{\rho}\left(\frac{\partial \rho}{\partial T}\right)_p \quad (49)$$

With:

$$V = \frac{m}{\rho}$$

With ρ: density[g/m^3], m: mass[g], V: volume[m^3] and T: temperature[K]

$$\alpha_p = -\frac{1}{\rho}\left(\frac{\partial \rho}{\partial T}\right)_p = -\frac{1}{e^{ln(\rho)}}\left(\frac{\partial e^{ln(\rho)}}{\partial T}\right)_p = -\frac{1}{e^{(A+B\cdot T+C\cdot T^2)}}\left(\frac{\partial e^{(A+B\cdot T+C\cdot T^2)}}{\partial T}\right)_p$$
$$= -\frac{1}{e^{(A+B\cdot T+C\cdot T^2)}}\left((B+2C\cdot T)e^{(A+B\cdot T+C\cdot T^2)}\right) \quad (50)$$
$$= -(B+2C\cdot T)$$

With:

$$\ln\left(\frac{\rho}{kg\cdot m^{-3}}\right) = A + B\cdot T + C\cdot T^2$$

With ρ: density[g/m^3], T: temperature[K], A[K^{-1}], B[K^{-1}] and C[K^{-2}] are fitting parameters

Vogel-Fulcher-Tammann-Hesse (VFTH) equation in its original form with the decadic logarithm

$$log_{10}(\eta) = -\mathrm{A}' + \frac{\mathrm{B}' \cdot 10^3}{T - \mathrm{T}_0}$$

$$\frac{\ln(\eta)}{ln(10)} = -\mathrm{A}' + \frac{\mathrm{B}' \cdot 10^3}{T - \mathrm{T}_0}$$

$$\ln(\eta) = -\mathrm{A}' \cdot ln(10) + \frac{\mathrm{B}' \cdot 10^3 \cdot ln(10)}{T - \mathrm{T}_0}$$

$$\ln(\eta) = ln\left(10^{-A'}\right) + \frac{\mathrm{B}' \cdot 10^3 \cdot ln(10)}{T - \mathrm{T}_0}$$

$$\eta = exp\left[ln\left(10^{-A'}\right) + \frac{\mathrm{B}' \cdot 10^3 \cdot ln(10)}{T - \mathrm{T}_0}\right] \quad (51)$$

$$\eta = exp\left[ln\left(10^{-A'}\right)\right] \cdot exp\left[\frac{\mathrm{B}' \cdot 10^3 \cdot ln(10)}{T - \mathrm{T}_0}\right]$$

$$\eta = 10^{-A'} exp\left[\frac{\mathrm{B}' \cdot 10^3 \cdot ln(10)}{T - \mathrm{T}_0}\right]$$

By comparison of coefficients

$$\eta_\infty = 10^{-A'} \; and \; B_\eta = B' \cdot 10^3 \cdot ln(10)$$

Vogel-Fulcher-Tammann-Hesse (VFTH) equation in the exponential form

$$\eta = \eta_\infty \cdot \exp\left[\frac{B_\eta}{T - \mathrm{T}_0}\right]$$

$$\ln(\eta) = ln(\eta_\infty) + \frac{B_\eta}{T - \mathrm{T}_0}$$

with $\ln(\eta) = log_{10}(\eta)\ln(10)$

$$log_{10}(\eta)\ln(10) = ln(\eta_\infty) + \frac{B_\eta}{T - \mathrm{T}_0} \quad (52)$$

$$log_{10}(\eta) = \frac{ln(\eta_\infty)}{\ln(10)} + \frac{\frac{B_\eta}{\ln(10)}}{T - \mathrm{T}_0}$$

By comparison of coefficients

$$A' = -\frac{ln(\eta_\infty)}{\ln(10)} \text{ and } B' = \frac{B_\eta}{\ln(10)}$$

7.2 Additional Experimental and Literature Data

Table S 1 Comparison of the atomic radii and atomic contributions to the molecular volume from A. Bondi, D. W. M. Hofmann, S. Alvarez and Y. H. Zhao [66–68]. *(a) The values are not given in the reference, but were calculated from values given there with the formula for the volume of a sphere $V=4/3\pi r^3$ or $r=(3V/4\pi)^{1/3}$.*

Element	r(Bondi) / Å	r(Alvarez) / Å	r(Hofmann) / Å (a)	r(Zhao) / Å
H	1.20	1.20	1.07	1.20
C	1.70	1.77	1.49	1.70
N	1.55	1.66	1.41	1.55
O	1.52	1.50	1.40	1.52
F	1.47	1.46	1.39	1.47
P	1.80	1.90	1.91	1.80
S	1.80	1.89	1.82	1.80

Element	V_{atom}(Bondi) / Å^3 (a)	V_{atom}(Alvarez) / Å^3 (a)	V_{atom}(Hofmann) / Å^3	V_{atom}(Zhao) / Å^3
H	7.24	7.24	5.08	7.24
C	20.58	23.23	13.87	20.58
N	15.60	19.16	11.80	15.60
O	14.71	14.14	11.39	14.71
F	13.31	13.04	11.17	13.31
P	24.43	28.73	29.05	24.43
S	24.43	28.28	25.20	24.43

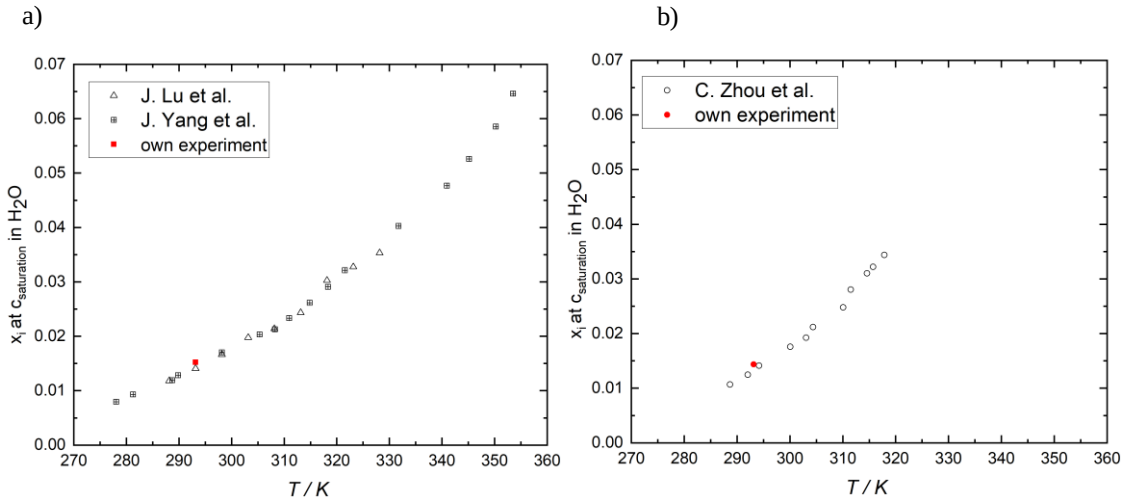

Figure S 1 a) Mole fraction x_i of taurine i.e. SEA zwitterion in water at the saturation concentration from own experiments (red symbol) and from J. Lu et al.[162] *and J. Yang et al.*[163] *b) Mole fraction x_i of SOEA zwitterion in water at the saturation concentration from own experiments (red symbol) and from C. Zhou et al.*[164].

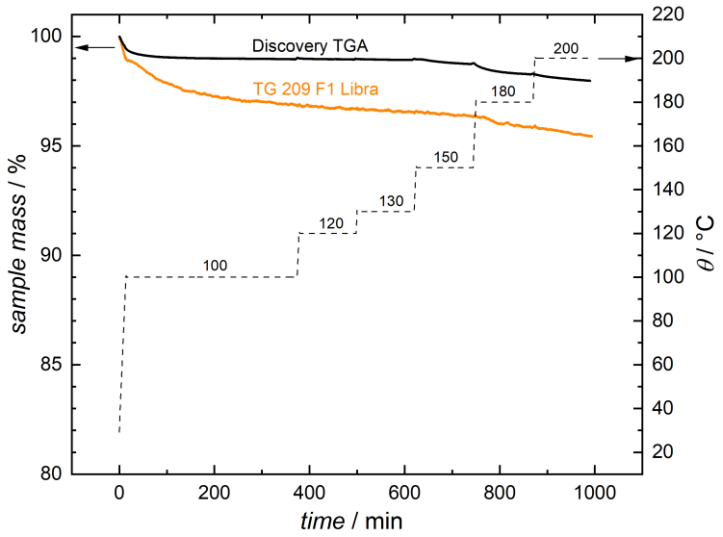

Figure S 2 Isothermal TGA measurements of [DESPA⁺][HMDS⁻] with a Discovery TGA and a TG 209 F1 Libra. Both experiments are performed in synthetic air (20 v% O_2 and 80 v% N_2) in aluminum crucibles. The heating rate between the isothermal steps was 5 K·min $^{-1}$. The sample mass was 2.8 mg and 2.2 mg in the experiments with the TG 209 F1 Libra and Discovery TGA respectively.

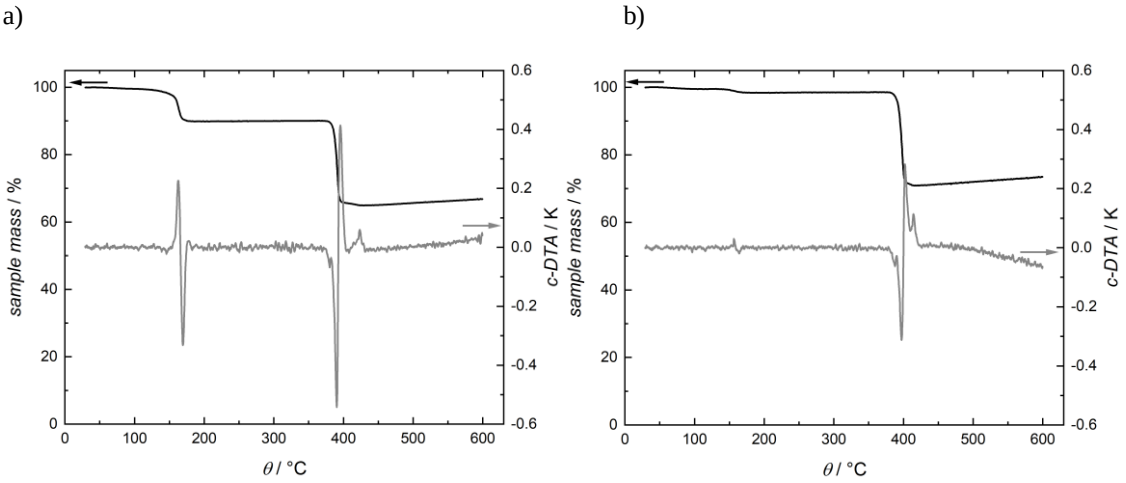

Figure S 3 TGA and c-DTA curves of a) 2^{end} and b) 3rd batch of self-synthesized barium methanedisulfonate. The measurements are performed with aluminum crucibles in synthetic air with 5 K·min^{-1} heating rate.

a) b)

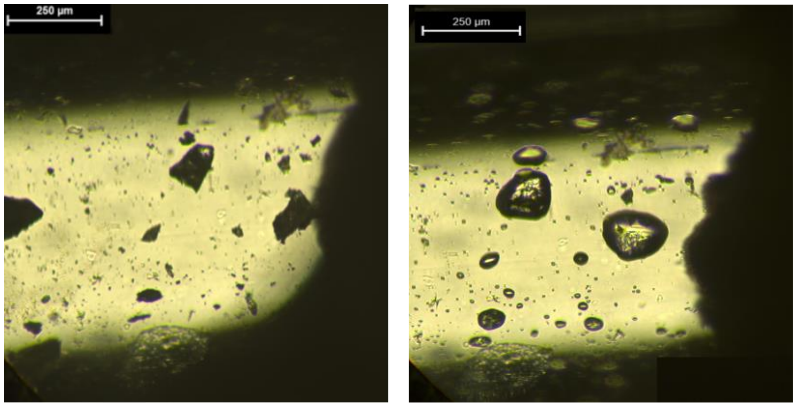

Figure S 4 Optical microscope image of H2MDS in the melting capillary a) before the melting process at ambient temperature without temperature control. b) after 3 min at 80 °C. In between the pictures the sample was heated with 5 K·min^{-1} to 40 °C and then with 2 °C·min^{-1} to 80 °C.

Table S 2 Calculated molar volume V_m of the [MDS^{2-}] anion from crystal structures. The calculation was performed according to equation (45). The values $V_m(C^+)$ are from [64].(a) own calculation of V_{cell} from angle and axis of unit cell, considering the space group. (b) V_{cell} from the reference.

Chemical structure	CCDC Identifier	V_m $CH_2O_6S_2^{2-}$= [MDS^{2-}]/ Å^3	V_{Cell} / Å^3	Z	$V_m(C^+)$ / Å^3	Reference
$Ca[(CH_2O_6S_2)(H_2O)_3]$	original CAMSOA/ revised CAMSOA02	123	864.58(a)	4	20.1+3·24.5	[165]
$Ca[(CH_2O_6S_2)(H_2O)_3]$	CAMSOA01	124	870.26(a) 870.30(b)	4	20.1+3·24.5	[166]
$K_2[CH_2(SO_3)_2]$	not listed	122	709.99(a)	4	2·27.7	[167]
$(NH_4)_2[CH_2(SO_3)_2]$	not listed	119	761.88(a)	4	2·35.6	[167]
$K_2[CH_2(SO_3)_2]$	POTMES	122	707.85(a) 707.90(b)	4	2·27.7	[168]
$Cs_2[CH_2(SO_3)_2]$	LARXOT	126	838.95(a) 838.95(b)	4	2·42.0	[169]

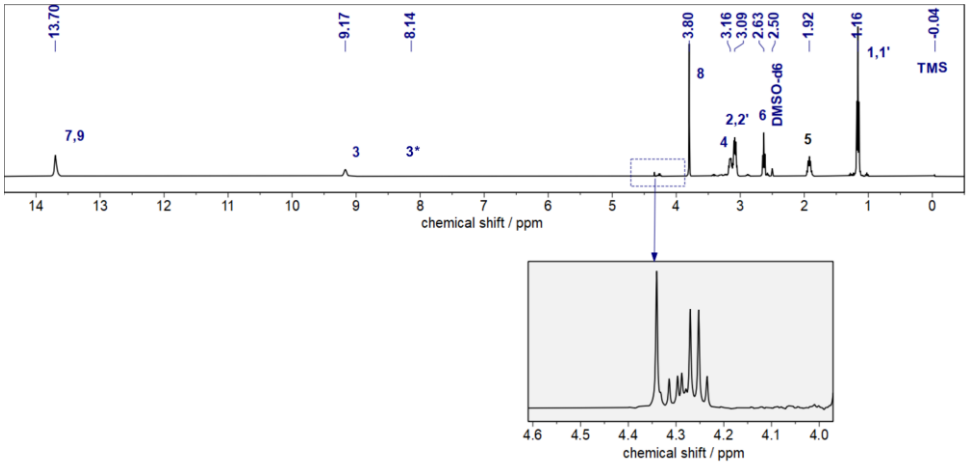

Figure S 5 ^{1}H-NMR of [DESPA^{+}][HMDS^{-}] in DMSO-d$_6$. The synthesis was performed in a 1:2 mixture of absolute methanol/ethanol. The zoom highlights impurities formed by the synthesis in the alcohols. The numbers for the peak assignment are the same like in Figure 37.

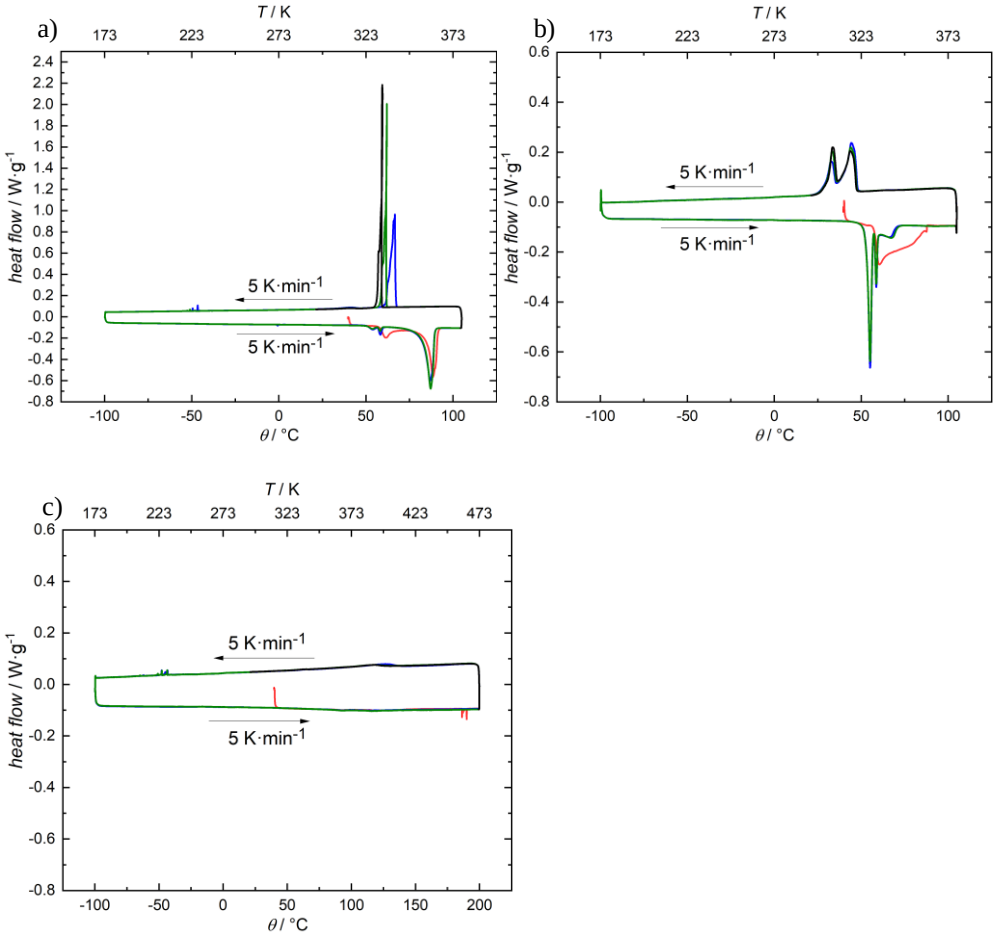

Figure S 6 DSC curves of crystals from an equimolar mixture of aqueous H2MDS and K2MDS solutions. First heating ramp red, 1st complete cycle blue, 2nd cycle olive and final cooling to 40 °C black. a) and b) data from two different crystals. c) DSC curves after recrystallisation from water.

Table S 3 Overview on density and isobaric thermal expansivity of some imidazolium based ILs. [(a)] The two temperature values are the boarders of the studied temperature range. [(b)] ρ in the table is converted to $g \cdot cm^{-3}$ and rounded to three decimal places. [(c)] For consistency reasons, the slope from the linear fit of the density is here reported with a negative sign, although positive values are given in the original publications and the sign is placed in front of the slope in the fitting equation. The slope here is equivalent to b in equation (15). [(d)] The isobaric thermal expansivity α_p was calculated according to equation (15). [(e)] The pressure is not reported.

IL	T/ K[(a)]	ρ (303.15 K) / $g \cdot cm^{-3}$ [(b)]	Data point	Linear fit slope / $g \cdot cm^{-3} \cdot K^{-1} \cdot 10^{-4}$ [(c)]	α_p (303.15 K) / $K^{-1} \cdot 10^{-4}$ [(d)]	Pressure / kPa [(e)]	Reference
$[4MIM^+][(C_2F_5SO_2)_2N^-]$	288.15 313.15	1.498	6	-10.30	6.9	-	170
$[4MIM^+][TFSI^-]$	288.15 313.15	1.435	6	-9.40	6.6	-	
$[4MIM^+][TfO^-]$	288.15 313.15	1.297	6	-8.00	6.2	-	
$[4MIM^+][PF_6^-]$	288.15 313.15	1.367	6	-8.69	6.4	-	
$[4MIM^+][CF_3CO_2^-]$	288.15 313.15	1.211	6	-7.54	6.2	-	
$[4MIM^+][BF_4^-]$	288.15 313.15	1.200	6	-7.26	6.1	-	
$[1MIM^+][TFSI^-]$	288.15 313.15	1.549	5	-10.6	6.8	-	171
$[2MIM^+][TFSI^-]$	288.15 313.15	1.517	6	-10.0	6.6	-	
$[6MIM^+][TFSI^-]$	288.15 313.15	1.361	6	-10.2	7.5	-	
$[8MIM^+][TFSI^-]$	288.15 313.15	1.317	6	-10.0	7.6	-	

Table S 4 Overview on density and isobaric thermal expansivity of [Pyr_{14}^+][$TFSI^-$]. The density values are from the "NIST Standard Reference Database 147: NIST Ionic Liquids Database - (ILThermo)" Version 2.0 by National Institute of Standards and Technology, Gaithersburg MD, 20899, http://ilthermo.boulder.nist.gov. (Updated 28.12.2022). Further information about the database can be found in [172] *. Data are retrieved on 02.07.2023. Only experiments with vibrating tube method at approximately atmospheric pressure and with at least 10 data points are considered.* [(a)] *The two temperature values are the boarders of the studied temperature range.* [(b)] *ρ in the table is converted to g·cm^{-3} and rounded to three decimal places. The two values correspond to the density at the lowest and highest investigated temperature, respectively.* [(c)] *The slope was calculated with the SLOPE function of Microsoft Excel 2019 MSO (16.0.10399.20000) 64-Bit.* [(d)] *The isobaric thermal expansivity α_p was calculated according to equation (15) for the lowest and highest temperature in a data set.*

IL	T/ K[(a)]	ρ / g·cm^{-3} [(b)]	Data point	Linear fit slope / g·cm^{-3}·K^{-1} ·10^{-4} [(c)]	α_p / K^{-1}·10^{-4} [(d)]	Pressure / kPa	Data set from ILThermo
[Pyr_{14}^+][$TFSI^-$]	278.15 343.15	1.412 1.355	14	-8.82	6.2 6.5	100	Ramos-Estrada et al. 2018
	293.15 413.15	1.400 1.296	11	-8.66	6.2 6.7	100	Sas et al. 2018
	283.15 343.15	1.408 1.355	13	-8.87	6.3 6.5	101.325	Yebra et al. 2018
	298.15 373.15	1.395 1.330	13	-8.68	6.2 6.5	100	Sanchez-Ramirez et al. 2017
	288.15 363.15	1.403 1.338	16	-8.69	6.2 6.5	101.325	Zorebski et al. 2017b
	293.15 363.15	1.406 1.345	15	-8.72	6.2 6.5	101.325	Rodrigues et al. 2016
	293.15 343.15	1.399 1.355	11	-8.76	6.3 6.5	101.325	Seoane et al. 2012b
	293.15 353.15	1.399 1.342	13	-9.41	6.7 7.0	101.325	Vranes et al. 2012
	278.15 373.15	1.413 1.330	20	-8.71	6.2 6.5	101.325	Gacino et al. 2011
	273.15 363.15	1.417 1.338	14	-8.70	6.1 6.5	101.325	Harris and Woolf 2011
	292.2 309.7	1.401 1.386	19	-8.14	5.8 5.9	101.325	Katsuta et al. 2010
	289 309.1	1.404 1.389	11	-7.85	5.6 5.7	101.325	Kumelam et al. 2010
	278.15 343.15	1.412 1.355	14	-8.77	6.2 6.5	101.325	Pereiro et al. 2009
	293.49 414.93	1.398 1.294	10	-8.57	6.1 6.6	101.325	Jacquemin et al. 2008c
	298.15 348.15	1.394 1.366	11	-5.22	3.7 3.8	101.325	Kato and Gmehling 2005a

$$\alpha_p \equiv -\frac{b}{\rho} = -\frac{b}{a + b \cdot T}$$

With $\rho = a + b \cdot T$

$$\Delta\alpha_p = \sqrt{\left(\frac{\partial \alpha_p}{\partial b} \cdot \Delta b\right)^2 + \left(\frac{\partial \alpha_p}{\partial a} \cdot \Delta a\right)^2 + \left(\frac{\partial \alpha_p}{\partial T} \cdot \Delta T\right)^2} \tag{53}$$

$$\Delta\alpha_p = \sqrt{\left(\frac{a}{(a + b \cdot T)^2} \cdot \Delta b\right)^2 + \left(-\frac{b}{(a + b \cdot T)^2} \cdot \Delta \mathrm{a}\right)^2 + \left(-\frac{b^2}{(a + b \cdot T)^2} \cdot \Delta \mathrm{T}\right)^2}$$

[$DESPA^+$][$HMDS^-$] $\Delta\alpha_p = 4.9 \cdot 10^{-7}$ K

[$DESPA^+$][TfO^-] $\Delta\alpha_p = 9.5 \cdot 10^{-7}$ K

With Δb and Δa the uncertainties of the linear fit of ρ versus T (see Table 7), ΔT of Anton Paar DMA 4100 M according to manual 0.05 °C. For T 293 K, the lowest investigated temperature, was chosen, because lower temperatures lead to a higher measurement uncertainty according to the formula.

Table S 5 Literature review about diffusion coefficients in PILs measured by NMR techniques. D_+ , D_- and D_{H+} are the diffusion coefficients of the cation, anion and from the acidic proton, respectively. "-" marks missing values in the publication. [(a)] The values are extracted from a graph in the reference.

Reference	PIL	H_2O/ ppmw	T/K	D_+ / $cm^2\ s^{-1}$	D_-/ $cm^2\ s^{-1}$	D_{H+}/ $cm^2\ s^{-1}$	D_{H+}/ D_+	D_{H+}/ D_-	D_+/ D_-
149	[MSEA$^+$][TfO$^-$]	7500-8000	363	6.60E-07	-	1.31E-06	1.98	-	-
		60000		1.65E-06	-	6.00E-06	3.64	-	-
104	[N221H$^+$][Ac$^-$]	-	298	1.31E-06	8.46E-07	9.03E-07	0.69	1.07	1.55
	[N221H$^+$][TFAc$^-$]	-		3.97E-07	3.90E-07	3.93E-07	0.99	1.01	1.02
	[N221H$^+$][MS$^-$]	-		2.45E-07	2.48E-07	2.46E-07	1.00	0.99	0.99
	[N221H$^+$][TfO$^-$]	-		4.35E-07	1.91E-07	4.40E-07	1.01	2.30	2.28
144	[N222H$^+$][MS$^-$]	<100	373	1.55E-06	1.60E-06	1.59E-06	1.03	0.99	0.97
	[N222H$^+$][MS$^-$]	1291		1.24E-06	1.29E-06	1.49E-06	1.20	1.16	0.96
	[N222H$^+$][TFSI$^-$]	138		2.14E-06	1.71E-06	2.18E-06	1.02	1.27	1.25
	[N222H$^+$][BETI$^-$]	219		1.16E-06	7.97E-07	1.16E-06	1.00	1.46	1.46
	[N222H$^+$][$AlCl_4^-$]	very low		2.30E-06	-	2.30E-06	1.00	-	-
151	[PyrHH$^+$][HSO_4^-][(a)]	200-30000	367	2.45E-11	2.45E-11	8.85E-11	3.61	3.61	1.00
			287	6.87E-12	7.35E-12	2.52E-11	3.66	3.42	0.94
145	[N222H$^+$][Ac$^-$]	-	340	2.51E-06	2.95E-06	3.54E-06	1.41	1.20	0.85
	[N222H$^+$][TFAc$^-$]	-		1.97E-06	1.94E-06	1.90E-06	0.96	0.98	1.02
	[N222H$^+$][TFSI$^-$]	-		1.27E-06	9.70E-07	1.29E-06	1.02	1.33	1.31
150	[N222H$^+$][PF$^-$]	-	373	7.20E-07	5.63E-07	1.56E-06	2.17	2.77	1.28
	[N222H$^+$][TfO$^-$]	-		2.35E-07	1.92E-06	2.46E-07	1.05	0.13	0.12
	[N33HH$^+$][TfO$^-$]	-		4.58E-07	4.24E-07	5.30E-07	1.16	1.25	1.08
	[N333H$^+$][TfO$^-$]	-		5.73E-06	4.94E-06	6.45E-07	0.11	0.13	1.16
	[Pyr4H$^+$][TfO$^-$]	-		1.30E-06	1.18E-06	1.55E-06	1.19	1.31	1.10
	[BMEA$^+$][PF$^-$]	-		6.95E-07	6.70E-07	8.35E-07	1.20	1.25	1.04
	[BMEA$^+$][TfO$^-$]	-		1.48E-06	1.46E-06	1.41E-06	0.95	0.97	1.01
	[BMEA$^+$][TFSI$^-$]	-		3.20E-06	2.03E-06	3.35E-06	1.05	1.65	1.58
90	[N222H$^+$][MS$^-$]	-	373	1.74E-06	1.73E-06	1.91E-06	1.10	1.10	1.01
	[N222H$^+$][TfO$^-$]	-		2.35E-06	1.92E-06	2.46E-06	1.05	1.28	1.22
148	[2-SEMA$^+$][TfO$^-$]	8000	343	2.00E-08	2.60E-08	4.20E-08	2.10	1.62	0.77
		20000		2.30E-08	3.00E-08	7.40E-08	3.22	2.47	0.77
		40000		4.10E-08	4.70E-08	1.47E-07	3.59	3.13	0.87
		60000		7.50E-08	2.05E-07	4.12E-07	5.49	2.01	0.37
	[2-SEMA$^+$][TfO$^-$]	60000	363	1.70E-06	-	5.60E-06	3.29	-	-
	[HEIM$^+$][TfO$^-$]	68000	363	1.24E-04	-	1.71E-04	1.38	-	-
	[N221H$^+$][TfO$^-$]	70000	303	1.12E-05	-	1.13E-05	1.01	-	-

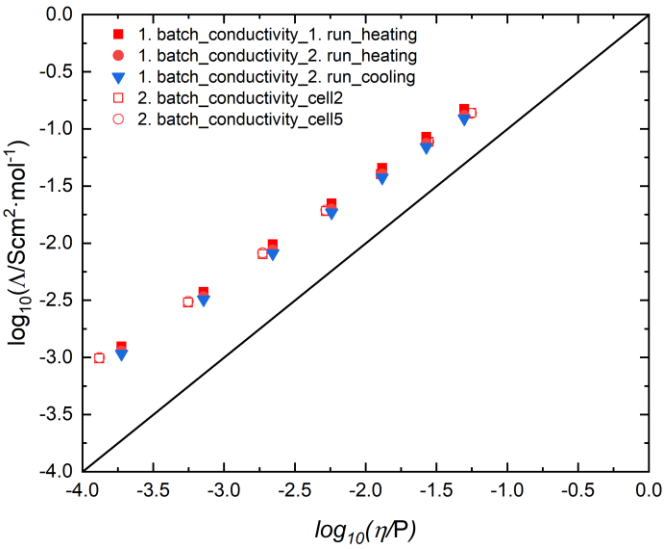

Figure S 7 Walden plot containing all data about [DESPA⁺][HMDS⁻] obtained in this thesis. For the synthesis of the 1. batch self-synthesized H2MDS was used. The 2. batch was prepared with commercial H2MDS. Heating and cooling denotes the scan direction of the conductivity measurement. For the 1. batch all ionic conductivity measurements shown were performed with the same cell and sample. For the second batch two different conductivity cells are compared. For each batch a set of viscosity values was measured. For the first batch the experiments were performed with a Teflon-coated cone-plate geometry. The second batch was measured with the plate-plate geometry, described in the experimental section.

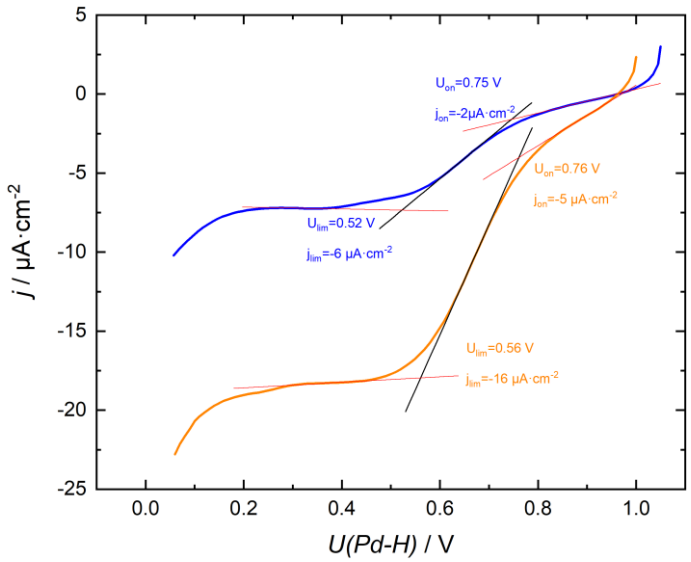

Figure S 8 Example for the determination of the onset potentials in [DESPA⁺][HMDS⁻] with the tangent method. The black lines are tangents and the red lines are linear fits of the upper and lower baseline.

Table S 6 Diffusion coefficient of O_2 (D_{O2}) and saturation concentration of O_2 (c_{O2}) measured at 90 °C and 120 °C in [$DESPA^+$][$HMDS^-$] (1.83-2.31 wt% H_2O) by chronoamperometry with a disc-shaped Pt microelectrode (radius r_0=125 µm). The potential jump was performed from the OCV (1-1.025 V) to a potential in the diffusion-limited range (0.25-0.425 V). Data were evaluated by fitting the curve of the cell current vs. time to the Shoup-Szabo equation in OriginPro 2019.

	90 °C			120 °C		
No.	$D_{O2}.10^{-7}$ /$cm^2 \cdot s^{-1}$	$C_{O2}.10^{-6}$ /$mol \cdot cm^{-3}$	R^2	$D_{O2}.10^{-7}$ /$cm^2 \cdot s^{-1}$	$C_{O2}.10^{-6}$ /$mol \cdot cm^{-3}$	R^2
1	0.68	1.92	0.9980	1.67	1.77	0.9997
2	0.50	2.26	0.9982	1.88	1.51	0.9997
3	0.75	1.42	0.9962	2.27	1.35	1.0000
4	0.22	3.20	0.9975	1.87	1.62	0.9998
5	0.78	1.32	0.9971	2.62	1.19	1.0000
6	0.81	1.23	0.9967	2.59	1.20	1.0000
7	0.38	2.05	0.9997	1.63	1.96	0.9996
8	0.21	2.47	0.9973	1.86	1.55	0.9999
9	0.27	2.14	0.9973	1.22	2.01	0.9999
10	0.69	1.46	0.9998	1.39	2.20	0.9996
11	1.73	0.74	0.9993	1.26	2.08	0.9999
12	1.39	0.83	0.9991	1.84	2.10	0.9996
13				1.93	1.76	0.9998
14				2.20	1.85	0.9998
15				1.75	1.96	0.9998
Average	**0.70**	**1.75**		**1.86**	**1.74**	
Standard deviation	**0.46**	**0.72**		**0.42**	**0.33**	

8. Acknowledgement

I want to express my gratitude to Prof. Dr. Stefano Passerini for giving me the chance to pursue my doctoral thesis in his group on a very current topic. Without his enduring trust, patience, and support, this work would not have been possible. Thank you also for the opportunity to be part of a very international and open-minded team. Without these experiences, I would surely not be the same person today, both scientifically and personally.

I thank Prof. Dr. Rolf Schuster for being the second supervisor of my thesis.

I owe my thanks to Matteo Bonomo and Stefano Nejrotti from Turin University for performing the PGSE NMR measurements of [$DESPA^+$][$HMDS^-$] and the evaluation of the data

I thank all cooperation partners in the HiFi-PEFC project for the fruitful work, especially Hui Hou, Ying Chen and Carsten Korte from the IEK-14 at Research Center Jülich. for the support with the electrochemical experiments on the ESW, ORR and C_{O2} and D_{O2}, during my one-month research stay in the group. Jürgen Giffin is thanked for his work in the management of the HiFi-PEFC project.

Thanks to Xinpei Gao for his introduction to the IL synthesis and donation of the DESPA and DEMSPA zwitterions and some IL samples.

Thanks to Christian Tontsch from the Institute of Organic Chemistry I of Ulm University for performing numerous monodimensional NMR experiments and always being open for discussions about non-standard measurements.

I thank the Institute of Analytical and Bioanalytical Chemistry (IABC) of University Ulm for providing the CHNS analysis service.

Jason Lelovas and Jakob Aschenbauer from HIU are thanked for performing the ICP-OES measurements.

I would like to thank Alessandro Mariani for the organization of the HIFI-PEFC project on the HIU side. His numerous ideas and our sometimes passionate discussions have contributed to this work and my scientific and personal development. Thank you for the introduction into the world of science, especially the ionic liquids community, and for establishing and supporting the collaboration with Matteo Bonomo and Stefano Nejrotti

Thanks to all HIU members, especially, Alex, Haipeng and Dominik K1&K2 and Matthias, Nikhil and Clemens for the fruitful discussions and your support in the lab.

Thanks to Alessandro Innocenti for the support with VFTH fitting in Mathlab and all scientific talks. Thanks to Xilai for the support especially in the final phase of the writing.

Special thanks to my office mates Annika, Fanglin and Xu for always creating a pleasant atmosphere, which made the office my second home, and for your assistance with both the small and seemingly larger challenges of science and everyday life.

Thank you to all my friends and fellow students who supported me during my doctoral research and throughout my studies. Special thanks to my fellow students from the Bachelor's program in Konstanz. Without you, the start of my chemistry studies might not have gone so smoothly.

The financial support of the Federal Ministry for Economic Affairs and Energy (HiFi-PEFC, project number: 03ETB003A+ 03ETB003B) and the support of the Helmholtz Association is gratefully acknowledged.

At last I would like to give my heartful gratitude to my parents and brothers and sister. Without your support a chemistry study would not have been possible in this way. Thank you for always supporting me to overcome all private and professional challenges. Big thanks to my grandparents Max† and Margarete† and granduncle and grandaunt Toni† and Maya. Your interest in my studies and support was fundamental for this work.

Finally, I thank Baokun, my girlfriend. You have always supported me with full dedication, believed in me, and comforted me. Thank you for our scientific discussions, the delicious Chinese food, and even hands-on support in the laboratory ;-). You have sacrificed a lot, especially during the long 1 ½ years of the writing phase. Without your support, this work would have been hardly possible, and life outside my PhD journey wouldn't have been as sunny.

9. List of Abbreviations

AIL(s)	**A**protic **I**onic **L**iquid(s)
BaMDS	**B**arium **m**ethane**di**sulfonate
BDEs	**b**ond **d**issociation **e**nergies
c-DTA	**C**alculated **D**ifferential **T**hermo **A**nalysis
D_2O	fully deuterated water (heavy water)
DMSO-d_6	fully deuterated **D**i**m**ethyl **s**ulf**o**xide
DSC	**D**ifferential **S**canning **C**alorimetry
DTA	**D**ifferential **T**hermal **A**nalysis
H2MDS	**M**ethane**di**sulfonic acid
HRMS	**H**igh-**r**esolution **M**ass **S**pectrometry
ICP-OES	**I**nductively **C**oupled Plasma **O**ptical **E**mission **S**pectroscopy
IL(s)	**I**onic **L**iquid**(s)**
IT-PEMFC	**I**ntermediate **T**emperature **P**roton-**e**xchange **M**embrane **F**uel **C**ell
K2MDS	Dipotassium **m**ethane**di**sulfonate
KF titration	**K**arl **F**ischer titration
NMR	**N**uclear **M**agnetic **R**esonance
ORR	**O**xygen **R**eduction **R**eaction
PAcIL(s)	**P**rotic **A**cidic **I**onic **L**iquid(s)
PEMFC	**P**roton-**e**xchange **M**embrane **F**uel **C**ell
PFSA	**P**er**f**luoro**s**ulfonic **a**cid
PGSE (NMR)	**P**ulsed-Field **G**radient **S**pin-**E**cho (**N**uclear **M**agnetic **R**esonance)
PIL(s)	**P**rotic **I**onic **L**iquid(s)
ppmw	**P**arts **p**er **m**illion (by **w**eight), $1 \mu g \cdot g^{-1}$
Ref.	reference
RF	**R**adio **F**requency
TGA	**T**hermo**g**ravimetric **A**nalysis
v%	**v**olume percentage
VFTH (equation/theory)	**V**ogel-**F**ulcher-**T**ammann-**H**esse (equation/theory)
wt%	**w**eigh**t** percentage

10. Scientific contributions

[8] **H. M. Schütz**, S. Nejrotti, H. Adenusi, A. Mariani, E. Bodo, M. Bonomo, A. Innocenti, C. Barolo, X. Gao, S. Passerini, Superionicity by design: high proton conductivity in a fluorine-free protic ionic liquid. Journal of Materials Chemistry A 2024, 12, 18412–18422, doi:10.1039/d4ta02880e.

[7] G. de Araujo Lima e Souza, M. E. Di Pietro, F. Castiglione, P. H. Marques Mezencio, P. Fazzio Martins Martinez, A. Mariani, **H. M. Schütz,** S. Passerini, M. Middendorf, M. Schönhoff, A. Triolo, G. B. Appetecchi, A. Mele, Implications of Anion Structure on Physicochemical Properties of DBU-Based Protic Ionic Liquids, The Journal of Physical Chemistry B 2022 126 (36), 7006-7014, doi:10.1021/acs.jpcb.2c02789

[6] X. Liu, M. Zarrabeitia, A. Mariani, X. Gao, **H. M. Schütz**, S. Fang, T. Bizien, G. A. Elia, S. Passerini, Enhanced Li^+ Transport in Ionic Liquid-Based Electrolytes Aided by Fluorinated Ethers for Highly Efficient Lithium Metal Batteries with Improved Rate Capability, Small Methods 2021, 5, 2100168, doi: 10.1002/smtd.202100168

[5] H. Hou, **H. M. Schütz**, J. Giffin, K. Wippermann, X. Gao, A. Mariani, S. Passerini, C. Korte, Acidic Ionic Liquids Enabling Intermediate Temperature Operation Fuel Cells, ACS Applied Materials & Interfaces 2021, 13, 7, 8370–8382, doi: 10.1021/acsami.0c20679

[4] Y.-J. Ma, Y. Ma, G. Giuli, H. Euchner, A. Groß, G.O. Lepore, F. d'Acapito, D. Geiger, J. Biskupek, U. Kaiser, **H. M. Schütz**, A. Carlsson, T. Diemant,R. J. Behm, M. Kuenzel, S. Passerini, D. Bresser, Introducing Highly Redox-Active Atomic Centers into Insertion-Type Electrodes for Lithium-Ion Batteries, Advanced Energy Materials 2020, 10, 2000783, doi: 10.1002/aenm.202000783

[3] S. Cwik, D. Mitoraj, O. Mendoza Reyes, D. Rogalla, D. Peeters, J. Kim, **H. M. Schütz**, C. Bock, R. Beranek, A. Devi, Direct Growth of MoS2 and WS2 Layers by Metal Organic Chemical Vapor Deposition, Advanced Materials Interfaces 2018, 5, 1800140, doi: 10.1002/admi.201800140

[2] D. Peeters, O. Mendoza Reyes, L. Mai, A. Sadlo, S. Cwik, D. Rogalla, H.-W. Becker, **H. M. Schütz,** J. Hirst, S. Müller, D. Friedrich, D. Mitoraj, M. Nagli, M. Caspary Toroker, R. Eichberger, R. Beranek, A. Devi, CVD-grown copper tungstate thin films for solar water splitting, Journal of Materials Chemistry A 2018, 6, 10206-10216, doi: 10.1039/c7ta10759e

[1] C.M. Frey, A. Eifert, **H. Schütz**, H. Barth, B. Mizaikoff, C. Kranz, Macroscopic and microscopic electrochemical investigation of Clostridium botulinum C2IIa embedded in supported lipid membranes, Electrochimica Acta 2016, 209, 341–349, doi: 10.1016/j.electacta.2016.05.055

Poster
5. International Conference on Ionic Liquid-based Materials (ILMAT)
Taurine-like based Ionic Liquids in High-Temperature Polymer Electrolyte Fuel Cells (HT-PEFC)

11. References

1. Doyle, A. C. Adventures of Sherlock Holmes. ADVENTURE I.—A SCANDAL IN BOHEMIA. *The Strand Magazine* **2,** 61–75 (1891).

2. Ernst, R. R. & Anderson, W. A. Application of Fourier Transform Spectroscopy to Magnetic Resonance. *Rev. Sci. Instrum.* **37,** 93–102 (1966).

3. Ernst, R. R. Nuclear Magnetic Resonance Fourier Transform Spectroscopy. in *Nobel Lecture* (ed. Malmström, B. G.) 12–57 (World Scientific Publishing Co., Singapore, 1992).

4. Chalk, S. J., McNaught, A. D. & Wilkinson, A. *The IUPAC Compendium of Chemical Terminology (3. edition)*. (International Union of Pure and Applied Chemistry (IUPAC), 2019). doi:10.1351/goldbook

5. Atkins, P. & de Paula, J. *Physical Chemistry (8. edition)*. (W.H. Freeman and Company, 2006).

6. Claridge, T. D. W. *High-Resolution NMR Techniques in Organic Chemistry (2. edition)*. (Elsevier Ltd, 2009).

7. Raja, P. M. V. & Barron, A. R. LibreTexts Chemisty 4.7: NMR Spectroscopy. at <https://chem.libretexts.org/Bookshelves/Analytical_Chemistry/Physical_Methods_in_Chemistry_and_Nano_Science_(Barron)/04%3A_Chemical_Speciation/4.07%3A_NMR_Spectroscopy>

8. Hesse, M., Meier, H. & Zeeh, B. *Spektroskopische Methoden in der organischen Chemie (6. edition)*. (Georg Thieme Verlag, 2002).

9. National Institute of Advanced Industrial Science and Technology. Spectral Database for Organic Compounds SDBS. at <https://sdbs.db.aist.go.jp>

10. Mariani, A., Bonomo, M., Gao, X., Centrella, B., Nucara, A., Buscaino, R., Barge, A., Barbero, N., Gontrani, L. & Passerini, S. The unseen evidence of Reduced Ionicity: The elephant in (the) room temperature ionic liquids. *J. Mol. Liq.* **324,** 115069 (2021).

11. Mittermaier, A. K. & Kay, L. E. Observing biological dynamics at atomic resolution using NMR. *Trends Biochem. Sci.* **34,** 601–611 (2009).

12. Walderhaug, H., Söderman, O. & Topgaard, D. Self-diffusion in polymer systems studied by magnetic field-gradient spin-echo NMR methods. *Prog. Nucl. Magn. Reson. Spectrosc.* **56,** 406–425 (2010).

13. Ahmed, H. M., Persson, A., Ökvist, L. S. & Björkman, B. Reduction Behaviour of Self-reducing Blends of In-plant Fines in Inert Atmosphere. *ISIJ Int.* **55,** 2082–2089 (2015).

14. Füglein, E. & Schmölzer, S. *Application Note: TG-Messung und c-DTA-Bestimmung an Polymeren*. at <https://analyzing-testing.netzsch.com/de/application-literature/tg-messungen-und-c-dta-r-bestimmung-an-polymeren>

15. Cowie, J. M. G. *Polymers: Chemistry and Physics of Modern Materials (2. edition)*. (Chapman and Hall, 1991).

16. Höhne, G., Hemminger, W. F. & Flammersheim, H.-J. *Differential Scanning Calorimetry (2. edition)*. (Springer, 2013).

17. Skoog, D. A., Holler, F. J. & Crouch, S. R. *Principles of Instrumental Analysis (6. edition)*. (Thomson Brooks/Cole, 2007).

18. Danley, R. L. New heat flux DSC measurement technique. *Thermochim. Acta* **395,** 201–208 (2002).

19. Danley, R. L. Heat Flux Differential Scanning Calorimeter Sensor, U.S. Patent No. 6,431,747 B1. (2002).

20. Elias, H.-G. *Makromoleküle Physikalische Struckturen und Eigenschaften (6. edition), Makromoleküle Band 2*. (Wiley-VCH Verlag GmbH, 2001).

21. Seddon, K. R., Stark, A. & Torres, M.-J. Influence of chloride, water, and organic solvents on the physical properties of ionic liquids. *Pure Appl. Chem.* **72,** 2275–2287 (2000).

22. Muhr, H.-J. & Rohner, R. *Good Titration Practice ™ in Karl Fischer Titration*. (Mettler-Toledo AG, 2009).

23. Fischer, K. Neues Verfahren zur maßanalytischen Bestimmung des Wassergehaltes von Flüssigkeiten und festen Körpern. *Angew. Chem.* **48,** 394–396 (1935).

24. Sigma Aldrich. Sicherheitsdatenblatt für 109257 CombiCoulomat fritless Karl Fischer Reagenz für die coulometrische Wasserbestimmung für Zellen mit und ohne Diaphragma Aquastar®. (2020).

25. Larsson, W. *New Approaches to Moisture Determination in Complex Matrices based on the Karl Fischer Reaction in Methanolic and Non-Alcoholic Media*. *PhD thesis* (Umeå University, 2008).

26. Gonzalez-Salgado, D., Troncoso, J. & Romani, L. Experimental Techniques 2: Vibrating Tube Densimetry. in *Volume Properties: Liquids, Solutions and Vapours* (eds. Wilhelm, E. & Letcher, T.) 100–113 (Royal Society of Chemistry, 2014).

27. Anton Paar. *Instruction Manual DMA 4100 M DMA 4500 M DMA 5000 M (Firmware Version V2.21)*. (Anton Paar GmbH, 2012).

28. Wilhelm, E. Volumetric Properties: Introduction, Concepts and Selected Applications. in *Volume Properties: Liquids, Solutions and Vapours* (eds. Wilhelm, E. & Letcher, T.) 1–55 (Royal Society of Chemistry, 2014).

29. Tiesinga, E., Mohr, P. J., Newell, D. B. & Taylor, B. N. Codata recommended values of the fundamental physical constants: 2018. *Rev. Mod. Phys.* **93,** 025010 (2021).

30. Costa, A. J. L., Soromenho, M. R. C., Shimizu, K., Marrucho, I. M., Esperança, J. M. S. S., Lopes, J. N. C. & Rebelo, L. P. N. Density, Thermal Expansion and Viscosity of Cholinium-Derived Ionic Liquids. *ChemPhysChem* **13,** 1902–1909 (2012).

31. Haynes, W. M., Lide, D. R. & Bruno, T. J. *CRC Handbook of Chemistry and Physics (97. edition)*. (CRC Press, 2017).

32. Mezger, T. *The Rheology Handbook (4. edition)*. (Vincentz Network, 2014).

33. Piednoir, A., Steinberger, A., Cottin-Bizonne, C. & Barentin, C. Apparent Non-Newtonian Behavior of Ionic Liquids. *J. Phys. Chem. B* **124,** 2685–2690 (2020).

34. RAMAN, C. V. A theory of the viscosity of liquids. *Nature* **111,** 532–533 (1923).

35. Andrade, E. N. da C. The Viscosity of Liquids. *Nature* **125,** 309–310 (1930).

36. Tammann, G. & Hesse, W. Die Abhängigkeit der Viscosität von der Temperatur bei unterkühlten Flüssigkeiten. *Z. Anorg. Allg. Chem.* **156,** 245–257 (1926).

37. Vogel, H. Das Temperaturabhängigkeitsgesetz der Viskosität von Flüssigkeiten. *Phys. Z.* **22,** 645–646 (1921).

38. Fulcher, G. S. ANALYSIS OF RECENT MEASUREMENTS OF THE VISCOSITY OF GLASSES. *J. Am. Ceram. Soc.* **8,** 339–355 (1925).

39. Cohen, M. H. & Turnbull, D. Molecular Transport in Liquids and Glasses. *J. Chem. Phys.* **31,** 1164–1169 (1959).

40. Williams, M. L., Landel, R. F. & Ferry, J. D. The Temperature Dependence of Relaxation Mechanisms in Amorphous Polymers and Other Glass-forming Liquids. *J. Am. Chem. Soc.* **77,** 3701–3707 (1955).

41. Ratner, M. A., Johansson, P. & Shriver, D. F. Polymer Electrolytes: Ionic Transport Mechanisms and Relaxation Coupling. *MRS Bull.* **25,** 31–37 (2000).

42. Quartarone, E. & Mustarelli, P. Electrolytes for solid-state lithium rechargeable batteries: recent advances and perspectives. *Chem. Soc. Rev.* **40,** 2525–2540 (2011).

43. Chagas, L. G., Jeong, S., Hasa, I. & Passerini, S. Ionic Liquid-Based Electrolytes for Sodium-Ion Batteries: Tuning Properties To Enhance the Electrochemical Performance of Manganese-Based Layered Oxide Cathode. *ACS Appl. Mater. Interfaces* **11,** 22278–22289 (2019).

44. Bio-Logic Science Instruments SAS. *Installation and Configuration Manual for MCS10*. (Bio-Logic Science Instruments SAS, 2015).

45. Walden, P. Über organische Lösungs- und Ionisierungsmittel. III. Teil: Innere Reibung und deren Zusammenhang mit dem Leitvermögen. *Z. Phys. Chem.* **55U,** 207–249 (1906).

46. Walden, P. Ueber die Molekulargrösse und elektrische Leitfähigkeit einiger geschmolzenen Salze. *Bull. Acad. Imp. Sci. St.-Pétersbourg* **8,** 405–422 (1914).

47. Angell, C. A., Imrie, C. T. & Ingram, M. D. From Simple Electrolyte Solutions Through Polymer Electrolytes to Superionic Rubbers: Some Fundamental Considerations. *Polym. Int.* **47,** 9–15 (1998).

48. Yoshizawa, M., Xu, W. & Angell, C. A. Ionic Liquids by Proton Transfer: Vapor Pressure, Conductivity, and the Relevance of ΔpKa from Aqueous Solutions. *J. Am. Chem. Soc.* **125,** 15411–15419 (2003).

49. Xu, W. & Angell, C. A. Solvent-Free Electrolytes with Aqueous Solution-Like Conductivities. *Science* **302,** 422–425 (2003).

50. Xu, W., Cooper, E. I. & Angell, C. A. Ionic Liquids: Ion Mobilities, Glass Temperatures, and Fragilities. *J. Phys. Chem. B* **107,** 6170–6178 (2003).

51. Angell, C. A., Byrne, N. & Belieres, J.-P. Parallel Developments in Aprotic and Protic Ionic Liquids: Physical Chemistry and Applications. *Acc. Chem. Res.* **40,** 1228–1236 (2007).

52. Schreiner, C., Zugmann, S., Hartl, R. & Gores, H. J. Fractional Walden Rule for Ionic Liquids: Examples from Recent Measurements and a Critique of the So-Called Ideal KCl Line for the Walden Plot. *J. Chem. Eng. Data* **55,** 1784–1788 (2010).

53. Hnedkovsky, L. & Hefter, G. Densities and Apparent Molar Volumes of Aqueous Solutions of $NaClO_4$, $KClO_4$, and KCl at Temperatures from 293 to 343 K. *J. Chem. Eng. Data* **66,** 3645–3658 (2021).

54. Kestin, J., Khalifa, H. E. & Correia, R. J. Tables of the dynamic and kinematic viscosity of aqueous KCl solutions in the temperature range 25–150 °C and the pressure range 0.1–35 MPa. *J. Phys. Chem. Ref. Data* **10,** 57–70 (1981).

55. Robinson, R. A. & Stokes, R. H. *Electrolyte Solutions (2. edition)*. (Dover, 2002).

56. Barthel, J., Feuerlein, F., Neueder, R. & Wachter, R. Calibration of Conductance Cells at Various Temperatures. *J. Solution Chem.* **9,** 209–219 (1980).

57. Angell, C. A., Ansari, Y. & Zhao, Z. Ionic Liquids: Past, present and future. *Faraday Discuss.* **154,** 9–27 (2012).

58. Belieres, J.-P. & Angell, C. A. Protic Ionic Liquids: Preparation, Characterization, and Proton Free Energy Level Representation. *J. Phys. Chem. B* **111,** 4926–4937 (2007).

59. Zhao, Z., Ueno, K. & Angell, C. A. High Conductivity, and 'dry' Proton Motion, in Guanidinium Salt Melts and Binary Solutions. *J. Phys. Chem. B* **115,** 13467–13472 (2011).

60. Cukierman, S. Et tu, Grotthuss! and other unfinished stories. *Biochim. Biophys. Acta* **1757,** 876–885 (2006).

61. Agmon, N. The Grotthuss mechanism. *Chem. Phys. Lett.* **244,** 456–462 (1995).

62. MacFarlane, D. R., Forsyth, M., Izgorodina, E. I., Abbott, A. P., Annat, G. & Fraser, K. On the concept of ionicity in ionic liquids. *Phys. Chem. Chem. Phys.* **11,** 4962–4967 (2009).

63. Krossing, I., Slattery, J. M., Daguenet, C., Dyson, P. J., Oleinikova, A. & Weingärtner, H. Why Are Ionic Liquids Liquid? A Simple Explanation Based on Lattice and Solvation Energies. *J. Am. Chem. Soc.* **128,** 13427–13434 (2006).

64. Glasser, L. & Jenkins, H. D. B. Internally Consistent Ion Volumes and Their Application in Volume-Based Thermodynamics. *Inorg. Chem.* **47,** 6195–6202 (2008).

65. Hofmann, D. W. M. Fast estimation of crystal densities. *Acta Cryst.* **B58,** 489–493 (2002).

66. Bondi, A. van der Waals Volumes and Radii. *J. Phys. Chem.* **68,** 441–451 (1964).

67. Alvarez, S. A cartography of the van der Waals territories. *Dalton Trans.* **42,** 8617–8636 (2013).

68. Zhao, Y. H., Abraham, M. H. & Zissimos, A. M. Fast Calculation of van der Waals Volume as a Sum of Atomic and Bond Contributions and Its Application to Drug Compounds. *J. Org. Chem.* **68,** 7368–7373 (2003).

69. Hou, H., Schütz, H. M., Giffin, J., Wippermann, K., Gao, X., Mariani, A., Passerini, S. & Korte, C. Acidic Ionic Liquids Enabling Intermediate Temperature Operation Fuel Cells. *ACS Appl. Mater. Interfaces* **13,** 8370–8382 (2021).

70. Backer, H. J. Préparation Simple De L'Acide Methionique. *Recl. Trav. Chim. Pays-Bas* **48,** 949–952 (1929).

71. Yi, Z. Method For Preparing Methanedisulfonic Acid, U.S. Patent No 9,440,915 B2. (2016).

72. Wippermann, K., Wackerl, J., Lehnert, W., Huber, B. & Korte, C. 2-Sulfoethylammonium Trifluoromethanesulfonate as an Ionic Liquid for High Temperature PEM Fuel Cells. *J. Electrochem. Soc.* **163,** F25–F37 (2016).

73. Wieser, C. Novel Polymer Electrolyte Membranes for Automotive Applications - Requirements and Benefits. *Fuel Cells* **4,** 245–250 (2004).

74. Rosli, R. E., Sulong, A. B., Daud, W. R. W., Zulkifley, M. A., Husaini, T., Rosli, M. I., Majlan, E. H. & Haque, M. A. A review of high-temperature proton exchange membrane fuel cell (HT-PEMFC) system. *Int. J. Hydrog. Energy* **42,** 9293–9314 (2017).

75. Li, Q., Hjuler, H. A., Aili, D. & Jensen, J. O. *High Temperature Polymer Electrolyte Membrane Fuel Cells - Approaches, Status, and Perspectives*. (Springer International Publishing, 2016).

76. Wainright, J. S., Wang, J. -T., Weng, D., Savinell, R. F. & Litt, M. Acid-Doped Polybenzimidazoles: A New Polymer Electrolyte. *J. Electrochem. Soc.* **142,** L121–L123 (1995).

77. Kaserer, S., Caldwell, K. M., Ramaker, D. E. & Roth, C. Analyzing the Influence of H_3PO_4 as Catalyst Poison in High Temperature PEM Fuel Cells Using in-operando X-ray Absorption Spectroscopy. *J. Phys. Chem. C* **117,** 6210–6217 (2013).

78. Klinedinst, K., Bett, J. A. S., Macdonald, J. & Stonehart, P. Oxygen Solubility And Diffusivity In Hot Concentrated H_3PO_4. *J. Electroanal. Chem. Interfacial Electrochem.* **57,** 281–289 (1974).

79. Seselj, N., Alfaro, S. M., Bompolaki, E., Cleemann, L. N., Torres, T. & Azizi, K. Catalyst Development for High-Temperature Polymer Electrolyte Membrane Fuel Cell (HT-PEMFC) Applications. *Adv. Mater.* **35,** 2302207 (2023).

80. Pilinski, N. & Wagner, P. Ion Chromatography of Process Waters of Various Fuel Cell Systems. in *4th Eur. PEFC H_2 Forum 2013* (2013). doi:10.13140/2.1.1245.7927

81. Kakinuma, K., Taniguchi, H., Asakawa, T., Miyao, T., Uchida, M., Aoki, Y., Akiyama, T., Masuda, A., Sato, N. & Iiyama, A. The Possibility of Intermediate–Temperature (120 °C)–Operated Polymer Electrolyte Fuel Cells using Perfluorosulfonic Acid Polymer Membranes. *J. Electrochem. Soc.* **169,** 044522 (2022).

82. Susan, Md. A. B. H., Noda, A., Mitsushima, S. & Watanabe, M. Brønsted acid–base ionic liquids and their use as new materials for anhydrous proton conductors. *Chem. Commun.* **3,** 938–939 (2003).

83. Angell, C. A., Xu, W., Belières, J.-P. & Yoshizawa, M. Ionic Liquids And Ionic Liquid Acids With High Temperature Stabilit For Fuel Cell And Other High Temperature Applications, Method Of Making And Cell Employing Same, WO Patent No. 2004/114445 A1. (2004).

84. Glasser, L. & Jenkins, H. D. B. Predictive thermodynamics for ionic solids and liquids. *Phys. Chem. Chem. Phys.* **18,** 21226–21240 (2016).

85. Plechkova, N. V. & Seddon, K. R. Applications of ionic liquids in the chemical industry. *Chem. Soc. Rev.* **37,** 123–150 (2008).

86. Eshetu, G. G., Armand, M., Ohno, H., Scrosati, B. & Passerini, S. Ionic liquids as tailored media for the synthesis and processing of energy conversion materials. *Energy Environ. Sci.* **9,** 49–61 (2016).

87. MacFarlane, D. R., Forsyth, M., Howlett, P. C., Kar, M., Passerini, S., Pringle, J. M., Ohno, H., Watanabe, M., Yan, F., Zheng, W., Zhang, S. & Zhang, J. Ionic liquids and their solid-state analogues as materials for energy generation and storage. *Nat. Rev. Mater.* **1,** 15005 (2016).

88. Zelenay, P., Scharifker, B. R., Bockris, J. O. & Gervasio, D. A Comparison of the Properties of CF_3SO_3H and H_3PO_4 in Relation to Fuel Cells. *J. Electrochem. Soc.* **133,** 2262–2267 (1986).

89. Wesseler, E. P., Iltis, R., Clark, L. C. Jr. THE SOLUBILITY OF OXYGEN IN HIGHLY FLUORINATED LIQUIDS. *J. Fluor. Chem.* **9,** 137–146 (1977).

90. Iojoiu, C., Martinez, M., Hanna, M., Molmeret, Y., Cointeaux, L., Leprêtre, J.-C., Kissi, N. El, Guindet, J., Judeinstein, P. & Sanchez, J.-Y. PILs-based Nafion membranes: a route to high-temperature PEFMCs dedicated to electric and hybrid vehicles. *Polym. Adv. Technol.* **19,** 1406–1414 (2008).

91. Thomson, J., Dunn, P., Holmes, L., Belieres, J.-P., Angell, C. A. & Gervasio, D. A Flourinated Ionic Liquid as a High-Performance Fuel Cell Electrolyte. *ECS Trans.* **13,** 21–29 (2008).

92. Nakamoto, H. & Watanabe, M. Brønsted acid–base ionic liquids for fuel cell electrolytes. *Chem. Commun.* 2539–2541 (2007).

93. Yasuda, T. & Watanabe, M. Protic ionic liquids: Fuel cell applications. *MRS Bull.* **38,** 560–566 (2013).

94. Miran, M. S., Yasuda, T., Tatara, R., Susan, Md. A. B. H. & Watanabe, M. Amphoteric water as acid and base for protic ionic liquids and their electrochemical activity when used as fuel cell electrolytes. *Faraday Discuss.* **206,** 353–364 (2018).

95. Burrell, G. L., Burgar, I. M., Separovic, F. & Dunlop, N. F. Preparation of protic ionic liquids with minimal water content and ^{15}N NMR study of proton transfer. *Phys. Chem. Chem. Phys.* **12,** 1571–1577 (2010).

96. Schütz, H. M., Nejrotti, S., Adenusi, H., Mariani, A., Bodo, E., Bonomo, M., Innocenti, A., Barolo, C., Gao, X. & Passerini, S. Superionicity by design: high proton conductivity in a fluorine-free protic ionic liquid. *J. Mater. Chem. A* **12,** 18412–18422 (2024).

97. Hasani, M., Nordstierna, L. & Martinelli, A. Molecular dynamics involving proton exchange of a protic ionic liquid-water mixture studied by NMR spectroscopy. *Phys. Chem. Chem. Phys.* **21,** 22014–22021 (2019).

98. Fiore, M., Madanamoothoo, W., Berlioz-Barbier, A., Maniti, O., Girard-Egrot, A., Buchet, R. & Strazewski, P. Giant vesicles from rehydrated crude mixtures containing unexpected mixtures of amphiphiles formed under plausibly prebiotic conditions. *Org. Biomol. Chem.* **15,** 4231–4240 (2017).

99. Zon, G., Ludeman, S. M. & Egan, W. High-Resolution Nuclear Magnetic Resonance Investigations of the Chemical Stability of Cyclophosphamide and Related Phosphoramidic Compounds. *J. Am. Chem. Soc.* **99,** 5785–5795 (1977).

100. Gilard, V., Martino, R., Malet-Martino, M., Niemeyer, U. & Pohl, J. Chemical Stability and Fate of the Cytostatic Drug Ifosfamide and Its N-Dechloroethylated Metabolites in Acidic Aqueous Solutions. *J. Med. Chem.* **42,** 2542–2560 (1999).

101. Tahoori, F., Balalaie, S., Sheikhnejad, R., Sadjadi, M. & Boloori, P. Design and synthesis of anti-cancer cyclopeptides containing triazole skeleton. *Amino Acids* **46,** 1033–1046 (2014).

102. Gai, K., Huang, Y., Liu, B. & Zhang, Y. Synthesis of obeticholic acid, a farnesoid X receptor agonist, and its major metabolites labeled with deuterium. *J. Label. Compd. Radiopharm.* **61,** 799–804 (2018).

103. de Araujo Lima e Souza, G., Di Pietro, M. E., Castiglione, F., Marques Mezencio, P. H., Fazzio Martins Martinez, P., Mariani, A., Schütz, H. M., Passerini, S., Middendorf, M., Schönhoff, M., Triolo, A., Appetecchi, G. B. & Mele, A. Implications of Anion Structure on Physicochemical Properties of DBU-Based Protic Ionic Liquids. *J. Phys. Chem. B* **126,** 7006–7014 (2022).

104. Davidowski, S. K., Thompson, F., Huang, W., Hasani, M., Amin, S. A., Angell, C. A. & Yarger, J. L. NMR Characterization of Ionicity and Transport Properties for a Series of Diethylmethylamine Based Protic Ionic Liquids. *J. Phys. Chem. B* **120,** 4279–4285 (2016).

105. Lemal, D. M. Perspective on Fluorocarbon Chemistry. *J. Org. Chem.* **69,** 1–11 (2004).

106. Guthrie, J. P. Hydrolysis of esters of oxy acids: pKa values for strong acids; Brønsted relationship for attack of water at methyl; free energies of hydrolysis of esters of oxy acids; and a linear relationship between free energy of hydrolysis and pKa holding over a range of 20 pK units. *Can. J. Chem.* **56,** 2342–2354 (1978).

107. Trummal, A., Lipping, L., Kaljurand, I., Koppel, I. A. & Leito, I. Acidity of Strong Acids in Water and Dimethyl Sulfoxide. *J. Phys. Chem. A* **120,** 3663–3669 (2016).

108. Buck, R. C., Franklin, J., Berger, U., Conder, J. M., Cousins, I. T., de Voogt, P., Jensen, A. A., Kannan, K., Mabury, S. A. & van Leeuwen, S. P. J. Perfluoroalkyl and Polyfluoroalkyl Substances in the Environment: Terminology, Classification, and Origins. *Integr. Environ. Assess. Manag.* **7,** 513–541 (2011).

109. Commission regulation (EU) 2021/1297 of 4 August 2021 amending Annex XVII to Regulation (EC) No 1907/2006 of the European Parliament and of the Council as regards perfluorocarboxylic acids containing 9 to 14 carbon atoms in the chain (C9-C14 PFCAs), their salts and C9-C14 PFCA-related substances. L 282/29 (2021).

110. Candidate List of substances of very high concern for Authorisation published in accordance with Article 59(10) of the REACH Regulation. (2023). at <https://www.echa.europa.eu/candidate-list-table>

111. ANNEX XV Restriction Report Consultation on Per- and polyfluoroalkyl substances (PFAS). submitted on 13-Jan-2023 at <https://echa.europa.eu/en/registry-of-restriction-intentions/-/dislist/details/0b0236e18663449b>

112. OECD. *Reconciling Terminology of the Universe of Per- and Polyfluoroalkyl Substances: Recommendations and Practical Guidance.* OECD Series on Risk Management No.61. (OECD Publishing Paris, 2021).

113. Korte, C. & Giffin, J. Abschlussbericht, Förderprojekt des Bundesministerium für Wirtschaft und Energie 03ETB003A + 03ETB003B, Hochtemperaturfeste Funktionalisierte Protonenleitende Ionische Flüssigkeiten für Mittel- bis Hochtemperatur- Polymerbrennstoffzellen. (2023).

114. Smith, T. L. & Elliott, J. H. Acid-Base Equilibria in Glacial Acetic Acid. *J. Am. Chem. Soc.* **75,** 3566–3571 (1953).

115. Brewster, P. M. & Jenkins, G. L. THE TITRATION CURVE OF METHIONIC ACID. *J. Am. Pharm. Assoc.* **28,** 144–146 (1938).

116. Amarasekara, A. S. Acidic Ionic Liquids. *Chem. Rev.* **116,** 6133–6183 (2016).

117. Wojnarowska, Z., Wang, Y., Paluch, K. J., Sokolov, A. P. & Paluch, M. Observation of highly decoupled conductivity in protic ionic conductors. *Phys. Chem. Chem. Phys.* **16,** 9123–9127 (2014).

118. Miran, M. S., Yasuda, T., Susan, Md. A. B. H., Dokko, K. & Watanabe, M. Binary Protic Ionic Liquid Mixtures as a Proton Conductor: High Fuel Cell Reaction Activity and Facile Proton Transport. *J. Phys. Chem. C* **118,** 27631–27639 (2014).

119. Song, D., Chen, J. & Liang, Y.-M. Anionic SO_3H-functionalized ionic liquid: An efficient and recyclable catalyst for the Pechmann reaction of phenols with ethyl acetoacetate. *Synth. Commun.* **48,** 692–698 (2018).

120. Cookson, R. F. Determination of Acidity Constants. *Chem. Rev.* **74,** 5–28 (1974).

121. Wang, G., Song, H., Li, R., Li, Z. & Chen, J. Olefin oligomerization via new and efficient Brönsted acidic ionic liquid catalyst systems. *Chin. J. Catal.* **39,** 1110–1120 (2018).

122. Zeisel, S. Ueber das Verhalten des Acetylens gegen concentrirte Schwefelsäure. *Liebigs Ann.* **191,** 366–375 (1878).

123. Schroeter, G. Ueber die Einwirkung von Acetylen auf rauchende Schwefelsäure. *Ber. Dtsch. Chem. Ges.* **31,** 2189–2190 (1898).

124. Muthmann, W. Bildung von Methandisulfonsäure durch Einwirkung von Acetylen auf rauchende Schwefelsäure. *Ber. Dtsch. Chem. Ges.* **31,** 1880–1884 (1898).

125. Strecker, A. Ueber eine neue Bildungsweise und die Constitution der Sulfosäuren. *Ann. Chem. Pharm.* **148,** 90–96 (1868).

126. Sartori, P., Jüschke, R., Boese, R. & Bläser, D. Zur Struktur von Dihydroxonium Alkandisulfonaten/The Structure of Dihydroxonium Alkanedisulfonates. *Z. Naturforsch. B* **49,** 1467–1472 (1994).

127. Sandler, S. R. Preparation of alkenedisulfonic acids, EP Patent No. 0 293 672 B1. (1988).

128. Werner, C., Kanschik-Conradsen, A., Hoffmeister, M., Heuduk, H. & Scholten, T. Low Pressure Process for the Preparation of Methanedisulfonic Acid Alkali Metal Salts, U.S. Patent No. 2006/0155142 A1. (2006).

129. Gramstad, T. & Haszeldine, R. N. 806. Perfluoroalkyl Derivatives of Sulphur. Part VII. Alkyl Trifluoromethanesulphonates as Alkylating Agents, Trifluoromethanesulphonic Anhydride as a Promoter for Esterification, and Some Reactions of Trifluoromethanesulphonic Acid. *J. Chem. Soc.* 4069–4079 (1957).

130. Opitz, G., Wiehn, W., Ziegler, M. L. & Nuber, B. Folgereaktionen von Sulfenen aus Sulfonylchloriden und tertiären Aminen, 3 [1,2] Kristallstrukturanalyse von Bis(trimethylammoniosulfonyl)methanid-tetraphenylborat.–n-σ*-Wechselwirkungen (Hyperkonjugation und Homohyperkonjugation) in Sulfen–Amin-S,N-Addukten. *Chem. Ber.* **125,** 1621–1626 (1992).

131. Goldwhite, H., Gibson, M. S. & Harris, C. FREE RADICAL ADDITION REACTIONS—IV: THE REACTION OF METHANESULPHONYL AND METHANEDISULPHONYL CHLORIDES WITH ALKENES. *Tetrahedron* **21,** 2743–2747 (1965).

132. Gramstad, T. & Haszeldine, R. N. 33. Perfluoroalkyl Derivatives of Sulphur. Part IV. Perfluoroalkanesulphonic Acids. *J. Chem. Soc.* 173–180 (1956).

133. Russell, D. G. & Senior, J. B. Studies on trifluoromethanesulfonic acid. Part 2. Conductivities of solutions of metal trifluoromethanesulfonates and other bases in trifluoromethanesulfonic acid. *Can. J. Chem.* **58,** 22–29 (1980).

134. Ausín, D., Parajó, J. J., Trenzado, J. L., Varela, L. M., Cabeza, O. & Segade, L. Influence of Small Quantities of Water on the Physical Properties of Alkylammonium Nitrate Ionic Liquids. *Int. J. Mol. Sci.* **22,** 7334 (2021).

135. Bockris, J. O., Richards, N. E. & Ubbelohde, A. R. J. P. The compressibilities, free volumes and equation of state for molten electrolytes: some alkali halides and nitrates. *Proc. R. Soc. A* **241,** 44–66 (1957).

136. Hou, H., Mariani, A., Suo, Y., Gao, X., Giffin, J., Rodenbücher, C., Passerini, S. & Korte, C. Tuning Polybenzimidazole Membrane by Immobilizing a Novel Ionic Liquid with Superior Oxygen Reduction Reaction Kinetics. *Chem. Mater.* **34,** 4298–4310 (2022).

137. Chin, D.-T. & Chang, H. H. On the conductivity of phosphoric acid electrolyte. *J. Appl. Electrochem.* **19,** 95–99 (1989).

138. Christensen, J. H. & Reed, R. B. Design and Analysis Data—Density of Aqueous Solutions of Phosphoric Acid Measurements at 25 °C. *Ind. Eng. Chem.* **47,** 1277–1280 (1955).

139. MacDonald, D. I. & Boyack, J. R. Density, Electrical Conductivity, and Vapor Pressure of Concentrated Phosphoric Acid. *J. Chem. Eng. Data* **14,** 380–384 (1969).

140. Vilčiauskas, L., Tuckerman, M. E., Bester, G., Paddison, S. J. & Kreuer, K.-D. The mechanism of proton conduction in phosphoric acid. *Nat. Chem.* **4,** 461–466 (2012).

141. Korte, C. Phosphoric Acid, an Electrolyte for Fuel Cells – Temperature and Composition Dependence of Vapor Pressure and Proton Conductivity. in *Fuel Cell Science and Engineering* (eds. Stolten, D. & Emonts, B.) 335–359 (Wiley-VCH Verlag GmbH & Co. KGaA, 2012).

142. Ansari, Y., Ueno, K. & Angell, C. A. Protic Ionic Liquids Can Be Both Free Proton Conductors and Benign Superacids. *J. Phys. Chem. B* **125,** 7855–7862 (2021).

143. Wojnarowska, Z., Kołodziejczyk, K., Paluch, K. J., Tajber, L., Grzybowska, K., Ngai, K. L. & Paluch, M. Decoupling of conductivity relaxation from structural relaxation in protic ionic liquids and general properties. *Phys. Chem. Chem. Phys.* **15,** 9205–9211 (2013).

144. Blanchard, J. W., Belières, J.-P., Alam, T. M., Yarger, J. L. & Holland, G. P. NMR Determination of the Diffusion Mechanisms in Triethylamine-Based Protic Ionic Liquids. *J. Phys. Chem. Lett.* **2,** 1077–1081 (2011).

145. Judeinstein, P., Iojoiu, C., Sanchez, J.-Y. & Ancian, B. Proton Conducting Ionic Liquid Organization as Probed by NMR: Self-Diffusion Coefficients and Heteronuclear Correlations. *J. Phys. Chem. B* **112,** 3680–3683 (2008).

146. Philippi, F., Rauber, D., Zapp, J. & Hempelmann, R. Transport properties and ionicity of phosphonium ionic liquids. *Phys. Chem. Chem. Phys.* **19,** 23015–23023 (2017).

147. Noda, A., Susan, Md. A. B. H., Kudo, K., Mitsushima, S., Hayamizu, K. & Watanabe, M. Brønsted Acid−Base Ionic Liquids as Proton-Conducting Nonaqueous Electrolytes. *J. Phys. Chem. B* **107,** 4024–4033 (2003).

148. Lin, J., Wang, L., Zinkevich, T., Indris, S., Suo, Y. & Korte, C. Influence of residual water and cation acidity on the ionic transport mechanism in proton-conducting ionic liquids. *Phys. Chem. Chem. Phys.* **22,** 1145–1153 (2020).

149. Lin, J. & Korte, C. Influence of the acid-base stoichiometry and residual water on the transport mechanism in a highly-Brønsted-acidic proton-conducting ionic liquid. *RSC Adv.* **10,** 42596–42604 (2020).

150. Iojoiu, C., Judeinstein, P. & Sanchez, J. Y. Ion transport in CLIP: Investigation through conductivity and NMR measurements. *Electrochim. Acta* **53,** 1395–1403 (2007).

151. Anouti, M., Porion, P., Brigouleix, C., Galiano, H. & Lemordant, D. Transport properties in two pyrrolidinium-based protic ionic liquids as determined by conductivity, viscosity and NMR self-diffusion measurements. *Fluid Ph. Equilib.* **299,** 229–237 (2010).

152. Pogodina, N. V., Nowak, M., Läuger, J., Klein, C. O., Wilhelm, M. & Friedrich, C. Molecular dynamics of ionic liquids as probed by rheology. *J. Rheol.* **55,** 241–256 (2011).

153. Shakeel, A., Mahmood, H., Farooq, U., Ullah, Z., Yasin, S., Iqbal, T., Chassagne, C. & Moniruzzaman, M. Rheology of Pure Ionic Liquids and Their Complex Fluids: A Review. *ACS Sustainable Chem. Eng.* **7,** 13586–13626 (2019).

154. Seddon, K. R., Stark, A. & Torres, M.-J. Viscosity and Density of 1-Alkyl-3-methylimidazolium Ionic Liquids. in *Clean Solvents* (eds. Abraham, M. A. & Moens, L.) **819,** 34–49 (ACS Symposium Series; American Chemical Society, 2002).

155. Timperman, L., Skowron, P., Boisset, A., Galiano, H., Lemordant, D., Frackowiak, E., Béguin, F. & Anouti, M. Triethylammonium bis(tetrafluoromethylsulfonyl)amide protic ionic liquid as an electrolyte for electrical double-layer capacitors. *Phys. Chem. Chem. Phys.* **14,** 8199–8207 (2012).

156. Machanová, K., Boisset, A., Sedláková, Z., Anouti, M., Bendová, M. & Jacquemin, J. Thermophysical Properties of Ammonium-Based Bis{(trifluoromethyl)sulfonyl}imide Ionic Liquids: Volumetric and Transport Properties. *J. Chem. Eng. Data* **57,** 2227–2235 (2012).

157. Appetecchi, G. B., Montanino, M., Carewska, M., Moreno, M., Alessandrini, F. & Passerini, S. Chemical-physical properties of bis(perfluoroalkylsulfonyl)imide-based ionic liquids. *Electrochim. Acta* **56,** 1300–1307 (2011).

158. Appetecchi, G. B., Montanino, M., Zane, D., Carewska, M., Alessandrini, F. & Passerini, S. Effect of the alkyl group on the synthesis and the electrochemical properties of N-alkyl-N-methyl-pyrrolidinium bis(trifluoromethanesulfonyl)imide ionic liquids. *Electrochim. Acta* **54,** 1325–1332 (2009).

159. Kunze, M., Jeong, S., Appetecchi, G. B., Schönhoff, M., Winter, M. & Passerini, S. Mixtures of ionic liquids for low temperature electrolytes. *Electrochim. Acta* **82,** 69–74 (2012).

160. Montanino, M., Moreno, M., Alessandrini, F., Appetecchi, G. B., Passerini, S., Zhou, Q. & Henderson, W. A. Physical and electrochemical properties of binary ionic liquid mixtures: (1 − X) $PYR_{14}TFSI$−(x) $PYR_{14}IM_{14}$. *Electrochim. Acta* **60,** 163–169 (2012).

161. Burrell, G. L., Dunlop, N. F. & Separovic, F. Non-Newtonian viscous shear thinning in ionic liquids. *Soft Matter* **6,** 2080–2086 (2010).

162. Lu, J., Zhou, X., Chen, L.-W., Zhang, L.-J. & Rohani, S. Solid−Liquid Equilibria of the Na_2SO_4 + $H_2NCH_2CH_2SO_3H$ + H_2O System from (288.15 to 328.15) K. *J. Chem. Eng. Data* **59,** 2115–2119 (2014).

163. Yang, J., Zhou, C.-R. & Shi, X.-H. Determination and Correlation of the Solubility for Taurine in Water and Organic Solvent Systems. *J. Chem. Eng. Data* **55,** 2620–2623 (2010).

164. Zhou, C., Wang, H., Shi, X. & Jiang, D. Calculation of the Solubilities for 2-Aminoethyl Hydrogen Sulfate and Taurine in Water by Wilson Equation. *Adv. Mat. Res.* **233–235,** 11–16 (2011).

165. Charbonnier, F., Faure, R. & Loiseleur, H. Double Conformation du Groupement Méthanedisulfonato à l'Intérieur d'un Même Cristal de Méthanedisulfonate d'Argent(I): $Ag_2(SO_3CH_2SO_3)$. *Acta Cryst.* **B35,** 1773–1775 (1979).

166. Karipides, A. The Structure of Calcium Methanedisulfonate Trihydrate. *Acta Cryst.* **B37,** 2232–2234 (1981).

167. Jones, D. W. A preliminary X-ray study of some alkali aminedisulphonates and methanedisulphonates. *Acta Cryst.* **8,** 66–67 (1955).

168. Truter, M. R. 670. The Crystal Structure of Potassium Methylenedisulphonate. *J. Chem. Soc.* **2,** 3393–3399 (1962).

169. Jianrattanasawat, S. & Mezei, G. 3,5-Dimethylpyrazole promoted sulfonation of acetic anhydride by H_2SO_4 to sulfoacetic acid and methanedisulfonic acid, and crystal structures of the complexes with Co^{2+}, Zn^{2+}, Ba^{2+}, Pb^{2+} and Cs^{+}. *Inorg. Chim. Acta* **384,** 318–323 (2012).

170. Tokuda, H., Hayamizu, K., Ishii, K., Susan, Md. A. B. H. & Watanabe, M. Physicochemical Properties and Structures of Room Temperature Ionic Liquids. 1. Variation of Anionic Species. *J. Phys. Chem. B* **108,** 16593–16600 (2004).

171. Tokuda, H., Hayamizu, K., Ishii, K., Susan, Md. A. B. H. & Watanabe, M. Physicochemical Properties and Structures of Room Temperature Ionic Liquids. 2. Variation of Alkyl Chain Length in Imidazolium Cation. *J. Phys. Chem. B* **109,** 6103–6110 (2005).

172. Dong, Q., Muzny, C. D., Kazakov, A., Diky, V., Magee, J. W., Widegren, J. A., Chirico, R. D., Marsh, K. N. & Frenkel, M. ILThermo: A Free-Access Web Database for Thermodynamic Properties of Ionic Liquids. *J. Chem. Eng. Data* **52,** 1151–1159 (2007).

173. Angell, C. A. Viscous Flow and Electrical Conductance in Ionic Liquids: Temperature and Composition Dependence in the Light of the Zero Mobility Concept. *J. Chem. Phys.* **46,** 4673–4679 (1967).

174. Angell, C. A. Electrical Conductance of Concentrated Aqueous Solutions and Molten Salts: Correlation through Free Volume Transport Model. *J. Phys. Chem.* **69,** 2137 (1965).

175. Görbitz, C. H., Prydz, K. & Ugland, S. Taurine. *Acta Cryst.* **C56,** e23–e24 (2000).